THE EFFECT OF HETEROGENEOUS ROUGHNESS ON CONVEYANCE CAPACITY AND APPLICATION TO THE SHIONO-KNIGHT METHOD

BY

MICHAEL JESSON

A thesis submitted to

The University of Birmingham

for the degree of

DOCTOR OF PHILOSOPHY

School of Civil Engineering

The University of Birmingham

2011

Abstract

Understanding the physical processes which occur within open-channel flow is necessary if the modelling of river flow is to be improved. This thesis examines in detail the flow in a type of channel which is common in natural rivers yet little researched, the heterogeneous channel (one whose bed is laterally horizontal but of varying roughness). The 3-D velocity field in a heterogeneous channel is mapped more fully and at a higher resolution than was achieved by the few previous studies of such channels, allowing the propagation and structure of turbulence within the channel to be investigated for the first time, using techniques such as Quadrant-Hole and Conditional Time Series analysis. Two bed configurations are examined - one of full-length strip roughness (with one half of the channel width rough and the other smooth) and the second of alternating rough and smooth sections in a "checkerboard" pattern. The former allows the investigation of fully-developed flow, while the latter is shown to more closely resemble the bed variation of a natural river. The thesis goes on to provide recommendations as to how the Shiono-Knight Method (SKM) should be applied to model a heterogeneous channel, bringing the research towards a real-world application.

Contents

LIST OF FIGURES

LIST OF TABLES

NOMENCLATURE

∇	Vector differential operator, del
$\Im$	Time offset
α	SKM shorthand
β	SKM shorthand
β_v	Vegetation shape factor
Γ	SKM secondary flow parameter
$\delta\theta$	Probe misalignment around the z-axis
ε	Eddy viscosity
ϵ	Wavelength
ζ	SKM shorthand
η	SKM shorthand
κ	Karman's constant
λ	SKM eddy viscosity parameter
Λ	A closed volume of fluid
ρ	Water density
Π	Coles' wake parameter
σ	Standard deviation
τ	Shear stress
τ_b	Boundary shear stress
τ^R	Reynolds stress
τ_H^R	Horizontal [component of] Reynolds Stress
τ_V^R	Vertical [component of] Reynolds Stress
τ_{ij}	Shear stress in the plane perpendicular to the i axis along the j axis ($i, j =$

	$x, y, z)$
υ	Kinematic viscosity
ϕ	Wave phase
ψ	A normalisation of z
Ψ	Coles' wake function
ω	Vorticity
ω_b	Characteristic frequency
a	Constant in the DCM formula for n
A	Cross-sectional area of the flow
$\tilde{A}$	Vector of SKM constants
A_1 to A_4	SKM constants
A_{int}	Constant of integration
A_v	Cross-sectional area blocked by vegetation
ADF	Average Daily Flow
ADV	Acoustic Doppler Velocimeter
b	Length of measuring tank
B	Channel width
BC1/2	Bed Configuration 1 or 2
c	Speed of sound
C	Log-law constant
C_D	Drag co-efficient
CS	Cross-Section
d	Pipe diameter/Preston tube inner diameter
Δd	Depth change in measuring tank

D	Log-law constant
D_{xx}	Particle size definition – percentage (by mass) of particles with size $< xx$ mm
DCM	Divided Channel Method
E	Dissipation of mean flow energy
ECM	Electromagnetic Current Meter
f	Friction factor
f_N	Nyquist frequency
f_N	Sampling frequency
f_t	Frequency
F	Body force
F1/F2	Discharge [flow] 1 or 2
$F_t(f_t)$	Frequency spectrum
F_v	Vegetation drag force
g	Gravitational acceleration
G	Generation of turbulent energy
h_f	Head loss per unit length
H	Water depth
i	Index
I	Turbulence intensity
$I(t)$	Conditional time-series detection function
$I_{i,J}$	Quadrant-Hole exclusion function for quadrant i with hole size J
J	Quadrant-Hole analysis hole size
$\tilde{k}$	SKM solution vector
k_s	Nikuradse equivalent sand roughness
k_w	Wavenumber

l	Mixing length
l_m	Mean free-path length in the kinetic theory of gases
LES	Large Eddy Simulation
LGV	Last Good Value post-filtering value replacement method
LI	Linear Interpolation post-filtering value replacement method
m	Width of measuring tank
mPST	Modified Phase-Space Thresholding filtering method
n	Manning's resistance parameter
N	Number of elements in a summation
O	Co-efficient matrix for the solution of SKM boundary conditions
p	Pressure
P	Wetted perimeter
P_i	Q-H analysis proportion of the total shear stress from quadrant i event
PIV	Particle Image Velocimetry
PST	Phase-Space Thresholding filtering method
PTV	Particle Tracking Velocimetry
q	Unit flow rate
$q(t)$	A contiguous series of velocity measurements
Q	Discharge
Q-H	Quadrant-Hole [analysis]
R	Hydraulic radius
$R_x(r)$	Normalised spatial correlation function
Re	Reynolds number
RSB	Rough Smooth Boundary
s	Channel side-slope

$S(k_w)$	Spectral function
S_0	Bed slope
S_f	Friction (Energy) slope
S_w	Water surface slope
$S_{i,J}$	Quadrant-Hole shear stress for quadrant i with hole size J
$\%SF_w$	Percentage of total shear stress which is from the channel walls
SKM	Shiono-Knight Method
t	Time
T	A time interval
T_{adv}	Momentum transfer through advection
T_{mix}	Momentum transfer through turbulent mixing
TI	Turbulence Intensity
TKE	Turbulent Kinetic Energy
u	Instantaneous point velocity in the x-direction
u'	Turbulent fluctuation of point velocity in the x-direction
U	Mean point velocity in the x-direction
U_{rms}	RMS velocity in the kinetic theory of gases
U_*	Shear velocity
v	Instantaneous point velocity in the y-direction
v'	Turbulent fluctuation of point velocity in the y-direction
v_p	Instantaneous point velocity in the ADV probe's y-direction
V	Mean point velocity in the y-direction
V_T	Measure of the turbulent velocity in Prandtl's mixing length model of turbulence
VC	Velocity Correlation filtering method

VITA	Variable-Interval Time-Averaging
w	Instantaneous point velocity in the z-direction
w'	Turbulent fluctuation of point velocity in the z-direction
W	Mean point velocity in the z-direction
x	The streamwise measurement axis
x^*	Parameter in shear stress calculation method
y^*	Parameter in shear stress calculation method
y	The transverse measurement axis
z	The bed-normal measurement axis
z^+	A normalisation of z

1 INTRODUCTION

Since the first permanent human settlements were established, population centres have been situated on the banks of rivers, giving access to the vital resource of fresh water. With the exception of arid and semi-arid regions, few, if any, cities, towns or villages do not have their own water source in the form a river or a stream. However, while having clear advantages, this proximity to such open-channel flow systems has brought with it both dangers and the desire to control the river environment. Flooding is the most obvious danger – in 2007 a World Health Organization publication reported:

"Sri Lanka had flash floods in January followed by floods in May which displaced 132,000 people and killed 17. In February, Jakarta was virtually under water. As many as 40 people died and 400 000 were affected…

…[in Indonesia as] many as 59 villages were flooded and water stood one meter high. Two people were electrocuted and 101,952 affected by rising waters…

… Bangladesh, a country very vulnerable to floods, saw flash floods and landslides in the Chittagong district take as many as 100 lives and injure more than 60 people…

… In Nepal 26 districts have been affected by floods so far, leaving 72 dead and affecting 213,127 people…" (Saksena, 2007)

In the same year severe flooding hit the UK, flooding over 55,000 properties with insured losses of around £3 billion (Environment Agency, 2007). It is therefore evident that there is both a humanitarian and financial incentive to be able to model river flow in order to predict flood events. There are also engineering reasons for developing accurate modelling techniques. As towns and cities develop it is common

for the natural river to be diverted, or at least modified with walls, weirs, sluice gates and other control mechanisms. Similarly, flood defence work changes flow characteristics. The effects of such work on the channel's carrying capacity – its conveyance – must be modelled prior to carrying out the work in order to ensure the aims of the work are achieved.

Open-channel flow is therefore of great interest to engineers and hence has become a well-researched subject, with more recent studies aimed at understanding the physical processes occurring within an open-channel rather than simply obtaining empirical equations for discharge calculations. Such research has taken inspiration from general boundary layer theory, turbulence theory and duct flow, with features of these found in the motion of water through an open-channel. Measurement of 3-D velocity fields over cross-sections in both trapezoidal and rectangular open-channels has revealed secondary flow cells (stable lateral flow structures; see, for example, (Imamoto and Ishigaki, 1992, Nezu et al., 1993)). Shear layers and interface vortices have been seen in regions of high transverse gradient of streamwise velocity (see, for example, (Shiono and Knight, 1991)). More details of these phenomena may be found in Section 3. Quantitative studies of these phenomena have led to the development of the Shiono-Knight Method (SKM), which gives an analytical solution to the depth-averaged RANS equations, the governing equations of fluid flow (see Sections 3.3 and 3.7).

To a certain extent, the research to-date has neglected the case of a heterogeneous channel bed, one in which the bed is transversely horizontal but for which the hydraulic roughness of the bed is not transversely uniform, with well-defined boundaries between regions of uniform hydraulic roughness. Heterogeneous beds

are common (one may say ubiquitous – see, for example, the work of Padmore (1997) and Newson and Newson (2000) on the effects of channel bed variation on river habitats) in natural rivers due to transverse variation in bed material, such as patches of sediment, vegetation and gravel. It is therefore important to understand the effects of such a bed on river flow, and to determine how best to model such a system.

The experimental work described within this thesis tests the hypotheses that:

- "A heterogeneous bed will cause a high transverse gradient of streamwise velocity, leading to interaction between faster and slower moving regions of water. This interaction, in the form of secondary flows and regions of high transverse shear, will result in momentum transfer and turbulent dissipation of kinetic energy which significantly affect the channel conveyance."
- "Customisation of the SKM for a heterogeneous channel will improve the modelling of such a system"

The specific aims and objectives for this research are formalised in the next chapter (Section 2). When met, these will prove or disprove the stated hypotheses. Following the aims and objective is a literature review (Section 3) in which relevant theory is discussed and an overview of related research is presented. Those parts of the experimental apparatus which require particular knowledge are then discussed, before the experimental method and data processing methods used are described in Section 4. Once it has been explained how they have been obtained (Section 5), the experimental results are presented in a number of sections - Section 6 contains the

results of preliminary experiments which examine the channel characteristics and ensure consistency across the apparatus used, Section 7 presents the channel-scale results, such as measured stage-discharge curves, Section 8 examines the flow through channel cross-sections in detail, and Section 9 discusses the measurement and estimation of the boundary shear stress across the channel bed. The heterogeneous channel is modelled using the SKM in Section 10, with overall conclusions and recommendations detailed in Section 11. The thesis ends with a list of references and an appendix containing abstracts of the author's published papers, specifically:

- "An Experimental Study of Turbulence in a Heterogeneous Channel" (Proceedings of ICE – Water Management; In Press) (Jesson et al., 2011a)
- "Turbulent Flow Structures in a Heterogeneous Channel and their Effects on Conveyance Characteristics" – Presented at the First European IAHR Congress, Edinburgh, 4th May 2010 (Jesson et al., 2010)
- "Open-Channel Discharge Characteristics and Secondary Flow Development Over a Biotope-Scale Heterogeneous Channel Bed" – Presented at the 6th IASME / WSEAS International Conference on Water Resources, Hydraulics and Hydrology, 23rd February 2011 (Jesson et al., 2011b)

2 AIMS AND OBJECTIVES

The research described herein is aimed at answering two related questions, the answers to which together prove (or disprove) the hypothesis stated earlier:

1. How, if at all, does a heterogeneous bed affect open-channel flow, and what flow structures does it cause?
2. If they are shown to exist, how are these structures (and their influence on the flow) best modelled using the Shino-Knight Method?

Answering these questions will result in a better understanding of heterogeneous channel flow and an improvement in the modelling of the flow in a channel with a heterogeneous bed. With a broader view, it will go some way to improve conveyance estimation in natural rivers, though this initial research in this area must be seen as a stepping stone towards this long-term goal.

In order to answer these questions the following objectives were set:

(i) Construct stage-discharge curves for a heterogeneous channel with two bed configurations, one of full-length strip roughness, the other with a “checkerboard” pattern of alternating roughness sections. The former will give fully-developed, uniform flow, allowing the effect of the heterogeneity to be evaluated, while the latter is more representative of a natural river, These stage-discharge curves provide a mean of comparison between theoretical stage-discharge curves constructed using current modelling methods and the experimental data, quantifying the accuracy of such methods. The effects of differing bed configuration is also quantified.

(ii) Make detailed, high frequency, 3-D measurements of the velocity field over a cross-section of the channel in (i) at two different discharges. Parse this raw data for mean velocity and turbulent fluctuation data, allowing distributions of streamwise mean velocity and secondary flows to be elucidated, along with those of turbulence parameters such as Reynolds stresses, turbulence intensity (TI) and turbulence flux.

(iii) Critically evaluate these distributions in order to identify momentum transfer and turbulence generation/propagation mechanisms, using techniques such as Quadrant-Hole and conditional time-series analysis. Identifying such features gives the potential to explicitly model them, moving models onto a more physically rigorous footing.

(iv) Calculate the distribution of the SKM parameters over the measured cross-sections, apply the method and compare the model output with the experimental results. From these distributions, determine a methodology for customising and tuning the SKM for a heterogeneous channel, allowing recommendations to be made for the application of the SKM to natural, heterogeneous rivers.

3 LITERATURE REVIEW

3.1 Introduction

This section provides a background to the research presented in this thesis, giving an overview of the concepts which underlie the research and the current state of other research within closely related fields. It starts with a discussion of open channel flow and the empirical methods which have been developed to model flow in such channels, along with their limitations. The Reynolds Averaged Navier-Stokes (RANS) equations are then introduced, along with turbulent flow theory and secondary flows. Discussion of these concepts leads into their application in the Shiono-Knight Method (SKM), whose development and application are then described in detail. Finally, related research is discussed in order to show the foundation of knowledge which this thesis builds on.

Throughout this thesis an orthogonal co-ordinate system as shown in Figure 1 is adopted. Notation for the velocity components corresponding to the axes of this system is also shown, with capitals indicating mean values and primes indicating turbulent fluctuations. Within this thesis, the terms “cross-section” and “lateral” take specific meanings - a plane perpendicular to the streamwise flow (extending from the channel bed to the water surface and from bank to bank), and within such a cross-section respectively. Further, “transverse” is defined herein as lateral and parallel to the channel bed. In this co-ordinate system, these definitions of “lateral” and “transverse” correspond to the yz-plane and along the y-axis respectively. Taking the streamwise velocity as an example, time-average and series-mean values are defined by (1) and (2) respectively, in which $u(t)$ has been sampled over a time period $0 \leq t \leq T$ as a series of N discrete samples indexed by i:

$$U_{time} \equiv \frac{1}{T}\int_0^T u(t)dt \tag{1}$$

$$U_{series} \equiv \frac{1}{N}\sum_{i=1}^{N} u_i \tag{2}$$

As all velocity measurements are made at a constant frequency, $U_{time} = U_{series} = U$.

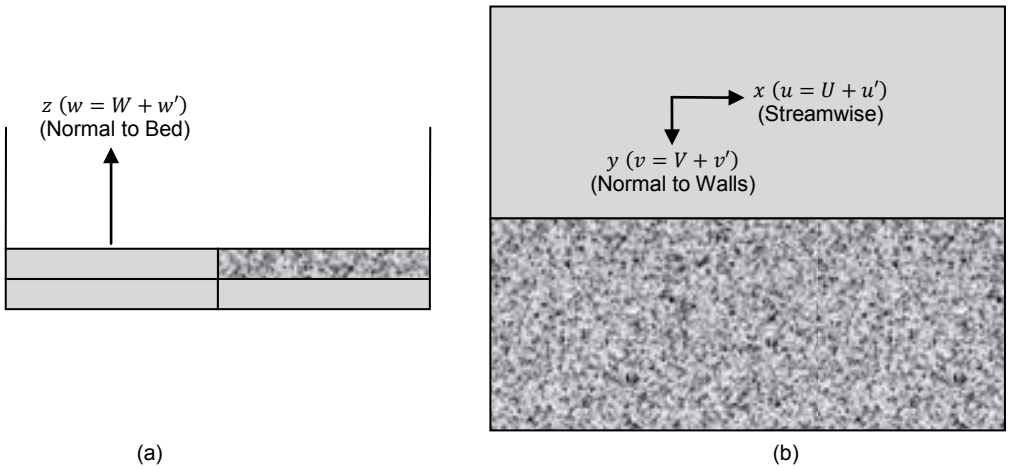

Figure 1: Measurement Co-ordinate System and Velocity Component Notation

Q is used to represent the discharge (SI units m^3s^{-1} but given in ls^{-1} throughout this thesis for convenience.

3.2 Open Channel Flow

Natural rivers are complex open-channel flow systems which vary laterally and from reach to reach. This makes the modelling of a river system extremely complicated, with factors such as the type of surface making up the river bed, the variation in channel cross-section (both with depth and position along the channel) and meanders adding to the complexity. In a natural river all of these physical factors vary – no natural river follows a straight, uniform channel or has a bed which is all formed of the same material.

In order to investigate open channel flow an idealised channel is considered, both in theoretical discussion and experimental work. Such a channel removes extraneous physical features (for example, unless meanders are under investigation the channel will be straight), simplifying the system in order that flow features caused by the physical feature under investigation may be isolated and evaluated. Within the context of this thesis (and ignoring heterogeneous beds for a moment), such a channel is straight, with a constant bed slope, S_0, and of uniform, rectangular cross-section over which the channel bed is horizontal, as illustrated in Figure 2. Figure 2 also illustrates the cross-sectional area of the flow, A, and the wetted perimeter, P, (the length of boundary in contact with the water); the hydraulic radius, R, is defined as their ratio, $R(\equiv A/P)$.

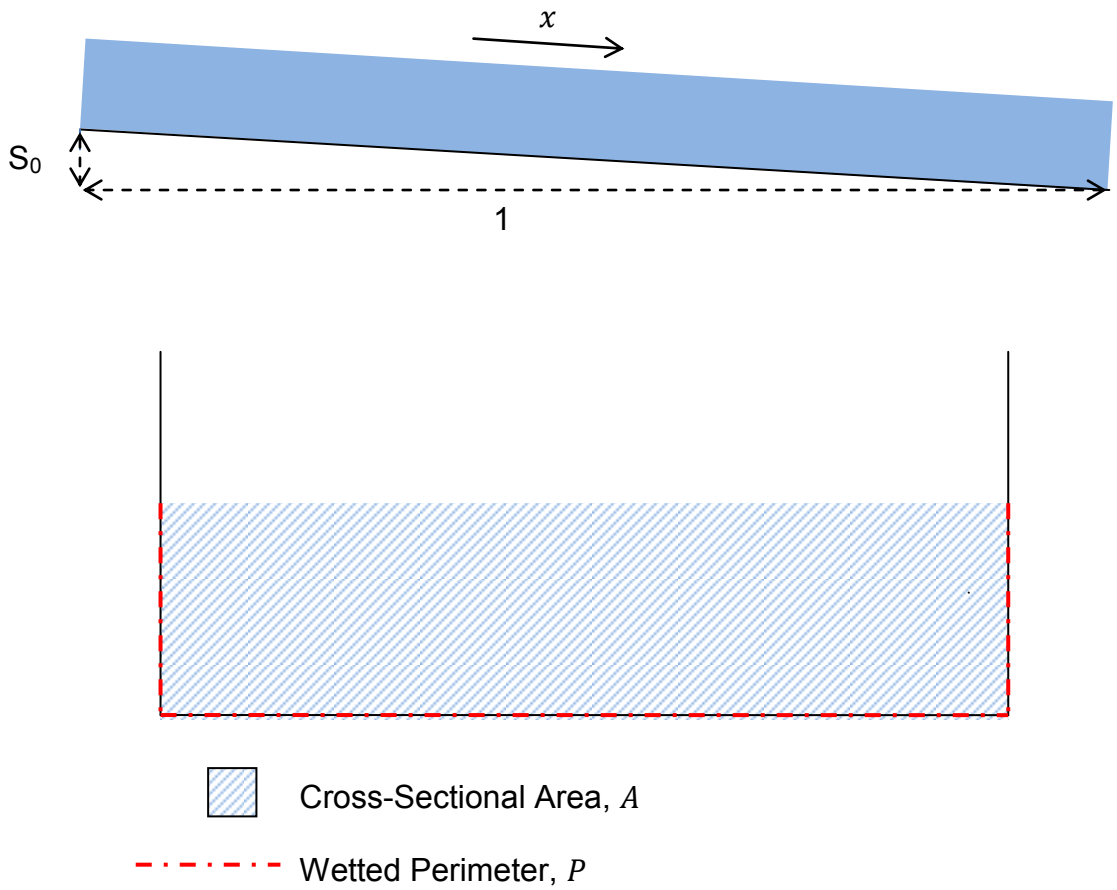

Figure 2: An Idealised Simple Open Channel; Profile (top) and Cross-Section (bottom)

Within the idealised channel, flow is uniform and steady-state, i.e. the flow shows no time variation in the mean properties of the flow, nor do the flow characteristics change with distance along the channel. Under these conditions, the water depth, H, will be the normal depth, h_n. Normal depth is dependent on the discharge, and is the depth that will occur in an infinitely long channel at a fixed discharge. The correct setting of normal depth flow is an important part of the experimental process (see (Sterling and Knight, 2000), for example). While ensuring constant depth along the channel goes someway to establishing uniform, normal depth flow, it has been shown that this is insufficient (Yen, 2003). Yen (2003) gives criteria which define a minimum channel length and suitable positioning of measuring apparatus within a channel in order that uniform, normal depth flow may be assumed, though notes that, at the time of writing, there was no experimental evidence to support these criteria for a rectangular channel. Figures of $160R - 200R$ are given for the distance downstream of the channel entrance for measuring apparatus, while a distance of $50R$ is recommended between the measured cross-section and the tailgate of an experimental channel, though Yen notes that these can be reduced by use of well designed flumes which incorporate honeycombs, screen or slots at the entrance and tailgate. Vermaas (2009) examined the transition at the start of parallel roughness strips, forming a heterogeneous channel bed in a rectangular channel, and found that a distance of approximately $80H$ was sufficient for velocity profiles and secondary flow cells to have developed. The work of Vermaas is discussed in more detail in Section 3.8.

Normal depth flow conditions also collapse three characteristic “slopes” of the flow onto one another. The friction slope, S_f, is the rate of change of energy with distance

along the channel (Chadwick et al., 2004), while the water surface slope, S_w, is simply the slope of the water surface. For normal depth flow, these are equal to the bed slope:

$$S_0 = S_f = S_w \tag{3}$$

In an experimental channel, in which outflow is controlled by a tailgate, the tailgate height governs S_w and must be set correctly to achieve normal depth flow. If the tailgate is set too high, $H > h_n$ and the water surface slope tends to the horizontal, in what is termed an M1 profile (Chadwick et al., 2004). Conversely, if the tailgate is too low, $H < h_n$ and S_w increases along the channel in an M2 profile. This property is used to attain normal depth flow, as discussed in Section 5.3.3.

Applying Newton's Second Law to the flow (which is not accelerating), gravitational forces are balanced by the frictional force between the water and the channel bed / walls and the boundary shear stress. The mean boundary shear stress, $\overline{\tau_b}$, may therefore be shown to be given by (4):

$$\overline{\tau_b} = \rho g R S_0 \tag{4}$$

where ρ is the density of water and g is the acceleration due to gravity.

A region in which the streamwise velocity is affected by the channel bed, the boundary layer, forms adjacent to the bed. The boundary layer is an important concept in the discussion of turbulence and velocity profile and is discussed fully in Section 3.5; briefly, the water immediately adjacent to the bed has zero velocity, with (even in turbulent flow) a thin, laminar (i.e. non-turbulent) layer (the *viscous sublayer*) next to this, bounded by what is termed the buffer layer. Different bed materials will

affects the flow in different ways. *Hydraulically smooth* beds do not project into this sublayer. *Incompletely rough* beds have “small” elements of roughness which project into the viscous sublayer, while the elements of a *completely rough* bed protrude above the viscous sublayer into the wall region, destroying the viscous sublayer (Nezu and Nakagawa, 1993). Quantifying the effect of a rough bed on the flow has long been a goal of researchers. From work on artificially roughened pipes, Nikuradse (1933) introduced the idea of a roughness coefficient, k_s (simply k in his notation). In his work k_s was the physical size of grains of sand used to create roughened pipes but, in the case of open-channel flow, this direct relationship between the size of roughness elements and their representation in models does not hold, for reasons which will be explained below.

Expressing the interaction between the bed and the flow is a fundamental problem when modelling rivers. However, it may be argued that, when modelling the large-scale effects of the bed (e.g. when constructing stage-discharge curves),the actual physical form of the roughness is unimportant; rather it is the effect of that roughness on the flow, often referred to as “resistance”, which is modelled. In open-channel flow, resistance may be categorised as being one of three types (Morvan et al., 2008): *skin drag* caused by small-scale surface irregularities (“*surface texture, grain roughness*”); *form drag* caused by large-scale irregularities (“*surface geometry, bed forms, dunes*”); *shape drag* caused by channel-scale changes such as meanders and bends. It is a term expressing this resistance, rather than the roughness, which is included in many models (Morvan et al., 2008). Nikuradse, who used sand grains of size 0.8mm (Nikuradse, 1933), would have been investigating skin drag only, hence the equivalence of size and roughness. However, channel flow also generally

involves form drag and so k_s cannot be the physical size – consequently it is now known as the Nikuradse equivalent sand roughness size. Further, k_s in an open-channel has been shown to vary with depth and other parameters – more details may be found in (Morvan et al., 2008).

As is pointed out by Morvan et al. (2008), the governing Navier-Stokes equations (see Section 3.3) implicitly include all energy losses due to the channel bed, and the need to explicitly represent the channel roughness only arises due to necessary simplifications required to solve the equations. For 1-D models, this is taken as a lumped value representing the whole channel. Perhaps the most well-known example of a 1-D model is Manning's Equation:

$$Q = \frac{1}{n} A R^{\frac{2}{3}} S_f^{\frac{1}{2}} \tag{5}$$

where the resistance is represented by Manning's n and S_f is the friction slope. Manning's Equation, and slight variations on it, will be used later (Section 7.2) to calculate alternative theoretical stage-discharge curves for comparison with the experimental data.

Alternatively, a friction factor, f, may be used to represent resistance. The Darcy-Weisbach equation was originally developed for pipe flow, in the form:

$$h_f = \frac{f l U^2}{2gd} \tag{6}$$

where h_f is the head loss along the pipe, d is the pipe diameter and l is the pipe length (Knight et al., 2010). As with a number of other equations for open channel flow, the pipe flow equation is modified for an open channel by substituting:

$$d = 4R \tag{7}$$

which itself is derived from the definition of the hydraulic radius for a pipe running full. However, unlike for flow through a full pipe, R is not a constant for an open-channel and varies with flow depth – from (4) it follows that $\overline{\tau_b}$ is a function of H, i.e. $\overline{\tau_b} = \overline{\tau_b}(H)$. Substitution gives:

$$S_0 = \frac{\mathrm{fU}^2}{8\mathrm{gR}} \tag{8}$$

which may be rearranged to provide an expression for f:

$$f = \frac{8\tau_b}{\rho U^2} \tag{9}$$

Being a "correction" for simplifications in modelling, the meaning of f (or any resistance parameter) is dependent on the model being used, particularly its dimensionality. In 1-D models f is the sole resistance parameter and so must represent energy loses due to turbulence generated by boundary shear and also any macroscopic interactions such as those due to secondary flows. More complex models may explicitly model these macroscopic interactions and contain, for example, a secondary flow parameter in addition to f – f then has a different meaning as it exclude secondary flow effects. Further, in 1-D models the friction factor represents the effect of the entire wetted perimeter on the flow, and is in some sense a mean value, while in a 2-D model such as the SKM it represents the shear stress at the base of a vertical column of water (Morvan et al., 2008) and so may show lateral variation. For more detail the reader is directed to the discussion paper of Morvan et al. (2008) on the difference between roughness and resistance and

application to numerical models. The friction factor is an important parameter in the SKM, as will be discussed further in Section 3.7.

In addition to boundary shear stress, two other flow features exist which affect open-channel flow – secondary flow cells and shear layers at the boundary between regions of high and low streamwise velocity. These are discussed more fully later in the thesis, and are mentioned here for completeness. Secondary flow cells (see Section 3.6) contribute to large-scale, lateral momentum transfer within the flow. The shear layer can also cause large-scale, transverse momentum transfer through the production of interface vortices (see Figure 3), but also contributes to turbulent momentum transfer due to the production of turbulence and the resulting Reynolds stresses (see Section 3.3). This is analogous to the turbulence produced near the channel bed. These momentum transferring phenomena affect the overall flow, making understanding their effect important in modelling channel conveyance.

For the purpose of this research, a heterogeneous channel is defined as one in which the bed is horizontal across the channel but for which the bed roughness is not uniform across the channel (Figure 4).

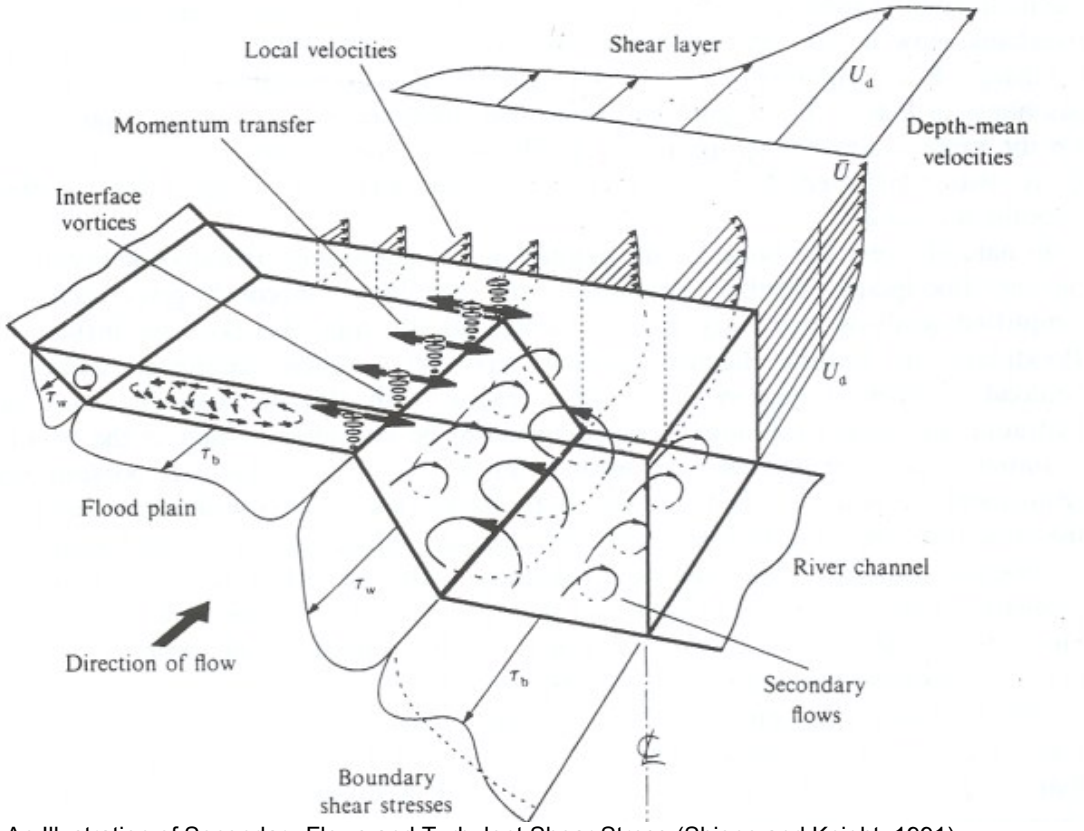

Figure 3: An Illustration of Secondary Flows and Turbulent Shear Stress (Shiono and Knight, 1991)

Figure 4: Heterogeneous Channel Schematic

Semi-empirical formulae have been suggested for channels such as this heterogeneous channel, in which there are obvious divisions into sub-channels. These were typically derived for the case of overbank flow, in which the floodplain and main channel have very different characteristics both in terms of roughness and in flow depth. These divided channel methods split the channel into a small number of sub-channels, each with its own value of n, and results for the full, compound

channel are obtained by combining the sub-channel values. A number of methods for this combination have been suggested, with a common approximation to Manning's n for a compound channel being:

$$n = \left(\frac{\sum_{i=1}^{N} P_i n_i^a}{P} \right)^{\frac{1}{a}} \tag{10}$$

where N is the number of sub-channels, subscript i indexes those sub-channels and a is a constant. This equation, with a values of $3/2$ and 2, is used by Horton (1933) and Pavlovskij (1931) (both cited by (James and Jordanova, 2010)) respectively in their standard approximations for the compound n, and these values are used later in this thesis to construct theoretical stage-discharge curves for comparison with the experimental results. James and Jordanova (2010), who have investigated the use of equation (10) for heterogeneous channel beds, note that this simple equation takes no account of transverse momentum transfer between the sub-channels (more details of their research are given in Section 3.8). This is a deficiency in such an approximation - due to the difference in roughness on each side of the bed, it would be predicted that the streamwise velocity would be greater on the smooth side of the channel than on the rough side. As with the case of a compound channel, this would be expected to lead to the creation of interface vortices at the rough-smooth boundary. Secondary flows, which occur due to non-uniform boundary shear stress, would also be predicted, and in a different form to a simple channel of the same cross-sectional shape. It is one of the aims of this research to measure experimentally such effects of the heterogeneous bed and its rough-smooth boundary.

3.3 The Navier-Stokes Equations and the Reynolds Averaged Navier-Stokes (RANS) Equations

The motion of a volume of fluid is governed by Newton's Second Law, which states that the rate of change of a body's momentum is equal to the sum of the forces acting upon it. In the case of fluid flow, these forces are body forces, F, forces due to viscosity and forces due to pressure, p. Application to a volume of a Newtonian fluid leads to the three dimensional Navier-Stokes equation:

$$\frac{D\boldsymbol{u}}{Dt}\left(\equiv \frac{\partial \mathbf{u}}{\partial \mathrm{t}} + (\mathbf{u}.\nabla)\mathbf{u}\right) = -\nabla\left(\frac{p}{\rho}\right) + \nu\nabla^2\mathbf{u} + \mathbf{F} \tag{11}$$

in which bold text is used to represent vector quantities, ρ is the density of the fluid and ν is the kinematic viscosity of the fluid. The left-hand side is the convective derivative, the rate of change in $\boldsymbol{u}$ with motion through space as well as with time (Davidson, 2004).

The RANS equations are a time-averaged version of the Navier-Stokes equation. These are derived by substituting the instantaneous velocity, $\boldsymbol{u}$, in (11) by its mean and fluctuating parts:

$$\boldsymbol{u} = \boldsymbol{U} + \boldsymbol{u}' \tag{12}$$

and taking a time-average. Noting that, for steady, uniform flow, $\frac{\partial p}{\partial x} = 0$, $\frac{\partial \boldsymbol{U}}{\partial t} = \overline{\frac{\partial \boldsymbol{u\prime}}{\partial t}} = \mathbf{0}$ and that, for an incompressible fluid, $\nabla.\boldsymbol{u} = 0$ gives, for the x-component:

$$\frac{\partial}{\partial \mathrm{y}}\left(\overline{\mathrm{UV}} + \overline{\mathrm{u'v'}}\right) + \frac{\partial}{\partial \mathrm{z}}\left(\overline{\mathrm{UW}} + \overline{\mathrm{u'w'}}\right) = \nu\nabla^2\mathrm{U} + \mathrm{F_x} \tag{13}$$

In the case of open channel flow in a sloping channel it may be shown that F_x in (13) is the x-component of the gravity force per unit mass:

$$F_x = gS_0 \tag{14}$$

and, through the assumption that viscous stresses are negligible in relation to turbulent stresses (Chadwick et al., 2004), the RANS become:

$$\rho\left[\frac{\partial(UV)}{\partial y}+\frac{\partial(UW)}{\partial z}\right] = \rho g S_0 + \frac{\partial(\overline{-\rho u'v'})}{\partial y}+\frac{\partial(\overline{-\rho u'w'})}{\partial z} \tag{15}$$

The bracketed parts of the second and third terms on the RHS are the horizontal and vertical Reynolds stresses respectively (henceforth, τ_H^R and τ_V^R respectively). The Reynolds stresses are not true stresses, but instead represent the loss of mechanical energy by the main flow due its interaction with turbulence.

An alternative derivation of the Reynolds stresses, based on a physical argument of momentum transfer through a small area is presented by Schlichting (1987).

3.4 Turbulence Theory

3.4.1 Introduction

> *"either the elements of the fluid follow one another along lines of motion which lead in the most direct manner to their destination, or they eddy about in sinuous paths the most indirect possible."* Osborne Reynolds (1901)

In the 19th century Osborne Reynolds performed a series of experiments examining the flow in pipes, noting the existence of three types of flow – laminar, transitional and turbulent (Reynolds, 1901). In laminar flow fluid particles follow parallel streamlines (in the "direct manner" described by Reynolds; streamlines are lines tangential to the velocity at any point along the streamline, and so mark the path followed by any fluid particle which is on that streamline), while in turbulent flow random velocity fluctuations lead to "sinuous paths". Transitional flow is laminar flow in which bursts of turbulent flow appear, whose energy is dissipated by viscous forces before the turbulence can develop and become self-sustaining through the mechanism described in this section.

From his experimental results Reynolds concluded that whether a flow would be laminar or turbulent was dependent on a parameter now known as the Reynolds number, Re, the ratio of the inertial force to the friction force (the force due to viscosity, which damps turbulence) on a fluid element (Schlichting, 1987):

$$Re = \frac{Ud}{\nu} \tag{16}$$

where U is the mean flow velocity, d is the pipe diameter and ν is the kinematic viscosity of the fluid. Calculating the Reynolds number for range of pipe flows, Reynolds found that for Re < 2000 flow was laminar, for Re > 4000 flow was turbulent and for ranges in between the flow was transitional (Reynolds, 1901). This shows that, in order for turbulence to be generated and sustained, inertial forces must far exceed the friction force.

Calculation of the Reynolds number requires use of an appropriate length scale (d in the case of pipe flow) and the hydraulic radius, R, can be used for open-channel flow (Chadwick et al., 2004), giving:

$$Re = \frac{UR}{\nu} \tag{17}$$

From (16) and (17) it can be seen that, as $d = 4R$ for a pipe flowing full, $Re_{pipe} = 4Re_{channel}$. Thus the limiting values for laminar and turbulent flow become $Re < 500$ and $Re > 1000$ for open channel flow. However, the upper limit is usually taken as $Re > 2000$ due to it being more poorly defined (Chadwick et al., 2004).

However, the Reynolds number alone does not determine whether the flow type will be laminar or turbulent. As will be discussed later (Section 3.4.2), the turbulence and the main flow are inextricably linked, with the main flow providing energy for the turbulence and the turbulence shaping the main flow. The energy of the turbulence is dissipated through viscous forces, and the Reynolds number may be seen as an (inverse) measure of this dissipation. The onset of turbulence requires a disturbance (such as roughness on a channel surface) which causes an instability in the main flow; for a low Reynolds number flow the energy of this instability will be dissipated before turbulence can develop, while for high Reynolds number flow the energy

dissipates much more slowly and so the turbulence can extend. The Reynolds number determines the susceptibility of the flow to becoming turbulent under the presence of this instability - a disturbance which will make flow turbulent in a high Reynolds number flow will not necessarily make flow turbulent if the Reynolds number is sufficiently small.

The magnitude of turbulence is expressed as the turbulence intensity, defined by Equation (18) (Nezu et al., 1993) for the x-direction and similarly for y and z:

$$I_x = \frac{\sigma_x}{U} = \frac{\sqrt{\overline{u'u'}}}{U} \tag{18}$$

Much of the theory related to turbulent flow is directed at explaining the interaction between the main flow and the turbulence, and the mechanism for energy dissipation. The current theories relating to these two aspects are outlined in this chapter.

3.4.2 Energy Transfer Between Turbulence and the Main Flow

The mechanical energy lost by the main flow through the Reynolds stresses (themselves formed by turbulence) is transferred to the turbulence as kinetic energy. Thus the turbulence itself is providing a mechanism for energy to be transferred to it from the main flow. (Davidson, 2004)

The physical mechanism for this energy transfer is thought to be vortex stretching. In a shear flow there will be a strain on any fluid element and this will stretch vortices within that element. By conservation of angular momentum, this stretching leads to an increase in vorticity (a measure of the local rotation of a fluid element, defined

formally in Section 3.4.3 and denoted by $\boldsymbol{\omega}$) and kinetic energy, and so energy is transferred to the turbulence (see (Davidson, 2004) for a more rigorous explanation).

An alternative mechanism, a transport theory based on momentum transfer analogous to molecular transport in gases, is used in some models (see Section 3.4.4), but evidence for the 3-D nature of turbulence suggests that such 2-D models are not representative of the physical processes involved (Reynolds, 1901). Indeed, the use of hydrogen-bubble tracers and flow visualisation techniques has proved the existence so-called “hairpin” vortices (see Figure 5) over both rough and smooth channel beds, showing their formation and stretching (Nezu and Nakagawa, 1993).

For its part, the vorticity affects the velocity field according to the Biot-Savart law:

$$\boldsymbol{u}'(\boldsymbol{x}) = \frac{1}{4\pi}\int \frac{\boldsymbol{\omega}(\boldsymbol{x}') \times (\boldsymbol{x} - \boldsymbol{x}')}{(\boldsymbol{x} - \boldsymbol{x}')^3} d\boldsymbol{x}' \tag{19}$$

where $\boldsymbol{x}$ is the position at which the velocity is calculated and the integral over $\boldsymbol{x}'$ is over all other points in the fluid. Hence the vorticity is fuelled by the main flow, which it then distorts.

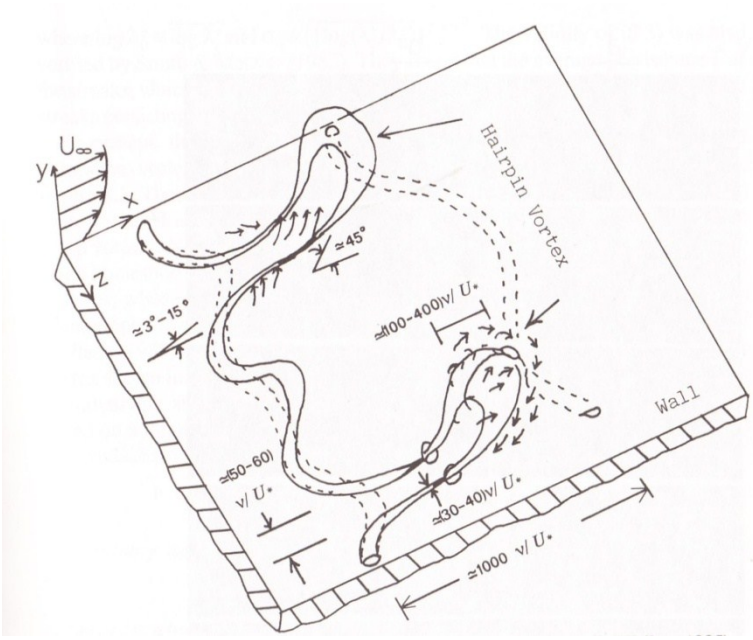

Figure 5: Illustration of Hairpin Vortices (from (Nezu and Nakagawa, 1993); note that y and z-axes are switched relative to the notation adopted within this thesis)

3.4.3 Energy Dissipation

It may be shown (for example, (Davidson, 2004)) that in a closed volume of fluid, Λ, mechanical energy is transformed to heat energy through viscous stress (and subsequently dissipated) at a rate:

$$\nu \int (\nabla \times \boldsymbol{u})^2 \, d\Lambda \equiv \nu \int \boldsymbol{\omega}^2 \, d\Lambda \tag{20}$$

where $\boldsymbol{\omega} \equiv \nabla \times \boldsymbol{u}$ is the vorticity. Vorticity is independent of the global rotation of the fluid - a 2-D shear flow (in which velocity varies with depth but streamlines are horizontal) has no global rotation but non-zero vorticity, while a flow with concentric, circular streamlines has global rotation without vorticity, as illustrated in Figure 6.

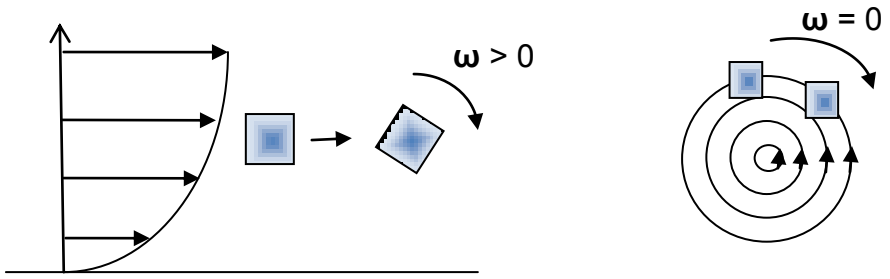

Figure 6: Flows with Independent Global Rotation and Vorticity (adapted from Davidson(2004))

A governing equation for the vorticity may be derived from the Navier-Stokes equation, Equation (11), giving:

$$\frac{D\boldsymbol{\omega}}{Dt} = (\boldsymbol{\omega}.\nabla)\boldsymbol{u} + \upsilon\nabla^2\boldsymbol{\omega} \tag{21}$$

Discussions of turbulence frequently use the term “eddy” to represent a blob of vorticity which can be regarded as having its own size and velocity field which are in some sense independent of other eddies. Turbulent flow can then be considered to consist of a large number of these eddies, with observation showing a continuum of eddy sizes, or scales. Richardson (1920, 1922) explained the transfer of the energy from the large scale to the small scale by means of an energy cascade, in which mechanical energy is transferred from a large eddy to a slightly smaller one and from there to a slightly smaller one, until the receiving eddy is of a small enough scale for dissipation to be significant:

> *“big whirls have little whirls that feed on their velocity, and little whirls have lesser whirls and so on to viscosity - in the molecular sense.”* Lewis Richardson (Richardson, 1922)

As with the transfer of energy from the main flow, the mechanism for this is vortex stretching - an eddy within the velocity field of another eddy will be distorted by that eddy, though it can be demonstrated that this distortion is only significant if the two eddies are of comparable size (Davidson, 2004). Thus vortex stretching will occur due to a slightly larger eddy, transferring energy down the cascade.

For an eddy, the Reynolds number is defined by its size (Davidson, 2004). For large eddies, in which the typical length and velocity scales are the so-called *integral* scales, the viscous effects may be assumed negligible and the characteristic Reynolds number is much less than unity. For the smallest eddies (whose typical length and velocity scales are called the *Kolmogorov microscales*) viscous dissipation occurs at an equal rate to inertial generation, and so the characteristic Reynolds number is approximately equal to one. If the cascade system is to be stable, the rate at which energy is passed from the largest eddies must equal that at which it is dissipated by the smallest eddies. This provides a mechanism for estimating the Kolmogorov length scale (i.e. the size of the smallest eddies), giving a value of less than one millimetre (see (Davidson, 2004) for more details). Along with the experimental evidence of vorticity being concentrated in the smaller scales, this supports the hypothesis that energy is dissipated by the small scale eddies. Thus eddies may be grouped into three sub-ranges (Kaimal and Finnigan, 1994), based on their size and thus their interaction with the flow. Shear forces transfer energy from the main flow into the turbulent flow through the creation of large scale eddies in the *energy-containing sub-range*. Energy is transferred from these large eddies, through the medium-sized eddies of the *inertial sub-range*, to the smallest eddies. Vorticity is

concentrated in these small eddies and so, in accordance with Equation (20), most of the dissipation of mechanical energy occurs within this *dissipation sub-range*.

These eddies manifest themselves as different frequencies/wavenumbers (the wavenumber is represented by $k_w(\equiv 2\pi f/U)$, where f is the frequency) in the velocity fluctuation spectrum, which may be divided into the *productive* (low wavenumber), *inertial* and *viscous* subranges, corresponding to the eddy size ranges (Nezu and Nakagawa, 1993). The 1-D, normalized spectral function of the streamwise velocity fluctuations, $S(k_w)$, defined as the cosine transform of a normalised spatial correlation function ($R_x(r) \equiv \overline{u(x)u(x+r)}/\sigma_u^2$; see (Nezu and Nakagawa, 1993) for details), is an important parameter when examining these sub-ranges. The dissipation rate in wavenumber-space is governed by $k_w^2 S(k_w)$, and it may be shown that $S(k_w) \propto k_w^{-5/3}$ for large k_w (Nezu and Nakagawa, 1993). This is known as Kolmogoroff's $-5/3$ power law. Further, for practical applications, $S(k_w)$ may be approximated (outside the productive sub-range) by:

$$S(k_w) \cong \frac{U}{2\pi} F_t(f_t) \tag{22}$$

where $f_t = Uk_w/2\pi$ and $F_t(f_t)$ is the frequency spectrum, which is simply the Fourier transform of the velocity fluctuations (Nezu and Nakagawa, 1993).

3.4.4 Eddy-Viscosity Models

The second, non-linear term of the convective derivative in Equation (11) represents the change in velocity of the fluid element as it moves through the non-uniform velocity field representing the flow and leads to the chaotic velocity field seen in turbulent flow (Davidson, 2004). Given initial conditions, such a chaotic system can

(theoretically) be solved numerically to give values for $\boldsymbol{u}(\boldsymbol{x},t)$, the velocity field at any point $\boldsymbol{x}$ at time t. However, the velocity field is chaotic in nature and so, for an infinitesimally small change in those initial conditions, the calculated point velocities change unpredictably. This results in a need for an impractically large number of calculations in order to model all points of a real flow where initial conditions vary, and so a statistical approach is preferable.

Unfortunately, attempts to develop governing equations for these statistical properties always result in an unsolvable set of *n* equations for *n+1* unknowns – the closure problem of turbulence. In order to use such governing equations it is necessary to apply other heuristic hypotheses, making additional assumptions about the nature of the turbulence in order to render the system solvable. Different sets of assumptions (referred to as turbulence models) have been suggested. The Shiono-Knight method uses the Boussinesq turbulence model (Shiono and Knight, 1988) – see Section 3.7.

In this model, Boussinesq (1877) (cited by (Davidson, 2004, Schmitt, 2007)) suggested that the shear stress and Reynolds stress be modelled as:

$$\bar{\tau}_{xy} + \frac{\partial(\overline{-\rho u'v'})}{\partial y} \equiv \bar{\tau}_{xy} + \tau_{xy}^{R} = \rho(\nu + \varepsilon)\frac{\partial \mathrm{U}}{\partial y} \tag{23}$$

where ε is the eddy viscosity. The turbulence is thus seen as increasing the viscosity of the fluid, increasing momentum transport. This definition does not constitute a true model as the distribution of ε must be defined (Nezu and Nakagawa, 1993).

To make use of this assumption it is necessary to quantify ε. The first suggestion for a method of estimating ε was by Prandtl (Davidson, 2004). Viscosity, a macroscopic

property, is modelled at the molecular level (by the kinetic theory of gases models) as being caused by the transfer of fast and slow moving molecules between fast and slow moving layers of fluid. Similarly, Reynolds stress can be regarded as the movement of high and low momentum fluid elements. By analogy with the mean free-path of the kinetic theory of gases:

$$\nu = \frac{1}{3} l_m U_{rms} \tag{24}$$

where l_m is the mean free-path length of the molecules and U_{rms} is their root mean square speed , Prandtl suggested that an analogous length (the mixing length, l) existed for the eddy viscosity:

$$\varepsilon = \frac{1}{3} l V_T \tag{25}$$

where V_T is a suitable measure of the turbulent velocity (Davidson, 2004).

By making assumptions about momentum transfer and comparison with the Boussinesq equation (23), Prandtl arrived at an expression for ε:

$$\varepsilon = l^2 \left| \frac{\partial U}{\partial z} \right| \tag{26}$$

Assuming that l can be determined by experiment, (26) allows ε and thus the Reynolds stress to be calculated. In fact, Nezu and Rodi (1986) showed that l has a parabolic distribution in 2-D open-channel flows (Figure 7), and this may be approximated by (Sharifi, 2009):

$$l = \kappa z \sqrt{1 - \frac{z}{H}} \tag{27}$$

where $\kappa \cong 0.419$ is the Karman constant, which will be discussed in Section 3.5.1. This, in turn, by substitution into (26), gives:

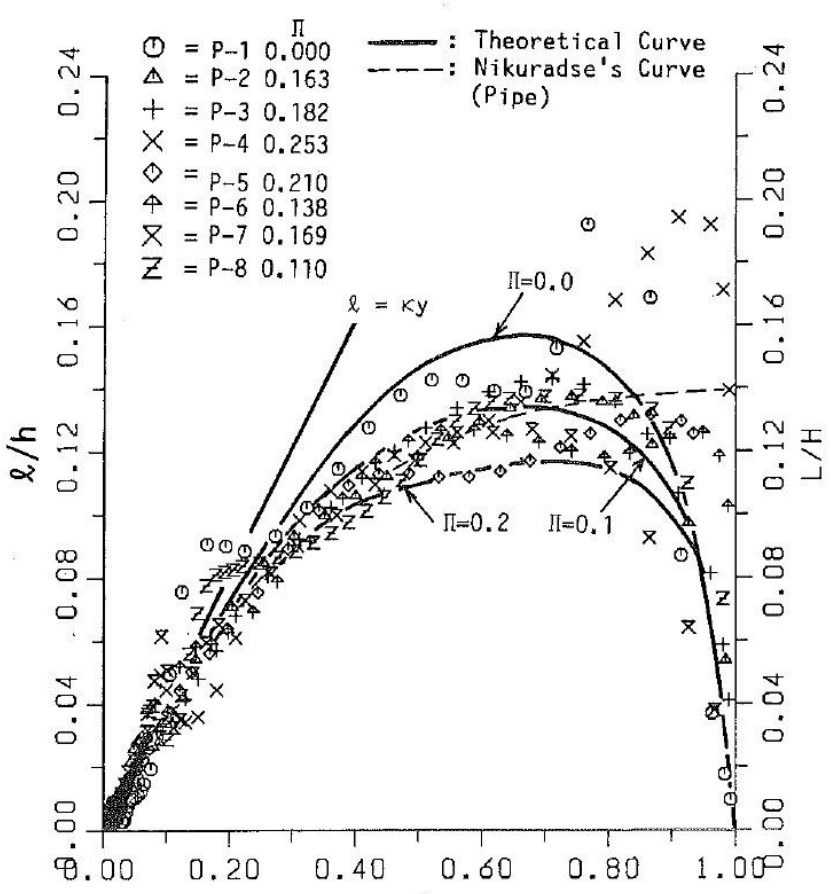

Figure 7: Distribution of Mixing Length (Nezu and Rodi, 1986) (Note that the y-axis in the figure is the vertical axis, corresponding to the z-axis in the notation of this thesis)

$$\varepsilon = \kappa^2 z^2 \left(1 - \frac{z}{H}\right) \left|\frac{\partial U}{\partial z}\right| \tag{28}$$

As will be shown in Section 3.5.1:

$$\frac{\mathrm{U}}{U_*} = \frac{1}{\kappa} \ln\left(\frac{U_* z}{\upsilon}\right) + A_{int} \tag{29}$$

where A_{int} is a constant and U_* is the shear velocity (defined as $U_* \equiv \sqrt{\tau_b/\rho}$) and so (28) becomes:

$$\varepsilon = \kappa z U_* \left(1 - \frac{z}{H}\right) \tag{30}$$

Integration over the water column gives a mean value of ε, $\bar{\varepsilon}$:

$$\bar{\varepsilon} = \frac{1}{H}\int_0^H \varepsilon\, dz = \frac{\kappa U_*}{H}\int_0^H z\left(1-\frac{z}{H}\right)dz = \frac{\kappa H U_*}{6} \tag{31}$$

This expression will be used later in the discussion of the SKM (Section 3.7).

3.5 Boundary Layer Theory

The boundary layer is the region in which the flow is affected by the presence of a fixed boundary such as a channel bed or wall. As will be shown, the streamwise velocity is reduced within the boundary layer and increases with distance from the wall. The boundary layer thickness is defined as the perpendicular distance from the wall at which U is 1 percent of the free stream velocity, the velocity sufficiently far from the wall that the wall has no effect (Wang, 1972). The idea of turbulence as "blobs" of vorticity fits existing observations of boundary layers if the fixed boundary is considered to be a source of vorticity which then diffuses out from this fixed boundary - within the boundary layer velocity gradients are large and so vorticity is intense; outside the boundary layer the velocity gradients are small and vorticity negligible (Davidson, 2004).

In open-channel flow the boundary layer may extend the full flow depth (Nezu and Nakagawa, 1993) and such fully developed flow is assumed (and verified) in the research presented within this thesis.

As with many problems in hydraulics, a discussion of boundary layer theory is best started with a look at the relatively simple case of uniform, 1-D flow; in his wind tunnel study of the effects of longitudinal strip roughness on flow over a flat plate, Wang (1972) found that it was reasonable to treat *"the non-uniform three dimensional surface conditions as a small perturbation about a 2-dimensional state"*. A brief

outline is presented here, while an excellent, more detailed overview may be found in (Nezu and Nakagawa, 1993).

3.5.1 Turbulent Flow in a Channel – the Log-Law of the Wall and the Wake Function

In fully developed turbulent flow the presence of a wall dictates the nature of the flow, due to the fact that turbulent fluctuations must be zero near the wall (Davidson, 2004) and at the free surface (Nezu and Nakagawa, 1993). The log-law of the wall describes the structure of the boundary layer against a channel wall, with the wake function being an adjustment to the log-law for regions further from the wall. In a similar manner to other results in studies of flow (such as the Reynolds number), the log-law was derived based on pipe flow (see, for example, (Davidson, 2004) for an account of these laws for pipe flow).

Taking a 1-D, fully developed mean flow with $\boldsymbol{U} = (U(z), V, W) = (U(z), 0, 0)$ it may be shown (Nezu and Nakagawa, 1993, Davidson, 2004) that:

$$\frac{\tau}{\rho} \equiv -\overline{uw} + \nu\frac{\partial U}{\partial z} = \frac{\tau_b}{\rho}\left(1 - \frac{z}{H}\right) = U_*^2\left(1 - \frac{z}{H}\right) \tag{32}$$

where τ_b is the wall shear stress and H is the flow depth.

The RHS terms of the initial definition $\left(\frac{\tau}{\rho} \equiv -\overline{uw} + \nu\frac{\partial U}{\partial z}\right)$ form the basis for the theoretical equations for the generation of turbulent energy from mean flow energy, G, and dissipation of mean flow energy through viscosity, E (Nezu and Nakagawa, 1993):

$$G \equiv -\overline{uw}\frac{\partial U}{\partial z} \tag{33}$$

$$E \equiv \nu \frac{\partial U}{\partial z}\frac{\partial U}{\partial z} = \nu\left(\frac{\partial U}{\partial z}\right)^2 \tag{34}$$

Integration of the sum, $G + E$, over the entire flow depth may be shown (Nezu and Nakagawa, 1993) to equal the work done by the mean flow against boundary shear stress. Thus the bed shear is causing energy loss through viscosity and the creation of turbulence, whose energy is then dissipated as heat by small-scale eddies.

From (32) it is apparent that the boundary layer flow can then be split into two regions defined by distance from the wall. Adjacent and close to the wall (where $\frac{z}{H} \ll 1$) is the *inner region* (or wall region, (Nezu and Nakagawa, 1993)), in which τ is approximately constant and equal to τ_b (Davidson, 2004). Although τ is constant over this region, its components $\bar{\tau}_{xz}$ and τ_{xz}^R (the Reynolds stress, see Section 3.3) vary, with $\tau \approx \bar{\tau}_{xz}$ at the wall and $\tau \approx \tau_{xz}^R$ a short distance from the wall. At this point, where the laminar stress is negligible, a second region starts. This is the *outer region*, defined as the region where:

$$z^+ = \frac{U_* z}{\nu} \gg 1 \tag{35}$$

z^+ and $\psi = z/H$ are normalisations of z which are used to define regions within the boundary layer.

The inner region itself may be thought of as consisting of three sublayers. The *viscous sublayer* starts at the wall and occupies the region where $z^+ < 5$. In this sublayer of the inner region the flow is partially laminar and so (Nezu and Nakagawa, 1993, Davidson, 2004):

$$U \cong \frac{U_*^2 z}{\nu} \tag{36}$$

Between the viscous sublayer and the next characterisable sublayer lies the *buffer layer*, covering the region $5 < z^+ < 40$ (it should be noted that this upper limit is approximate – Nezu and Nakagawa (1993) give a range $5 < z^+ < 30$).

The *inertial sublayer, or overlap region,* covers the remainder of the inner region and is defined as where $z^+ > 40$ and $\psi < 0.2$. In the inertial sublayer laminar stress is negligible and the shear stress, τ, is approximately constant. For this region it may be shown that (Davidson, 2004):

$$\frac{\mathrm{U}}{U_*} = \frac{1}{\kappa}\ln z^+ + A_{int} \tag{33}$$

This is the log-law of the wall, with κ being Karman's constant and A_{int} a constant of integration. These constants have been shown to be independent of the Reynolds and Froude numbers for a number of types of flow (including boundary layers and closed-channel (Nezu and Nakagawa, 1993)), with values of $\kappa = 0.419$ and $A_{int} = 5.29$ measured for open-channel flow (Nezu and Rodi, 1986).

The distinction between these three sublayers is important in terms of turbulence production. In the viscous sublayer, close to the wall, the flow is partially laminar and the turbulence cannot sustain itself as velocity fluctuations are overwhelmed by viscous effects (Reynolds, 1901). The buffer layer is the region where neither the viscous nor Reynolds stresses are negligible and turbulent energy production peaks as viscous forces and Reynolds stresses are of similar magnitudes (Reynolds, 1901).

In the outer region τ is no longer constant. This makes it necessary to add a correction to the logarithmic variation of U seen in the adjoining inertial sublayer of

the inner region (Vermaas et al., 2007). The best correction for open channel flow appears to be Coles' wake function, $\Psi(\psi) = \frac{2\Pi}{\kappa}\sin\left(\frac{\pi\psi}{2}\right)$ correction, in which Π is Coles' wake parameter (Nezu and Nakagawa, 1993), giving the velocity defect law:

$$\frac{U_{max} - U}{U_*} = -\frac{1}{\kappa} ln\, \psi + \frac{2\Pi}{\kappa}\cos^2\left(\frac{\pi\psi}{2}\right) \tag{37}$$

Nezu and Nakagawa (1993) suggest that in the case of open channel flow (in which, as noted above, the boundary layer can extend the full depth) the flow is better described in terms of three overlapping regions – the wall region (corresponding to the inner region, with velocity and length scales U_* and ν/U_*, and in which turbulent energy production, G, greatly exceeds dissipation, E), the intermediate region (corresponding to the inertial sub-range of the velocity fluctuation spectrum in the sense that $G \cong E$ and turbulent energy is approximately constant) and the free-surface region (scaled by U_{max} and h, where $E > G$). The free-surface region in particular differs from conduit flows as vertical velocity fluctuations are damped by the free surface.

These regions are illustrated in Figure 8:

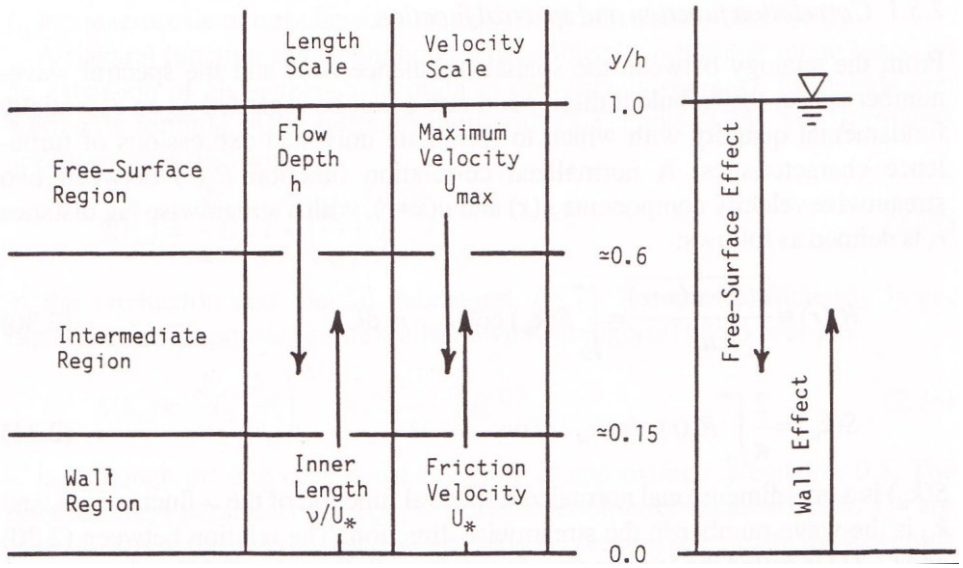

Figure 8: The Regions of Open-Channel Turbulent Flow (from (Nezu and Nakagawa, 1993) (Note that y in the figure corresponds to z in the notation of this thesis).

The vorticity in the boundary layer all originates from the wall (Davidson, 2004). This is transferred through the viscous sublayer by bursts of turbulent fluid from the wall, and this process maintains the turbulence in the boundary layer. Similar bursts are seen at the upper edge of the layer. This edge is not smooth and this provides the mechanism for energy transfer from the mean flow to the turbulence through vortex stretching of vortices protruding into the main flow.

The turbulence resides within this boundary layer. Velocity fluctuations are seen outside the boundary layer, but these are due to pressure waves caused by velocity fluctuations within the boundary layer which then induce velocity fluctuations in remote areas of the flow.

3.5.2 Coherent Structures

It has been suggested that the coherent structures (large-scale eddies) in open-channel turbulence consist of two types, bursting phenomena and large-scale vortical structures (Nezu and Nakagawa, 1993). The former, which occur near the bed, are turbulence while the latter are (generally – see (Nezu and Nakagawa, 1993) for details) steady in nature and not considered here.

The bursting phenomena consists of eddies whose creation is temporally and spatially random but whose behaviour is coherent. This behaviour consists of ejections of parcels of low-speed fluid from the wall and a compensatory sweep of high-speed fluid from above. Such motions have been visualised by Nezu using the hydrogen bubble technique (Nezu and Nakagawa, 1993). Nezu and Nakagawa present some of Nezu's images along with a concise and informative description of the process:

"An individual low-speed parcel of fluids, i.e., a 'low-speed streak', lifts away from the wall [Figure 9a]*, oscillates in three dimensions* [Figure 9b] *and then breaks down* [Figure 9c]*; in the process, a substantial portion of the low-speed fluid is ejected into the outer flow. Subsequently, a high-speed parcel of fluid approaches the wall and sweeps away the retarded fluid that remains there from the ejection process. This part is called the 'sweep' or 'inrush' process* [Figure 9d-f]*."*

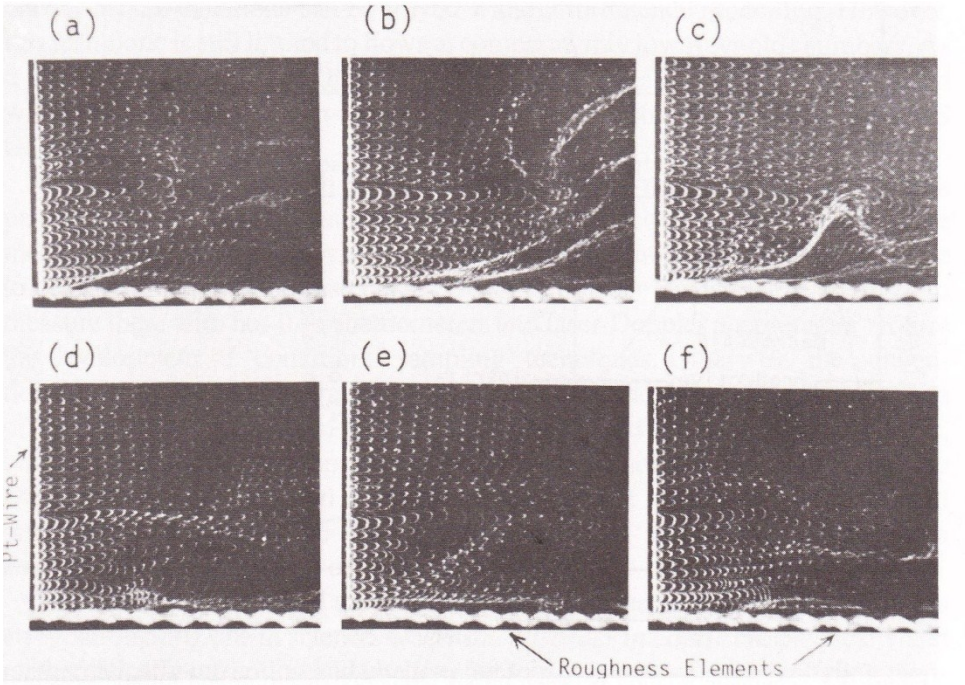

Figure 9: Some typical photographic images of ejection motions, a), b) and c); and sweep motions, d), e) and f) in rough open-channel flows (from (Nezu and Nakagawa, 1993)).

These motions may be surmised to lead to the vortex stretching (and thus propagation of turbulence) described in Section 3.4.2.

3.6 Secondary Flow Theory

Secondary currents in fluid flow are classified as being “of the first kind” or “of the second kind”, following the work of Prandlt (cited in (Perkins, 1970)). Secondary flows of the first kind are caused by skewing of the mean flow (at a river bend, for example), while those of the second kind are caused by non-uniformities in wall turbulence (Perkins, 1970) and take the form of streamwise vortices. Only secondary flows of the second kind are important to this research due to its restriction to a straight channel.

Prandlt concluded that distortions in measured isovels were due to tangential velocity fluctuations exceeding perpendicular fluctuations (direction relative to the isovels),

causing a centrifugal acceleration which propels fluid radially outwards (Perkins, 1970). Einstein & Li and Hinze (cited by (Perkins, 1970)) have shown that Second Kind flows are produced by anisotropic wall turbulence. In a study of secondary flows in square ducts, Gessner (1973) concluded that secondary flow "*originates because of small differences between transverse static pressure and Reynolds stress gradients in the flow*."

Gessner (1973) suggests that, for a square cross-section duct, in developing flows there are a number of secondary vortices, but these collapse until, in a fully developed flow, there is one secondary flow vortex per octant of the channel cross-section. The theoretical development of this vortex arrangement implies the existence of:

- Static pressure maxima and minima along the boundary
- An undulating isovels pattern
- Positive and negative values of W in the boundary layer above the wall

Gessner showed experimentally that the dominant energy fluxes in the corner region are a gain from convective transfer of energy due to secondary currents and a loss due to the work done by the main flow against transverse turbulent shear stress gradients. Further, his results showed that the primary flow cannot convect sufficient energy to compensate for losses, necessitating the existence of secondary flows as an alternative means of energy transport.

The aforementioned work focussed on air flow in ducts, but research has been performed to investigate secondary flows in open channels. For flow in a open channel with rectangular cross-section, the aspect ratio, B/H, determines the effects

of the secondary flow (Nezu, 2005). For a smooth channel, Nezu places a limit of $(B/H)_{crit} = 5$, below which secondary currents affect the whole channel and above which the central part of the channel is unaffected. This central part is defined by:

$$\left|\frac{y'}{H}\right| \leq \frac{\left[\frac{B}{H} - \left(\frac{B}{H}\right)_{crit}\right]}{2} \tag{38}$$

where y' is the lateral distance from the centre of the channel. This critical value of the aspect ratio is used to classify such channels as “narrow” or “wide” respectively (Nezu et al., 1993, Nezu, 2005).

In narrow channels the effect of secondary currents is seen in the creation of a “velocity dip”, where the maximum velocity in a vertical section is seen just below the free surface, rather than at the free surface (Nezu et al., 1993). The velocity dip is thought to be caused by the transport of low momentum fluid from close to the channel walls towards the centre and vice versa (Nezu et al., 1993).

Tominaga et al. (1989), Rhodes and Knight (1994) and others have shown experimentally that secondary currents form in trapezoidal channels as illustrated in Figure 10, while similar currents have been seen in rectangular channels (Figure 11). However, some doubt has been cast on the positional stability of these cells, with flow visualisation by Imamoto and Ishigaki (1992) indicating that time-mean velocities of lateral velocities do not accurately determine the position of these cells as their location varies with time (Figure 12). It may be argued that the time-mean velocity gives an indication of the effect of a flow cell on the overall flow, and this may explain why a link has been seen by a number of researchers cited by Nezu et al. (1993)

between transverse oscillations seen in the boundary shear stress and time-mean secondary flows, despite the instability seen by Imamoto and Ishigaki.

Shiono & Knight (1991) noted the increased complexity of the boundary shear stress distribution seen in a compound channel, and attributed this to secondary flows and transverse shear stress.

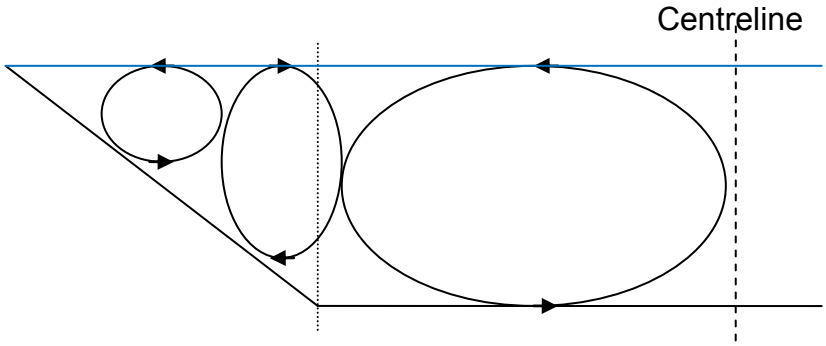

Figure 10: Secondary Flows in Half a Trapezoidal Channel (after (Tominaga, Nezu et al., 1989)

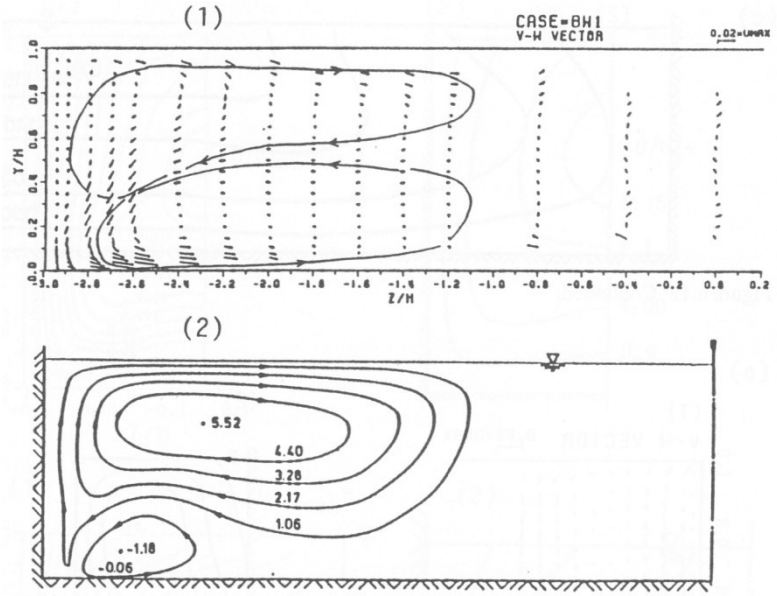

Figure 11: Secondary Flow Cells in Half a Rectangular Channel ((Nezu and Nakagawa, 1993)

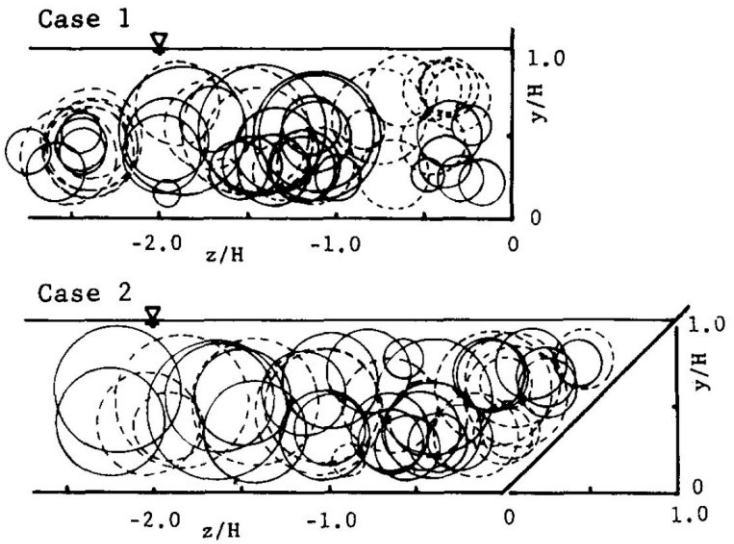

Figure 12: Movement of Secondary Flow Cells. Solid lines indicate clockwise cells, dotted lines indicate anti-clockwise cells (Imamoto and Ishigaki, 1992)

3.7 The Shiono-Knight Method

The Shiono-Knight Method (SKM) is a two-dimensional model of open channel flow based on the RANS equations (Shiono and Knight, 1988). In its original form it modelled the turbulent interaction between the main channel flow and the flood-plain flow in a compound channel, and was subsequently extended to include the effects of secondary flows (Shiono and Knight, 1991). In the case of a compound channel with secondary flows it can be shown to have an analytical solution (Shiono and Knight, 1991).

3.7.1 Mathematical Development

Shiono and Knight developed the SKM as outlined in this section (see (Shiono and Knight, 1988, Shiono and Knight, 1991) for more detail). Assuming that $W(H) = W(0) = 0$, the depth-mean-average of (15) is:

$$\frac{\partial(\rho UV)_d}{\partial y} = \rho g S_0 + \frac{\partial\left(-\rho\overline{u'v'}\right)_d}{\partial y} + \frac{\partial\left(-\rho\overline{u'w'}\right)_d}{\partial z} \tag{39}$$

where:

$$(\rho UV)_d = \frac{1}{H}\int_0^H \rho UV\, dz \tag{40}$$

By consideration of the forces on a fluid element, and conservation of momentum, (39) may be shown to be equivalent (Shiono and Knight, 1988) to:

$$\frac{\partial H(\rho UV)_d}{\partial y} = \rho g H S_0 + \frac{\partial H\bar{\tau}_{yx}}{\partial y} - \tau_b\left(1 + \frac{1}{s^2}\right)^{\frac{1}{2}} \tag{41}$$

where τ_b is the shear stress at the channel bed, s is the side-slope and:

$$\bar{\tau}_{yx} = \frac{1}{H}\int_0^H (-\rho\overline{u'v'})\,dz \tag{42}$$

is the depth-mean Reynolds stress due to interface vortex turbulence, the depth-mean transverse shear stress. The term on the left hand side of (41), $\frac{\partial(HUV)_d}{\partial y}$, is the force due to secondary flow effects.

3.7.2 Modelling of Momentum Transfer Due to Secondary Flows and Interface Vortices

3.7.2.1 *Secondary Flows*

In adapting the SKM to take secondary flows into account, Shino and Knight (1991) adopted a simple model in which the secondary flows were assumed to be at a maximum at clearly defined transverse points, and decrease linearly on either side. Omran and Knight (2006) and Knight et al. (2007) suggested a refinement to the secondary flow model for simple trapezoidal channels, based on the experimental work mentioned in Section 3.6.

This work indicated that, irrespective of the exact channel dimensions, the secondary flows in such a channel take the form shown in Figure 13. The streamwise velocity, U, is always positive but varies with depth as shown in Figure 14, while, as is evident from Figure 13, at a given y position the transverse velocity, V, alternates between positive and negative with depth. Figure 14 also shows the variation with depth of V and the product UV at one vertical section. In this example, the depth-averaged value of UV, $(UV)_d$, is positive due to the height-symmetrical, zero mean, variation of $|V|$ and increasing, positive U. Similarly, if V were positive at the bed then $(UV)_d$would be negative. The sign of V at the bed depends on the y position at which V is

measured, and alternates across the channel. Maxima of $(UV)_d$ occur at the centreline of each clockwise secondary flow vortex, minima occur at the centreline of each anticlockwise vortex, and zeroes at the boundary between adjacent vortices. This is shown in Figure 13. Omran & Knight (2006) and Knight et al. (2007) suggested $(UV)_d$ be assumed to vary linearly between the maxima and minima. This method splits the channel into four panels, with $\frac{\partial(H\rho UV)_d}{\partial y} = constant$ in each one, as shown in Figure 13. Thus each panel represents a region in which secondary flow effects are constant:

$$\frac{\partial H(\rho UV)_d}{\partial y} = \Gamma_{\mathrm{i}} \tag{43}$$

where $\Gamma_{\mathrm{i}} = constant$ is the rate of variation of the secondary flow force in panel i.

The use of sub-panels (splitting panels 2 and 3) to further refine the model was also investigated but showed little improvement in the prediction of distributions of U_d and τ_b (Omran and Knight, 2006). Knight et al. (2007) studied data from previous experiments and determined that for aspect ratios of $2B/H \geq 4.0$ the addition of a fifth panel was necessary due to existence of an additional vortex adjacent to the channel centre. Sharifi *et al*. (2008) successfully applied the SKM to predict boundary shear stress in both four and five panel scenarios, comparing the model output to experimental data.

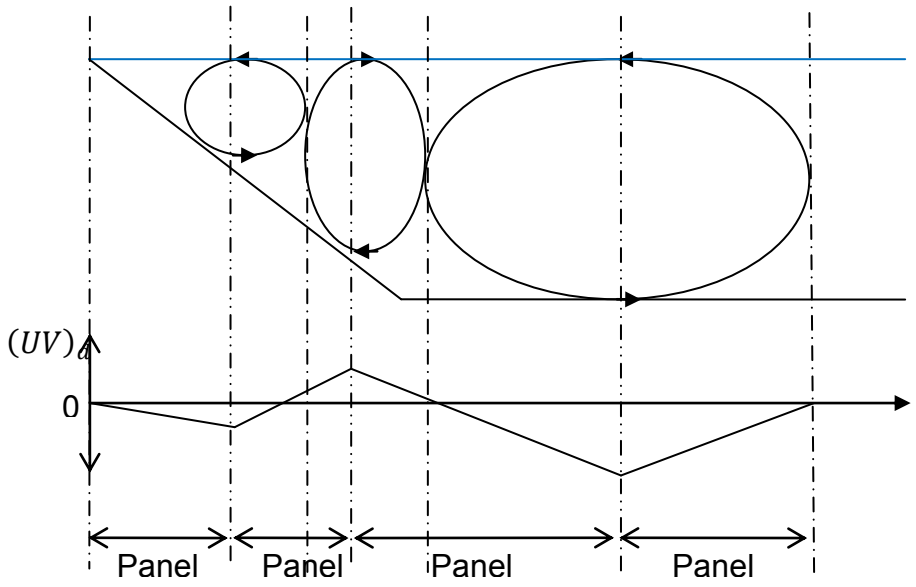

Figure 13: Secondary Flows in a Trapezoidal Channel (after (Knight et al., 2007))

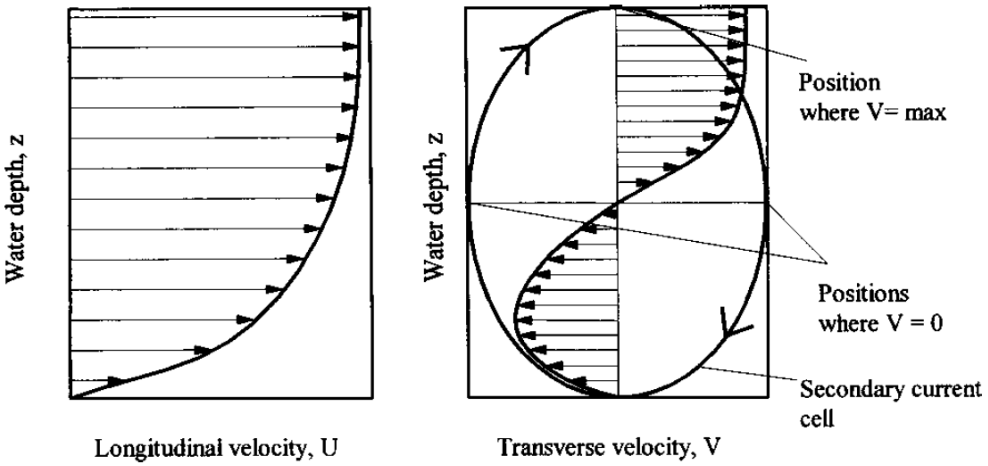

Figure 14: Qualitative Illustration of the Variation of U, V and UV with Depth (Knight et al., 2007). Note that effects of secondary flows on U near the free surface are ignored.

3.7.2.2 *Vertical Shear Layers*

In the SKM the vertical shear layer occurring between regions of differing streamwise velocity is modelled using an eddy-viscosity approach in which $\bar{\tau}_{yx}$, the depth-mean lateral shear, is modelled using the Boussinesq eddy viscosity, ε_{yx} (Shiono and Knight, 1988, Shiono and Knight, 1991):

$$\bar{\tau}_{yx} = \rho \varepsilon_{yx} \frac{\partial U}{\partial y} \tag{44}$$

where:

$$\varepsilon_{yx} = \lambda H U_* \tag{45}$$

in which λ is the eddy viscosity co-efficient. From (31) (Section 3.4.4, in which eddy-viscosity models are discussed in more depth), and assuming that that analysis is applicable for the lateral shear:

$$\varepsilon_{yx} = \frac{\kappa H U_*}{6} \tag{46}$$

which gives rise to the "standard" value of $\lambda = \kappa/6 \cong 0.07$.

3.7.3 The Analytical Solution

Shiono & Knight (1991) showed that model constructed above has an analytical solution for the depth-mean velocity, U_d. If the i^{th} panel is in a constant depth region then U_d is given by:

$$U_d = \left[A_{i1} e^{\gamma y} + A_{i2} e^{-\gamma y} + \frac{8 g S_0 H}{f} (1 - \beta) \right]^{\frac{1}{2}} \tag{47}$$

If it is in a region with side-slope s then U_d is given by:

$$U_d = [A_{i1} \xi^{\alpha_1} + A_{i2} \xi^{-\alpha_1 - 1} + \zeta \xi + \eta]^{\frac{1}{2}} \tag{48}$$

where:

$$\gamma = \left(\frac{2}{\lambda} \right)^{\frac{1}{2}} \left(\frac{f}{8} \right)^{\frac{1}{4}} \frac{1}{H} \tag{49}$$

$$\beta = \frac{\Gamma}{\rho g S_0 H}$$

$$\alpha_1 = -\frac{1}{2} + \frac{1}{2}\left[1 + \frac{s(1+s^2)^{\frac{1}{2}}}{\lambda}(8f)^{\frac{1}{2}}\right]^{\frac{1}{2}}$$

$$\zeta = \frac{gS_0}{\frac{(1+s^2)^{\frac{1}{2}}}{s}\left(\frac{f}{8}\right) - \frac{\lambda}{s^2}\left(\frac{f}{8}\right)^{\frac{1}{2}}}$$

$$\eta = -\frac{\Gamma}{\frac{(1+s^2)^{\frac{1}{2}}}{s}\rho\left(\frac{f}{8}\right)}$$

and ξ is the depth function on the side-slope. Detail of the derivation of the analytical solution for the constant depth case is given in Appendix C. The unknowns $A_{i1}$and A_{i2} are evaluated from boundary conditions, as shown by Shiono and Knight (1991). As it is specific to the experimental channel, detail of the evaluation of $A_{i1}$and A_{i2} is reserved until Section 8.4.6.

The three parameters, λ, Γ and f, must be known in order to use Equation (48). In simple terms, λ, Γ and f represent three separate physical processes which affect the flow. λ models the effect of lateral shear, Γ that of secondary flows in the plane of the cross-section and f that of friction between the fluid and the channel bed/walls (Abril and Knight, 2004).

However, it has been shown by Tominaga et al. (1989) and Abril & Knight (2004) that there is a relationship between the secondary currents and the friction factor, and so there is a link between the values of f and Γ used in the SKM. For higher values of f

(over the flood plain, for example) a higher value of Γ/H is required to calibrate the model.

f has been shown to have the most influence on the model, followed by Γ, with λ being relatively unimportant (Liao and Knight, 2007) and thus able to be modelled using standard values without loss of accuracy. In order to remove discontinuities in τ_b, f may be varied laterally across panels. This method uses common f values at panel boundaries and assumes that f varies linearly between these values (Omran and Knight, 2006, Knight et al., 2007).

3.7.4 Application and Development of the SKM

The Environment Agency's Conveyance Estimation System (CES) uses the Colebrook-White Law to calculate values for f from local values of Manning's n (see Chadwick et al. (2004) for details of the Colebrook-White Law and Manning's n), and bases λ and Γ on the work of Abril and Knight (2004) along with "standard" values for λ_{mc}, the value of the eddy-viscosity coefficient in the main channel (McGahey et al., 2006). This approach of calculating f from an n value is widely used ((Knight et al., 2007), for example). The CES differs slightly from the original SKM method through its use of the continuity of q, the unit flow rate, as the source of the boundary conditions (McGahey et al., 2006). In its original form, the SKM used the continuity of the depth-averaged velocity but this may be discontinuous in the case of step changes in channel depth.

While each of λ, Γ and f has its own physical meaning, they may be considered purely as tuning coefficients for the SKM, and this technique has been used to a varying degree in a number of studies. In research aimed at addressing issues with

the boundary shear stress distribution obtained from the SKM, Omran and Knight (2006) calculated f from the Darcy-Weisbach equation, used a "*'standard' value*" for λ but used Γ purely as a tuning parameter, albeit following a sign pattern based on the secondary flow cells.

In a study based on rectangular channels, Chlebek and Knight (2006) used a method of holding two of these parameters constant while varying the third to obtain an optimum value for the variable parameter, determined by comparison of the theoretical results to available flow data. This process was repeated for all three parameters, using the optimum values obtained for the constant coefficients as these became available. A positive (in regard to the SKM remaining a true model of physical processes) is that Chlebek and Knight used a range of realistic values of f, thus maintaining a link to the physical channel, for the initial calibration. However, Chlebek and Knight found that in deep flow the optimum f value was dependent on which of the two control parameters (discharge and percentage of total shear stress from the channel walls, $\%SF_w$, taken from experimental values) was used for the testing of the accuracy of the SKM. Based on their calculation, Chlebek and Knight developed relationships between the channel aspect ratio and the SKM parameters. Their study is, as they note, limited somewhat by the use of a single panel for each channel half-width. However, application of their relationships to additional experimental data showed good results.

The method of Chlebek & Knight is limited to finding a single set of values for λ, Γ and f. Sharifi et al. (2008, 2009) used multi-objective evolutionary algorithms to obtain values for these parameters. In this new approach, Sharifi et al. showed that

multiple solutions exist, and ranked these solutions by comparison with experimental data. A negative (from a pure hydraulics view point) to the method of Sharifi et al. is that it divorces the setting of these parameters from these interactions. However, Sharifi et al. did limit the possible range of parameters by "*adding sufficient margins to the stated range of the calibration parameters in literature*", i.e. the values were limited to a physically realistic range ($0.005 \leq f \leq 0.100$ over a smooth boundary, $0.005 \leq f \leq 1.000$ over a rough boundary, $0.005 \leq \lambda \leq 2.50$ and $-3.50 \leq \Gamma \leq 3.50$ (Sharifi, 2009)), meeting the criterion that when using "*calibration based on roughness values… …it should be ensured that roughness values remain within physically acceptable limits*" (Morvan et al., 2008). Additionally, the sign of the secondary flow term, Γ, (which should alternate between positive and negative; see Section 3.6), was used as a filter of possible solutions (Sharifi et al., 2009) to ensure a link to a physical solution. Whether this negative is important, or whether the success of the evolutionary algorithms (predictions within 3% of the measured discharge) when tested against experimental data overrides such considerations, is debateable.

3.8 Related Research

In addition to those mentioned previously, a number of studies have been carried out whose results are applicable to the research described in this thesis. In a very small number of cases this work has also involved experiments using a heterogeneous channel bed as for the current work. However, the majority involve different channel configurations but still provide qualitative results which may be usefully compared to those obtained from the experiments presented here.

Nezu and Nakagawa (1984) recognised that secondary currents may cause the formation of longitudinal sediment ridges, such as sand ribbons, in rivers. They hypothesised that once formed, these ribbons may cause additional secondary flow cells to form. Unable to make accurate measurements in water, Nezu and Nakagawa performed experiments using air flowing in a square conduit. Initially they made measurements in a smooth conduit, using a number of aspect ratios, finding that clearly defined secondary flow cells only appeared in the corner regions. However, when Nezu and Nakagawa placed longitudinal ridges within the conduit (as would form due to the corner flow cells) they found that additional secondary flow cells appeared. Preliminary experiments using water open-channel flow showed similar results, as shown in Figure 15, however Nezu and Nakagawa decided to continue their experiments using air as the medium.

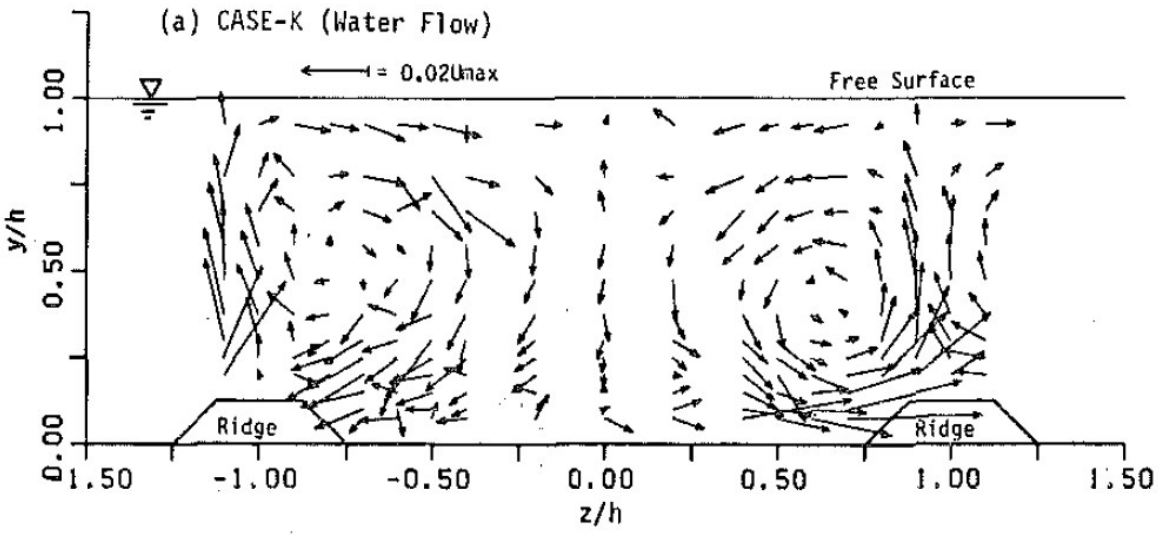

Figure 15: Secondary Flow Cells Over Longitudinal Ridges (from (Nezu and Nakagawa, 1984))

In an investigation of the secondary flows caused by a heterogeneous bed, Studerus (1982) used an experimental channel of similar dimensions to that used in this study,

with length 25m and width 600mm. Bed heterogeneity was formed by 60mm wide, longitudinal strips of 2.5mm diameter quartz sand, alternating with 100mm wide strips of smooth plastic. He identified secondary flows with velocities of 1% to 2% of the mean streamwise velocity, with upward flow over the smooth sections and downward over the rough.

Rather than manually creating a heterogeneous channel bed, McLelland et al. (1999) investigated the creation and effect of a heterogeneous channel bed from an initially homogeneous bed formed from bimodal (sand and gravel) material. They found that stripes of differing roughness formed naturally after approximately 40 minutes and remained stable for the 15 hour lifetime of their experiments. McLelland et al. made two dimensional (vertical and streamwise), 160Hz velocity measurements using Laser Doppler Anemometers (LDAs), calculating turbulence intensity and vertical Reynolds stress. Their results are reproduced in Figure 16. For the streamwise velocity, McLelland et al. noted a velocity dip near the free surface (which would normally be associated with narrow open-channel flow) and little variation due to the rough-smooth boundaries. This lack of variation may be due to the small size of the roughness elements, with the "rough" stripes having $D_{50} = 1.21mm$ (D_{xx} being a classification of particle size for a granular material, such as gravel, defined as the size of mesh through which $xx\%$ of the mass of material will pass) and the smooth $D_{50} = 0.871mm$. In the central region, secondary flow cells were seen with the same direction as those of Studerus, though the narrow width of their channel (0.3m) meant that corner effects spread throughout the channel. Streamwise turbulence intensity was found to be roughly inversely proportional to streamwise velocity, while vertical TI was a minimum at the free surface, which McLelland et al. ascribed to

damping of turbulent fluctuations by the free surface. Further, they noticed that over the "smooth" stripes vertical TI was a maximum just above the channel bed, possible due to the secondary flow cells transporting TI laterally and then upwards from the channel bed over the rough stripes. Reynolds stress was seen to decrease with depth but, as with the streamwise velocity, McLelland et al. noted no lateral variation with roughness.

Of additional interest in the work of McLelland et al. (and of direct relevance to the work contained in this thesis) is their attempt to estimate the boundary shear stress using three methods:

(i) Linear regression from Reynolds stress measurements in the bottom 30% of the flow

(ii) Calculation of the shear velocity from the law of the wall for the bottom 30% of the flow

(iii) The mean value as given by $\rho g h S_0$

These estimates gave:

Method	$\boldsymbol{\tau_b}$ $(\boldsymbol{Nm^{-2}})$
(i) at $y = 30mm$	0.549
(ii) at $y = 30mm$	0.568
(iii)	0.601

Table 1: Boundary Shear Stress Estimates of McLelland et al (1999)

Wang and Cheng (2005, 2006) performed similar experiments, using LDAs to obtain two-dimensional velocity measurements over longitudinal strip roughness and longitudinal ridges and troughs. Recognising that the secondary flow cells would

affect the streamwise flow field, Wang and Cheng surmised that assumptions made by other researchers (that the Reynolds stress distribution could be approximated as linear and the log-law of the wall was valid) may be incorrect. From their experimental data Wang and Cheng (2005) deduced analytical formulae for the vertical distribution of Reynolds stress and streamwise velocity over a heterogeneous bed formed of longitudinal stripes of alternating roughness. These formulae, which were specific to their channel, were transversely periodic, with sinusoidal variation matching the transverse roughness variation.

In a further analysis of their experimental data, Wang and Cheng (2006) examined the time-mean secondary flow structure. The case most pertinent to the research in this thesis is that of alternating rough and smooth strips with equal width. Vertical velocities were found to be small ($< 2\%$ of the mean streamwise velocity), with upflow over the smooth strips and downflow over the rough strips, as seen in the research outlined above. Sidewall effects were seen to be limited to a region within $\sim 37mm$ of the walls, meaning that secondary flow cells in the central region were due to the heterogeneous roughness only. The magnitude of the mean vertical velocity was found to peak in the centres of the strips; conversely mean transverse velocity had its maximum magnitude at the strip boundaries, as seen in Figure 17.

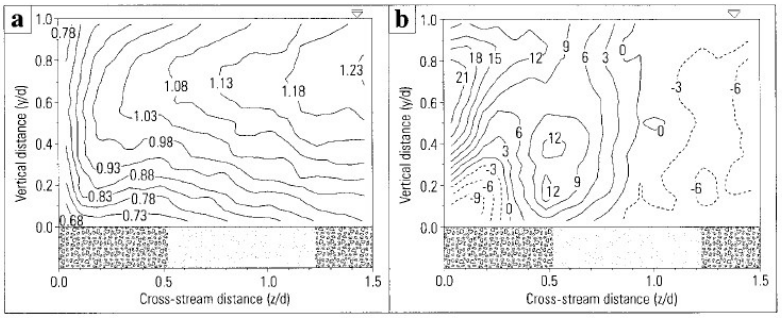

FIG. 4. Contour Plots of: (a) Dimensionless Streamwise Velocity (U/U_m); and (b) Dimensionless Vertical Velocity ($V/U_m \times 10^{-3}$) in y, z-plane. Flow Is into Page. Plot Shows Flow in Half of Channel with Location of Fine- and Coarse-Grained Sediment Stripes Being Illustrated below Contours

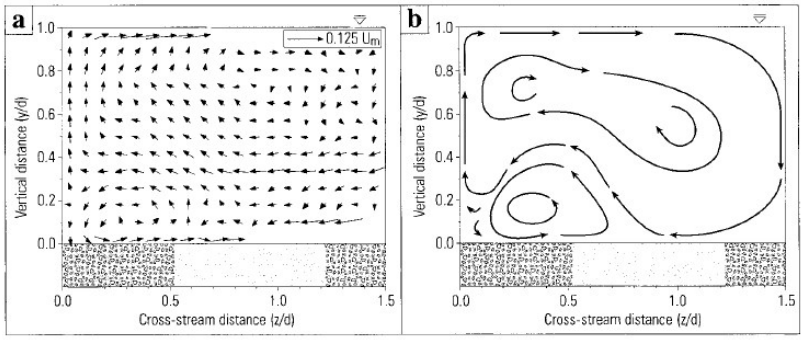

FIG. 5. (a) Vector Plot of Pattern of Secondary Circulation with Cross-Stream Velocities Calculated using Eq. (3); (b) Schematic Plot of Inferred Pattern of Secondary Flow. Flow Is into Page and Stripe Locations Are Shown below Contours

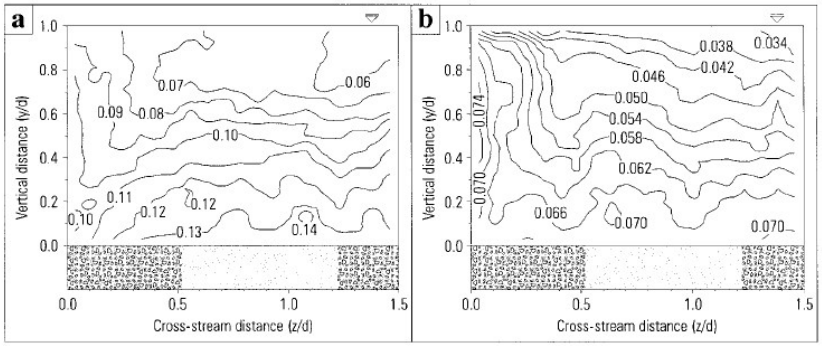

FIG. 6. Contour Plots of: (a) Dimensionless Downstream Turbulence Intensity (u'_{RMS}/U_m); (b) Dimensionless Vertical Turbulence Intensity (v'_{RMS}/U_m). Flow Is into Page and Stripe Locations Are Shown below Contours

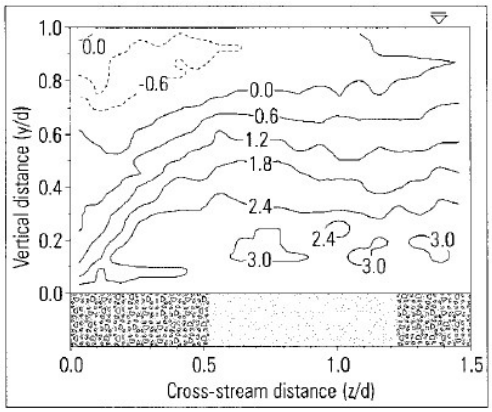

FIG. 7. Contour Plot of Dimensionless Reynolds Stress $[\tau_r/(U_m^2)]$. Flow Is into Page and Stripe Locations Are Shown below Contours

Figure 16: The Results of McLelland et al (from (McLelland et al., 1999))

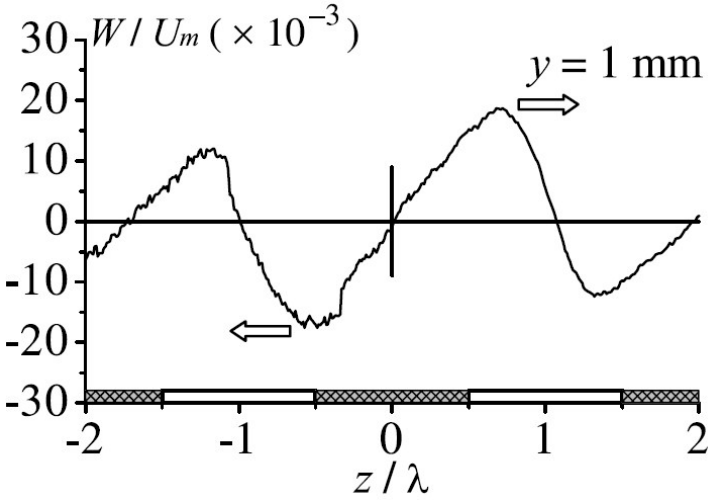

Figure 17: Variation of Transverse Velocity Over Alternating Strip Roughess (from (Wang and Cheng, 2006); note that the z-axis in the figure is the lateral axis, corresponding to the y-axis in the notation of this thesis)

The secondary flow cells identified are shown in Figure 18, and may be seen to extend for the full flow depth and to be of a diameter equal to the strip width:

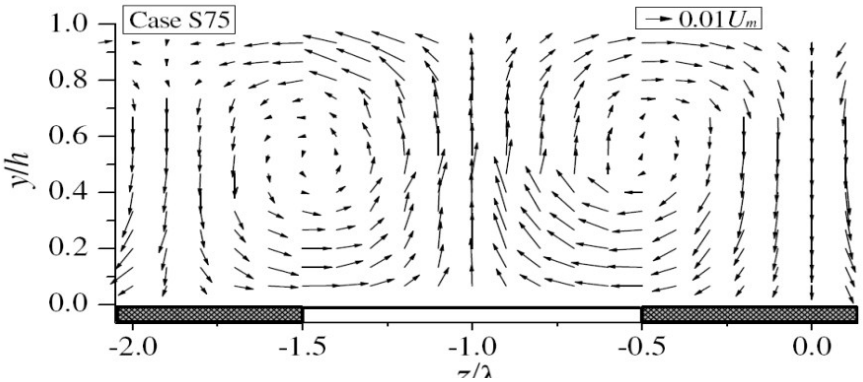

Figure 18: Secondary Flows Cells Over Alternating Strip Roughness (from (Wang and Cheng, 2006))

The work of Vermaas et al. (2007) and Vermaas (2009) is particularly relevant to the research described in this thesis and so it is discussed here in some depth. In his thesis, Vermaas (2009) investigated the role of momentum transfer through turbulent mixing at the boundary between the rough and smooth sides of the channel (henceforth the rough-smooth boundary, RSB) and through advection due to secondary currents using a 2m wide, horizontal bed experimental channel. As with

the research described in this thesis, this channel was split along the centreline into a rough side and smooth side. In further experiments, Vermaas examined the effects of a checkerboard arrangement of alternating rough and smooth sections of 4m length. Additionally, he used Large Eddy Simulation (LES) to model the channel in detail, using his experimental measurements as validation of the simulation.

Vermaas used a combination of ADV and Particle Tracking Velocimetry (PTV) measurements, with the PTV allowing capture of velocity measurements close to the water surface, a region inaccessible to the ADV. The ADV measurements concentrated on the RSB, with a 20mm transverse separation of the measuring points close to the RSB and a wider spacing distant from the RSB, as shown in Figure 19.

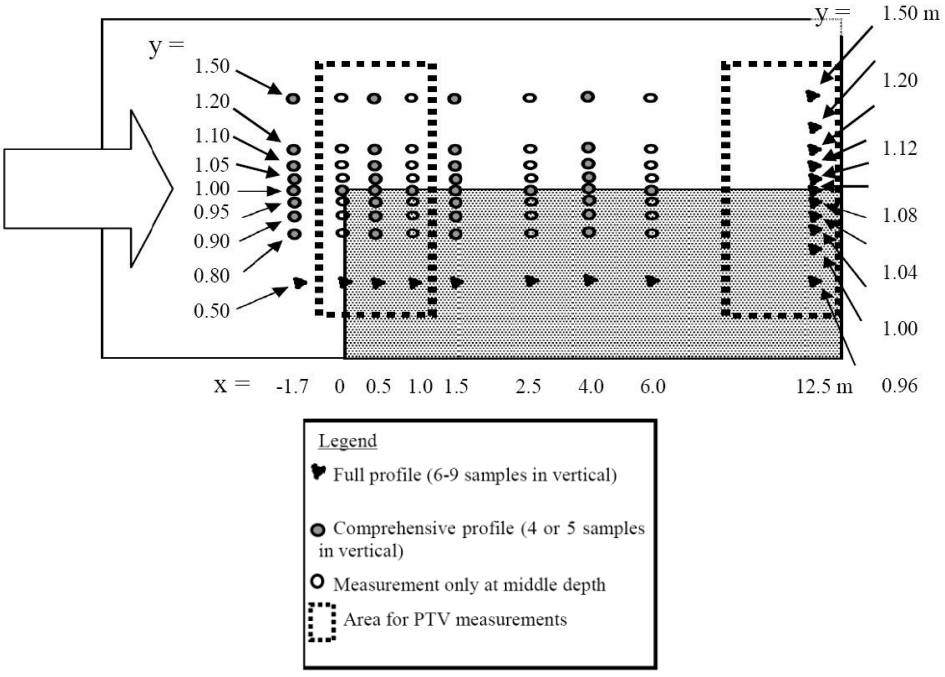

Figure 19: Measuring Points Used By Vermaas (from (Vermaas, 2009))

Using these measuring points, Vermaas was able to investigate the longitudinal development of the flow as well as examining the fully-developed flow cross-section

at $x = 12.5m$. An example of the transverse mean streamwise velocity profile measured by Vermaas is shown in Figure 20.

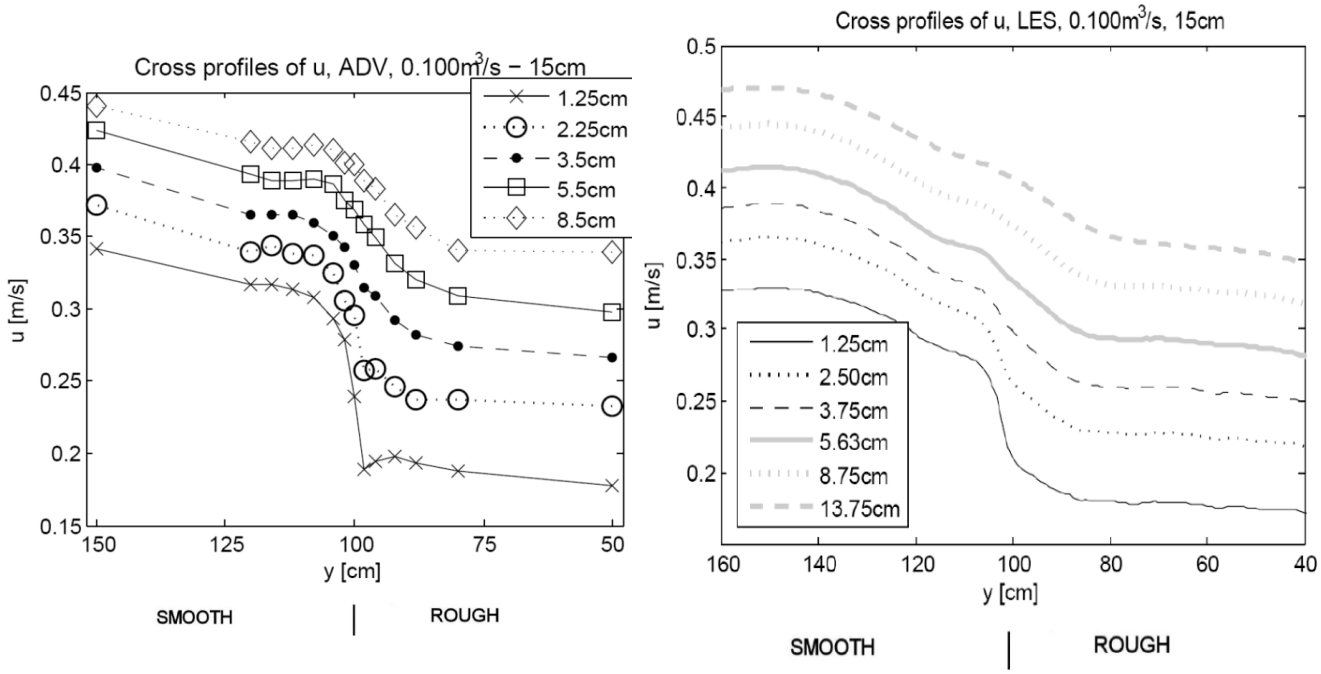

Figure 20: Transverse Mean Streamwise Velocity Profile of Vermaas (Left – ADV, Right – LES; from (Vermaas, 2009))

Vermaas notes that $\frac{dU}{dy} \cong 0$ a distance of between $2H$ and $4H$ (300-600mm) from the RSB on the smooth side, but a shorter distance (between $1H$ and $2H$; 15-20cm) on the rough side. However, from Figure 20 (which shows the $H = 15cm$ case - the only one for which Vermaas provides both the ADV and LES data), it may be seen that there are no experimental measurements in this region. The extreme measuring points have significantly different U values to the last points in the central region, and so U appears to be varying linearly, with $\frac{dU}{dy} \neq 0$. Further, $\frac{dU}{dy} \cong 0$ around the outside central points on the smooth side $(y \cong 120cm)$. Additionally, the LES results appear to smooth out this flattening while exaggerating the positive bulge at $y \cong 108cm$ and

removing the negative bulge at $y \cong 98cm$ - Vermaas notes both of these bulges in his text.

In the case of secondary flows, Vermaas found flows with velocities of 1-2% of the streamwise velocity, with cells having a width in the order of $2H$, with the centre slightly below $0.5H$. Vermaas' results for $H = 15cm$ are shown in Figure 21.

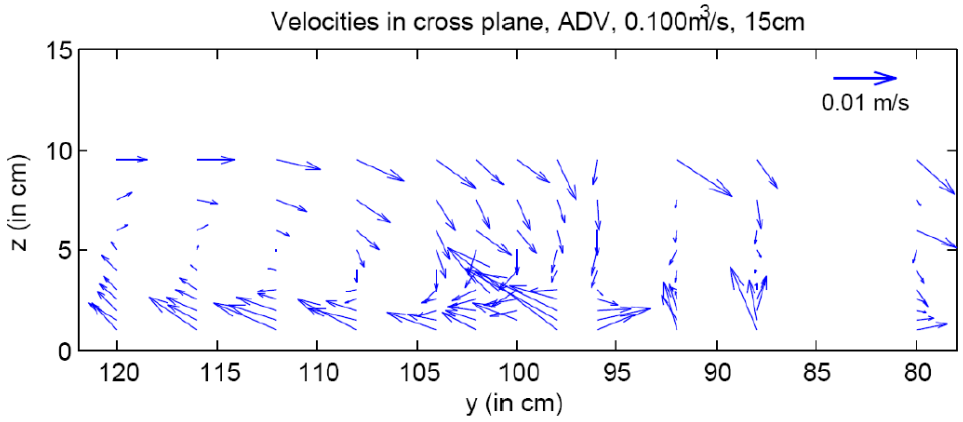

Figure 21: Secondary Flow Cells as Measured by Vermaas (from (Vermaas, 2009))

The location of the secondary flow cell, with its centre offset from the RSB, differs from the results of Wang and Cheng and Studerus reported earlier, in which the cells are centred at the RSB.

Vermaas calculated the momentum transfer through turbulent mixing, T_{mix}, and advection by secondary flow cells, T_{adv}, using Equation (50) and Equation (51) respectively.

$$T_{mix} = \frac{1}{H}\int_0^H (-\overline{u'v'})\, dz \tag{50}$$

$$T_{adv} = \frac{1}{H}\int_0^H \left(-U\left(V - \frac{1}{H}\int_0^H V\, dz\right)\right) dz \tag{51}$$

The $\frac{1}{H}\int_0^H V\,dz$ term in Equation (51) is used to account for transverse velocity due to equalisation of the pressure gradient across the channel; this should be zero for fully-developed flow and so T_{adv} simplifies to the depth-average of UV. Vermaas found that the two mechanisms were of equal order of magnitude, with advection dominating over the smooth side and turbulent mixing peaking at the RSB and being dominant over the rough side (Vermaas, 2009). Vermaas examined a number of flow depths, finding that advection became more important at greater flow depths, as may be anticipated due to the larger relative roughness at lower depths.

Anticipating that, in a natural river, flow over a heterogeneous bed would usually not be fully-developed (due to the relatively short length of the heterogeneous reaches), Vermaas investigated the development of the flow from the start of the heterogeneity at $x = 0m$. It was found that the mean transverse velocity, V - thought to be an indicator of redistribution of water from the rough side to the smooth side due to a pressure gradient at the start of the heterogeneous section - peaked at the start of the heterogeneity. Most of the redistribution of water was complete by $x = 4m$, and the longitudinal distribution of V was only weakly dependent on flow depth. However, as may be seen from Figure 22, V was non-zero for much of the channel length.

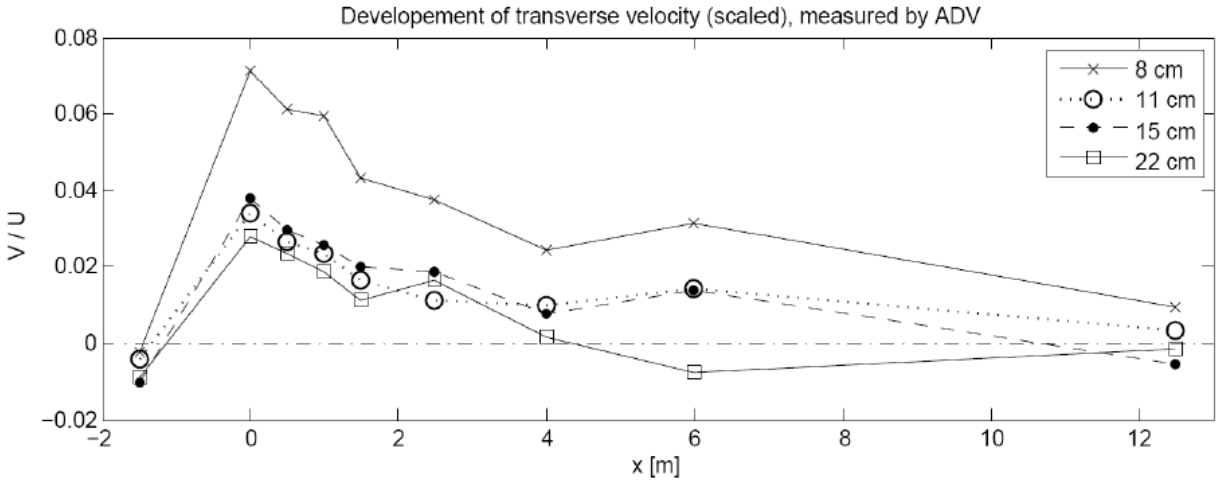

Figure 22: Longitudinal Distribution of Transverse Velocity, V (from (Vermaas, 2009); legend refers to flow depth)

A similar longitudinal development analysis was performed for shear stress (with a development length of $25H$), mixing layer $(50H)$ and secondary flow $(80H)$.

Using the checkerboard configuration, with section length $4m$, Vermaas found that at lower levels ($z = 1.5cm$ with $H = 15cm$) the transverse U distribution developed in a similar fashion to that for the continuous bed. At higher levels ($z = 7cm$) the distribution remained relatively constant along the section. Maximum depth-averaged U occurred on the smooth side, between 5-10cm from the RSB. After the switch of rough and smooth, the position of the peak depth-averaged velocity was seen to switch sides after $1m$ $(0.5B)$, and to have completely switched (mirroring the profile of the pre-switch section) after $2m$ $(1B)$. By integrating over the length of the channel, Vermaas found that the length-mean maximum of depth-averaged U occurred at the RSB.

Examination of the distribution of transverse velocity showed a maximum at the roughness switch, falling quickly within the first metre. Upward flow was seen at the

switch on the smooth-to-rough side, with downward flow on the rough-to-smooth side. Vermaas found that secondary flow cells were very weak or non-existent, making turbulent mixing the main source of momentum transfer. Bed shear stress was higher over the rough side than for the continuous bed configuration, while that on the smooth side was unchanged.

Another study of interest is that of Wang (1972), in which he presents the results of his experiments into the effect of longitudinal strip roughness on air flow over a flat plate. The pressure gradient of the flow was approximately zero, equivalent to normal open channel flow. The flat plate was (converting imperial measurements to metric approximations) 4m long and 1.5m wide. To this were attached four 150mm wide strips of rough sandpaper, with grain size 2.5mm "*averaged roughness height*", at a separation of 150mm, leaving smooth borders at each edge of the plate. Turbulent velocity measurements were made using a hot-wire anemometer, along with boundary shear stress measurements on the smooth surfaces using a Preston tube. Assuming periodicity of the flow structure over the laterally repeating bed structure, Wang made measurements in a 150mm wide strip laying between the centre line of a smooth strip and the adjacent rough strip. This assumption has been retrospectively supported by the results of Wang and Cheng (2006)

Also of interest, due to its causing of lateral variations in streamwise velocity, is the study of laterally-partially vegetated channels (i.e. half the channel width vegetated, the other half smooth) by, for example, Nezu and Onitsuka (2001), White and Nepf (2007, 2008) and Tang et al. (2010), which will be discussed in the following paragraphs.

Experimental work by Nezu and Onitsuka (2001) used both Particle Image Velocimetry (PIV) and LDA equipment in such a channel, using the former to measure velocities in a horizontal plane spanning the channel width and a streamwise length of the channel, and the latter to measure velocities over a channel cross-section. The horizontal plane showed the existence of vertical, interface vortices at the boundary between the vegetated and non-vegetated regions. Unfortunately only one such plane was measured, giving no indication of any decay of these vortices with height above the vegetation. The cross-section measurements revealed clear peaks in τ_H^R at the boundary (Figure 23). An interesting feature of this figure is the widening (onto the vegetated side) of the peak above the vegetation (which finishes at $y/H = 0.71$ – note that y is their vertical ordinate). This may be due to the transfer of turbulence by the interface vortices – again, a set of horizontal plane data for the non-vegetated side of the channel for $y/H < 0.71$ would be of interest to determine whether such vortices exist in any form below the top of the vegetation.

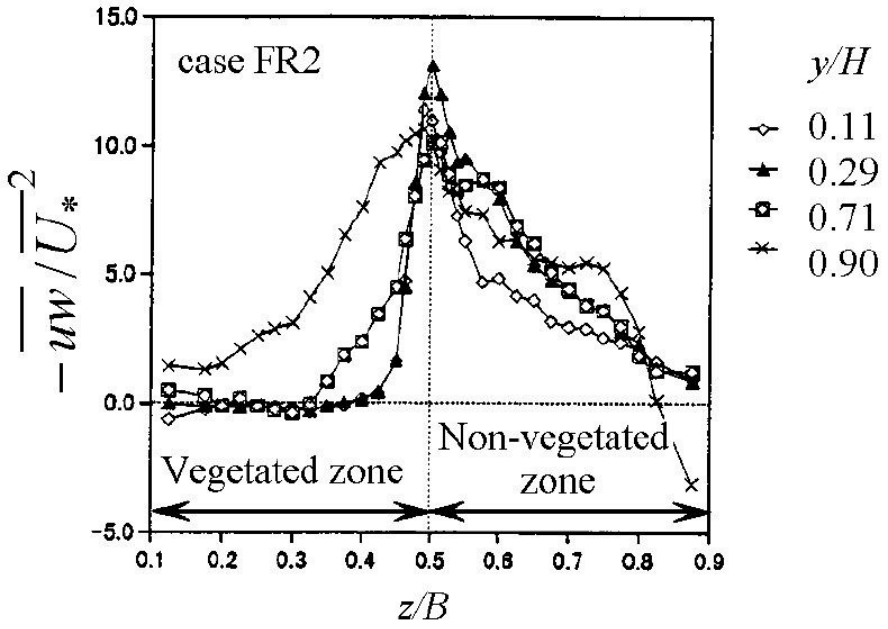

Figure 23: Horizontal Reynolds Stress Measurements Over a Partially Vegetated Channel (Note: y\v are vertical, z\w are horizontal) (Nezu and Onitsuka, 2001)

White and Nepf (2007, 2008) performed a similar study with an aim to develop a model to predict such flows, noting that the shear layer between the vegetated and non-vegetated regions could be split into two regions, analogous to those of a boundary layer. Their inner region consisted of the (narrow) strip of the vegetated side into which there was an appreciable incursion of faster water from the non-vegetated side. Within this region lay a point of inflexion in the transverse U distribution, an indication of Kelvin-Helmholtz instabilities known to cause coherent vortices. Both White and Nepf and Nezu and Onitsuka found that such coherency was evident from the time series of streamwise and transverse velocities, which showed coherent periodicity of the two velocities (Figure 24). Moving into the non-vegetated side, beyond the point of inflexion, White and Nepf found the velocity distribution to be similar to the logarithmic distribution seen in a boundary layer formed when the eddy viscosity is constant. This study is slightly limited by its restriction to shallow flows which are assumed to be 2-D – i.e. secondary flows are ignored.

In their later paper, White and Nepf go on to develop an empirically derived, vortex-based model to predict streamwise velocity distributions in a partially vegetated channel, but it is more instructive within the context of this thesis to discuss the work of Tang et al., who modelled such a system using the SKM (Tang et al., 2010). In order to model the effect of the vegetation, Tang et al. incorporated vegetation drag, F_v, through an additional term in the RANS equations based on the standard drag force equation:

$$F_v = \frac{1}{2}\rho C_D \beta_v A_v U^2 \tag{52}$$

where C_D is a drag co-efficient, β_v a vegetation shape factor and A_v is the cross sectional area blocked by the vegetation (i.e. excluding gaps between stems, etc.). Using an analytical solution to the modified SKM, with standard values of f, Γ and λ, Tang et al. demonstrated that such a model accurately predicted the U_d distribution seen in the experimental results from a number of partially vegetated channels, including those with vegetated flood plains. This modelling used a two-panel solution, as previously described for rectangular channels, which reduces the parameter input when compared to the four-panel model of White and Nepf. However, while its derivation supports non-emergent vegetation, all data sets modelled were for emergent (full-depth) vegetation. It remains to be seen how depth-dependency of Γ and λ, which may be anticipated in a channel with non-emergent vegetation, can be modelled using the SKM.

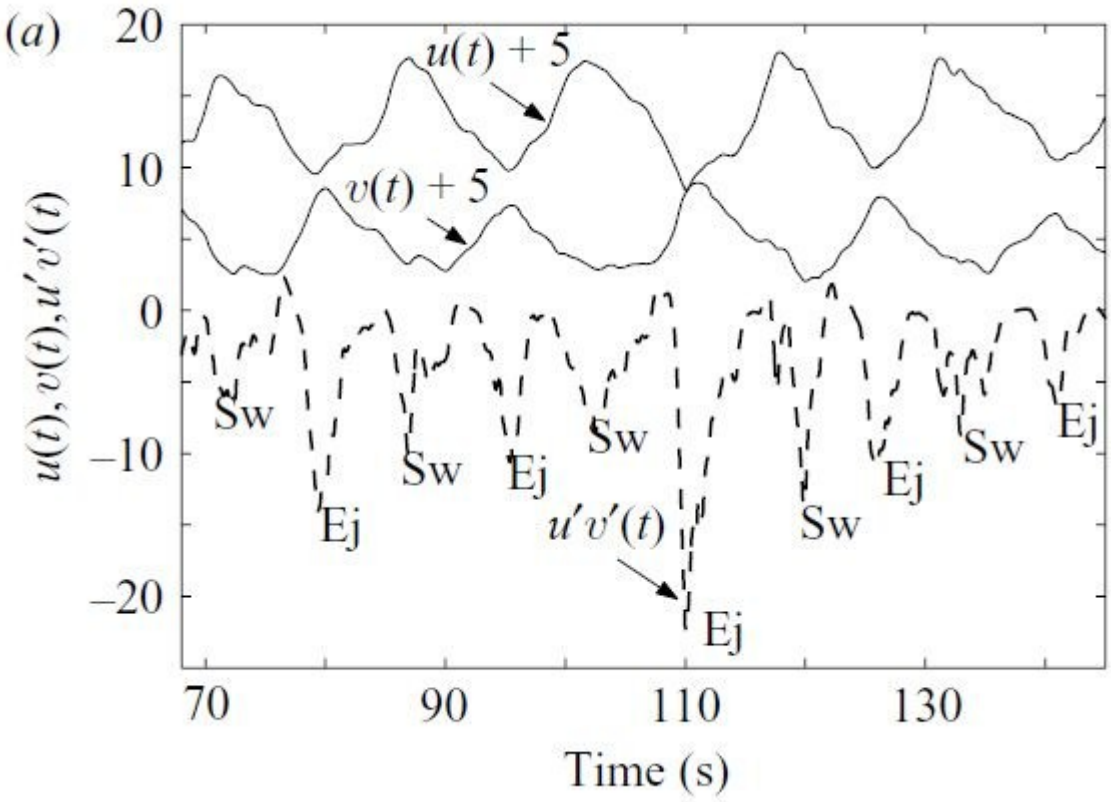

Figure 24: Periodicity of Streamwise and Lateral Velocity Components

Also of importance to the experimental work described within this thesis is the selection of an appropriate scale for the "checkerboard" bed configuration. In a natural river the channel bed varies along the length of the river and consequently the transverse pattern of heterogeneity will be dependent on streamwise position. The rate at which the bed changes would be expected to be of importance, though no direct data on this was found in the literature. In the study of river ecology and ecohydraulics the concept of physical biotopes is used, with each biotope representing a different wildlife habitat (Harvey and Clifford, 2009). Jowett (1993) has shown that in approximately two-thirds of cases these biotopes can be correctly identified from the flow characteristics such as velocity and Froude number. As such, the rate of change of physical biotope would seem to be a good indicator of changes in channel characteristics such as bed roughness. Newson and Newson (2000) give a rather vague quantification of this rate of change, stating that habitat changes:

"at channel length intervals which are small multiples of channel width"

Padmore (1997) used the concept of biotope "patchiness" to quantify the rate of change of biotope. She examined a number of rivers in the North-East of England, measuring the number of biotopes in a river reach of length $(10 \times Channel\ Width)$ at a number of flow rates. These flow rates were categorised as exceedences of the Average Daily Flow (ADF), and Padmore's results are shown in Figure 25: From this figure it may be seen that, at average flow rates (exceedence = 0%), the biotope changes between three and four times per ten channel widths. This gives a mean biotype length of approximately three channel widths.

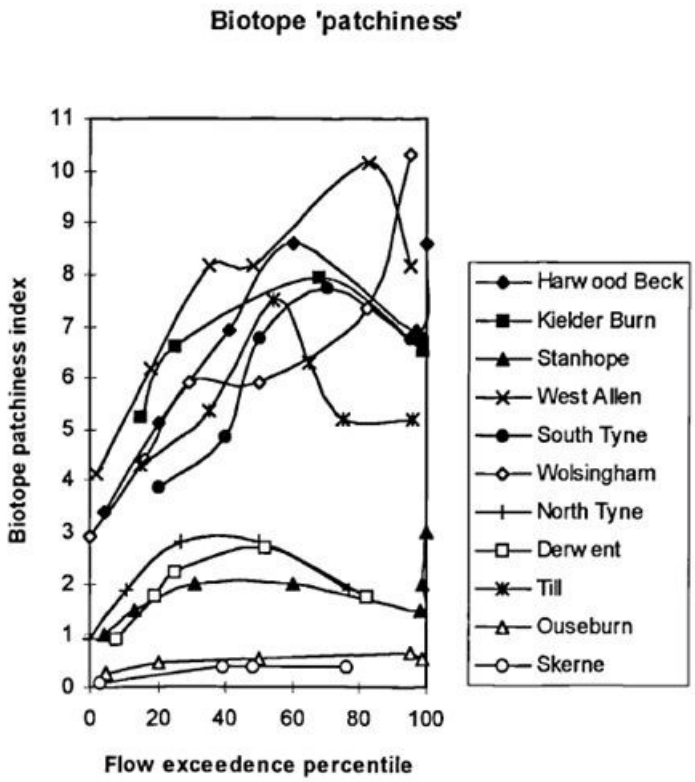

Figure 25: Streamwise Variation of Channel Bed Identified Through Biotype Variation (from (Padmore, 1997))

4 EXPERIMENTAL APPARATUS AND DATA ANALYSIS TECHNIQUES

4.1 Introduction

While the majority of the equipment used for this research is self-explanatory and can be described in a few lines, some pieces of apparatus require a more detailed explanation if their use and limitations are to be properly understood. Such apparatus is introduced in this section, as are those data analysis techniques which similarly require in-depth discussion.

4.2 Acoustic Doppler Velocimeters

The Acoustic Doppler Velocimeter (ADV) was developed by the US Army Engineer Waterways Experiment Station to provide an instrument capable of giving instantaneous velocity measurements in three dimensions (Lohrmann et al., 1994). It was designed to replace existing instruments such as laser Doppler velocimeters, Pitot tubes and hot film anemometers, which can only provide 1-D or 2-D measurements.

The Nortek Vectrino ADV probe used in this research consists of a transmitter and four receivers evenly spaced at 90° intervals around the transmitter, angled at 30° to the transmitter axis (see Figure 26). As the probe itself will disrupt the flow, it measures the velocity at a point approximately 50mm from the probe end in order to reduce any interference with the flow at the measuring point (Lohrmann et al., 1994). More details of the workings of the ADV may be found in Lohrmann et al. (1994) and Lane et al. (1998), while a summary is given below.

Figure 26: ADV Probe

4.2.1 Operational Principles

The ADV measures velocities using the principal of Doppler shift, where sound waves bounced off a moving object (in this case a particle carried in the water) have their frequency shifted by an amount proportional to the velocity of the object. The speed of sound in a given medium is constant, and so this frequency shift also manifests itself as a wavelength shift since the speed of sound, c, is related to the wavelength, ϵ, and the frequency, f_t, by:

$$c = \epsilon f_t \tag{53}$$

This frequency/wavelength shift can also be expressed as a shift in the phase of the wave, $d\phi$, by:

$$d\phi = \frac{2\pi}{\epsilon} d\epsilon \tag{54}$$

The Nortek Vectrino ADV used for this research calculates velocity based on the phase shift using a technique called pure coherent pulse-to-pulse processing (Lane et al., 1998). The probe transmits short pulses of 10MHz sound waves, at a sampling frequency of 200Hz. A large number of pulses are processed, with the phase shift being calculated from the covariance of pairs of consecutive pulses (see (Lane et al., 1998)).

The probe samples over a small volume of water, nominally a 6-mm diameter cylinder aligned with the probe axis and centred on the measuring point (Nortek, 2004). The height of the cylinder can be varied from 3 to 15mm (Nortek, 2004).

4.2.2 Issues Affecting the Accuracy of Measurements

The measurements obtained from an ADV can be compromised by a number of issues which affect their accuracy. The salinity and temperature of the water affect the speed of sound, leading to errors of over 3% for an uncalibrated probe (Lohrmann et al., 1994). However, the Vectrino probe automatically measures the water temperature and so temperature effects are not an issue for the velocity measurements in this research.

A phenomenon called aliasing occurs due to the fact that measurement of the phase shift is limited to the range -180° to +180°. Due to the periodicity of a wave, a phase shift outside this range is indistinguishable from a smaller shift within this range (for example, a shift of +200° is identical to a shift of -160°) and will be interpreted as being the smaller shift and hence as representing a smaller velocity. (Goring and Nikora, 2002), (Lane et al., 1998). Aliasing is illustrated in Figure 27.

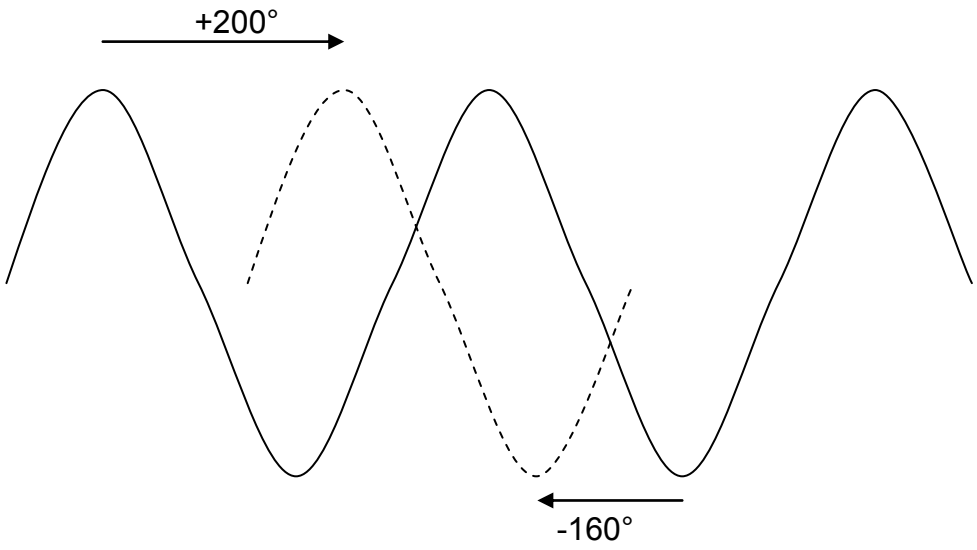

Figure 27: Aliasing

To prevent aliasing, the maximum velocity that is expected to be measured, U_{max}, may be set as part of the ADV configuration. This parameter is used to set the time interval between pulses, as U_{max} is inversely proportional to this time interval (Lane et al., 1998). While it may appear advantageous to set U_{max} as high as possible, Voulgaris & Trowbridge (1998) show that the Doppler noise is also inversely proportional to the time between pulses, signifying that the Doppler noise is proportional to U_{max}. Hence the prevention of aliasing and minimising of Doppler noise have conflicting requirements for U_{max}, and so U_{max} should be set to be the minimum value which exceeds the anticipated maximum velocity measurement (Lane et al., 1998), (Voulgaris and Trowbridge, 1998), (Nikora and Goring, 1998).

The resolution (highest detectable turbulent fluctuation frequency) is determined by the Nyquist frequency. Real-time velocity measurements in turbulent flow produce a signal which is formed by the superposition of a number of signals of different frequencies, with the low frequency components corresponding to large scale eddies and the high frequencies corresponding to the Kolmogorov microscales.

Sampling of any such composite signal at a rate f_S can detect component signals of frequencies up to half the sampling frequency. This limiting frequency is called the Nyquist frequency, f_N (Kaimal and Finnigan, 1994):

$$f_N = \frac{f_S}{2} \tag{55}$$

In a similar manner to the aliasing described above, component signals at frequencies greater than f_N wrap around and are measured as being of a lower frequency. With the Nortek Vectrino, the sampling rate is 200Hz, giving $f_N = 100Hz$.

Doppler noise is the name given to the error which is inherent in any device which uses Doppler backscattering to calculate velocities (Lohrmann et al., 1994). The cause of this noise is not fully understood, but it is thought that there are three main causes: particles entering and leaving the sampling volume during the interval between pulses, turbulence at scales smaller than the measuring volume, and beam divergence (Nikora and Goring, 1998). Nikora & Goring (1998) determined that the Doppler noise approximates a Gaussian white-noise and so has a constant energy spectrum. Further, they showed that measurements of horizontal velocities are subject to Doppler noise of a magnitude approximately thirty times greater than that of the vertical velocities, and that Doppler noise is dependent on the type of particles in the water.

Since the Doppler noise is white noise, Nikora & Goring suggest that the turbulent energy spectrum for a flow may be split into two parts, with the division at the frequency for which the turbulent energy equals the Doppler noise energy. This is

illustrated in Figure 28 below, with the characteristic frequency denoted as ω_b (note the use of radians/s in this figure – denoting the characteristic frequency in cycles per second as f_b, $f_b \equiv \omega_b/2\pi$).

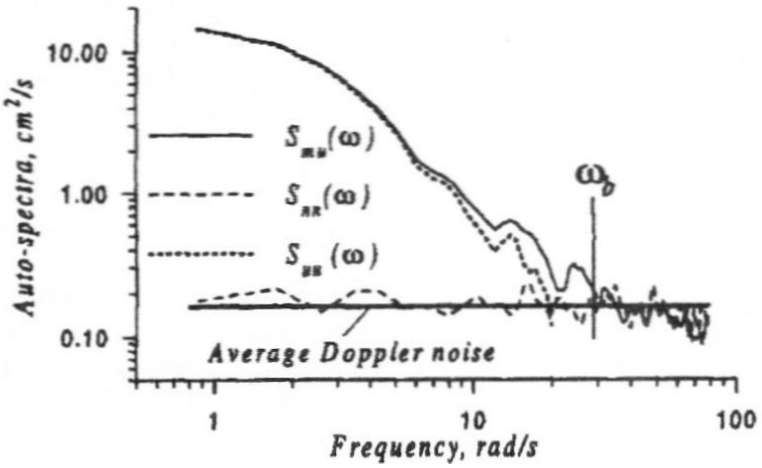

Figure 28: Turbulent Energy Spectrum and Doppler Noise Spectrum (Nikora and Goring, 1998)

At lower frequencies, where the turbulent energy is greater, the Doppler noise may be considered negligible. At higher frequencies the Doppler noise causes a flattening of the measured energy spectrum (note that the energy spectrum is not measured directly, but is the result of spectral analysis of the velocity measurements).

The Nyquist frequency becomes important when considering the effects of Doppler noise. If $f_b > f_N$ then the Doppler noise only becomes important outside the range of frequencies which the ADV can detect. Conversely, if $f_N > f_b$ then the Doppler noise reveals itself as a plateau in the energy spectrum. In the former case, there is no way of estimating the noise from the measured spectrum (Garcia et al., 2004). The Doppler noise effects on a high-energy, turbulent flow such as a boundary layer will be small (Lohrmann et al., 1994), while in low-energy flows it will make up a significant part of the energy spectrum (Garcia et al., 2004).

The 6mm diameter of the sampling volume also affects the ability of the ADV to detect eddies below this size. Only eddies which are larger than this are detectable - smaller eddies are completely enclosed by the sampling volume and thus their net contribution to the velocity is zero. It is acknowledged that at any instant some small eddies will span the volume boundary (being partially within the volume and partially outside), giving a non-zero contribution to the velocity, but (assuming that, on the scale of the sampling volume, the turbulence in homogeneous) then this distribution will be random and all spanning eddies may be assumed to have a total contribution of zero. With the mean streamwise velocities seen in this research (approximately $0.6ms^{-1}$), it will take approximately 0.001s for a 6mm diameter eddy to pass through the sampling volume, giving an upper detectable velocity fluctuation frequency of 100Hz.

4.2.3 Correlation and Signal to Noise Ratio (SNR)

As it is used to estimate the phase shift, the correlation between pulse pairs gives an indication of the quality of the measurements. It is recommended that any measurements with a correlation of less than 0.7 (on a scale of 0 to 1.0) are discarded (Lane et al., 1998). However, it has been suggested that correlation is not necessarily a good filtering parameter for turbulent flow as it is strongly affected by high-frequency fluctuations (Cea et al., 2007). Alternative filtering (despiking) methods are discussed in Section 4.2.5.

Reducing the sampling volume reduces the precision of the measurements (Nortek, 2004) due to an increase in Doppler noise (Lohrmann et al., 1994). The ratio of the signal strength to the noise, the SNR, is output by the Vectrino ADV. It is

recommended that an SNR of at least 15 is achieved in order to obtain good data (Lohrmann et al., 1994).

4.2.4 The Use of ADVs to Measure Turbulence

When using an ADV to measure the turbulent fluctuations in flow velocities, two important parameters which have to be set are the sample length and sampling rate. The former is the duration of time over which the velocity is measured at each sampling point, while the latter is the number of individual velocity measurements taken per second.

Sample length is entirely at the judgement of the user, while the sample rate is limited by the instrument. The Nortek Vectrino ADV is able to sample at a number of rates up to a maximum of rate of 200 measurements per second (200Hz). In determining the sample length to use, it is important to ensure that the sample length is long enough to capture the lowest frequency fluctuations seen in the flow. This may be interpreted as the point at which the standard deviation of all measurements since the start of the sample becomes approximately constant. Buffin-Belanger and Roy (2005) attempted to quantify appropriate minimum record lengths for ADV and Electromagnetic Current Meter (ECM) signals, using an ECM and ADV sampling at 20Hz and 25Hz respectively. Their results showed that the optimal record length was approximately equal in terms of the number of instantaneous measurements, but shorter (in terms of time) for the ADV due to the higher sampling rate. Buffin-Belanger and Roy found the optimal record length to be 60 to 90 seconds, but note that in highly turbulent flow this can increase. They note that other researchers have used records of twice this length in regions of high turbulence intensity.

A number of studies have investigated the errors which occur when using an ADV to measure the characteristics of turbulent flow, such as Reynolds stresses. Most of these (for example, (Nikora and Goring, 1998) and (Voulgaris and Trowbridge, 1998)) have used older ADV models, which only sampled at a maximum of 25Hz. A newer study by McLelland and Nicholas (2000) used probes with sampling rates of up to 100Hz and took into account the precise methodology used in the Nortek ADVs. McLelland and Nicholas examined the sources of noise (and therefore errors) in ADV measurements and their dependence on the sampling rate, using measurements taken at four rates (10Hz, 25Hz, 50Hz and 100Hz). The upper limit of 100Hz was determined by the capabilities of the ADV at that time.

Noting three sources of noise (velocity shear, phase uncertainty and Doppler noise), McLelland and Nicholas found that errors due to phase uncertainty and Doppler noise increased with sampling rate, while the error due to velocity shear was independent of the sampling rate. The error due to phase uncertainty was determined to be approximately equal to that due to Doppler noise at all sampling rates, as shown in Figure 29. Importantly, their examination of the shear stress components, illustrated in Figure 30, showed that the relative error due to noise was always less than 1.1% (except for one spurious result taken at 25Hz). This matches the findings of Voulgaris and Trowbridge (1998). Nikora and Goring (1998) saw greater errors, though McLelland and Nicholas suggest that this is probably caused by flaws in the method used to estimate the Doppler noise.

McLelland & Nicolas also noted that increasing the sampling rate from 25Hz to 100Hz increased the root-mean-square value (RMS) of the velocity components by 10, 4 and 40% for u', v' and w' respectively, which they attributed to the detection of

higher frequency fluctuations (McLelland and Nicholas, 2000). This is consistent with the idea of the Nyquist frequency described in Section 4.2.2, and indicates that use of an ADV should allow good measurement of the turbulent flow across the majority of length scales.

Taking into account both these aspects of their findings, it may be seen that a trade-off exists between minimising errors and maximising resolution. However, while increasing with sampling rate, the errors remain small. Additionally, McLelland & Nicholas' work was based on unfiltered data and they note the work of Nikora and Goring (1998) in showing the success of filtering methods in removing high frequency noise. In their conclusions, McLelland & Nicolas assert the suitability of the ADV to detect high frequency velocity fluctuations at the highest sampling rate available to them, 100Hz.

By inspection of the equations of the SKM (see (41) and its associated defining equations), it may be seen that it is the orthogonal Reynolds stress components, whose measurement accuracy was noted by McLelland & Nicholas, which must be measured accurately in any investigation of the SKM. The findings of the aforementioned research support the use of the ADV as a tool for such research. However, Voulgaris and Trowbridge (1998) show that there are problems with using the ADV close to a boundary due to the size of the sampling volume. From their work, they suggest that accurate measurements of mean velocity are only possible at elevations of more than 7.6mm above the bed, while accurate measurements of Reynolds stress are only possible at elevations more than 20mm $(> 0.1h)$ above the bed. Below this depth Reynolds stress measurements were shown to underestimate the Reynolds stress, attributed to the inability of the ADV to detect eddies smaller

than 22mm (vertically) and 15mm (horizontally) (Voulgaris and Trowbridge, 1998). However, Voulgaris and Trowbridge compare their experimental data with a theoretical curve which predicts Reynolds stress monotonically decreasing with height above bed, whereas this region lies within the inner region of the boundary layer in which the Reynolds stress would be expected to decrease approximately linearly (see Section 3.5.1). Therefore, the former of these limiting positions should be taken into account when making the measurements for this research, while the latter is open to debate. As will be seen later (Section 8.4.6, for example), analyses based on the turbulent fluctuations measured for this thesis show consistency between points at $z = 10mm$ and those higher up the water column.

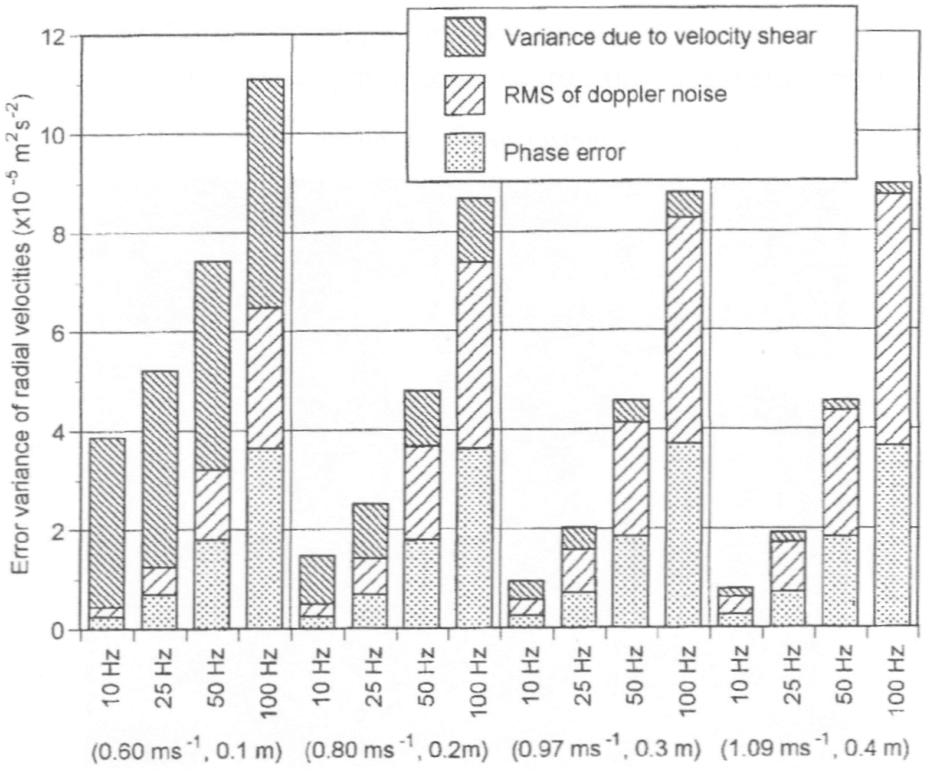

Figure 29: Breakdown of Noise Components Associated with Measurements at Four Different Flow Depths, Sampled at Four Different Frequencies. The Horizontal Axis Shows the Sampling Frequency of Each Measurement with the Instrument Height and Mean Downstream Flow Velocity for each Instrument Location in Parentheses (McLelland and Nicholas, 2000)

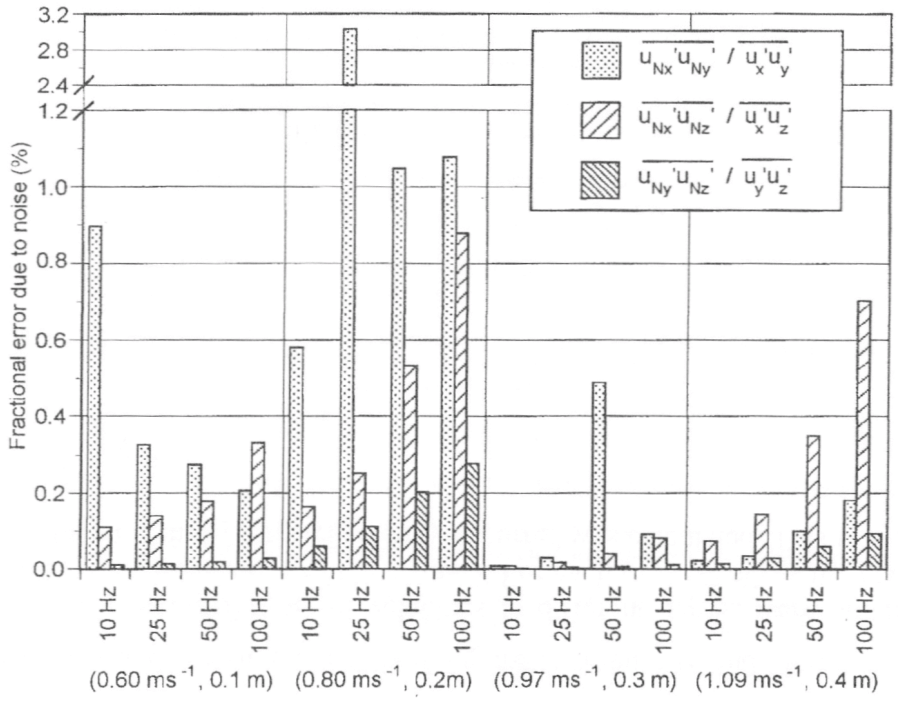

Figure 30: Fractional Error Associated with Each Component of the Reynolds Shear Stress. Horizontal Axis is the Same as in Figure 29 (McLelland and Nicholas, 2000)

4.2.5 Despiking

Doppler noise and aliasing (see Section 4.2.2) can lead to corrupted data in any set of turbulent flow velocity measurements (Cea et al., 2007). This corrupted data often appears in the form of spikes in the sample, as illustrated in Figure 31 below. Cea et al. found that spikes contribute significantly to turbulent kinetic energy in highly turbulent flows and so filtering is necessary.

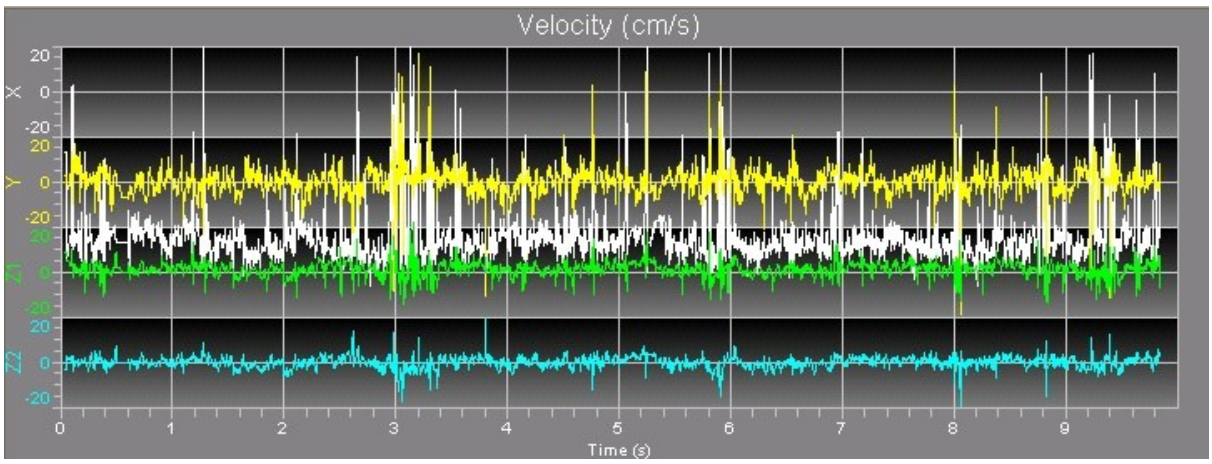

Figure 31: A Corrupted (Spiked) ADV Sample

Despiking is the process of removing and replacing the corrupted data, and is necessary to allow analysis of the turbulent flow characteristics. The intention is not to reconstruct the signal that would have been received in the absence of errors – this is not possible as it would require knowledge of the real measurements at the corrupted points – but to obtain a sample which is statistically equivalent in terms of the turbulent flow characteristics (Cea et al., 2007). There are two parts in the despiking process. Firstly, the corrupt data is identified and removed, and then the removed data is replaced using some kind of estimation process based on the "good" data surrounding the removed point. The majority of despiking methods are iterative, with spikes being removed and replaced and then another cycle of removal and

replacement occurring until no spikes are detected. This is necessary as these methods rely on the mean and variance of the sample to determine spikes (Cea et al., 2007) and these change as spikes are removed. There are several options available for both of these sub-processes:

4.2.5.1 *Removal*

The problem of spike removal lies in determining which of the data points are, in fact, spikes. This is a non-trivial problem, and a number of different filters have been suggested. Goring and Nikora (2002) despiked two ADV samples (one "clean" set with few spikes and one "contaminated" set with many spikes) using five different filtering methods:

- RC Filters Method - taken from electrical engineering in which similar problems occur. This involves a comparison of "rough" and "smooth" signals generated from the sample using digital filtering.

- Tukey 53H Method – a different approach following the same principles as the RC Filters Method.

- Acceleration Threshold Method – for each data point, the absolute deviation from the mean velocity and the acceleration based on the previous data point are calculated. Any point for which the deviation is greater than a defined factor of the standard deviation and the acceleration is greater than a defined factor of g, the acceleration due to gravity, is considered a spike. The factors are user-specified, a weakness of the method.

- Wavelet Thresholding Method – the signal is transformed to wavelet space in a transformation analogous to the Fourier transform. The wavelet coefficients are set to zero if they exceed a threshold level, and the inverse wavelet transform is used to create the despiked signal

- Phase-Space Thresholding Method (PST) – a method introduced by Goring and Nikora (2002). Data points are plotted on a phase-space plot of the velocity and its derivatives. An ellipsoid (whose size, position and orientation are defined by the method) is positioned in phase-space, with any points outside the ellipsoid being rejected. Goring and Nikora specify a polynomial replacement method (see Section 4.2.5.2 below).

For the “clean” sample, all methods except for the RC Filters Method were found to be satisfactory and give similar results. For the “contaminated” sample, the phase-space methods was considered to be preferable due to its performance in removing spikes and its objectivity due to its non-reliance on user-specified factors. See (Goring and Nikora, 2002) for more details.

A new filtering method, the Velocity Correlation Filter, was suggested and compared to the Phase-Space Thresholding Method in a similar study by Cea, Puertas & Pena (2007). This is similar to the Phase-Space Method but plots the three velocity components against each other. In this way the three velocity components are treated together – all other filtering methods treat the three directions separately. No data is replaced during the filtering, and mean flow statistics are calculated before any replacement is done – unlike most of the other methods, it is not iterative. Cea et

al. considered this non-iterative approach to be likely to give better results with highly turbulent flows.

Another new filter, the modified Phase-Space Thresholding (mPST) method has been proposed by Parsheh et al (2010). This filter pre-processes the velocity measurements, defining points within $\pm C_1\theta$ (where C_1 is a user-defined constant and θ is the absolute mean deviation) of the mean as being valid (and so unchangeable by the PST process), while values more than $\pm C_2\theta\sqrt{\ln(N)}$ (where C_2 is a user-defined constant and N is the number of measurements) from the mean are defined as spikes and hence invalid. When combined with a suitable method for replacing spike values with estimated values (see 4.2.5.2 below), this method has been shown to give better results when applied to an artificially contaminated signal (Parsheh et al., 2010). In particular, Parsheh et al found their mPST method to be advantageous when investigating the power spectra of a turbulent flow.

4.2.5.2 *Replacement*

Various methods of replacing the removed data have been suggested. These include extrapolation from a number of preceding points, replacement with the overall mean value, interpolation between the ends of the spike, polynomial interpolation and a smoothed estimate (Goring and Nikora, 2002). Goring and Nikora recommend the use of a cubic polynomial best-fit to the first 12 good data points on each side of the spike. However, Cea et al. (2007) recommend linear interpolation between the values surrounding the spike, due to the weak correlation between consecutive velocity measurements in highly turbulent flow.

In their paper describing their mPST method, Parsheh et al. show that the use of the last good value (LGV) to replace a removed spike can lead to an improved result. They noted the tendency of the unmodified PST method to incorrectly identify good data close to removed spikes as spikes, something not seen using their mPST with LGV replacement (Parsheh et al., 2010). However, it should be noted that Parsheh et al use linear interpolation as their replacement method for the unmodified PST, not the cubic polynomial suggested by Goring and Nikora.

As mentioned previously, Cea et al. also advocate the use of a non-iterative removal-replacement process. However, they were unable to find evidence to rate one filter over the others (Cea et al., 2007). While some differences were seen in the results when different filters were used, Cea et al. attributed much of these differences to the different replacement methods used.

4.2.5.3 *Choice of Filter and Replacement Method of the Research Herein*

The filter and replacement method chosen was the original Phase-Space Thresholding method with their recommended 12-point cubic polynomial replacement method. The reason for this was initially simply chronological – this method was the first of which the author was aware, and was thus applied to the experimental data. Subsequent application of the alternative methods was (as found by Cea et al.) inconclusive and so this method was retained. In the figures accompanying the following text the following abbreviations are used:

- PST – the original Phase-Space Thresholding filtering method
- VC – the Velocity Correlation filtering method
- mPST – the modified PST filtering method

- 12pt cubic – the 12 point cubic polynomial replacement method
- LGV – the Last Good Value replacement method
- LI – the Linear Interpolation replacement method

Comparison of mean velocities (Figure 32) shows negligible difference between the methods. The Reynolds stress components do show significant differences, but these are inconsistent over the combination of filtering and replacement methods (Figure 33 and Figure 34). The magnitude percentage difference for the τ_V^R is less than 5% except for one instance each of the PST-LGV and mPST-LGV cases, and between these the sign is different and so is inconclusive. The previous studies mentioned above seem to favour different replacement strategies. Parsheh et al. also claim improvements in the power spectral density distribution when mPST-LGV is used, but there is no clear difference between PST-12pt cubic and their method when applied to the experimental data (Figure 35). From the above it is difficult to recommend one method over another; conversely there is no strong argument not to continue with the PST-12pt cubic method.

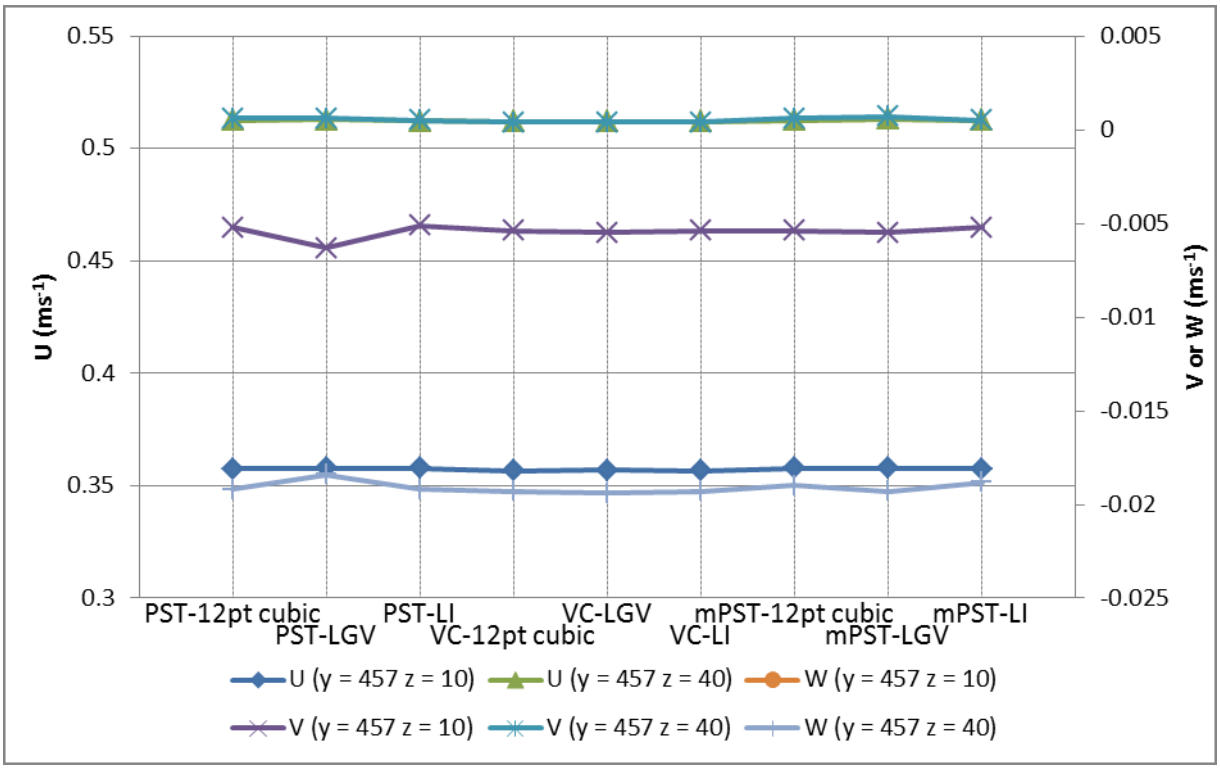

Figure 32: Variation of the Mean Velocity Components with Filtering Method and Replacement Method

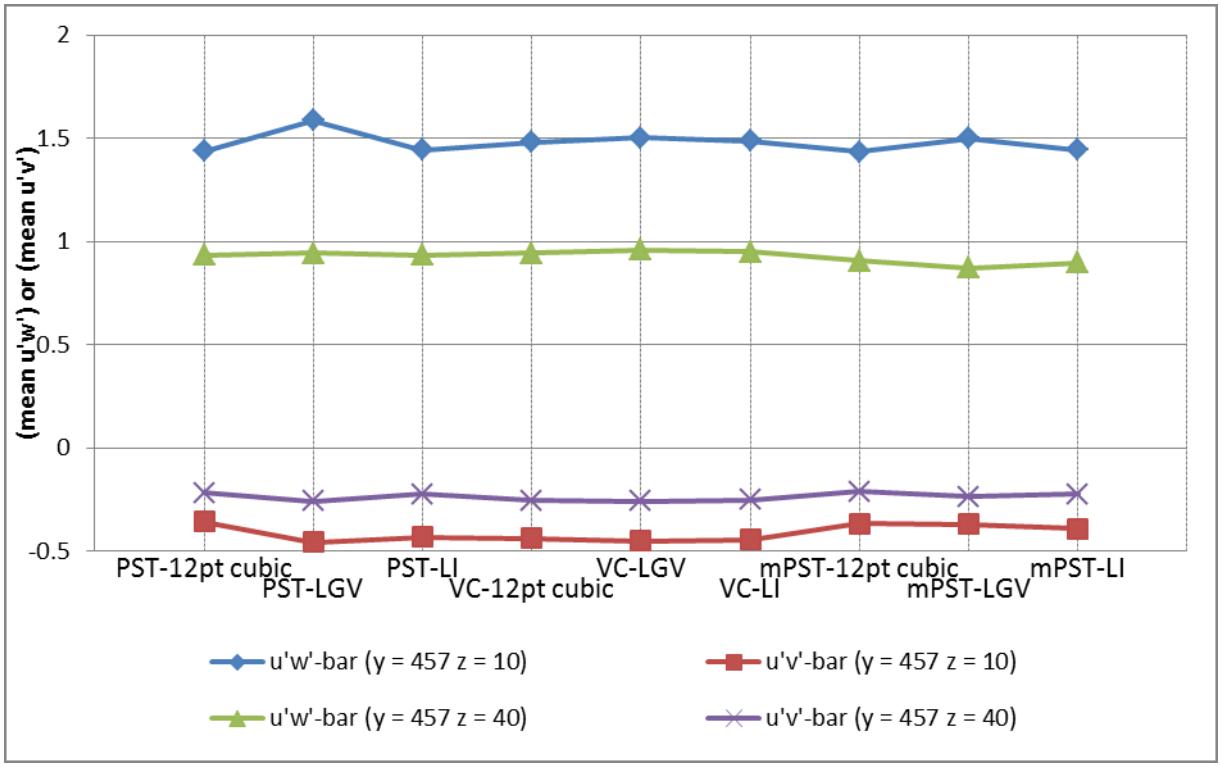

Figure 33: Variation of the Reynolds Stress Components with Filtering Method and Replacement Method

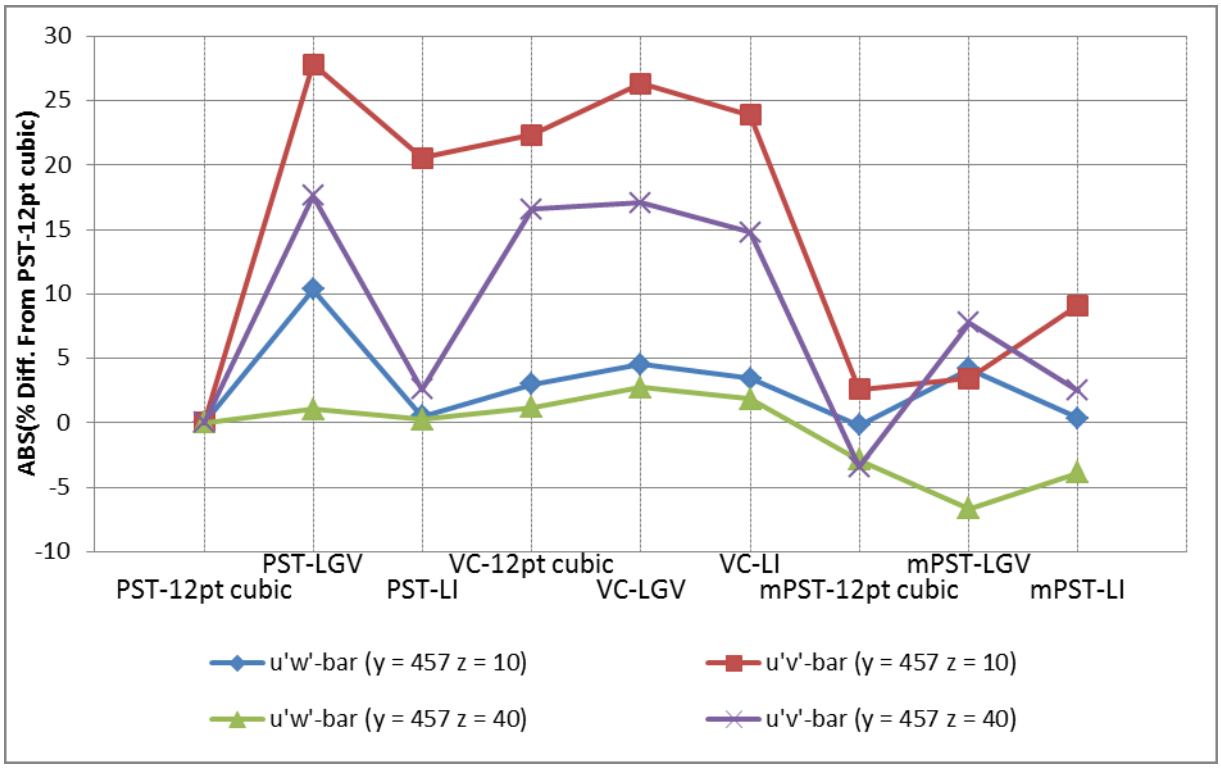

Figure 34: Variation of the Reynolds Stress Components with Filtering Method and Replacement Method as a Percentage of the "PST-12pt cubic" Value

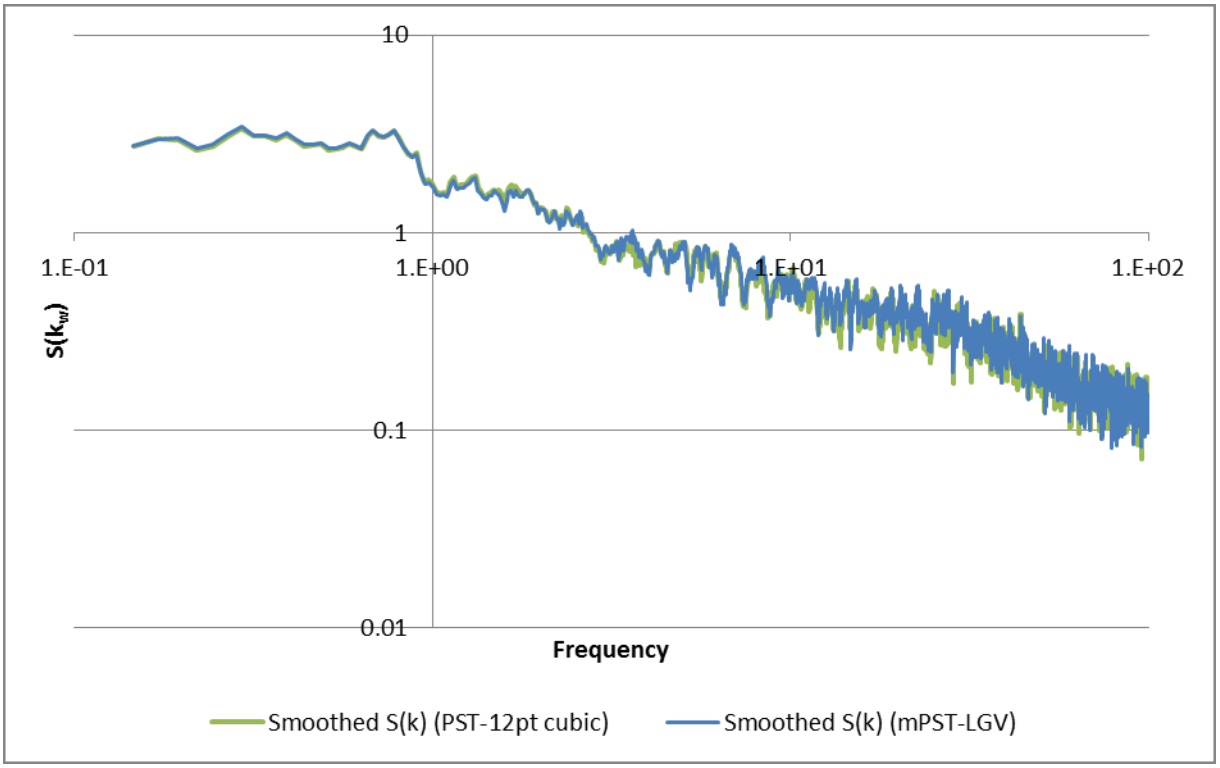

Figure 35: Spectral Function, $S(k_w)$for Data Point $y = 457mm$, $z = 10mm$ using Two Filtering and Replacement Methods

4.3 Preston Tubes, Pitot-Static Tubes and Boundary Shear Stress Measurements

The use of Pitot-static tubes to measure velocity from the difference in the stagnation head $\left(\frac{p}{\rho g}+\frac{u^2}{2g}\right)$ and pressure head $\left(\frac{p}{\rho g}\right)$ is well documented (for example, (Chadwick et al., 2004)). The Pitot-static tube measures both the stagnation head and pressure head, and shows the difference, h, allowing the velocity to be calculated from:

$$u=\sqrt{2gh} \tag{56}$$

It should be noted that the use of this equation is subject to some conditions, as specified in (British Standards Institute, 1983), which are met by the experimental work described herein.

Patel (1965) developed a method of calculating the boundary shear stress, τ_b, on a smooth boundary using a Preston tube and static pressure tube. The Preston tube is situated against the channel boundary, with the static pressure tube located in the free stream (distant from the bed to avoid interference from bed effects), and Patel proposed a relationship between the pressure difference, Δp, measured between the tubes and τ_b:

$$x^* = log\left(\frac{\Delta p d^2}{4\rho v^2}\right) \tag{57}$$

$$y^* = log\left(\frac{\tau_w d^2}{4\rho v^2}\right)$$

$$y^* = \frac{x^*}{2} + 0.037 \ (y^* < 1.5)$$

$$y^* = 0.8287 - 0.1381x^* + 0.1437(x^*)^2 - 0.0060(x^*)^3 \ (1.5 < y^* < 3.5)$$

$$x^* = y^* + 2log(1.95y^* + 4.10) \ (3.5 < y^* < 5.3)$$

where d is the Preston tube inner diameter and υ is the kinematic viscosity of the fluid.

Wu & Rajaratnam (2000) developed an analogous method for calculating τ_b on a rough boundary, though this is reliant on being able to position the Preston tube on the "surface" of the roughness. This positioning becomes difficult when roughness elements are large in relation to the tube diameter and short in relation to the tube length such as the gravel bed used in the experimental work presented in this thesis.

4.4 Quadrant-Hole Analysis

One of the first applications of Quadrant-Hole (Q-H) analysis was that of Lu and Willmarth (1973), who applied it to 2-D (streamwise and vertical) velocity measurements made in a boundary layer over a horizontal plate in a wind tunnel. Its aim is to categorise the velocity measurements into different types of "event", allowing the contribution to Reynolds stress of each event type to be determined. These events correspond to the ejections and sweeps described in Section 3.5.2. Further, the concept of a "hole", described more fully in Section 4.4.2, allows the contribution of events with a magnitude above a boundary value to be seen. The

output of the analysis is a set of normalised shear stress sums, each representing the contribution to shear stress of events of a particular type which exceed the minimum shear stress limit. The summing process is described in Section 4.4.3.

Lu and Willmarth describe the analysis in terms of a continuous time-series of measurements. In the experimental work for the research described in this thesis, velocity measurements were taken at a rate of 200Hz, giving a discrete time-series with a uniform interval ($\Delta t = 1/200\, secs$) between measurements. For this reason, the analysis is described here in terms of such a discrete measurement set. Although described in terms of u and w, the analysis is equally applicable to lateral shear stress through u and v.

Other detection methods, such as VITA (variable-interval time-averaging) have also been suggested. VITA and Q-H analysis have been shown to be mutually consistent (Alfredsson and Johnasson, 1984), while Nezu and Nakagawa (1993) determined that Q-H analysis is a suitable method for such a detection analysis.

4.4.1 Quadrants

To categorise the time-series of velocity measurements, the velocity fluctuations are used as the co-ordinates, $(u'(t), w'(t))$, in the u'-w' plane as shown in Figure 36:

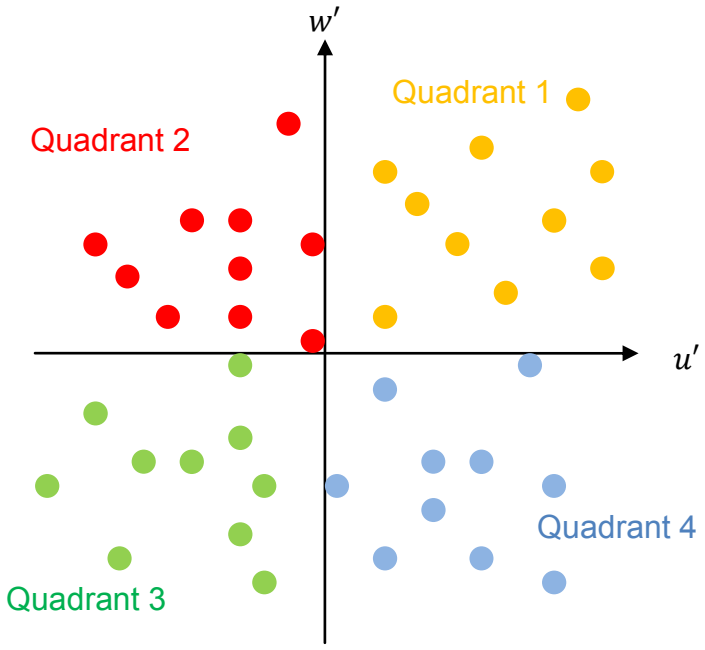

Figure 36: Schematic of Quadrant-Hole Analysis Categorisation

The measurements are thus split into four event types, each corresponding to a quadrant of the u'-w' plane. Events in quadrant i are termed quadrant i events.

4.4.2 Holes

To allow the contribution of different magnitude events to be analysed, a "hole" is used to determine whether or not to include an event in the shear stress sum. The hole size, J, is an integer value used to scale the product of the standard deviations of u and w. Only events for which the absolute product of u' and w' exceeds this limit (meeting the criterion in (58)) are included in the shear stress sum.

$$|u'w'| > J\sigma_u\sigma_w \tag{58}$$

4.4.3 Normalised Shear Stress Sum and Presentation of Results

For quadrant i and hole size J, the shear stress sum for a discrete time series of N samples is (after (Nezu, 2005); however, note that they used the factor $1/\sigma_u\sigma_w$ to make $S_{i,J}$ dimensionless):

$$S_{i,J} = \frac{1}{N}\sum_{n=0}^{N} u'_n w'_n I_{i,J} \tag{59}$$

where $i = 1, 2, 3, 4$, $J \in \mathbb{Z}^+$ and

$$I_{i,J} = \begin{cases} 1 & if\ the\ event\ is\ in\ the\ i^{th}\ quadrant\ and\ (58)\ is\ satisfied \\ 0 & otherwise \end{cases}.$$

As the hole size is increased more events are excluded and $S_{i,J}$ tends to zero by definition. In practice $S_{i,J}$ decreases rapidly, as is shown in Figure 37, and $J = 0, 1, \ldots, 10$ may be a sufficient range, although this will depend on the data being analysed. Following Sterling et al. (2003), the shear stress sums are normalised by S_{max}, their maximum, and the sums for quadrants 2 and 3 are multiplied by -1 and plotted against $-J$ so that the results appear in their respective quadrants when plotted as in Figure 37.

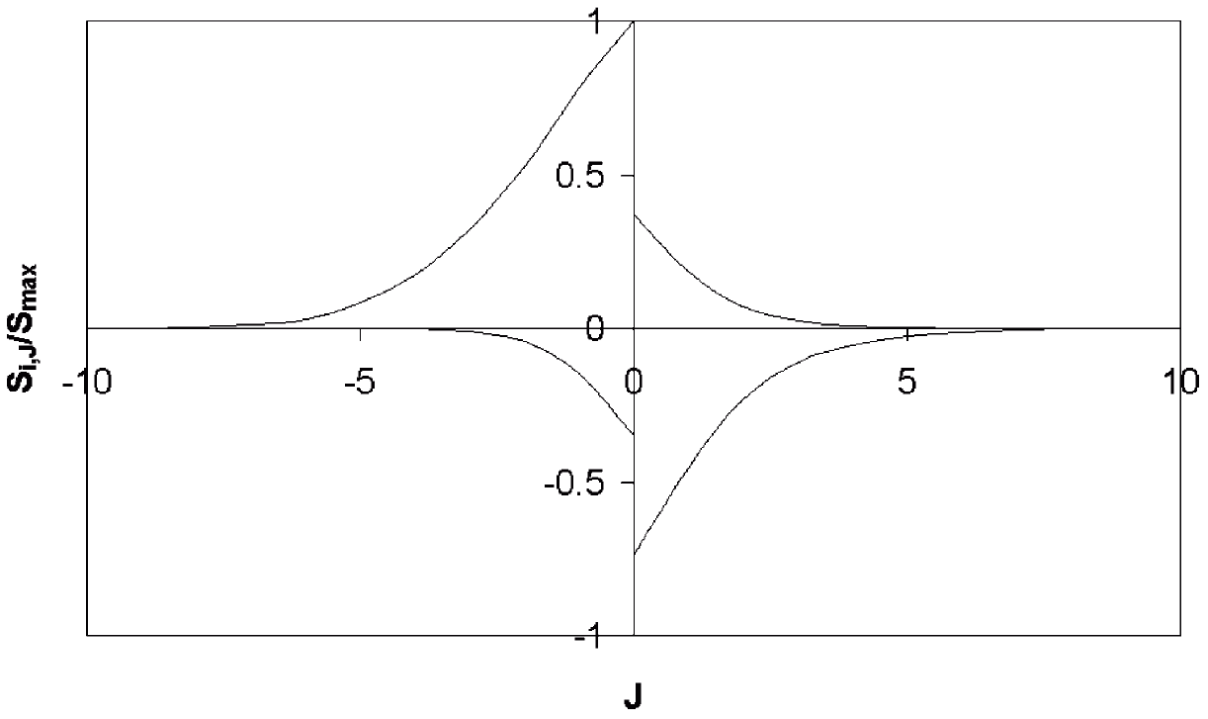

Figure 37: Quadrant-Hole Analysis Results Graph (Nezu, 2005)

4.4.4 Ejections and Sweeps

Quadrant 2 events are termed ejections (or bursts) and quadrant 4 events are termed sweeps. Ejections, with $u' < 0$ and $w' > 0$, are upward movements of slower water which, assuming a monotonically increasing vertical velocity profile, leads to a "negative" momentum transfer into the faster moving flow above. Conversely, sweeps (with $u' > 0$ and $w' < 0$) are downward movements of faster water, leading to a "positive" momentum transfer into the slower moving flow below. As may be seen from Figure 37, these ejections and sweeps contribute disproportionately to the total shear stress. Lu and Willmarth (1973) found that ejections contributed 77% of the mean shear stress, with sweeps contributing 55%, with -32% of the (vector) shear stress coming from quadrant 1 and 3 events. The imbalance between the momentum transfer due to ejections and sweeps is thought to be a characteristic of the

turbulence structure of the flow (Nezu, 2005) and evidence for the existence of a turbulence propagation mechanism such as hairpin vortices (Lu and Willmarth, 1973).

4.5 Conditional Time-Series

From the segregated Q-H events, conditional time-series data may be obtained in order to investigate coherence of the velocity components. In the context of this research, in which a single probe was used both as the detection and sampling probe, the conditional time-series were constructed using the ensemble mean defined in (60) (see (Nezu and Nakagawa, 1993) for a more general, two-probe form).

$$\langle q(\mathfrak{I})\rangle = \frac{\int_0^T q(t+\mathfrak{I})I(t)dt}{\int_0^T I(t)dt} \tag{60}$$

where $\mathfrak{I}$ is the time offset from the measurement used for the detection function, $I(t)$, $q(t)$ is the series of velocity measurements (taken over a time period T). In its simplest form $I(t)$ is as in (59), with J set to a selected hole size ("threshold"); this form is based on the assumption that only events over a certain magnitude are genuine ejections and sweeps, although the value of J is an arbitrary limit (Nezu and Nakagawa, 1993).

The resulting $\langle q(\mathfrak{I})\rangle$ (where $-\mathfrak{I}_{max} < \mathfrak{I} < \mathfrak{I}_{max}$; $2\tau_{max}$ is the (arbitrary) length of the ensemble-mean series), is the mean of all sub-series of $q(t)$, q_n, which span an interval $\mathfrak{I}_{max}$ either side of an event for which $I(t) = 1$:

$$q_n(\mathfrak{I}) = q(t_n^0 + \mathfrak{I}) \tag{61}$$

where t_n^0 is the n^{th} time at which condition (58) is met for the specified hole size, J, and the shear stress falls within the quadrant under examination. Applying this analysis to all three velocity components, $u(t)$, $v(t)$ and $w(t)$, using the same criteria for each (i.e., taking simultaneous sub-series), allows a comparison of the three components and time-correlations between them.

Nezu & Nakagawa propose a modification aimed at removing the arbitrary nature of selecting J. They suggest scaling $I(t)$ by the shear stress $u(t)v(t)$ (or $u(t)w(t)$) (Nezu and Nakagawa, 1993), exaggerating the velocity time-series during high-magnitude events and damping it elsewhere. This removes the need for the arbitrary choice of J but does not detect individual ejections and sweeps, relying instead on the averaging of a large number of measurements. Their results suggest that both the threshold detection function and this "weighted" function give consistent results, with the resulting data being smoothed in the weighted case due to the removal of fine turbulence. Examples of their results are shown in Figure 38:

While the results of these methods appear satisfactory in showing qualitatively the correlation between velocity components around ejections and sweeps, one possible issue with these methods is that there is no distinction between contiguous and non-contiguous high shear-stress events. If (taking the threshold method as an example for simplicity) $I(t) = 1$ for two or more consecutive events then the sub-series will overlap, resulting in a distortion of $\langle q(t) \rangle$ when compared to $q(t)$. This is illustrated in Figure 39 for a very simple detection function and time-series. Whether this occurs

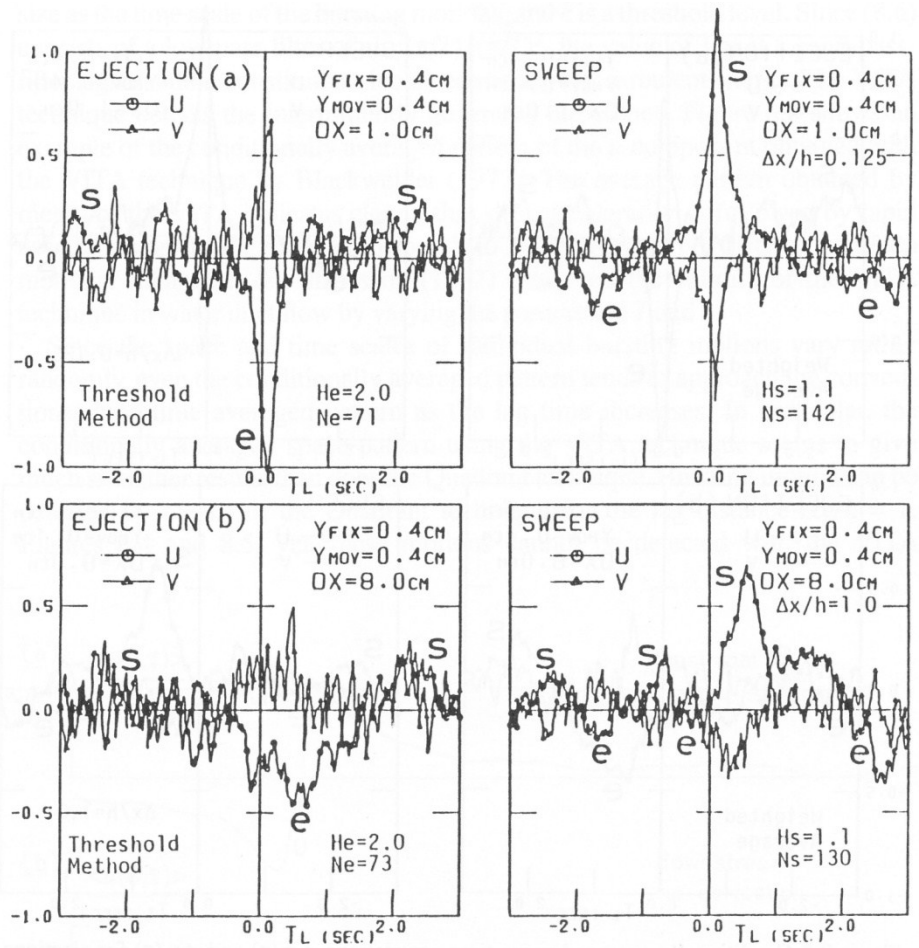

Figure 38: Conditionally-Averaged Time-Series (from (Nezu and Nakagawa, 1993))

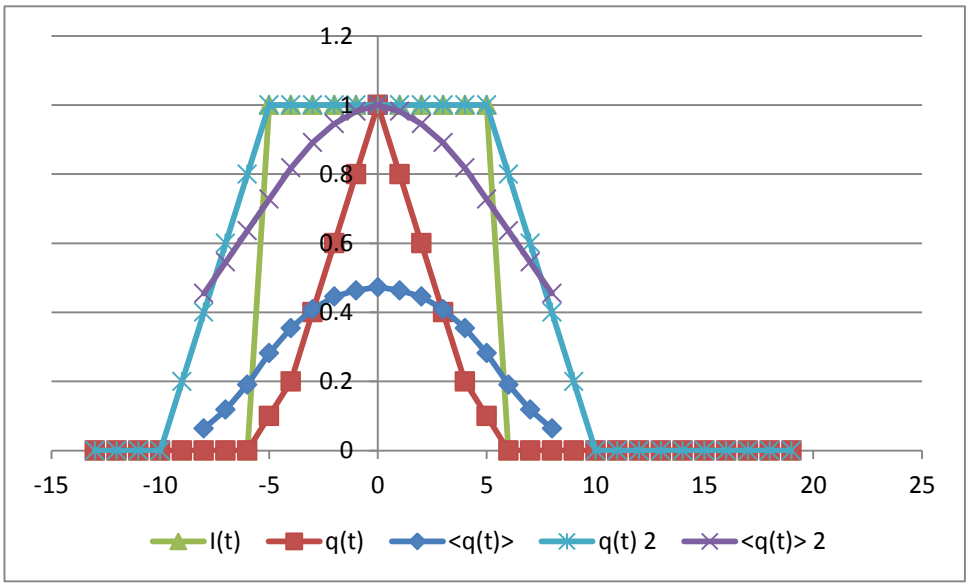

Figure 39: Distortion of $\langle q(t) \rangle$ Due to Sub-Series Overlap

sufficiently frequently in real turbulence measurements, and whether it has a significant effect on any conclusions which may be drawn from such an analysis, may be a subject worthy of investigation.

The threshold method may be modified from an integral method to a discrete method by the picking out of sub-series of length ΔT (where $\Delta T \ll T$) centred on measurements where $I(t) = 1$ (the weighted method is not suitable for this as it relies on integration over the whole series). This may be of computational benefit when dealing with large data sets, however it is reliant on correct choice of J. This assumes that J is set sufficiently high that only a small number of measurements pass the detection criteria. Alternatively, a statistical approach may be used, with events in the top percentile used. The ensemble-mean sub-series is calculated using:

$$\langle q(\mathfrak{I}) \rangle = \frac{1}{N} \sum_{i=0}^{N} q_i(\mathfrak{I}) \tag{62}$$

where N is the number of sub-series and $q_i(\mathfrak{I})$ is the value of u at time $\mathfrak{I}$ from the beginning of the i^{th} sub-series. This discrete method also has the advantage that sub-series could be selected to be non-overlapping, with the t_n^0 values being in the centre of any intervals of contiguous $I(t) = 1$, thus preventing the distortion due to overlapping discussed above.

5 THE EXPERIMENTAL METHOD

5.1 Measured Data

Before describing the experimental setup and method used to collect the experimental data it is useful to outline the data which was measured for this research. This may be broken into two subsets, the channel conveyance data and the detailed cross-sectional data. The former describe the overall channel characteristics and are either discharge-independent or made up of measurements taken at a number of different discharges, and are:

- Bed slope
- Stage-Discharge (Normal depth vs Discharge)

The latter are discharge-dependent. Data was collected at two discharges in order to examine the depth-dependency of:

- Point velocities
- Boundary shear stress

5.2 Experimental Setup

The experimental work for this research was performed using a $22\mathrm{m}$ long rectangular channel of width $B = 614\mathrm{mm}$ at the University of Birmingham Civil Engineering Laboratories. The channel is fed from a constant head tank in the laboratory roof, with flow into a stilling tank controlled by valves and measured by an electronic gauge. Outflow is controlled via a tailgate, which may be raised or lowered to obtain normal depth flow.

Vernier gauges were situated at approximately $1\mathrm{m}$ intervals along the channel length, allowing the water depth to be measured at these points. Point velocity measurements were made using ADVs – details of ADV use and the measurements made are in the following sections.

The ADV requires impurities in the water to scatter the sound waves it emits, reflecting them back to the receivers. Due to the clarity of the water used in the laboratory channel the ADV was unable to function correctly without the addition of extra impurities. A number of methods were attempted to achieve this, and finally a bubble generator was constructed to create microscopic bubbles in the flow. This method was considered more reliable and reproducible than the alternatives, which involved the addition of seeding particles to the water. This bubble generator was based on that used by Blankaert & Lemmin (2006) and consisted of two grids of fine wire spanning the channel approximately 1m upstream of the ADV probes, and connected to a power supply to act as an anode and cathode for the creation of hydrogen bubbles through hydrolysis.

In order to create a heterogeneous channel bed, the channel was divided along the centreline. Two bed configurations were used for the experiments. For bed configuration 1 (henceforth referred to as “BC1”), one half was covered with two layers of 10mm thick plastic sheeting, giving a total thickness of 20mm. The other half was covered with a single layer of identical sheeting onto which gravel had been glued to create a rough bed, as illustrated in Figure 40.

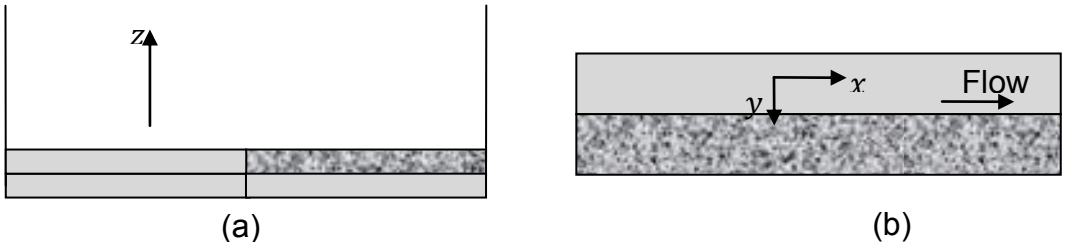

Figure 40: Cross-sectional (a) and Plan (b) Schematics of the Experimental Channel

For bed configuration 2 ("BC2") the same basic construction method was used, but rough and smooth sections were alternated to form a "checkerboard" pattern designed to match the rate of biotope change discussed in Section 3.8, with a roughness switch every 1825mm (≈*3B*). This configuration is illustrated in Figure 41.

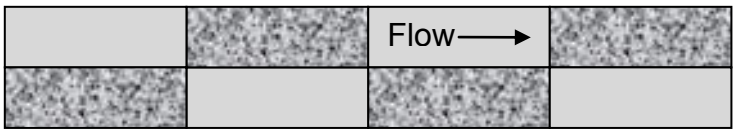

Figure 41: BC2

A sample of the gravel was characterised by sieve analysis. Sieve analysis involves passing the sample through a progressively smaller set of filters and measuring the percentage (by mass) of material which passes through each size of filter. The gravel used to create the rough bed was shown to have $D_{72} = 10mm$ and $D_4 = 5mm$, where the subscript gives the percentage of the sample which passed through that sized grid.

The gravel was attached to the plastic sheeting by covering the sheeting with a thin layer of waterproof adhesive and then covering this with a layer of gravel. The gravel

was pressed into place to ensure a good bond and excess gravel simply tipped off once the adhesive had set. The process is illustrated in Figure 42.

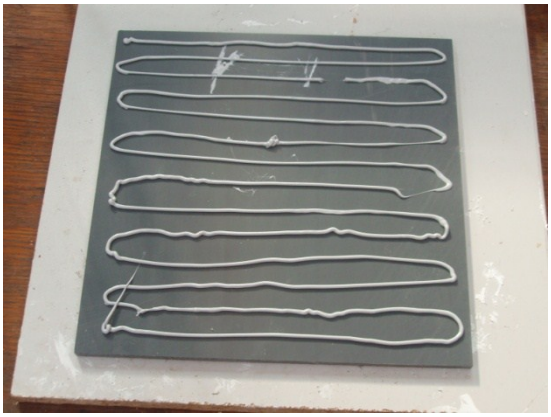

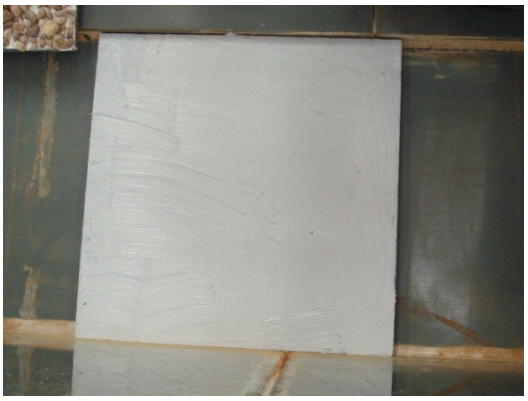

Figure 42: Preparation of the Rough Bed

5.3 Measuring Methods

5.3.1 Channel Discharge

The channel discharge was measured using an electronic gauge fitted to the pipe connecting the header tank and stilling tank. The outflow from the flume could also be directed into measuring tanks and the discharge calculated from these using Equation (63), in which Δd is the change in water depth in the tank, $m(= 1.5\mathrm{m})$ the tank width, $b(= 1.5\mathrm{m})$ the tank length and Δt the time interval over which the depth change takes place. The accuracy of this gauge was verified by comparison with that calculated by use of these tanks, Q_{tank}.

$$Q_{tank} = \frac{\Delta d \times m \times l}{\Delta t} \tag{63}$$

The results of this comparison are shown in Table 2. The second column shows the error in the measuring tank calculation, calculated using the standard experimental error formulae and the estimated errors shown in Table 3.

Q_{tank} (ls^{-1})	Error in Q_{tank} (l/s)	Q_{gauge} (ls^{-1})
4.5	±0.1	4.4
19.2	±0.2	19.2
40.0	±0.8	40.3
61.1	±1.7	61.7

Table 2: Comparison of Discharges Calculated from the Measuring Tank and Read from the Electronic Gauge

Error Term	Absolute Value
Δd	0.005
w	0.005
l	0.005
$m \times l$	0.011
Δt	1.0

Table 3: Experimental Error Estimations for the Parameters of Equation (63)

From these measurements the electronic gauge may be seen to give an accurate discharge measurement. However, it should be noted that the flow shown by this gauge is not constant but fluctuates slightly. Without additional logging of the instantaneous flow measurements from the gauge it is not possible to make a formal analysis of these variations, but visual inspection of the readout over a period of approximately 30 seconds shows a variation over a range of approximately $\pm 0.5 ls^{-1}$ about the mean value. It is therefore estimated that a discharge may be obtained from this gauge to an accuracy of about $\pm 0.25 ls^{-1}$.

5.3.2 Bed Slope

The bed slope was measured using a horizontal water surface as the datum. The tailgate was raised and sealed to prevent water leaving the channel, and the inlet valve opened to partially fill the channel. With the valve closed, the water was allowed to settle to give the required datum.

The water depth was measured using the Vernier gauges stationed along the channel and the bed slope calculated from these measured depths. The error in the depth measurements is estimated as $\pm 0.5mm$, while the error in measuring the

separation of the Vernier gauges is estimated as $\pm 1.0mm$. This method was repeated with a second quantity of water in the channel to provide verification of the measurements. The bed profile measured for Bed Slope 1 is shown in Figure 43.

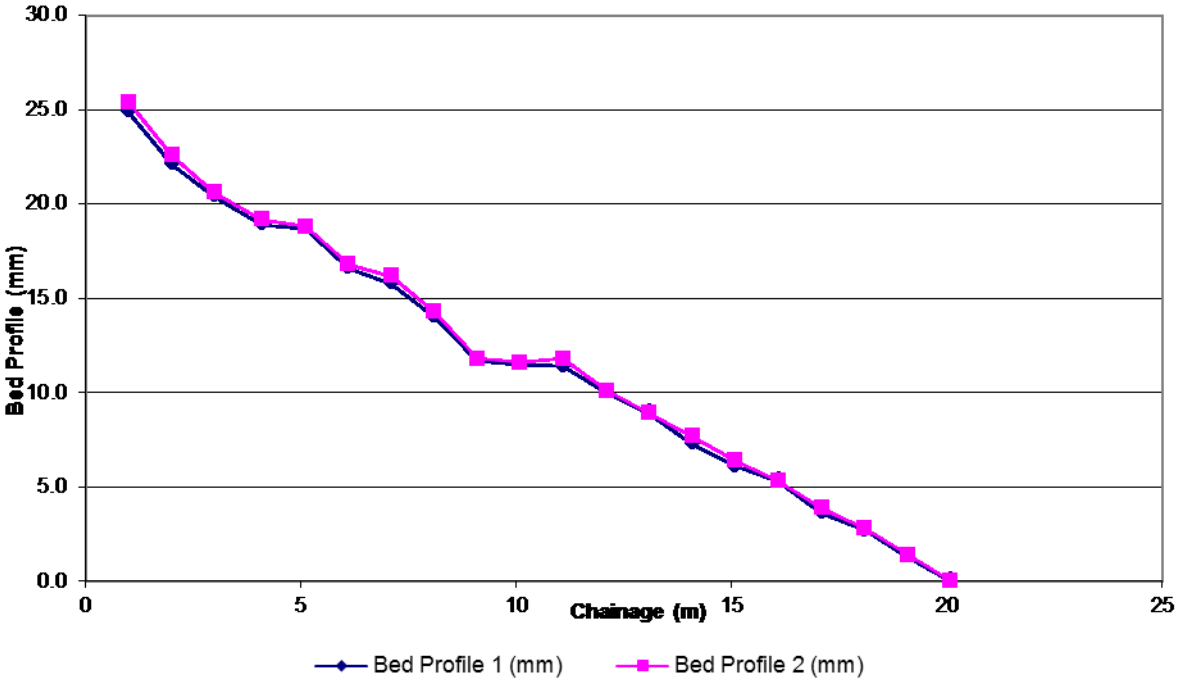

Figure 43: Streamwise Bed Profile

From Figure 43 it may be seen that the channel bed is uneven at the start of the channel. Due to the distance of the measured cross-section from these points, the effect of this distortion was considered negligible. Within the practical constraints of constructing such a channel the bed slope is constant. With the measured cross-section being $\sim 18m$ from the inlet, the bed is of particularly good quality in the $7m$ leading up to the cross-section.

Two methods were used to calculate the bed slope, S_0. Defining H_i and Δx_i as the depth at the i^{th} gauge and the distance of the i^{th} gauge from the $(i-1)^{th}$ gauge respectively, with N gauges, a "First-to-Last" mean was calculated:

$$S_0 = \frac{H_N - H_1}{\sum \Delta x_i} \tag{64}$$

along with a sectional mean:

$$S_0 = \frac{1}{N} \sum \frac{H_i - H_{i-1}}{\Delta x_i} \tag{65}$$

The calculated bed slopes are given along with the channel conveyance results in Section 7.

5.3.3 Stage-Discharge Curves

In order to construct a stage-discharge curve for the channel it was necessary to find the normal depth at a number of different discharges. For each discharge the tailgate was set and the water depth measured using the Vernier gauges sited along the channel. From these measurements the relative water surface slope (relative to the channel bed) was calculated. This process was repeated five times, with the tailgate adjustment aimed at giving two positive water surface slopes (M1 profiles), two negative (M2 profiles) and a final, near zero (normal depth flow) relative water slope. Plotting relative water surface slope and depth (measured at the Vernier gauge closest to the cross-section to be used for the detailed measurements), as in Figure 44, allowed normal depth to be evaluated graphically. From this figure, relative water surface slope is zero for a tailgate height of 49mm, corresponding to a depth of 47mm, the normal depth for this flow.

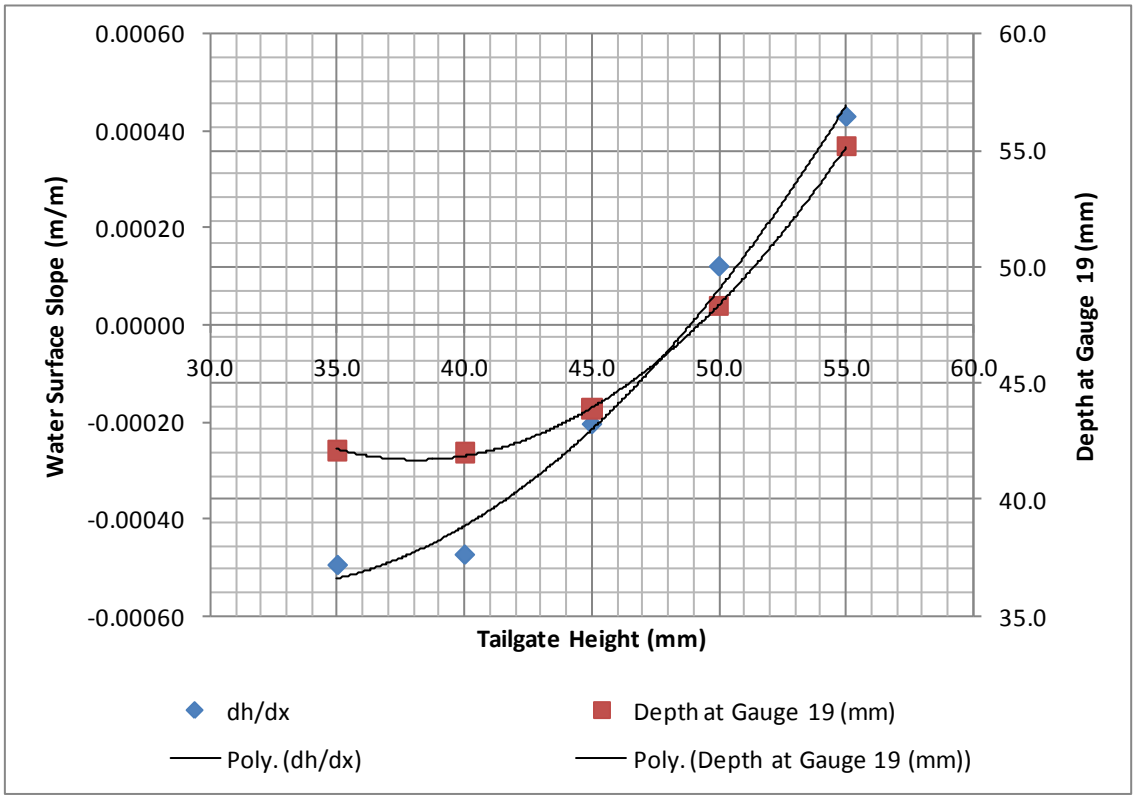

Figure 44: Example Relative Water Surface Slope (Zero when $S_f = S_0$) and Depth versus Tailgate Height Graph

This was repeated for a total of eleven discharges. Initial discharges were selected to cover a wide range of flow rates, with subsequent discharges chosen based on the standard stage-discharge curve in an effort to map the regions of interest.

5.3.4 Point Velocity Measurements

ADV measurements were made at points spanning a virtual grid located perpendicular to the main flow direction, and thus spanning a cross-section of the channel. The measured points were at 10mm horizontal separation over a grid centred on the RSB, except for close to the channel walls where a final spacing of 7mm was used to allow the points closest to the wall to be 10mm from the wall, the closest permitted by the ADV (see Section 4.2). This grid is illustrated in Figure 45. Vertical separation was 10mm, starting at 10mm above the channel bed.

The grid spacing balances resolution with the practicality of making the measurements in a reasonable timeframe, and is similar to that used successfully in previous research at the University of Birmingham (for example, (Alhamid, 1991)). 3-D velocity measurements were made at each point a rate of 200Hz for a period of 60 seconds using a Nortek Vectrino Acoustic Doppler Velocimeter (ADV). The choice of sampling rate and period are explained in Section 5.5.1 – the mean and standard deviations are shown to converge over this period, and (noting the high sampling rate) it matches the findings of Buffin-Belanger and Roy (2005) (see Section 4.2.4). In this way, 12000 individual, instantaneous velocity measurements were obtained at each data point. Velocities were measured against a co-ordinate system as shown in Figure 1.

For BC1 (with full-length strip roughness) this cross-section was located approximately 17.75m from the stilling tank, ensuring that the flow at the measured section was fully developed. For BC2 (with "checkerboard" roughness), a roughness switch occurred at approximately at this location. Two full cross-sections were measured, located 365mm upstream and downstream of the roughness switch, with partial cross-sections measured at x_{switch} = 0mm, x_{switch} = 912mm and x_{switch} = 1460mm, where x_{switch} is the x-position relative to the roughness switch. These cross-sections are referenced as in Figure 46. As the flow would be fully developed (in terms of distance from the channel inlet), it was assumed that CS4, when mirrored about the channel centreline (y/B = 0.5) would be equivalent to CS5; the partial cross-section at CS5 was used to validate this assumption (see Section 8.4). CS4 was preferred to CS5 for the full cross-section measurements to be consistent with

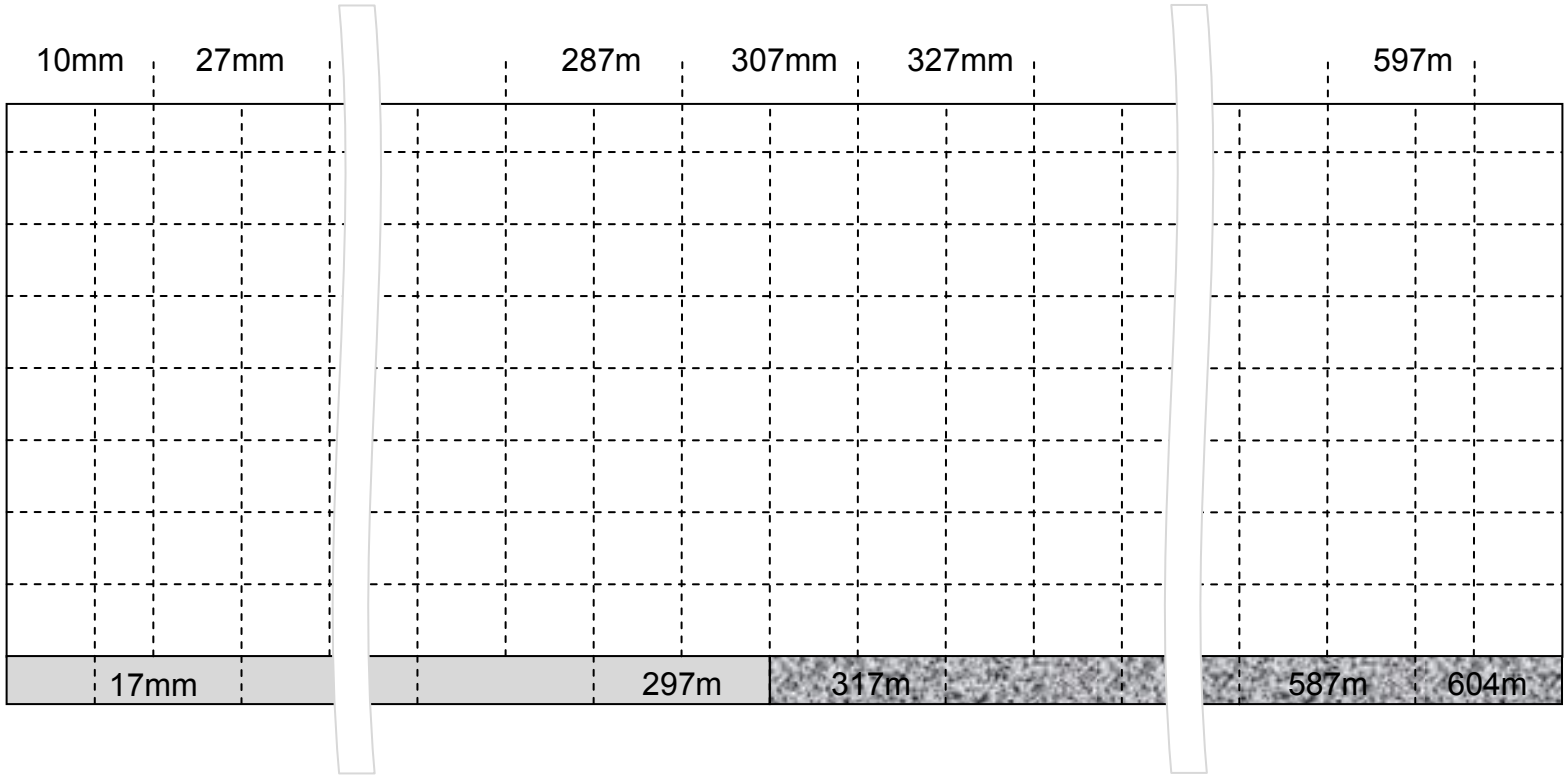

Figure 45: The ADV Measuring Grid (Flow into Page)

the positioning of the measured cross-section for BC1, and due to CS5 being potentially significantly closer to the tailgate. It is noted, however, that the validation using CS5 implies that these considerations were irrelevant. Thus the numbering sequence is in order of position downstream of the roughness switch, summarised in Table 4. Henceforth, the term “data set” is used to mean a full set of point velocity measurements taken at a specified bed configuration, discharge and cross-section, e.g. “BC1 F1” or “BC2 F2 CS4”.

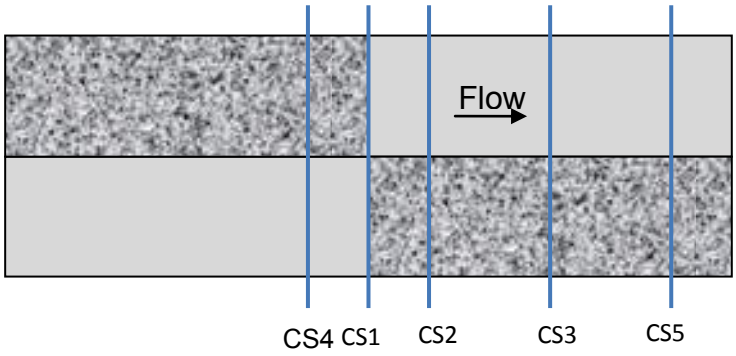

Figure 46: Measured Cross-Section Positions for BC2

Cross-Section	x_{switch} (mm)
CS1	0
CS2	365
CS3	912
CS4	1460
CS5	1460

Table 4: Measured Cross-Section Positions Relative to a Roughness Switch

A second, reference, ADV probe was also used and positioned upstream of the measured cross-section. Due to the large number of measuring points and the sampling time, it was not feasible to undertake all of the measurements in one session. It was therefore necessary to reset the flow before each session, and the velocity measurements from the fixed probe were used to ensure that the flow was consistent between sessions. As will be shown in the results (Section 8), all measurements from the fixed probe were within ±3% of the mean value, and this variation was seen over measurements taken within one session. This indicates that flow conditions were successfully replicated between sessions.

In order to securely hold the ADV probe, an adjustable clamping system was constructed (subsequently referred to as the probe harness). The harness was mounted on an existing rig which could be moved along the channel to the required cross-section and which allowed accurate vertical and horizontal movement of the probe, measured through fitted millimetre-increment rules.

The ADV measures at a point approximately 50mm from the probe tip and, due to this and the size of the probe, it was necessary to position the probe horizontally in order to take measurements within 30mm of the channel walls and 50mm of the water surface. All other measurements were taken with the probe positioned vertically. Additionally, limitations on the mobility of the rig used to position the probe necessitated the use of an extension to the harness for those measurements taken between 30 and 50mm from the channel walls. For the horizontal orientations a simple translation was performed to translate the measured velocities (in the probe axes) into the channel axes.

As mentioned above, the ADV measures at a point approximately 50mm from the probe tip. This distance is a property of the probe and is calculated by the manufacturers and stored as part of the probe configuration information. This may be retrieved (see (Mathiesen, 2008) for details) and for the two probes used the exact distances are given in Table 5.

Probe Serial Number	**Distance to Measuring Sample**
VNO-0334 (fixed probe)	46mm
VNO-0560 (mobile probe)	47mm

Table 5: ADV Probe Measuring Point Distances

5.3.5 Additional Velocity Measurements

Due to the size of the ADV probe measurements it was not possible to measure the velocity within 30mm of the water surface using the ADV. In order to obtain a more complete set of velocity data a Pitot-static tube was used to measure the velocity in this region. Over the central region (from $y/B = 0.34\ (y = 207mm)$ to $y/B = 0.66\ (y = 407mm)$) these measurements were made at horizontal intervals of 10mm, and at 20mm intervals over the remainder of the channel width. The vertical position of these measurements was at a distance of 10mm and 20mm below the water surface.

The Pitot-static tube was connected to an inclined manometer. The manometer was fitted in an adjustable, triangular stand, allowing the inclination angle, A, to be

calculated by measuring the three sides (of length a, b and c) and applying the cosine rule in the form:

$$cos\, A = \frac{b^2 + c^2 - a^2}{2bc} \tag{66}$$

Pitot-static tubes measure the stagnation pressure and pressure head (see Section 4.3) and the velocity was calculated using:

$$U = \sqrt{2gh} = \sqrt{2g|m_1 - m_2|\, sin\, A} \tag{67}$$

where m_1 and m_2 are the levels in the two manometer tubes.

5.3.6 Boundary Shear Stress Measurements

Boundary shear stress was measured along the smooth bed using a Preston tube and static pressure tube attached to the same manometer as used for the Pitot-static velocity measurements, and using the methodology outlined in Section 4. Similar measurements over the rough bed were impossible due to the random profile of the bed – such measurements are reliant on the tube being against the bed and this was not achievable due to the presence of larger pieces of gravel along the length of the horizontal, bottom section of the Preston tube.

In making these measurements there are a number of sources of experimental error. These include errors in the inclination angle of the manometer, errors in the construction/installation of the manometer (which may lead to a zeroing error) and errors in measurement of the water position in the manometer tubes. The first may be minimised by good practice when calculating the inclination angle. The second may be corrected for by placing both the kinematic and static pressure parts of the apparatus in still water, reading the (ideally zero) manometer head difference and

using this value as a correction. Therefore, the dominant source of error is in the measurement of the water position. With the variation seen in the manometer tubes, this error is approximated as being $\pm 2mm$. For the research described herein, this corresponds to $\sim \pm 5\%$.

5.4 Data Processing

5.4.1 Data Filtering

The data for each measured point was filtered using the Phase-Space Thresholding Method of Goring & Nikora (2002), previously discussed in Section 4.2.5. For a very small number of points (at most three of the 500+ measured points) this filtering failed due to the data being "dirty" - containing such a high percentage of spikes that the filtering was unable to identify them. These points were easily identified during the data gathering as the signal was obviously of a much lower quality than seen for the other points. Once filtered, these points also retained a higher standard deviation and visual inspection of the filtered and unfiltered data allowed these points to be discarded.

Filtered and unfiltered "dirty" and "clean" signals are shown in Figure 47. The reason for the signal being dirty at these points is unclear. Reflection from the channel walls and bed may cause an aliasing type effect (see Section 4.2.2), and so interference is caused by the channel geometry at certain points. The signal noticeably deteriorated in the upper central part of the flow, and this may be due to limitations of the bubble generator.

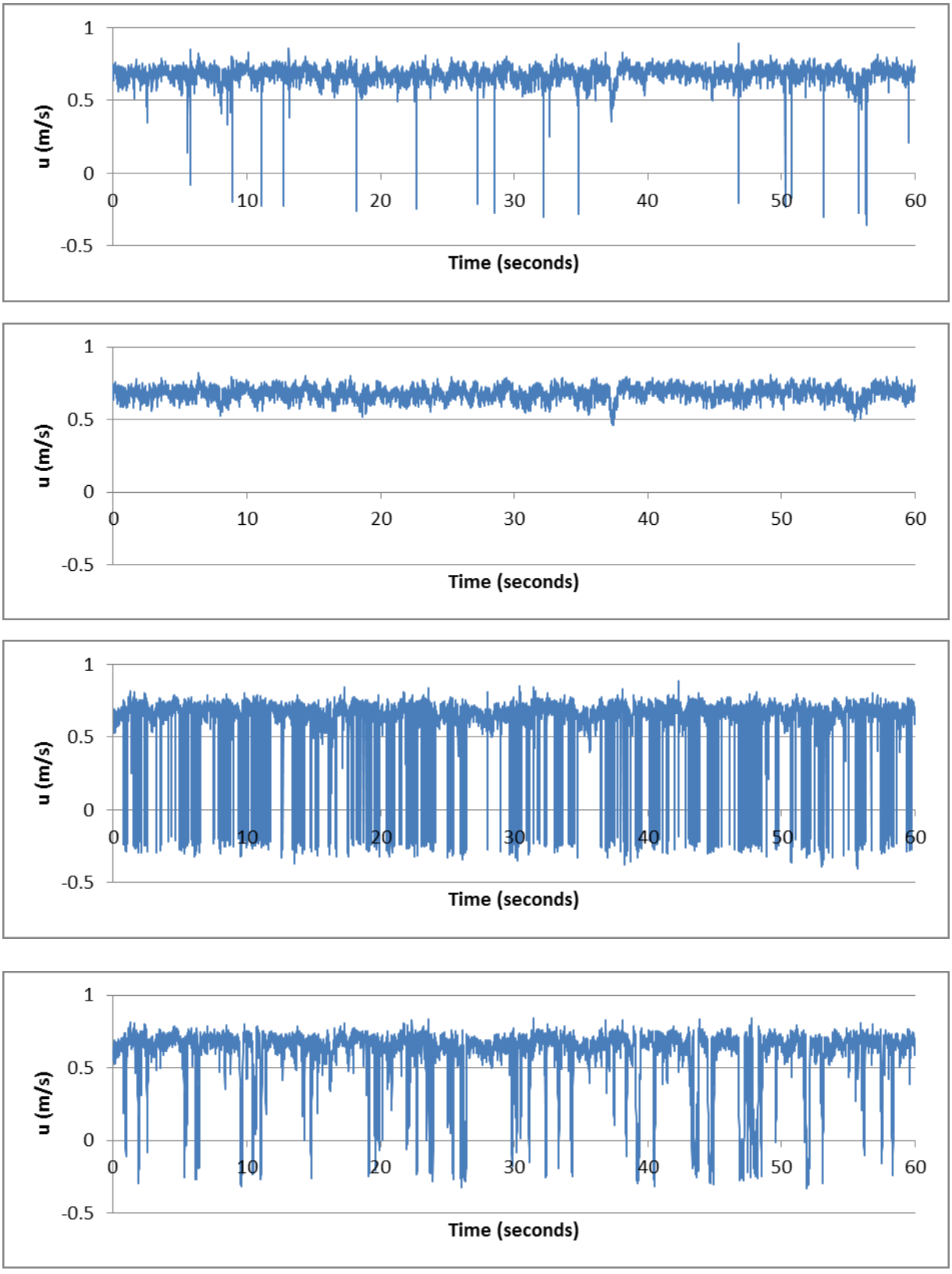

Figure 47: Example Filtered and Unfiltered Streamwise Velocity Time-series, $u(t)$ at Two Points (The top figure shows a "clean" signal before filtering, with the filtered time-series in the figure below. The bottom two figures show the equivalent for a "dirty" signal).

5.4.2 Rotation Correction

Ideally the probe would have been positioned with its measurement axes exactly parallel to the channel axes. However, in practice it was difficult to orientate the probe precisely, resulting in a small angular offset from the ideal position. As a result, the velocities measured by the probe were not the required u, v and w (the streamwise, transverse and vertical velocities respectively), but included an error due to the misalignment. Taking the example of a vertical probe, a small offset around the z-axis, $\delta\theta$, results in the measured velocity along the probe y-axis, v_p, actually containing a small amount of u:

$$v_p = v\cos\delta\theta + u\sin\delta\theta \tag{68}$$

In the case of v and w, this error may be significant due to the much larger magnitude of the streamwise velocity. Each set of measurements with the probe in a particular position, with or without the harness extension, were made in one session. The measurements may thus be split into batches, with each batch containing all measurements taken with one particular probe harness setup. Since the probe remained fixed in the harness for the duration of each batch, it is reasonable to assume that for all measurements in a particular batch the misalignment would be constant.

In order to correct for this error, a rotation correction was applied on a per batch basis. Defining (for example) the batch-mean transverse velocity as $V_b = \frac{1}{N}\sum_{batch} V$, where V is the point-mean transverse velocity and N is the number of measurements in the batch, the method for calculating this correction assumed that, due to the

relatively much larger magnitude of U, the point-mean streamwise velocity, any misalignment increases the batch-mean lateral velocities $V_b$and W_b. Hence applying the correction will minimise V_b and W_b. For each batch, U_b, V_b and W_b were calculated and a set of possible corrections, ranging from -50° to +50°, was applied to the rotation around each axis, with the values that minimised V_b and W_b being taken as the misalignment. Use of this range, which was far wider than any expected misalignment, ensured capture of the misalignment angle and provided validation of the method by not artificially limiting the correction to small angles. Any rotation around the x-axis does not result in the u velocity bleeding into $v_p$or w_p and so this method is not able to detect such a misalignment. The rotation corrections applied are shown in Table 6. Significant differences are seen between the maximum and mean values due to the necessity to apply the rotation correction procedure to relatively small batches (covering a lateral distance of 20mm) at the extreme y-positions, where the probe holder was once again required to allow measurements to be made.

Data Set	Theta Correction Magnitude (about y-axis; degrees)		Alpha Correction Magnitude (about z-axis; degrees)	
	Max.	Mean	Max.	Mean
BC1 F1	2.3	1.5	1.6	0.6
BC1 F2	1.7	1.4	1.7	1.1
BC2 F1 CS2	2.2	1.6	1.2	0.7
BC2 F1 CS4	2.1	1.9	0.3	0.3
BC2 F2 CS2	4.4	1.2	1.1	1.1
BC2 F2 CS4	1.9	1.8	0.7	0.5

Table 6: Maximum and Mean Rotation Correction Magnitudes by Data Set

5.5 Preliminary Experiments

5.5.1 ADV Sample Length and Sampling Rate

To determine the sample length and sampling rate to be used in the current research measurements were made at two points (one on the smooth side of the channel, at $y = 57mm$, and one on the rough side at $y = 457mm$) at sampling rates of 100Hz and 200Hz. The standard deviation of u was plotted against sample length (Figure 48) and the RMS of u' was calculated for each point and sampling rate. For both points, the calculated RMS value increased by approximately 10% (10% and 11%) when the sampling rate was increased from 100Hz to 200Hz, showing the advantage of using the higher rate (see Section 4.2). The standard deviation may be seen to settle at a sample length of around 30 seconds, though a sample length of 60 seconds was used for the experimental work to ensure full capture of the turbulent characteristics.

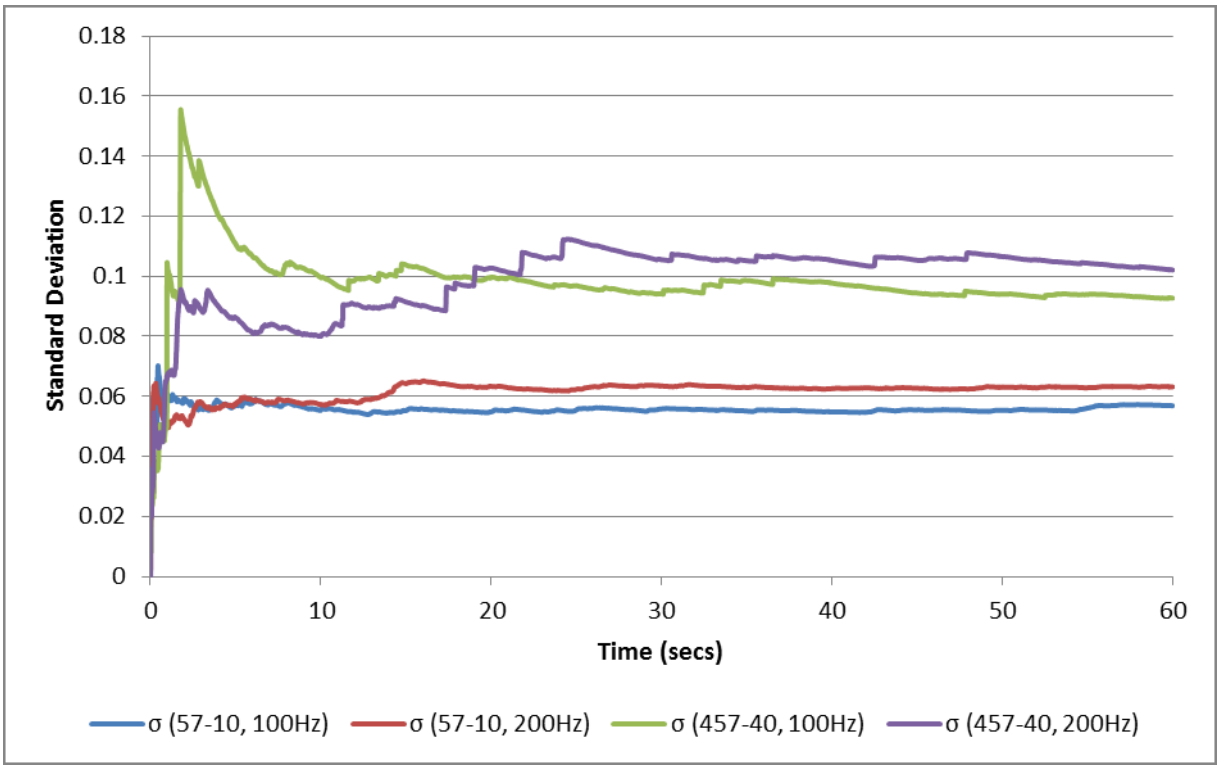

Figure 48: Variation of u Standard Deviation with Sample Length (From Unfiltered Velocity Data)

5.5.2 ADV Probe Alignment Effects

With the ADV probe horizontal it presents a relatively large obstacle in the flow. In order to ascertain the effect of this, three pairs of measurements were taken with the vertical fixed probe. The first measurement in each pair was made with the mobile probe remote from the fixed probe and so not affecting the flow. The second was made with the mobile probe orientated horizontally and situated as if it were measuring at the same point as the fixed probe. By comparison of the measurements in each pair an estimation of the effect of the horizontal probe was made.

Pair →	1	2	3
U_r (With 2nd Probe)	0.99	1.00	0.99
U_r (Single Probe)	1.01	1.01	1.02

Table 7: Probe Interference Test Measurement Pairs U_r Values

Table 7 shows the variation in U_r. It may be seen that U_r decreases by an average of 2% with the horizontal probe in place. The variation in lateral velocities is shown in Figure 49.

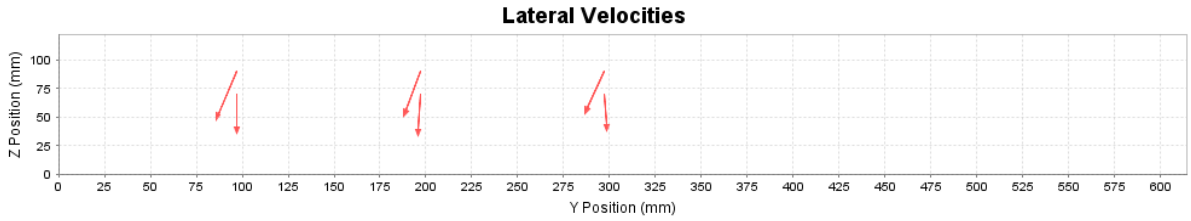

Figure 49: Probe Interference Test Lateral Velocity Measurements (position is for display purposes only – upper row is with the horizontal probe in place, lower row is without the horizontal probe)

It is thought likely that the effect of the orientation would depend on the horizontal position of the probe within the channel. Due to this, these measurements are unsuitable for determining a correction to be applied to the measurements taken with the probe horizontal, and only allow a judgement to be made as to the validity of such measurements.

It is concluded that the effect of the probe orientation on the measurement of streamwise velocity is sufficiently small to be neglected, bearing in mind that the probe is only in this orientation for a small number of measurements. However, the effect on lateral velocity and turbulent fluctuation measurements is considered sufficient to discard horizontal probe measurements from calculations requiring these values.

5.6 Additional Experiments

In the course of collecting and analysing the experimental data the collection of additional data was though necessary to further investigate certain characteristics of the flow:

- Transverse bed profile - the ADV provides a distance measuring function, which was used to survey the transverse bed profile at the measured cross-section.
- Upstream bed profile - the same functionality was also used to measure the bed profile upstream of the measured cross-section, close to the RSB.
- Velocity measurements at alternative cross-sections - velocity measurements were taken near the RSB, close to the channel bed, at a number of alternative cross-sections. These were made over a region spanning 30mm each side of the RSB.

. The results for these experiments are given in Section 6.

6 PRELIMINARY EXPERIMENTS

The following preliminary experiments were all carried out for BC1 F1.

6.1 Normal Depth Flow

To verify that the measured cross-section was in a suitable location to ensure fully-developed depth flow the vertical velocity profile was measured at $y/B = 0.50$, the RSB, at four x-positions upstream of the measured cross-section. These profiles are shown in Figure 50 below:

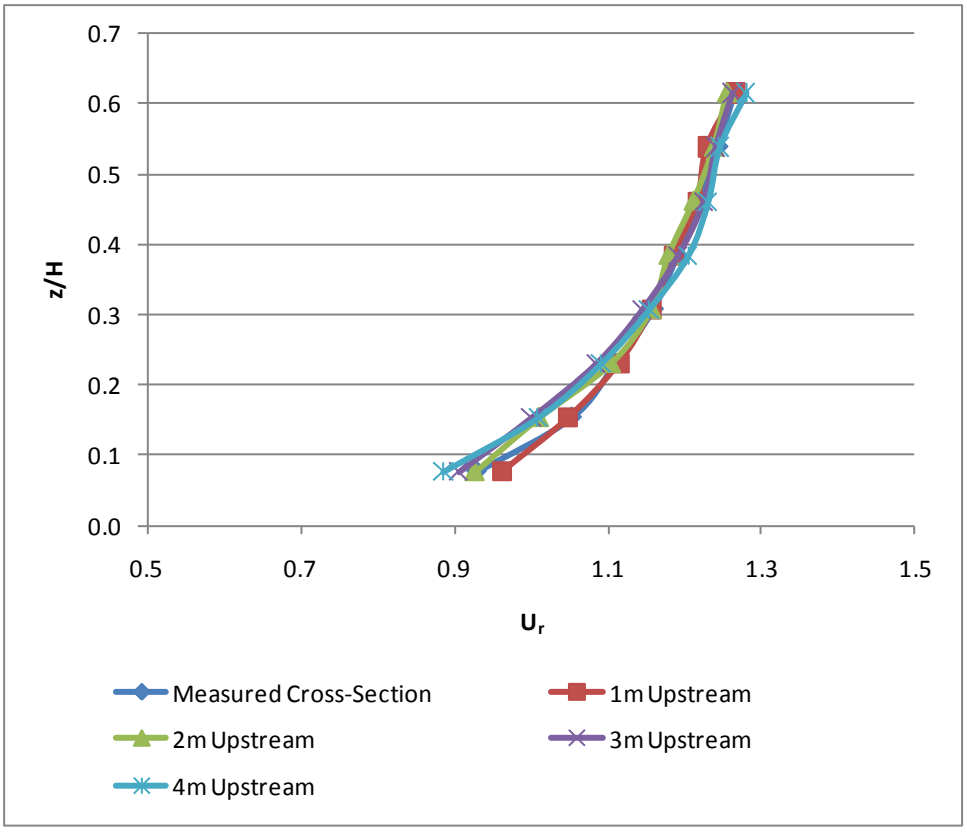

Figure 50: Vertical U_r Profiles at Different x-Positions (BC1 F1)

It may be seen that from $z/H \cong 0.20$ upwards the velocity profiles are negligibly different. Close to the bed the difference increases, but remains within $\pm 5\%$. The profiles at the measured cross-section and 1m upstream are almost identical, with a

discrepancy at the lowest measured point; however at this point the measured cross-section matches with the profile 2m upstream. These results demonstrate that the flow was fully developed and uniform at the measured cross-section, as required.

6.2 Transverse Bed Profile

The transverse bed profile was measured at the measured cross-section using the ADV's capability of measuring the distance to the channel bed. The profile is shown in Figure 51 below:

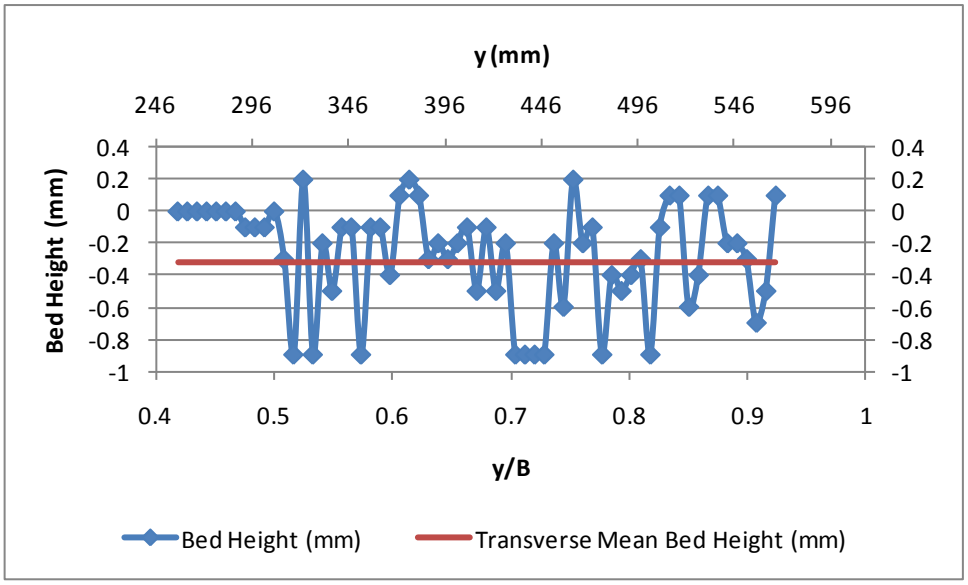

Figure 51: Transverse Bed Profile at the Measured Cross-Section (Height Relative to the First Measured Point on the Smooth Side)

Very slight (0.1mm) variation is seen on the smooth side of the channel $(y/B < 0.5)$, with the modal value of the smooth side measurements taken as the zero reference for the measurements. The mean bed height on the rough side is $\sim$3mm below the reference.

6.3 Upstream Bed Profile Near the RSB

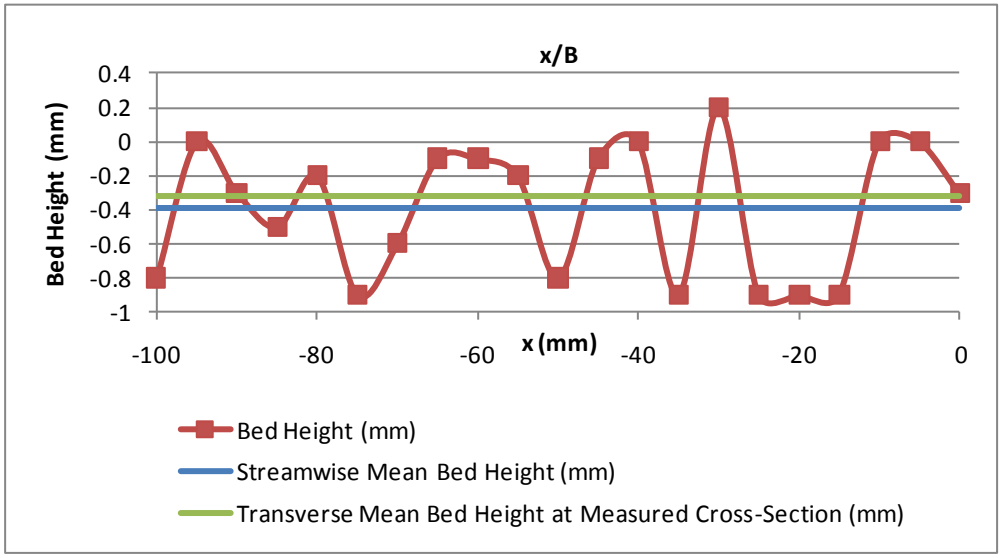

Figure 52: Streamwise Bed Profile Upstream of the Measured Cross-Section at $y/B \approx 0.51$

The streamwise bed profile was measured adjacent to the RSB, on the rough side of the channel. The profile is shown in Figure 52 and is very similar to that seen for the transverse profile.

6.4 Comparison of Pitot-Static Tube and ADV Velocity Measurements

As validation of the Pitot-Static tube and ADV velocity measurements a vertical velocity profile was measured at the RSB using both instruments for comparison. This is shown in Figure 53. From this figure it is evident that the measurements made by the two instruments were consistent over the entire profile.

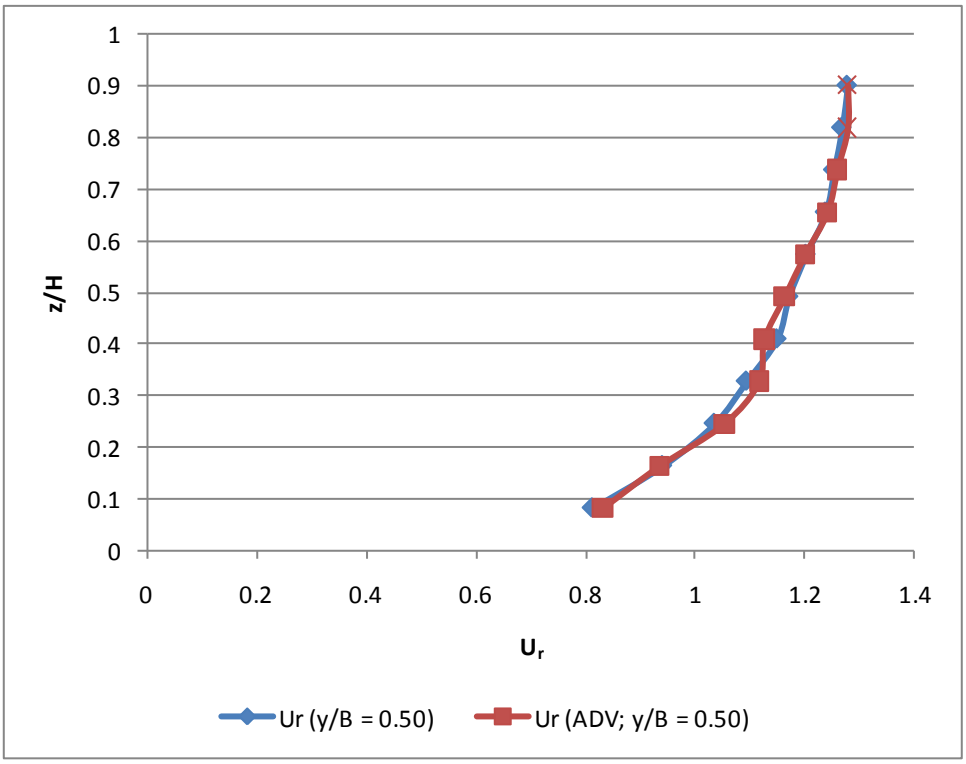

Figure 53: ADV and Pitot-Static Velocity Measurements (BC1 F1)

7 CHANNEL CONVEYANCE CHARACTERISTICS

This section presents and discusses the results of the measurement of the overall conveyance characteristics of the experimental channel for each of the bed configurations. Results for the bed slope measurements are given, followed by stage-discharge curves constructed for each bed configuration and a discussion of the channel resistance parameters, Manning's n and friction factor, f.

7.1 Bed Slope

The calculation of the bed slope is described in Section 5.3.2. The results were:

Set	"First-to-Last"	Sectional Mean
1	$0.00122 \pm 0.0003 m/m$	$0.00122 \pm 0.0002 m/m$
2	$0.00125 \pm 0.0003 m/m$	$0.00125 \pm 0.0002 m/m$

Table 8: Bed Slope Calculation Results

These values are consistent within the experimental error, and give a mean value of $S_0 = 0.00123 m/m$.

7.2 Stage-Discharge Curves

The stage-discharge curves for the experimental channel were constructed from the preliminary experiments for each bed configuration. These are shown in Figure 54 and Figure 55, which also include a number of theoretical curves calculated from:

(i) the compound channel method of Pavlovskij

(ii) the compound channel method of Horton

(iii) Manning's equation, using the standard n value for smooth plastic, $n = 0.010$ (Henderson, 1966)

(iv) Manning's equation, using the n value for a gravel bottomed channel with formed concrete sides, $n = 0.020$ (Chow, 1959). This is the most reasonable value from the standard values presented.

(v) a friction factor, f, calculated from the equation used by Vermaas (2007):

$$\frac{1}{\sqrt{f}} = \frac{1}{2}\sqrt{\frac{1}{\sqrt{f_{rough}}} + \frac{1}{\sqrt{f_{smooth}}}} \tag{69}$$

where f_{rough} and f_{smooth} are the friction factors for the rough and smooth sides of the channel respectively. f_{smooth} was calculated by applying the Darcy-Weisbach equation to each of the Q-H data points from (iii) to calculate the friction factor for each, and taking the mean of these values. f_{rough} was calculated in an identical manner using the data from (iv).

Allowing for fluctuations in the water surface, water depth was measured to an accuracy of $\pm 0.5mm$, while the discharge was measured to $\pm 0.25ls^{-1}$. As an indicator of the experimental error in these measurements, each absolute error is a relative error of the order of 0.5%. Error bars have been added to the experimental data points on certain figures in this section (due to the low magnitude of the experimental errors for these measurements, the error bars are insignificant on the other figures).

The data points are fitted with the best-fit power curve (of the form $y = Ax^B$, where A and B are positive constants, ensuring an intercept at the origin). For the theoretical series the power curves fit with correlation coefficient, R_{CC}, such that $R_{CC}^2 > 0.9996$ (with $R_{CC}^2 = 1.0$ being a perfect match). For the experimental results this correlation is

$R_{CC}^2 = 0.9991$ and $R_{CC}^2 = 0.9919$ for the first and second configurations respectively. This shows that the stage-discharge curves for the experimental channel follows the standard form for both configurations, being approximately linear at high flow rates and increasing in gradient at low flows.

It is evident from these figures that the models of Pavlovskij and Horton, which were developed for flows in transversely heterogeneous channels, underestimate the discharge for a given H. Although this underestimation is less than 5% at very low flow rates (Figure 56 and Figure 57 show the stage-discharge curves for the low flow region in more detail), it rapidly increases to approximately 15% with a flow depth of only $40mm$ and rises to over 20%.

Figure 58 and Figure 59 show the underestimation, as a percentage of the actual (experimental) discharge, of each of the methods outlined above. In this figure, the underestimation is plotted against H/B, the dimensionless rectangular channel aspect ratio, where H is the water depth and B the channel width.

From these figures, it may be seen that, as would be expected, treating the channel as if the bed were fully rough results in an underestimation of the discharge at all flow rates, while the fully smooth approximation overestimates the discharge. The difference is at least 20%, and is generally much greater.

The stage-discharge curves for the two configurations are shown together in Figure 60, with the difference in stage (aspect ratio) shown in Figure 61, both as a percentage and an absolute value. As the two stage-discharge curves were constructed using slightly different discharges, the data set for each configuration was extended (through linear interpolation from the closest data points) to include all

discharges in the other data set, thus providing values for the construction of Figure 61. This approach is considered suitable due to the small intervals over which the interpolation is applied.

Figure 60 and Figure 61 show that the absolute difference in aspect ratio is approximately constant at higher flow rates, with the stage-discharge curves for the two bed configurations being approximately parallel in the region where they are linear. In the non-linear, low discharge region the absolute difference falls, although as a percentage it increases rapidly for $H/B < \sim 0.12$, rising from $\sim 4\%$ at the highest discharge to $\sim 15\%$ at the lowest.

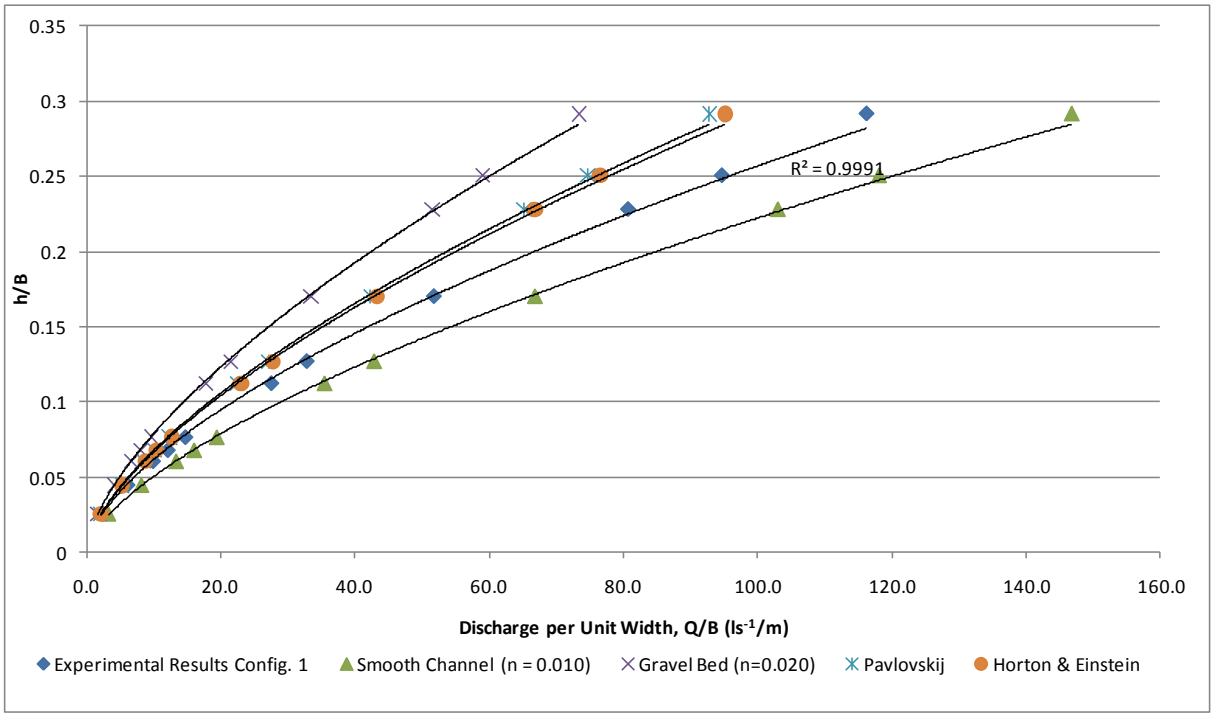

Figure 54: Stage-Discharge Curve for BC1

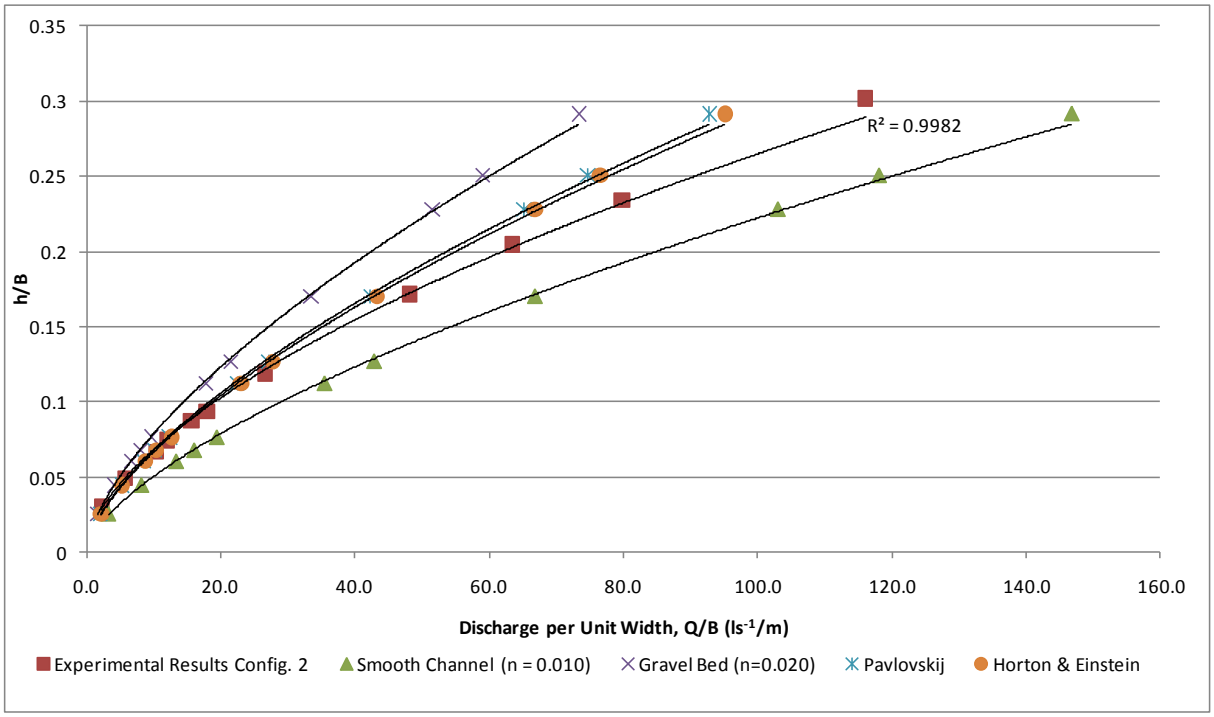

Figure 55: Stage-Discharge Curve for BC2

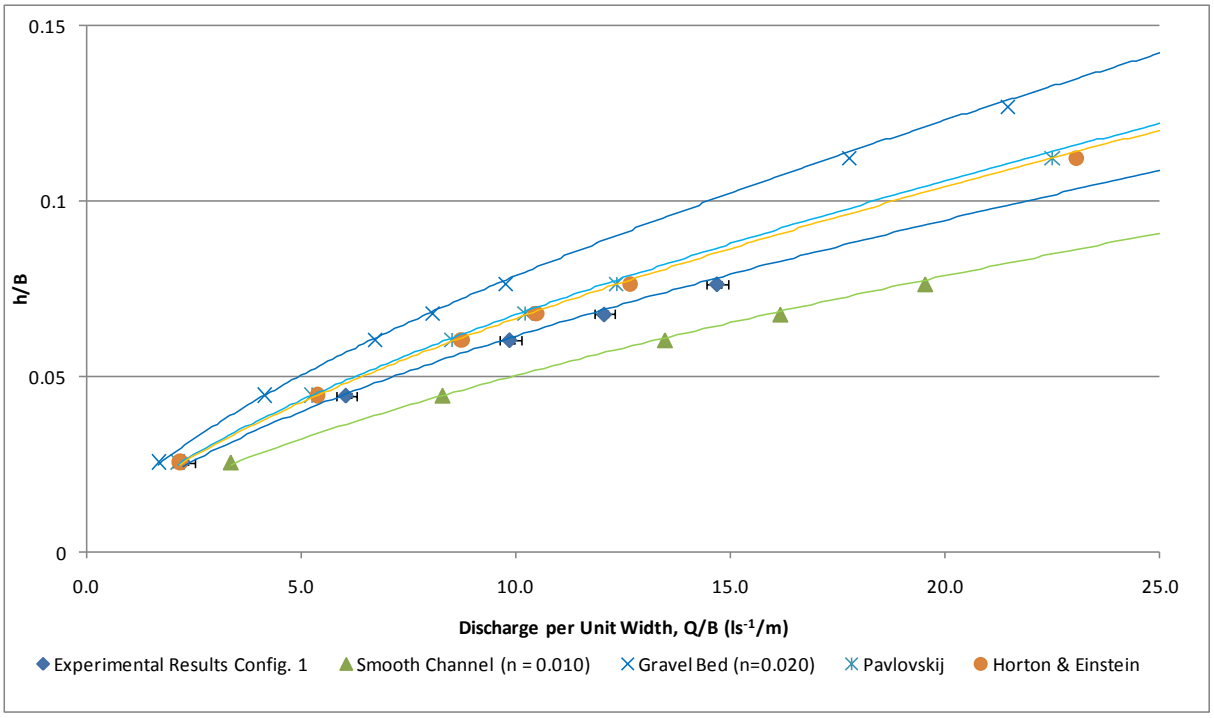

Figure 56: Low Discharge Stage-Discharge Curve for BC1

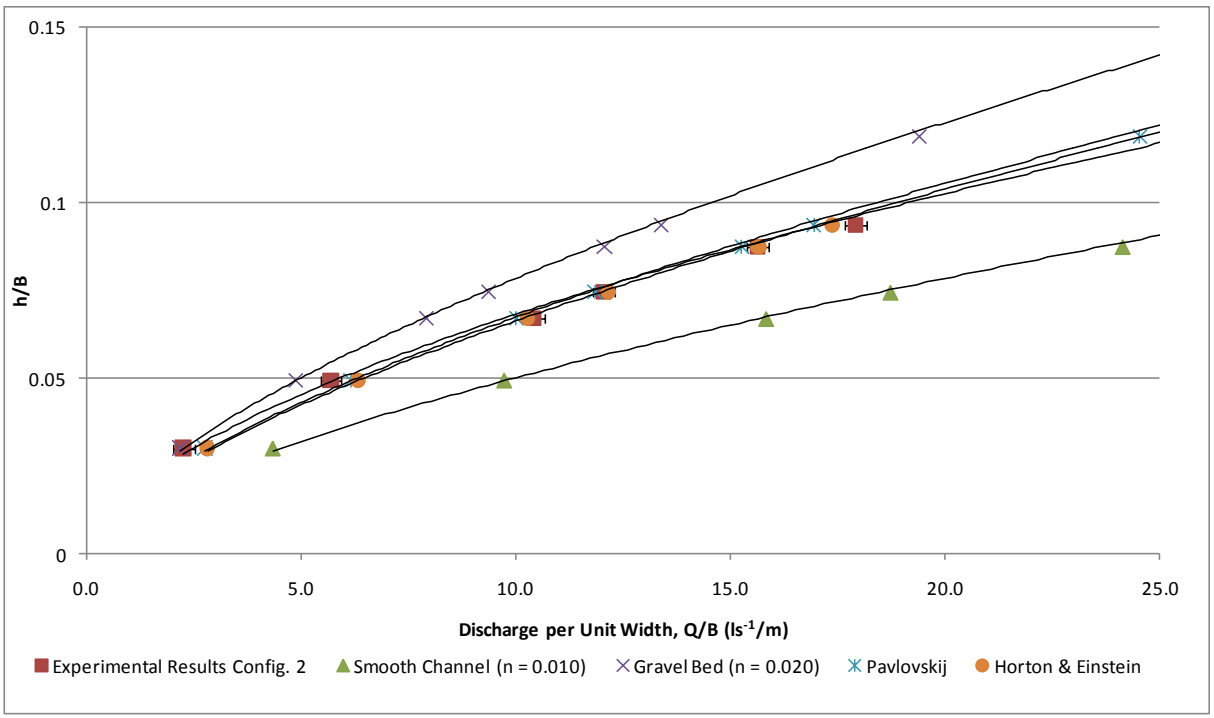

Figure 57: Low Discharge Stage-Discharge Curve for BC2

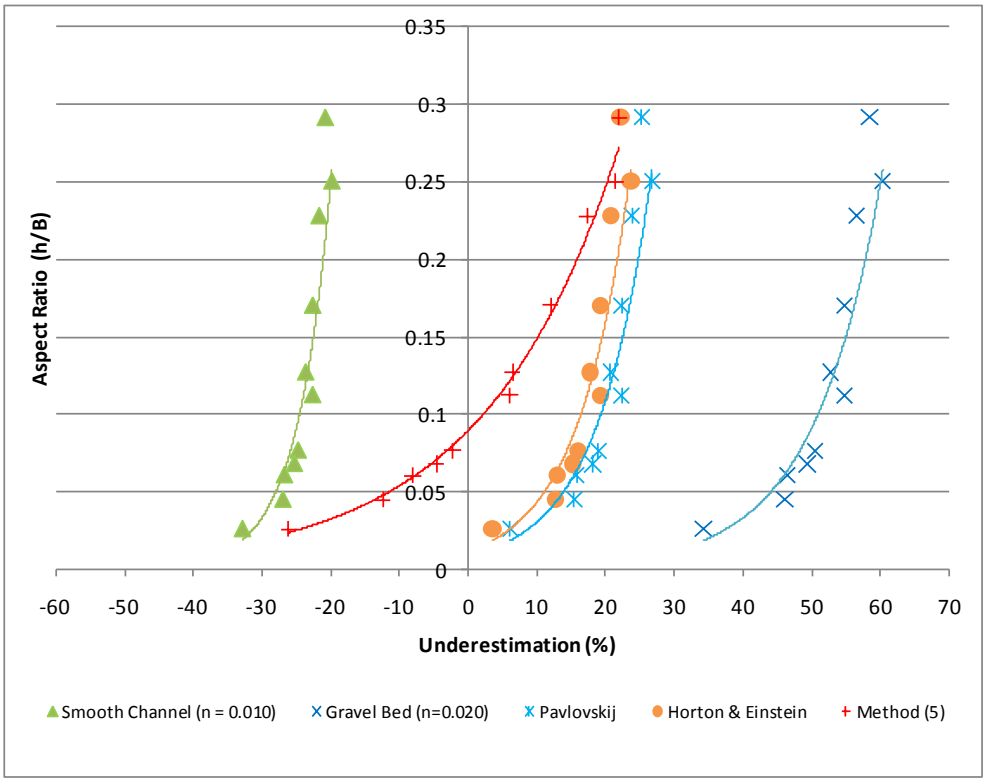

Figure 58: Percentage Underestimation by the Theoretical Discharge Calculation (BC1)

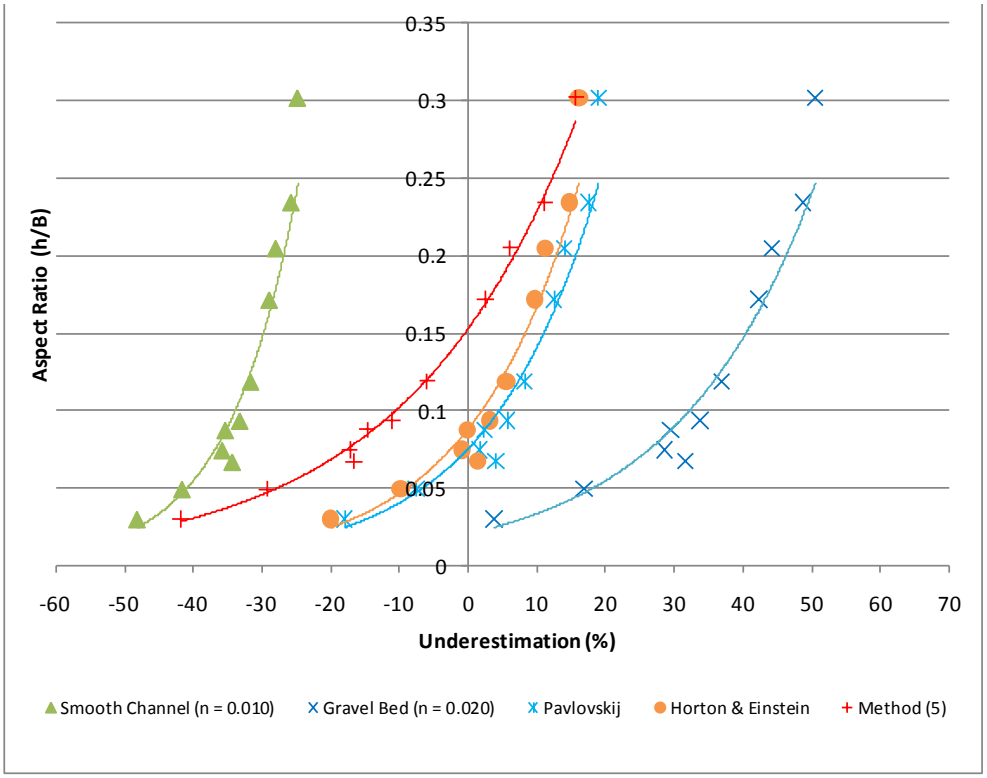

Figure 59: Percentage Underestimation by the Theoretical Discharge Calculation (BC2)

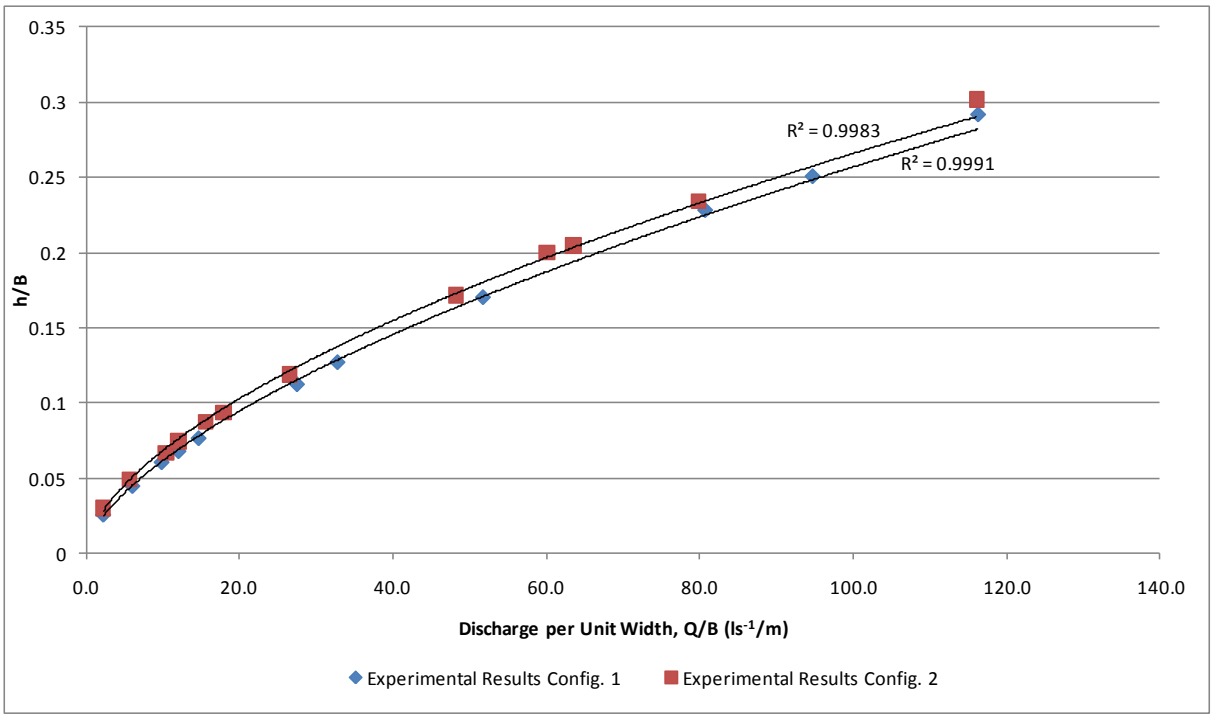

Figure 60: Stage-Discharge Curves for the Two Bed Configurations

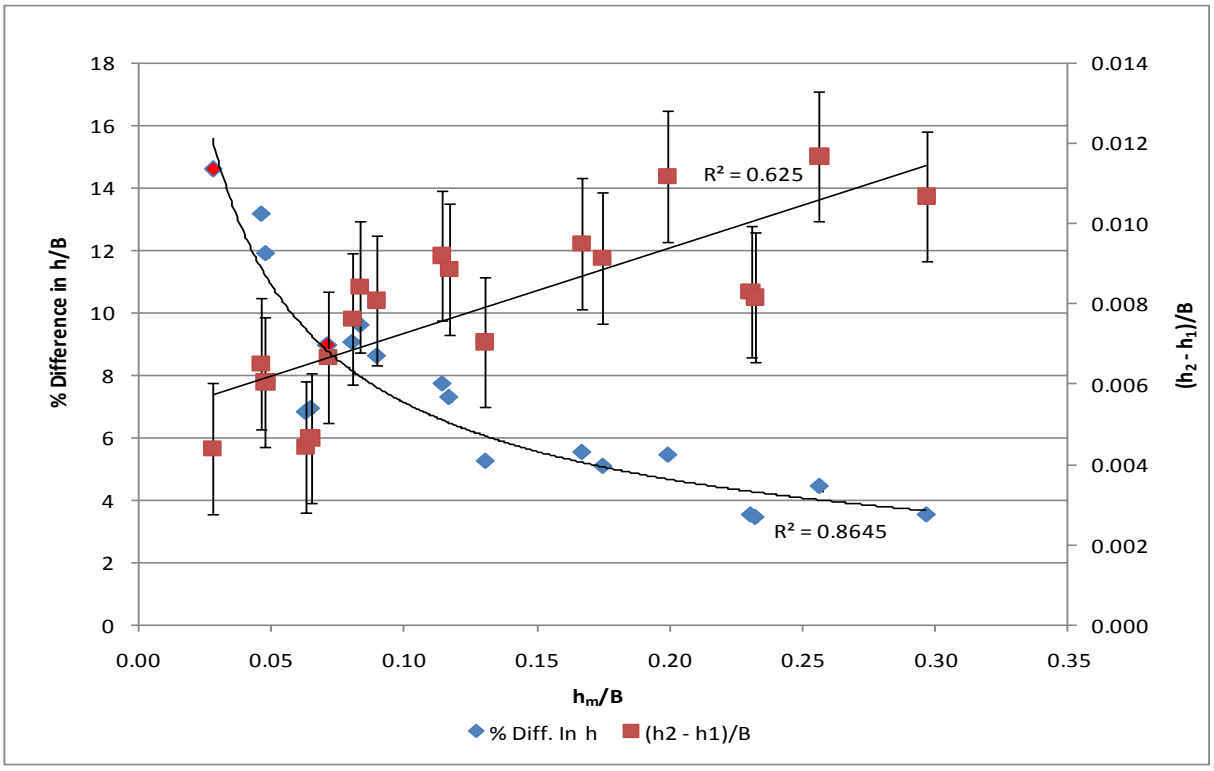

Figure 61: Percentage and Absolute Difference in Aspect Ratio for the Two Bed Configurations
(x-ordinate is the mean aspect ratio, $\frac{1}{B}\left(\frac{h_1+h_2}{2}\right)$; red % Difference points are those for which identical discharges were used for both configurations; subscripts refer to the configuration number)

At medium to high flow rates, method (5) performs better than the others, with the underestimation being smaller than that seen for the compound methods. However, at high flow rates the improvement over the compound methods is small (< 3%), while at low flow rates method (5) overestimates the discharge considerably.

Figure 62 and Figure 63 show the variation with aspect ratio of the friction factor, calculated using the Darcy-Weisbach formula, for each of the methods. This figure shows the cause of the limitations of method (5) – the friction factor cannot be considered constant over all stages but decreases with stage. Figure 64 shows the same effect in terms of Manning's n. For both bed configurations the n distribution is as would be expected intuitively, with the effect of the bed roughness reducing with height above the bed and affecting a smaller proportion of a deep flow than a shallow flow. In both cases the distribution is approximately linear at higher aspect ratios, $H/B > \sim 0.05$ and $H/B > \sim 0.075$ for configuration 1 and 2 respectively (these limits are reversed for the friction factor). Below this point there is a rapid increase in n - for the second configuration n reaches a value of 0.019 at the lowest discharge, near the value of 0.020 for a homogeneous gravel bed.

The BC2 n distribution, and its tending towards that of a homogeneously rough bed at low discharges, is due to the interaction of the flow over the smooth section with that over the preceding and following rough sections. The rough bed exerts a strong influence on the flow over and close to it, forming a layer of relatively slow moving water and the standard, non-linear vertical velocity distribution. The upper layers are affected to a much lesser degree. It is hypothesised that the flow in the upper levels, at higher discharges, is more longitudinally uniform than that seen close to the bed, with a streamwise velocity approximately the mean of that for a smooth channel and

a rough channel. At low discharges the rough bed affects the entire flow depth, with the flow over the rough sections preventing acceleration of the flow over the smooth sections, resulting in a pseudo-homogeneous rough channel.

Vermaas (2009) measured non-negligible mean transverse velocities with an alternating channel bed such as configuration 2, with flow from the rough side to the smooth at the beginning of each bed material switch. This would be due to a pressure gradient forming as the rough side flow slows and the smooth side flow accelerates, and would lead to momentum transfer between the two, explaining the higher stage (and thus lower channel-mean U) for the second configuration.

The differences in these flows are discussed formally and quantitatively in Section 8.4, where the results of the detailed velocity measurements are presented.

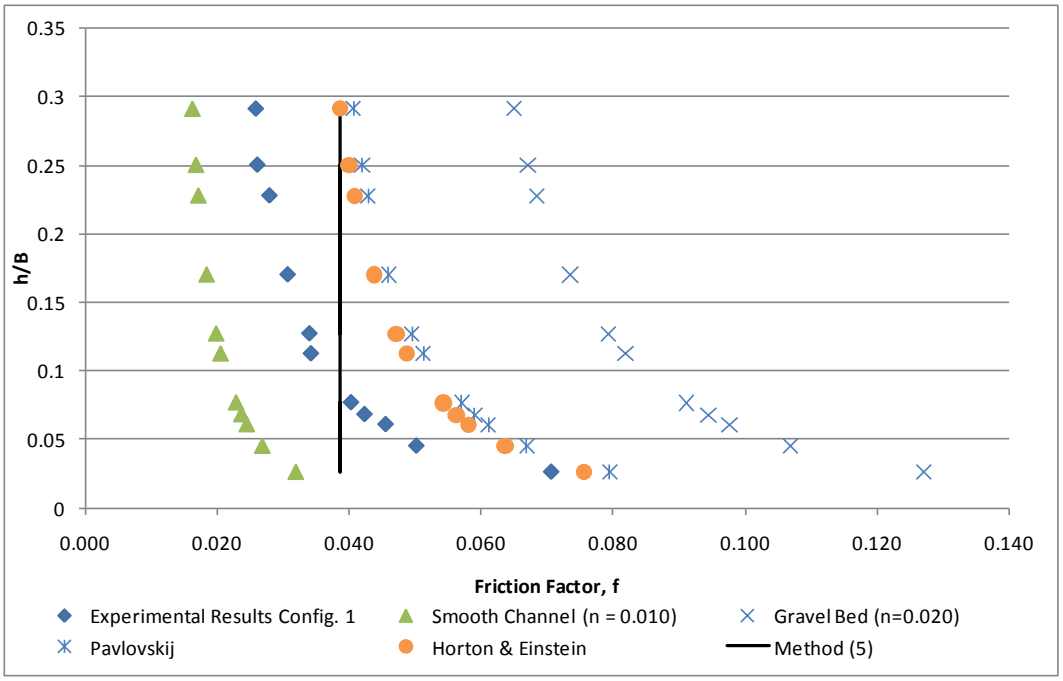

Figure 62: Variation of Friction Factor with Aspect Ratio for the Experimental Channel and Theoretical Channels (BC1)

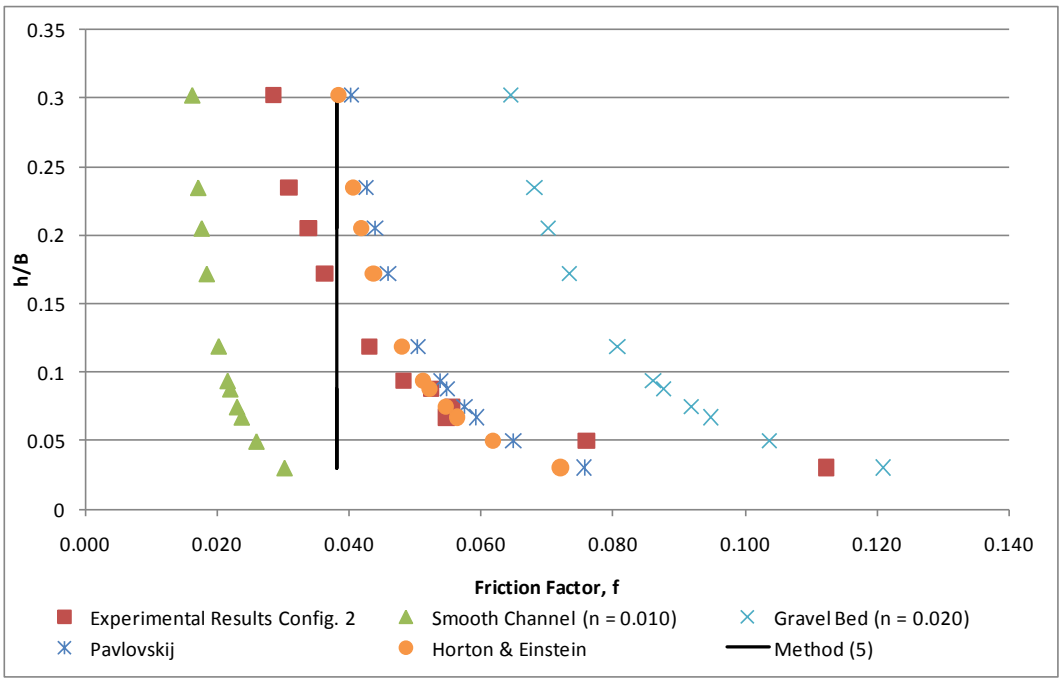

Figure 63: Variation of Friction Factor with Aspect Ratio for the Experimental Channel and Theoretical Channels (BC2)

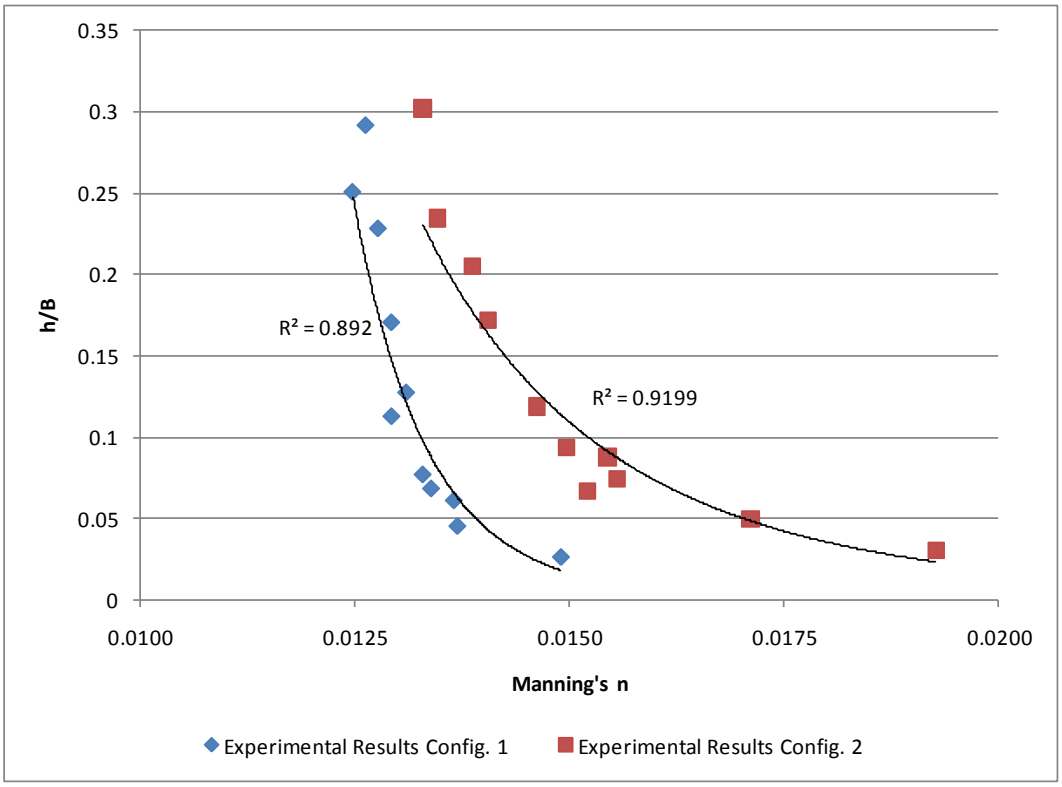

Figure 64: Variation of Manning's n with Aspect Ratio

8 DETAILED FLOW ANALYSIS

In this section the flow characteristics are examined in detail using the velocity data recorded at the measuring grid points. Each characteristic (velocity, shear stress, etc.) is presented individually, with cross-sectional distributions and vertical distributions at selected y-positions being shown. These y-positions are the nearest measured points to the centre of the smooth side, the rough-smooth boundary (RSB) and the centre of the rough side $(y/B \cong 0.25, y/B = 0.50, y/B \cong 0.75)$. For brevity these three sections are referred to as the *primary sections*. Where appropriate, additional vertical section distributions are shown for regions of interest such as a span of the RSB region.

A comparison between the results for different flow rates and/or bed configurations is included, although a discussion of the importance of each of the flow features mentioned is reserved for Section 10, in which the results are applied to the SKM.

The transverse distribution of depth-averaged values are also presented where appropriate. Denoting depth-averaging with a subscript d the depth-average calculation was performed using a discrete approximation to the integral:

$$f_d(y) = \frac{\int_0^h f(y,z)dz}{H} \cong \frac{\sum_{i=0}^{i=N(y)} f(y,z_i)\Delta z_i}{\sum_{i=0}^{i=N} \Delta z_i} \tag{70}$$

where $\Delta z_i = \begin{cases} (H - z_i) - \frac{(z_i - z_{i-1})}{2} & (uppermost\ point) \\ \frac{(z_{i+1} - z_i)}{2} - \frac{(z_i - z_{i-1})}{2} & (other\ points) \\ \frac{(z_{i+1} - z_i)}{2} & (bottom\ point) \end{cases}$ and $N(y)$ is the number of measured points at y.

Integrated channel mean values, denoted by capitals and subscript i, were calculated using

$$F_i = \frac{\int_L^R \int_0^h f(y,z)dz\,dy}{A} \cong \frac{\sum_{i=0}^{i=N} f(y,z_i)\Delta z_i \Delta y_i}{\sum_{i=0}^{i=N} \Delta z_i\,\Delta y_i} \tag{71}$$

Where L and R are the left and right bank positions respectively, $\Delta y = \begin{cases} (R - y_i) - \frac{(y_i - y_{i-1})}{2} & (rightmost\ point) \\ \frac{(y_{i+1} - y_i)}{2} - \frac{(y_i - y_{i-1})}{2} & (other\ points) \\ \frac{(y_{i+1} - y_i)}{2} - L & (leftmost\ point) \end{cases}$ and N is the number of measured points over the cross-section.

The term “relative” is used to denote division by the integrated channel mean:

$$f_r(y,z) = \frac{f(y,z)}{F_i} \tag{72}$$

with the exception of velocity measurements where the division is by the $U_{Q/A}$ value defined in Section 8.3 below.

Where a parameter has been scaled to a dimensionless value, a subscript nd is used. For example, the dimensionless τ_V^R is obtained by scaling by the mean boundary shear stress, $\overline{\tau_b}$ is given by:

$$(\tau_V^R)_{nd} = \frac{\tau_V^R}{\overline{\tau_b}} \tag{73}$$

The scaling factor will be specified at first use of the dimensionless parameter.

Derivatives were calculated using forward and backward finite difference methods at the first and last points of a series, and the central difference method at all other points.

8.1 Configuration Flow Properties

The flow properties for the different bed configurations and flow rates are shown in Table 9 for reference.

Configuration	Discharge (ls^{-1})	Water Depth, H (mm)	$U_{Q/A}$ (ms^{-1})	Re	Fr
BC1 F1	40.3	121.6	0.540	47000	0.49
BC1 F2	56.2	160.2	0.572	60000	0.46
BC2 F1	36.9	122.1	0.492	43000	0.45
BC2 F2	57.4	160.0	0.584	61000	0.47

Table 9: Configuration and Flow Properties

8.2 Mirrored Flow Assumption

Before discussing the details of the flows for each measured cross-section it is necessary to examine the assumption of mirrored flow (i.e., that the flow over channel sections with the rough bed on the left is a mirror image of the flow over channel section with the rough bed on the right - see Section 5.3.4) for BC2. For BC2 F1, this is supported by comparison of horizontal sections of CS4 and CS5 (Figure 65). These sections are consistent except at the RSB close to the bed, a region highly susceptible to slight differences in probe height and differences in the particular gravel distribution at that cross-section. The lateral velocity vectors (shown in Figure 66) are broadly consistent, with downflow over the rough bed and upflow over the smooth. It should be noted that the rotation correction procedure, which

assumes zero lateral velocities over the entire channel, is less accurate when used over a small section such as that in CS5 – this may go some way to explaining the differences seen in the upper levels of the CS4 and CS5 lateral velocity vectors.

Qualitatively, the mirrored flow assumption is supported for BC2 F2 by the measurements for CS4 and CS5 (Figure 67 and Figure 68). Quantitatively, however, CS4 has lower U values, as further evidenced by Figure 69, which shows the flow development along the channel section. There is some evidence for the acceleration/deceleration seen after CS1 for BC2 F1 (see Section 8.4.1), but this is masked by an apparent, depth-independent offset for the CS4 measurements (Figure 69(a) and (c)). Examination of the fixed probe measurements for CS2 and CS4 shows no evidence of differences in the flow which may have caused this offset – in fact the mean streamwise velocity from the fixed probe is $\sim 2\%$ greater for CS4 than CS2. A repeat of measurements for CS4 was impractical; it is acknowledged that this would benefit from examination in future work, however it is considered that the data provide a basis for a qualitative analysis when used in conjunction with those for BC2 F1.

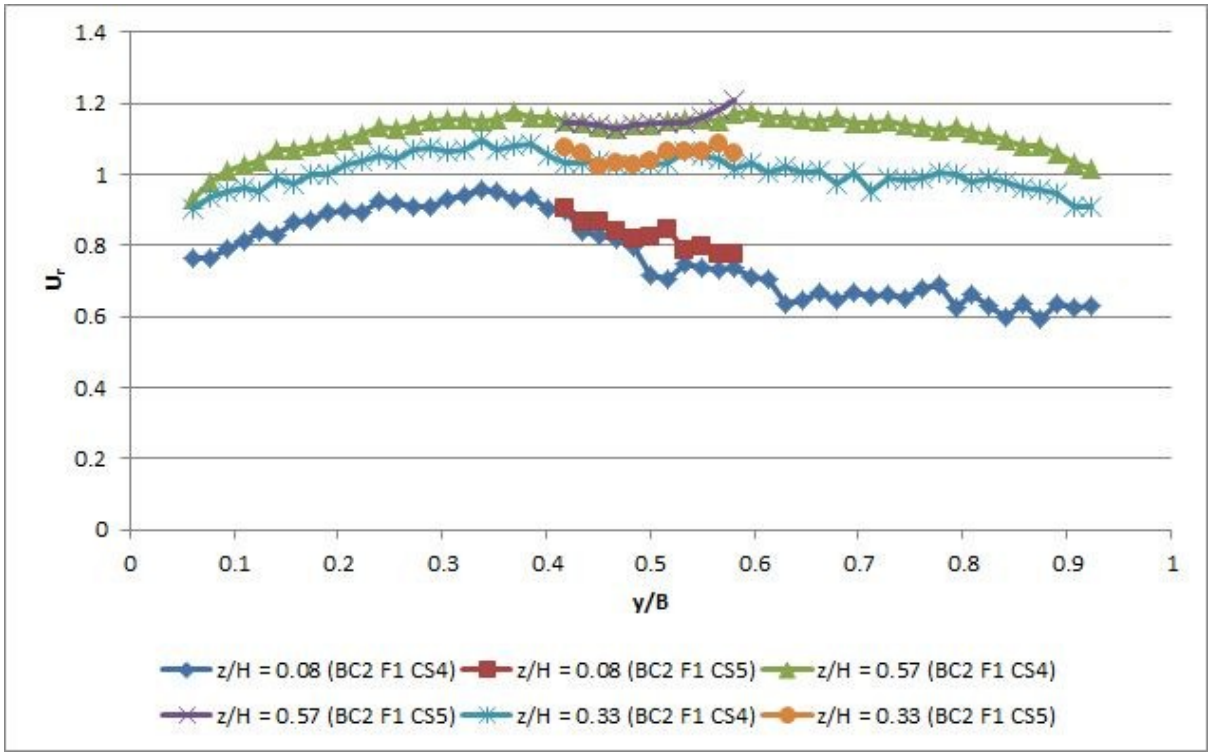

Figure 65: Horizontal Distribution of U_r over CS4 (mirrored) and CS5 (BC2 F1)

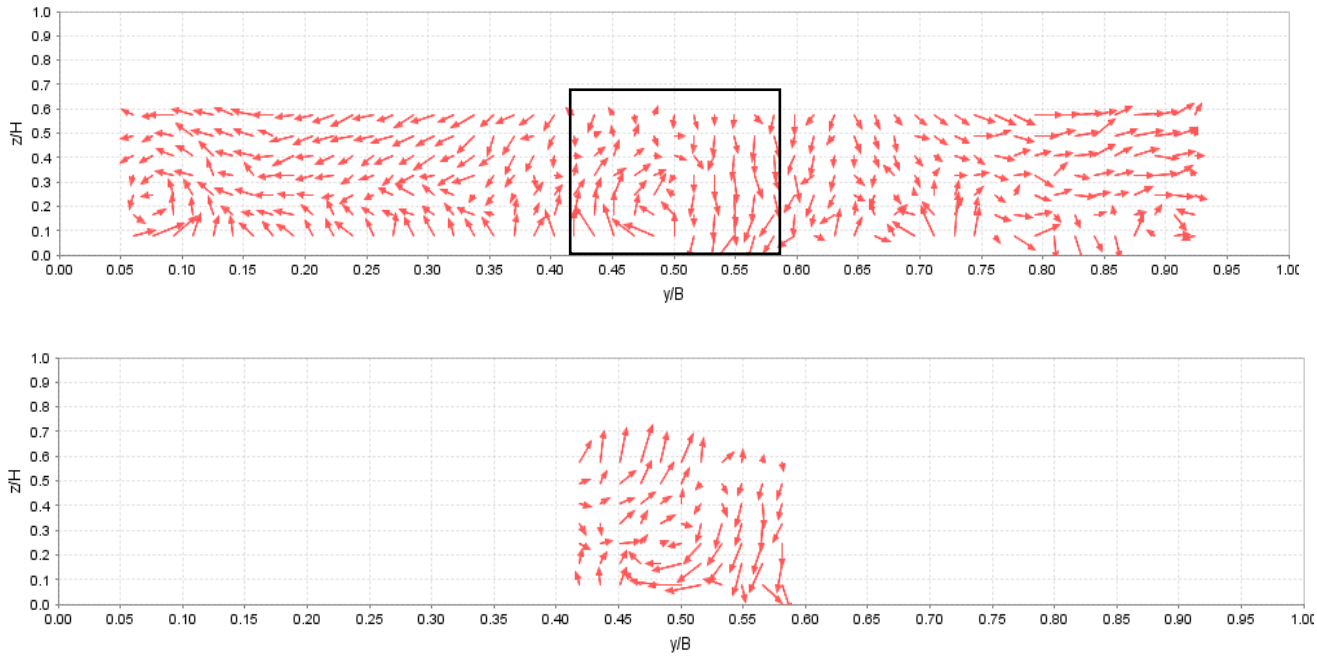

Figure 66: Lateral Velocity Vectors for CS4 (mirrored) and CS. The rectangle marked on CS4 indicates position of the CS5 measurements (BC2 F1)

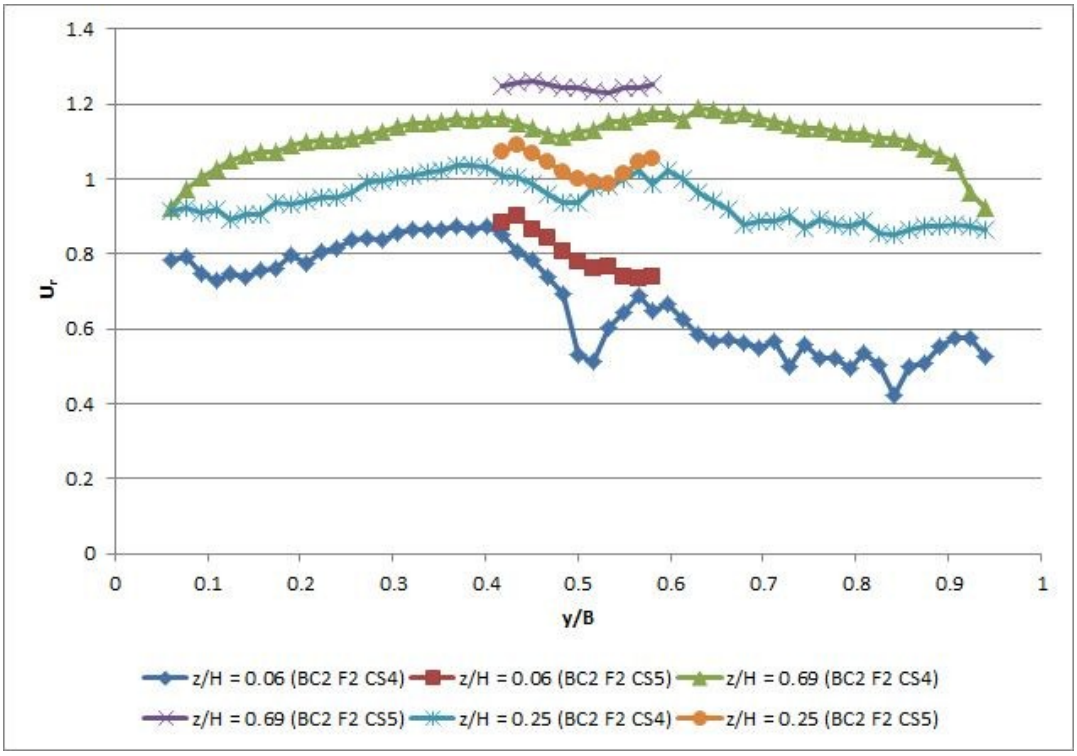

Figure 67: Horizontal Distribution of U_r over CS4 (mirrored) and CS5 (BC2 F2)

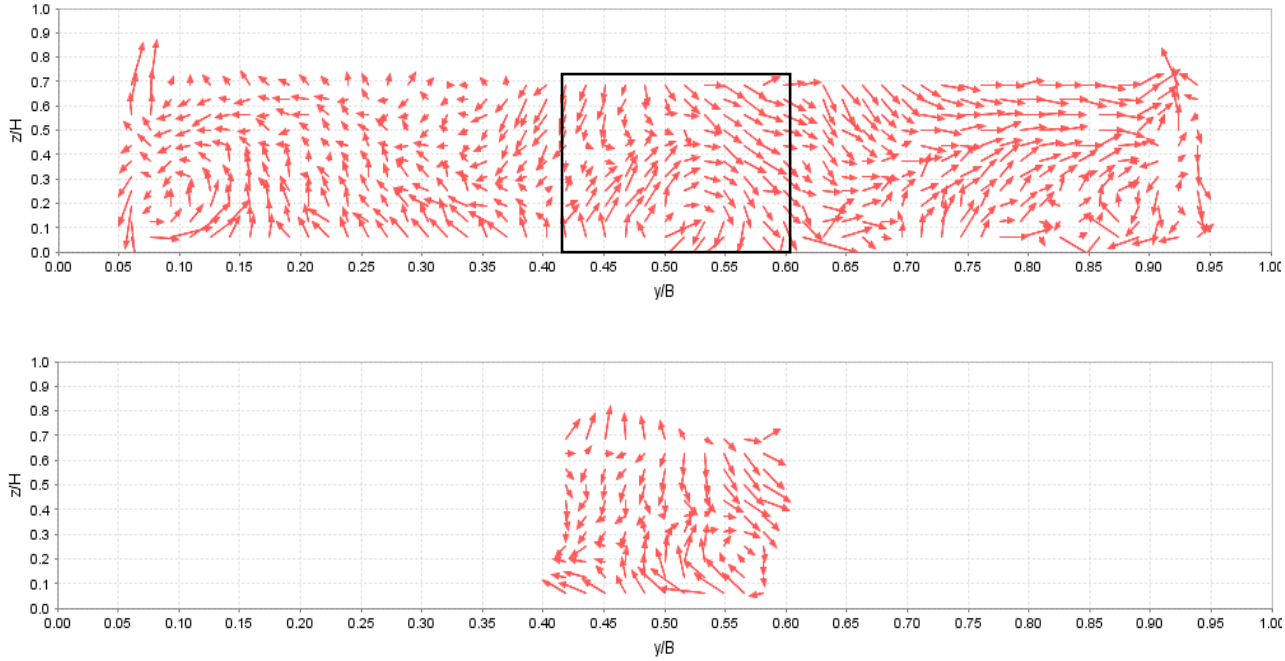

Figure 68: Lateral Velocity Vectors for CS4 (mirrored) and CS5 (BC2 F2). The rectangle marked on CS4 indicates position of the CS5 measurements

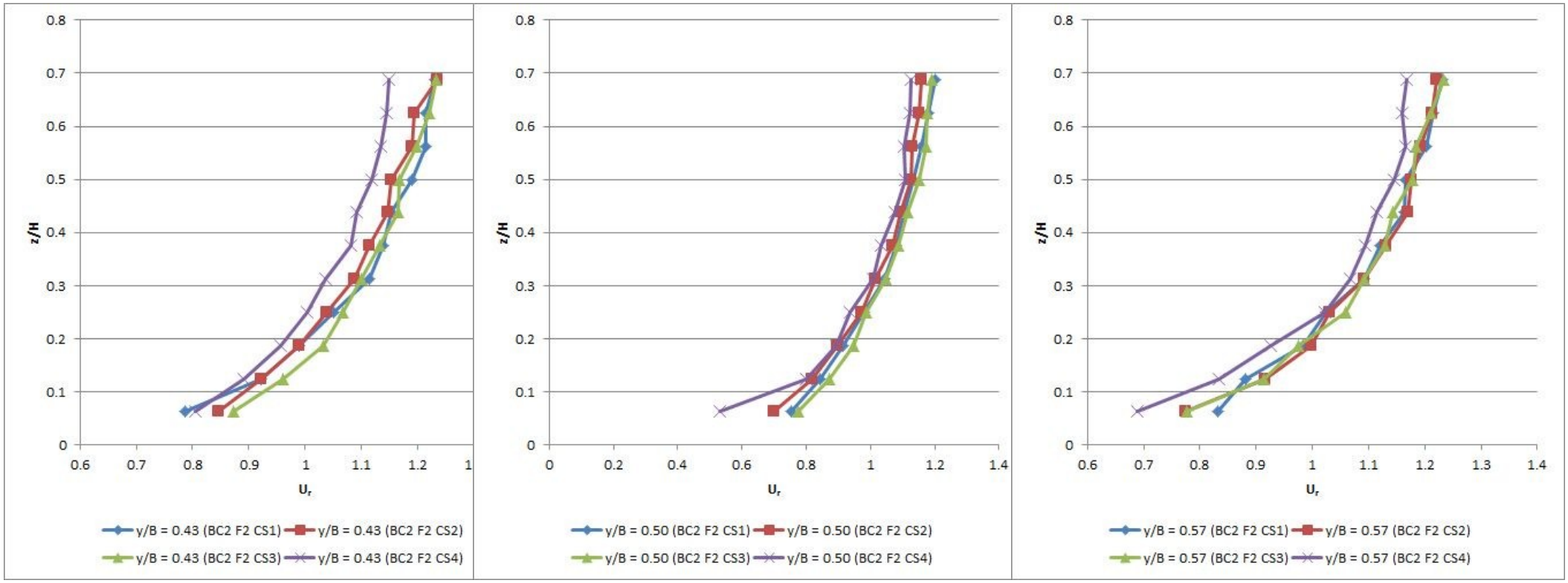

Figure 69: Flow Development Near the RSB after the Roughness Switch (BC2 F2). (a) Smooth side (left); (b) RSB (centre); (c) Rough side (right)

8.3 Structure of the Boundary Layer

As discussed in Section 3.5.1, the boundary layer may be split into a number of regions based on a normalised distance from the wall:

$$z^+ \equiv \frac{U_* z}{\nu} \equiv \frac{z}{\nu}\sqrt{\frac{\tau_b}{\rho}} \tag{74}$$

The measurement/estimation of τ_b is discussed fully in Section 9. In order to gain an insight into the structure of the boundary layer in the experimental channel, the boundary shear stress values are pre-emptively quoted here as approximate mean values by side (Table 10) to allow the position of these regions to be calculated (Table 11).

Configuration	Approximate Mean τ_b (Nm^{-2})	
	Smooth Side	Rough Side
BC1 F1	0.7	1.5
BC1 F2	0.7	1.5
BC2 F1 CS2	0.4	0.7
BC2 F1 CS4	0.5	1.2
BC2 F2 CS2	0.6	1.4
BC2 F2 CS4	0.7	1.5

Table 10: Approximate Side-Mean Boundary Shear Stress Values

Configuration	Upper Border Position (mm)					
	Viscous Sublayer $z^+ < 5$		Buffer Layer $z^+ < 30$		Wall Region $z/H < 0.2$	
	Smooth Side	Rough Side	Smooth Side	Rough Side	Smooth Side	Rough Side
BC1 F1	$\ll 1$	$\ll 1$	~ 1	~ 1	24	24
BC1 F2	$\ll 1$	$\ll 1$	~ 1	~ 1	32	32
BC2 F1 CS2	$\ll 1$	$\ll 1$	~ 1	~ 1	24	24
BC2 F1 CS4	$\ll 1$	$\ll 1$	~ 1	~ 1	24	24
BC2 F2 CS2	$\ll 1$	$\ll 1$	~ 1	~ 1	32	32
BC2 F2 CS4	$\ll 1$	$\ll 1$	~ 1	~ 1	32	32

Table 11: Upper Borders for the Boundary Layer Regions as Defined by Nezu & Nakagawa (1993)

While variation is seen in the calculated upper borders of the viscous sublayer and buffer layer, these variations are negligibly small in comparison to experimental errors. The Wall Region, in which the log-law of the wall is valid, may be seen to cover the region from approximately 1mm above the channel bed to a depth of 24mm (Flow 1) and 32mm (Flow 2).

8.4 Velocity Distribution

8.4.1 Streamwise Velocity

The point-mean velocity, U, was calculated from the measured data at each grid point; the U distribution is shown in for each data set in Figure 70 to Figure 73. Integration over the channel gave a channel-mean velocity, U_i, with an independent channel-mean also calculated using the discharge, Q, and flow cross-sectional area, A, as $U_{Q/A} = Q/A$. These values should be equal and the small difference, less than 3% except for BC2 F1 CS2 (see Table 12), provides verification of the ADV measurements. This difference seen in the two channel mean U values is comparable with the errors found by previous researchers at the University of Birmingham such as Yuen (1989) and Alhamid (1991) when using the same experimental channel. These studies, which were investigations of trapezoidal channels with velocity measured using a Pitot-static tube, calculated the integrated discharge to within 6% and 5% of the independently measured value respectively. It should also be noted that this 3% difference is the same as the variation seen at the fixed probe.

Configuration	U_i (ms^{-1})	$U_{Q/A}$ (ms^{-1})	% Difference
BC1 F1	0.550	0.540	2
BC1 F2	0.585	0.572	2
BC2 F1 CS2	0.510	0.492	4
BC2 F1 CS4	0.502	0.492	2
BC2 F2 CS2	0.594	0.584	2
BC2 F2 CS4	0.579	0.584	-1

Table 12: Channel Mean Streamwise Velocities

With regard to the BC2 F1 CS2 case, Vermaas (2009) made detailed measurements of the water depth along the flume used for his experiments, noting “shoulders” at the roughness switches (Figure 74). While Vermaas did not use normal flow conditions, it seems reasonable to assume a similar effect in the research described herein. With different water depths at the two cross-sections, continuity requires different U_i values for CS2 and CS4 and this may explain discrepancy between the integrated and Q/A channel mean values.

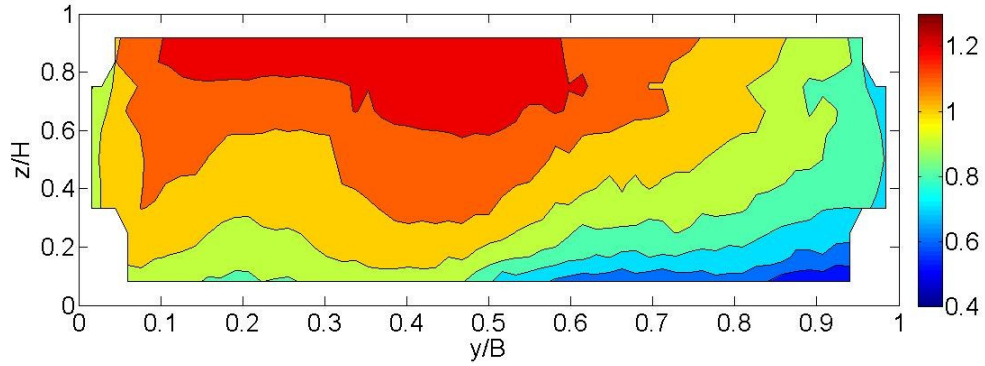

Figure 70: Relative U Distribution $(U/U_{Q/A})$. (BC1 F1)

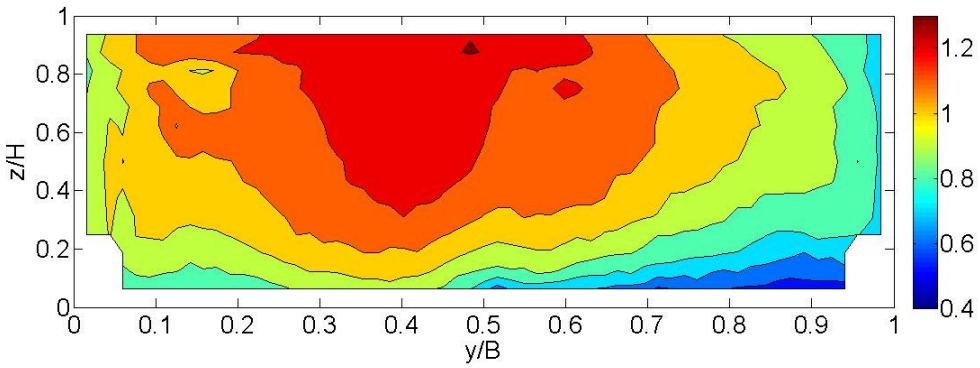

Figure 71: Relative U Distribution $(U/U_{Q/A})$ (BC1 F2)

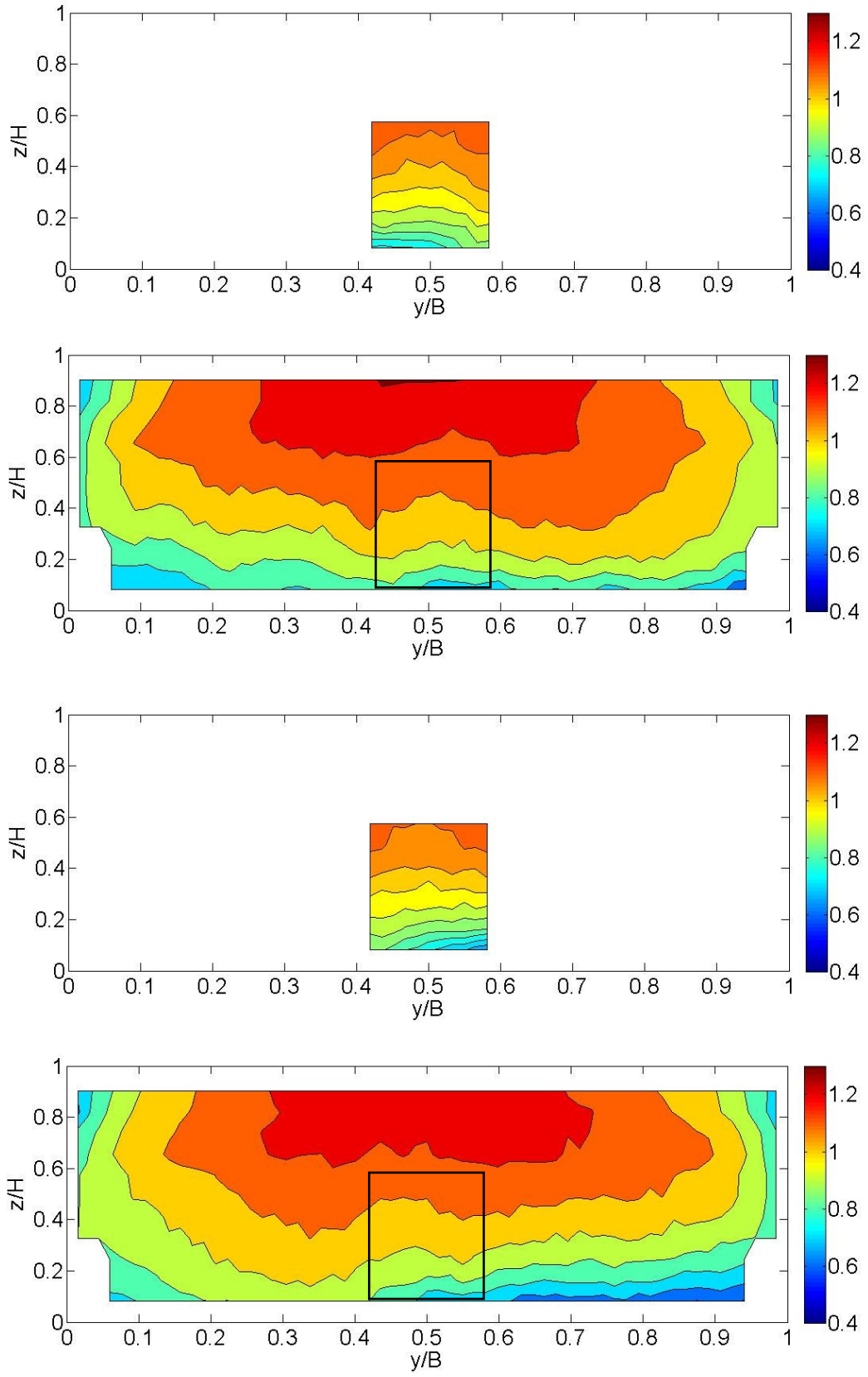

Figure 72: Relative U Distribution $\left(U/U_{Q/A}\right)$. CS1 (top) to CS4 (bottom). CS2 and CS4 include Pitot-static measurements. The rectangle marked on CS2 and CS4 indicates position of the CS1 and CS3 measurements (BC2 F1)

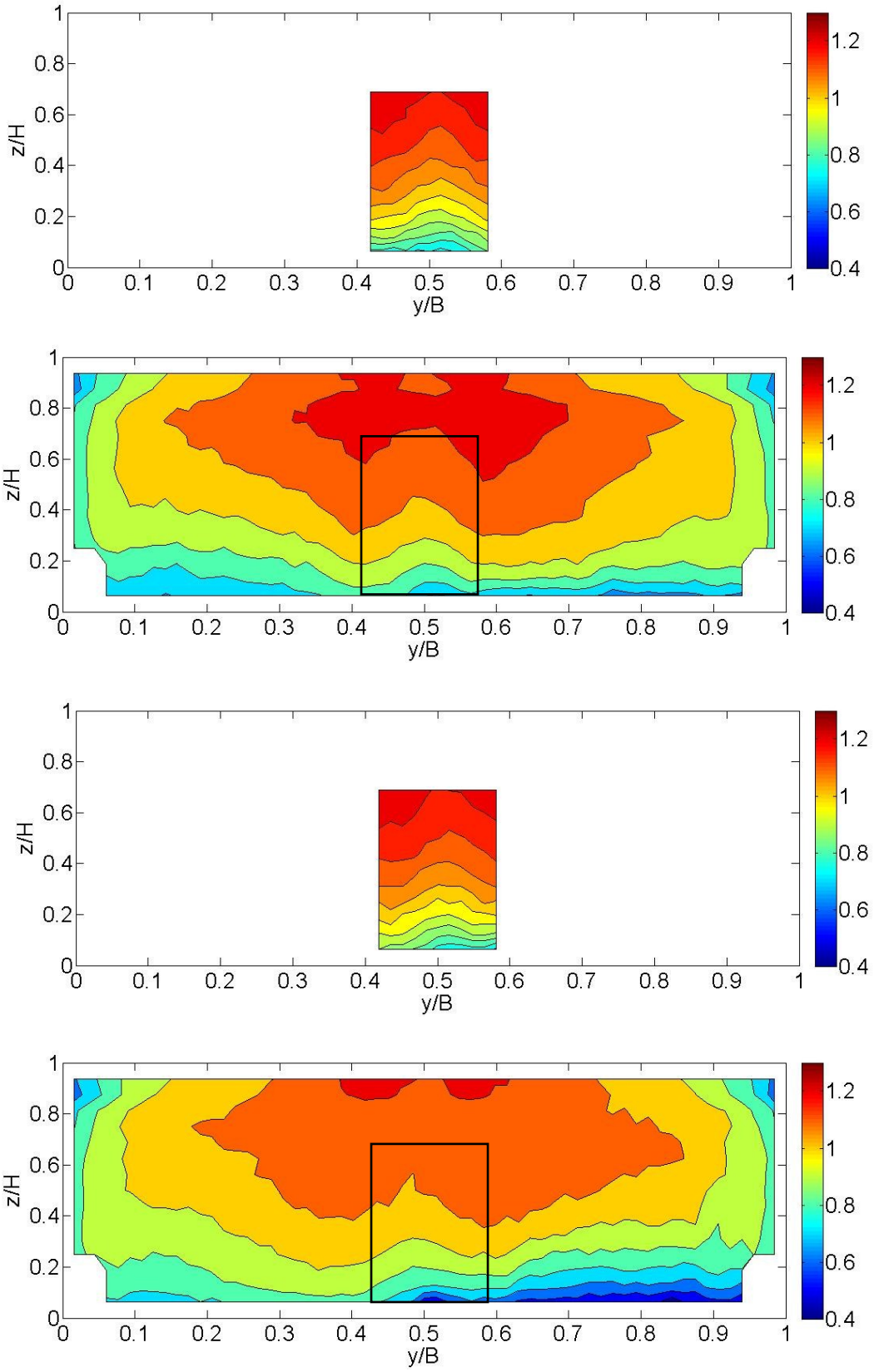

Figure 73: Relative U Distribution $\left(U/U_{Q/A}\right)$. CS1 (top) to CS5 (bottom). CS2 and CS4 include Pitot-static measurements. The rectangle marked on CS2 and CS4 indicates position of the CS1, CS3 and CS5 measurements (BC2 F2)

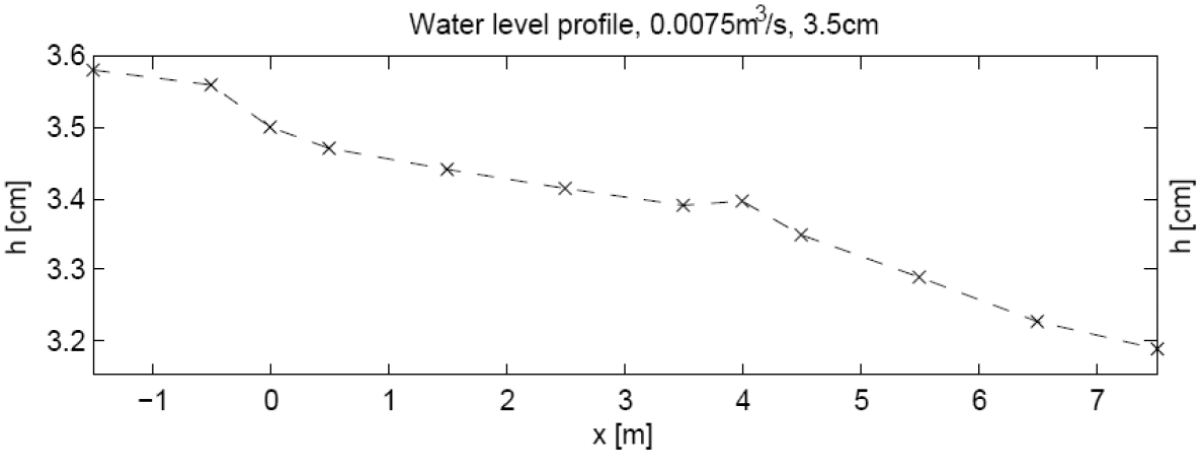

Figure 74: Water Surface Slope Over a Checkerboard Bed (Roughness Switches at x = 0m and x= 4m) (Vermaas, 2009)

For BC1, the interaction of the two (rough and smooth side) flow regions may be inferred from the extension of the blue-coloured, slower moving flow from the rough side to the smooth side near the channel bed, and a similar incursion by the red-coloured, faster moving flow in the opposite direction nearer the water surface.

For BC2, the U distribution for CS2 is approximately symmetrical about the RSB, with slow flow across the whole width of the channel close to the bed. By CS4 there is a clear distinction between the rough and smooth sides, as for BC1. For BC2 F2 the features of the U distribution are generally as for BC2 F1. Differences are seen in the upper regions of the flow, however these occur where either the ADV was positioned horizontally (which would have a greater effect on the flow) or the Pitot-static tube was used, which may be the cause of these dissimilarites.

The vertical U distributions respond quickly to the change in bed roughness. From Figure 75 (a) it may be seen that near the bed U is lower at CS1 (the rough side before the roughness switch) but increases over the newly smooth bed and is approximately constant from CS2 onwards. Figure 75 (c) shows the opposite effect

on the newly rough side, with the flow near the bed decelerating as it leaves the smooth side. At the RSB (Figure 75 (b)) U remains constant over the whole length of the channel section.

The horizontal U_r distributions are shown in Figure 76 to Figure 81. These figures also include velocities calculated using the Pitot-static tube measurements. The distributions taken with the two measuring methods are consistent, with the same major features being shown in each, with the exception of BC1 F2. In this case (Figure 77) dips are seen in the ADV measurements for the $z/H = 0.81$ data at $y/B \cong 0.15$ and $y/B \cong 0.52$ which are not present in the Pitot-static measurements. There is no evidence for the localised dip at $y/B \cong 0.15$ in the lower levels of the flow, and this is thought to be due to interference from the fixed probe which was located upstream (the experimental method was changed to prevent this occurring for subsequent data sets). The central dip is seen in the other ADV measurements for BC1 F2, and in the BC2 data sets – its non-appearance in the Pitot-static data can be attributed to experimental error (see Figure 82, in which error bars are included for the Pitot-static measurements).

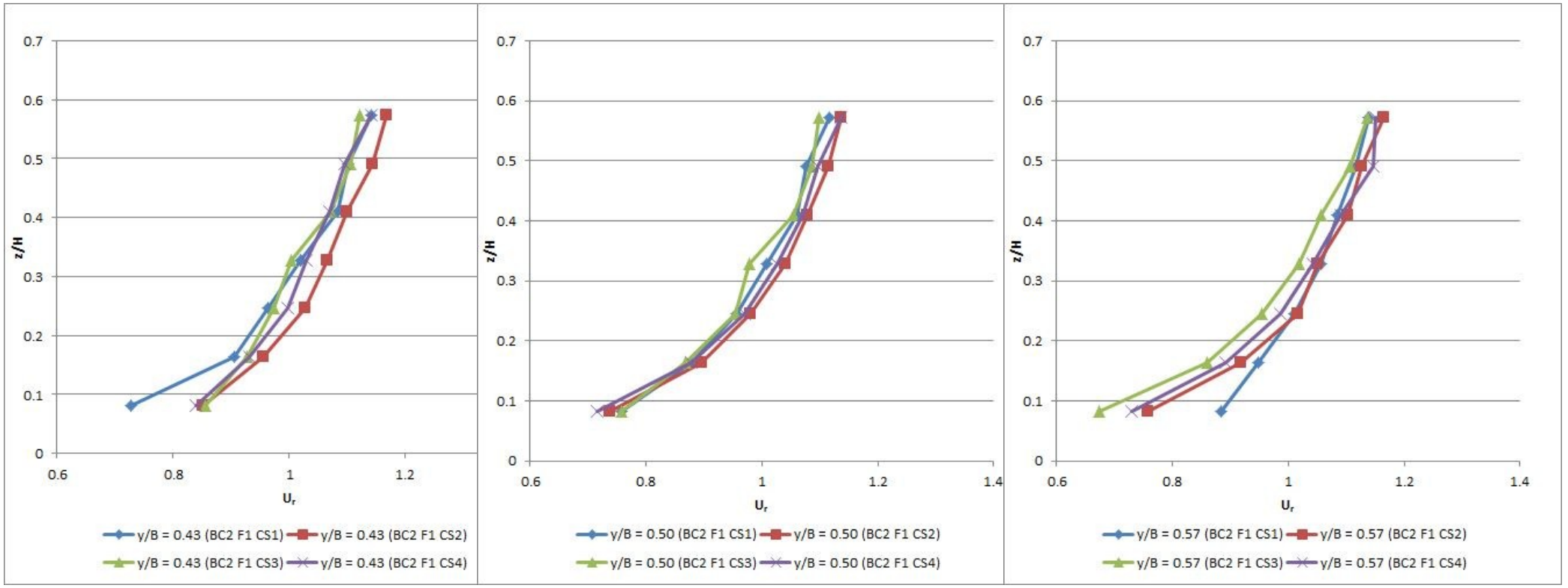

Figure 75: Flow Development Near the RSB after the Roughness Switch. (a) Smooth side (left); (b) RSB (centre); (c) Rough side (right) (BC2 F1)

For BC2 it is evident that the bed is only having a significant effect in the lower half of the flow. By CS2, U at $z/H = 0.08$ is already greater on the newly smooth side of the bed $(0 \leq y/B < 0.5)$ than on the newly rough side, while at $z/H = 0.25$ the highest U is still over the rough side. By CS4 the region of greater U at $z/H = 0.25$ has switched to the smooth side. The upper regions of the flow $(z/H > 0.50)$ show little difference, indicating that this region of the flow is little affected by the channel bed over the length of one of the channel sections. This is in contrast to BC1, showing that full-length strip roughness is not adequate to model a natural river.

For all data sets, a dip in U is seen at $y/B \cong 0.51$, i.e. just on the rough side of the RSB. For BC1 it was initially thought that this was a manifestation of the particular bed profile at the cross-section. However, this dip is also seen in the two cross-sections measured for BC2 and was noted by Vermaas (2009).

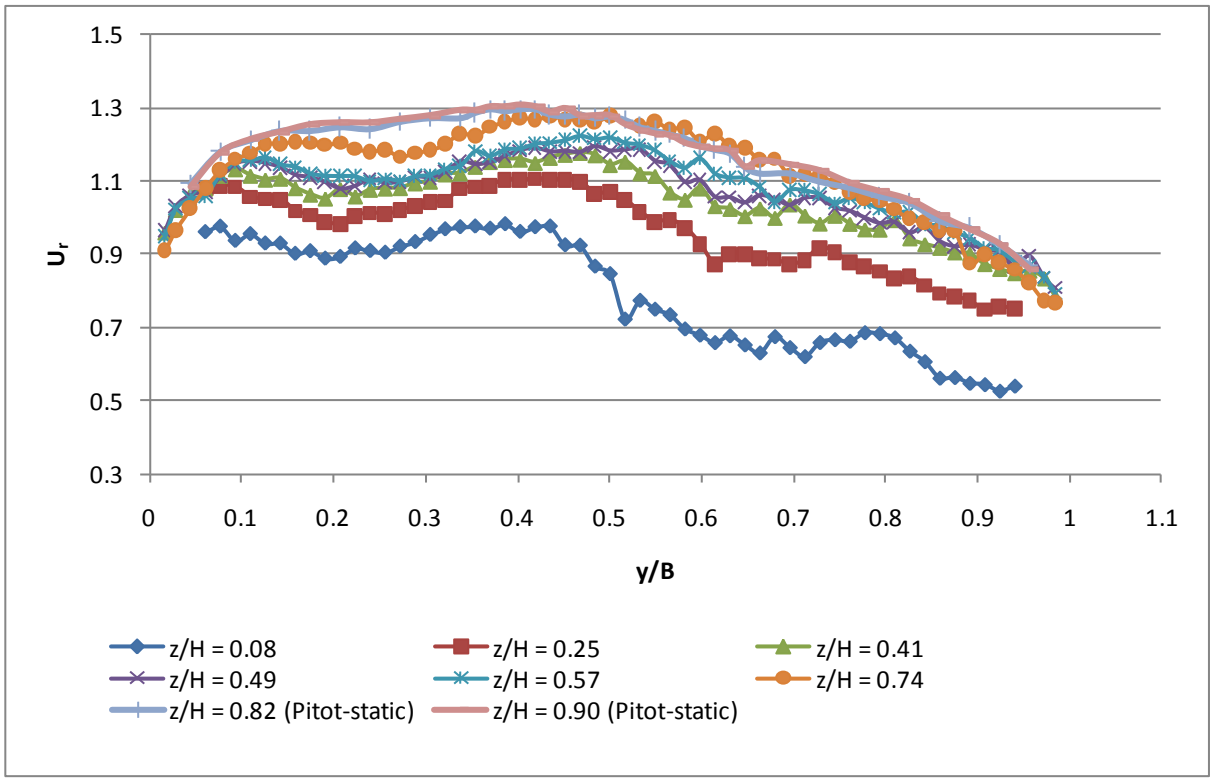

Figure 76: Horizontal Distribution of Relative U (from ADV measurements except at bed) (BC1 F1)

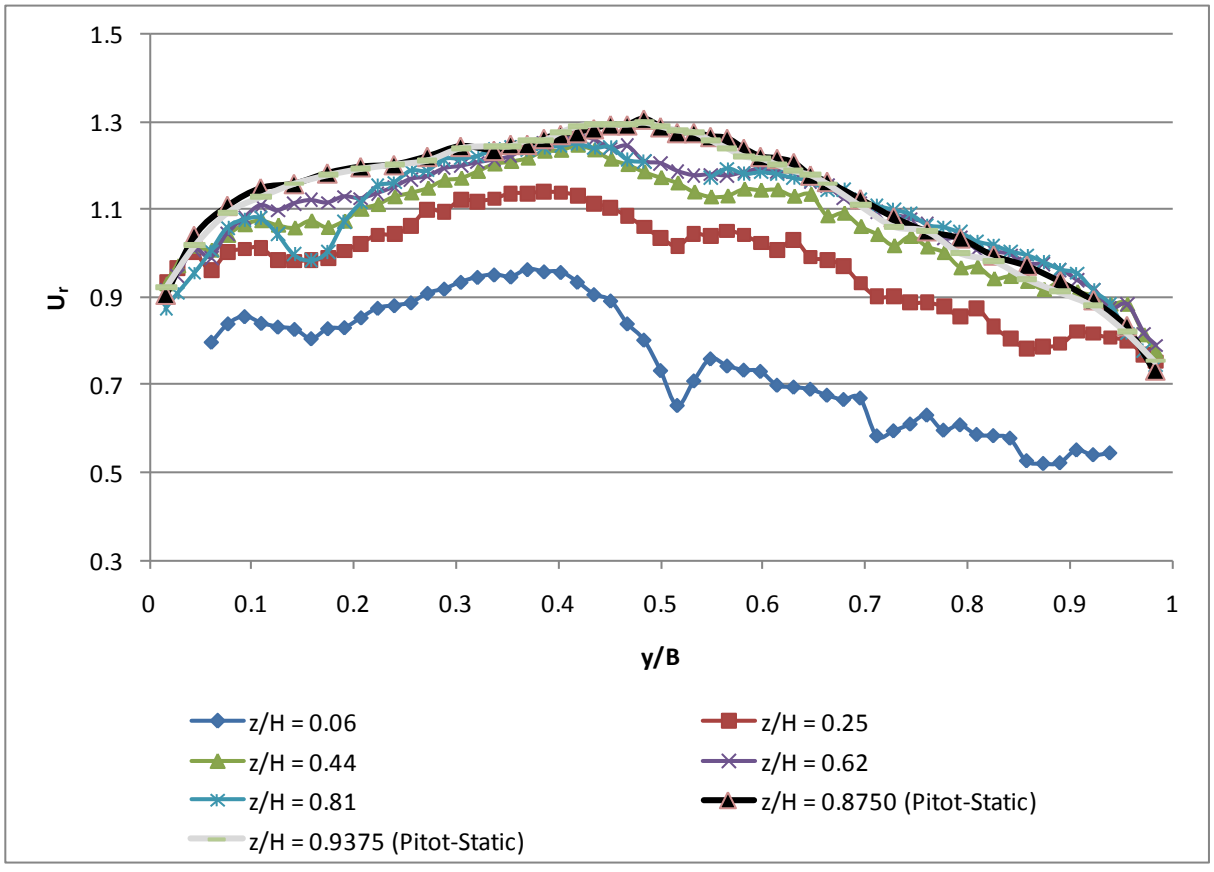

Figure 77: Horizontal Distribution of Relative U (from ADV measurements except at bed) (BC1 F2)

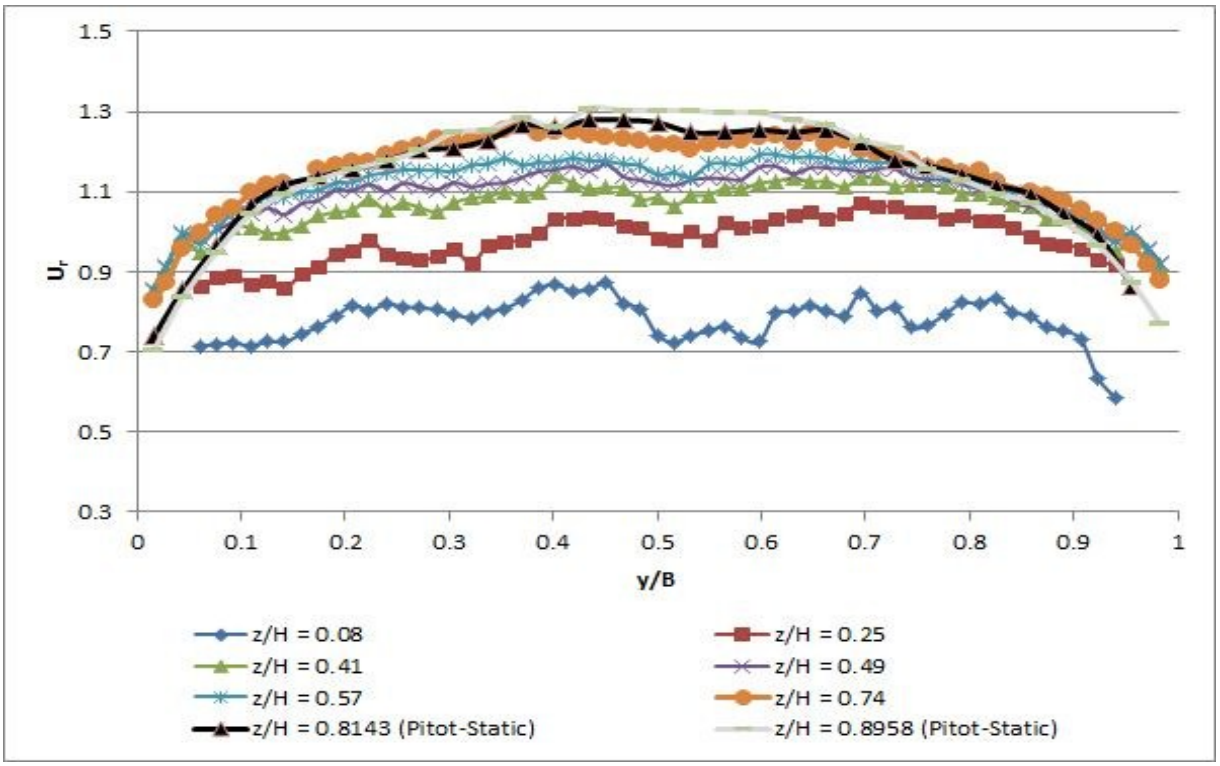

Figure 78: Horizontal Distribution of Relative U (from ADV measurements except as marked) (BC2 F1 CS2)

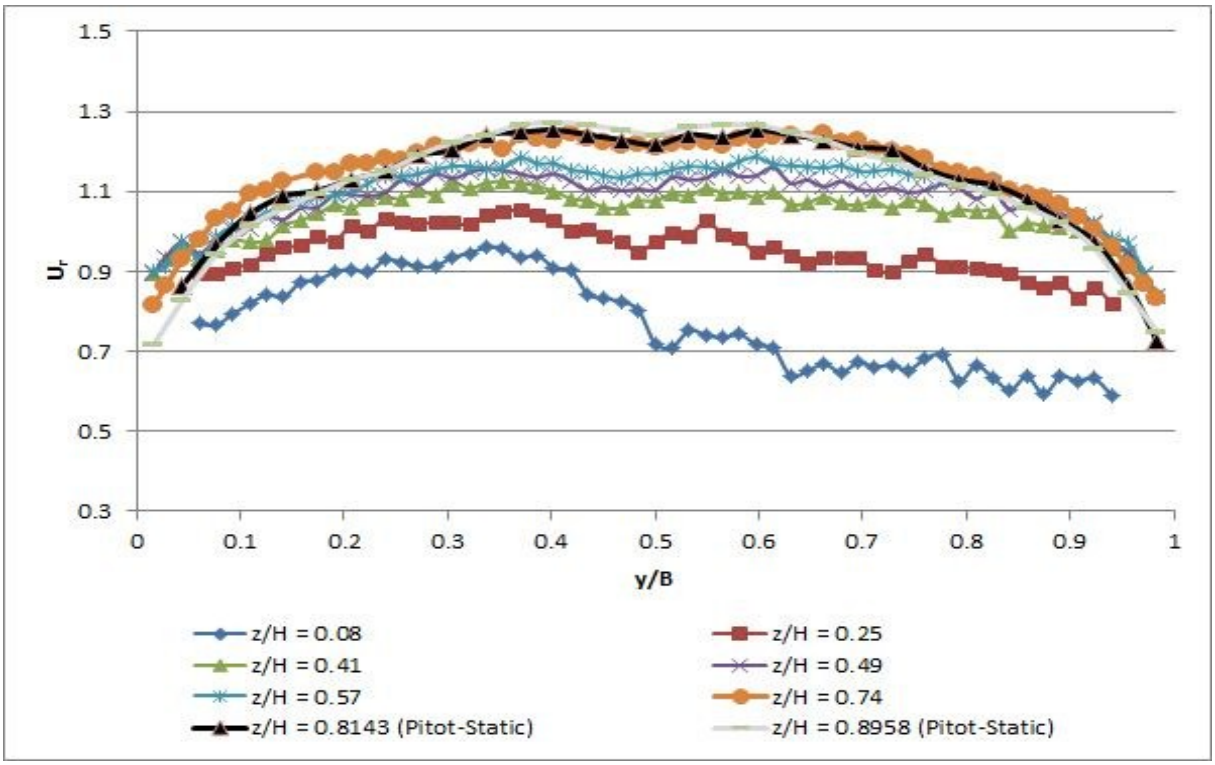

Figure 79: Horizontal Distribution of Relative U (from ADV measurements except as marked) (BC2 F1 CS4)

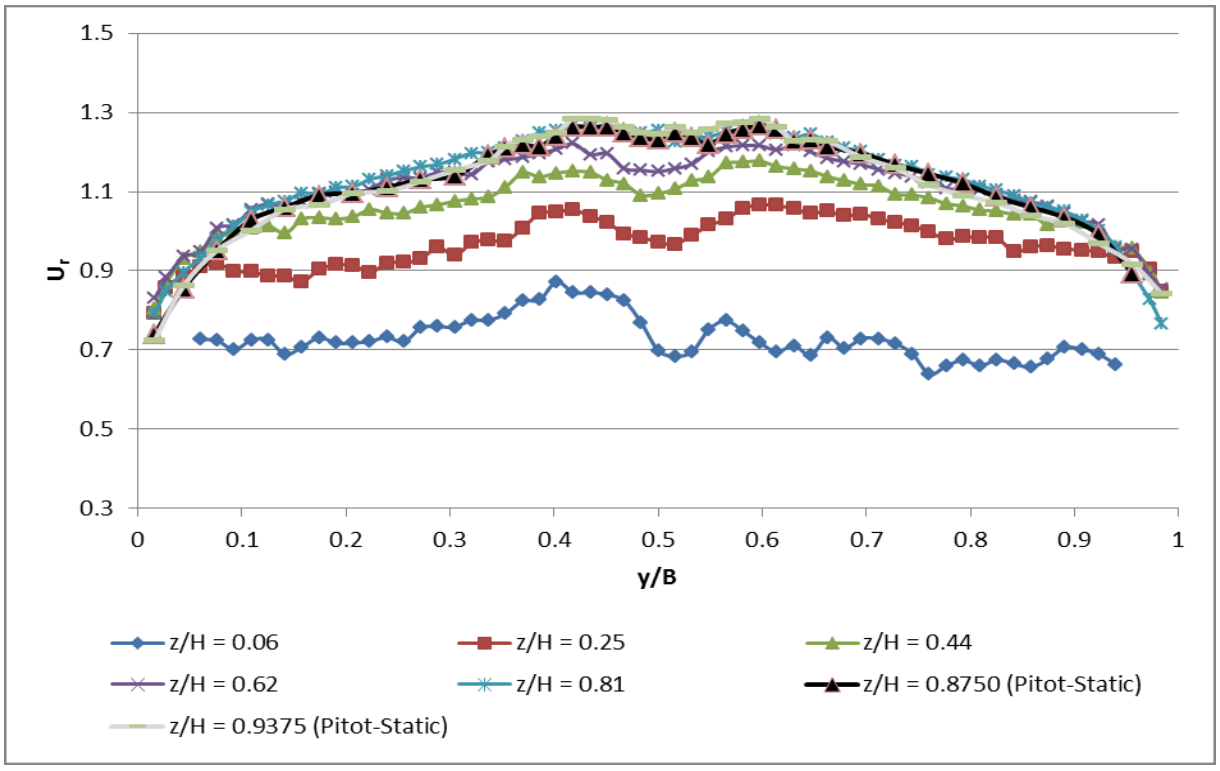

Figure 80: Horizontal Distribution of Relative U (from ADV measurements except as marked) (BC2 F2 CS2)

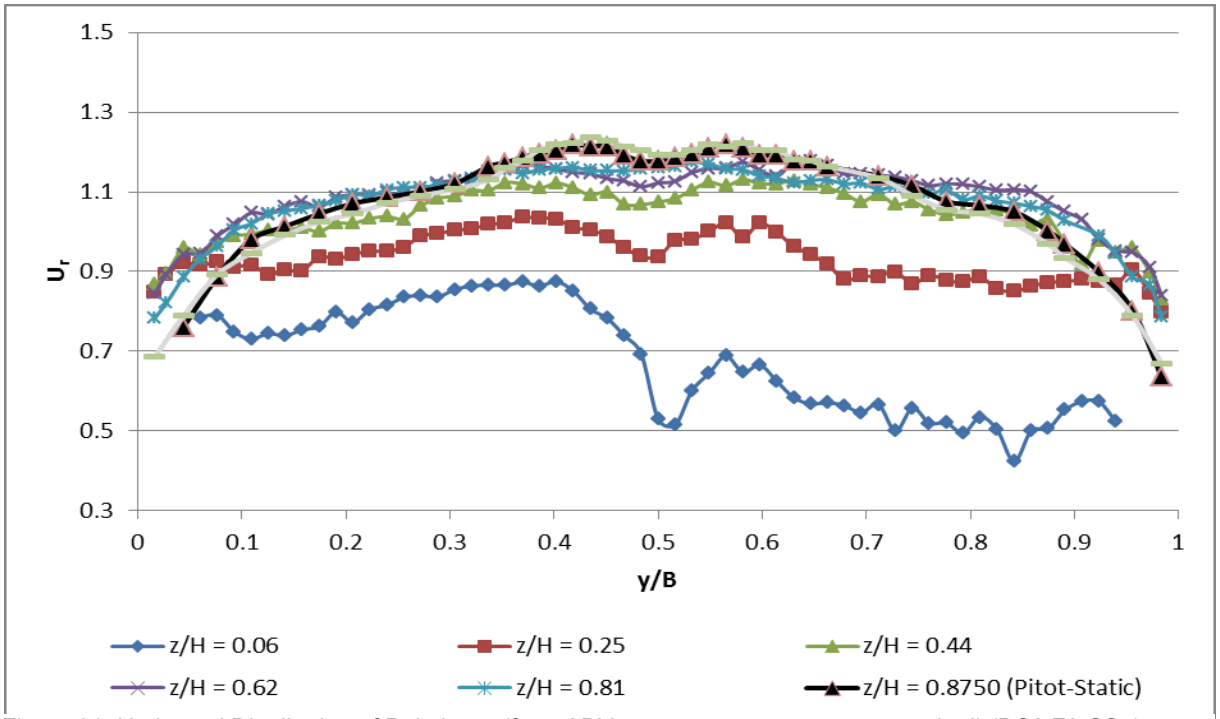

Figure 81: Horizontal Distribution of Relative U (from ADV measurements except as marked) (BC2 F2 CS4)

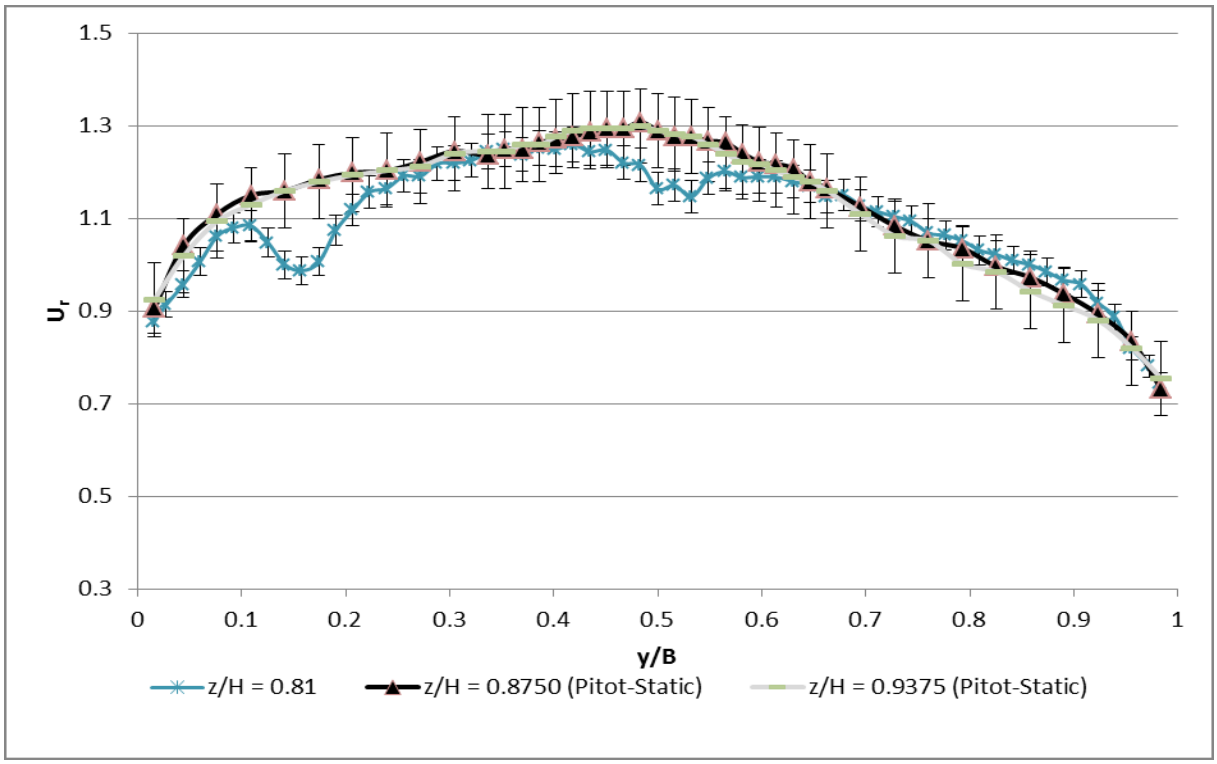

Figure 82: Comparison of the Upper Level ADV and Pitot-Static U measurements (BC1 F2)

Although the log-law of the wall is only truly applicable for the region $z/H < 0.2$ (see Section 3.5.1; outside this range a wake function correction should be applied) it has been assumed valid for practical applications with adjustments to the constants (Nezu and Nakagawa, 1993). The log-law may be re-written as:

$$U = Cln(z) + D \tag{75}$$

where C and D are constants which include all constants in the equation, such as the von Karman constant and the shear velocity. This range extension approximation is useful in the analysis of the experimental data due to the small number of points lying with the $z/H < 0.2$ region. Logarithmic plots of vertical U distributions at the primary sections (Figure 83 to Figure 88, which include 3% error bars on the U values) show that the distributions are approximately logarithmic. In the upper regions of BC1 F2 there is divergence from the logarithmic profile, though this would be anticipated due to the neglecting of the wake function. BC2 F2 CS4 shows more scatter, particularly at the RSB, but even in this case the logarithmic approximation appears to hold.

The BC2 CS2 primary section velocity distributions collapse onto one another for both F1 and F2, while by CS4 the BC2 distributions are similar to those seen for BC1. Estimation of the log-law constants, C and D, through curve fitting gives the values shown in Table 13. D may be seen to be approximately constant for all data sets – as this defines the $U(z = 0)$ value this would be expected as $U(0) = 0$. Inspection of the C values shows that the RSB velocity distribution remains approximately constant along the BC2 channel section, and is consistent with that seen for BC1. Interestingly, for BC2 the smooth and rough sides appear to have opposing effects on the flow – on the smooth side, the flow “corrects” to the BC1

distribution, while on the rough side C increases from the BC1 smooth value, exceeding the BC1 rough value. Physically, this shows that the effects of the newly rough bed are localised within the near-bed flow, with the vertical velocity gradient increasing along the channel section as the flow near the bed slows due to the roughness while the surface flow maintains its velocity.

Data Set	$y/B = 0.26$		$y/B = 0.50$		$y/B = 0.74$	
	C	D	C	D	C	D
BC1 F1	0.13	1.2	0.20	1.3	0.20	1.2
BC1 F2	0.12	1.2	0.19	1.3	0.20	1.2
BC2 F1 CS2	0.20	1.3	0.21	1.3	0.19	1.3
BC2 F1 CS4	0.12	1.2	0.22	1.3	0.25	1.3
BC2 F2 CS2	0.18	1.2	0.21	1.3	0.18	1.2
BC2 F2 CS4	0.12	1.1	0.23	1.2	0.25	1.2

Table 13: Log-law Constants for the Primary Sections

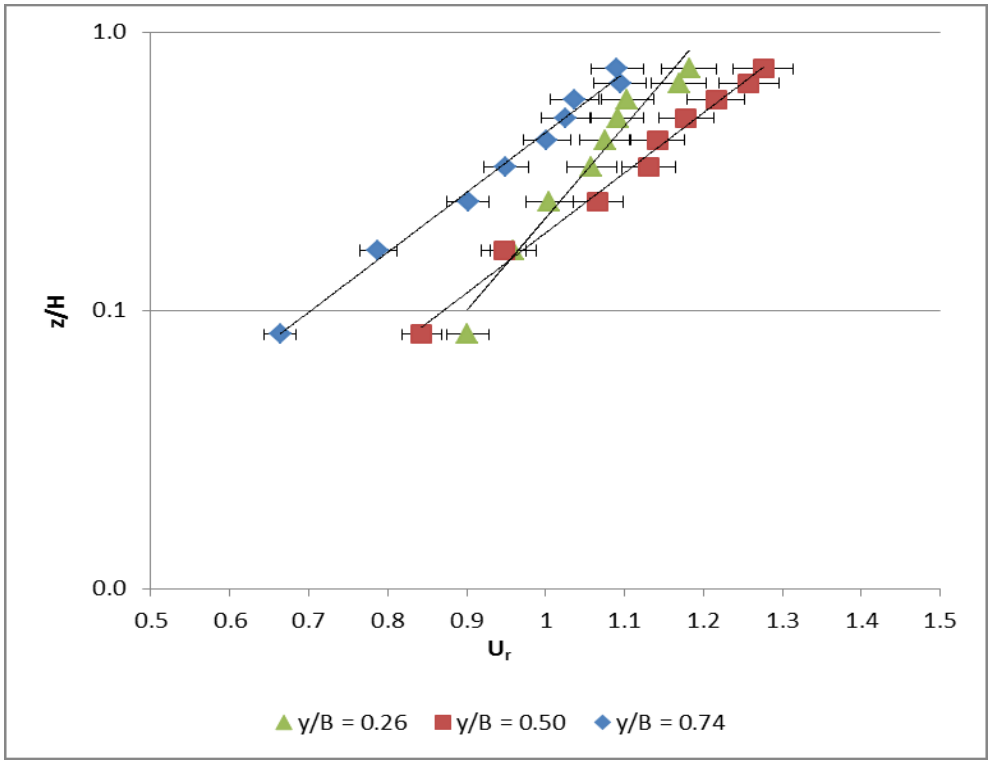

Figure 83: Vertical Ur Distribution at the Primary Sections (BC1 F1)

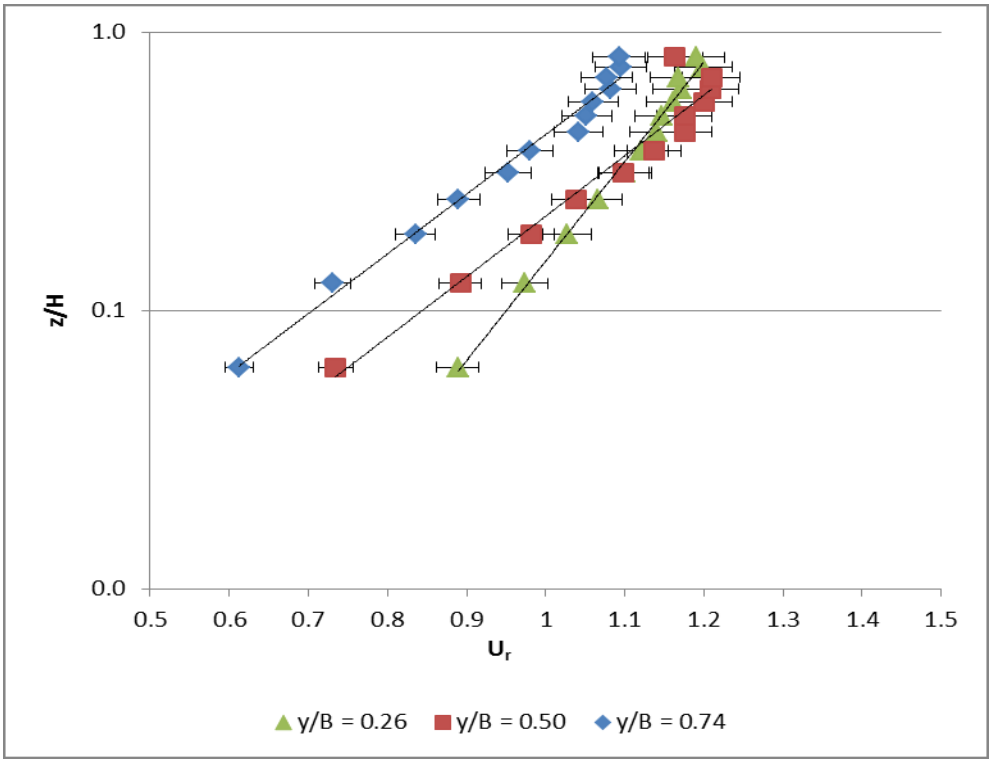

Figure 84: Vertical Ur Distribution at the Primary Sections (BC1 F2)

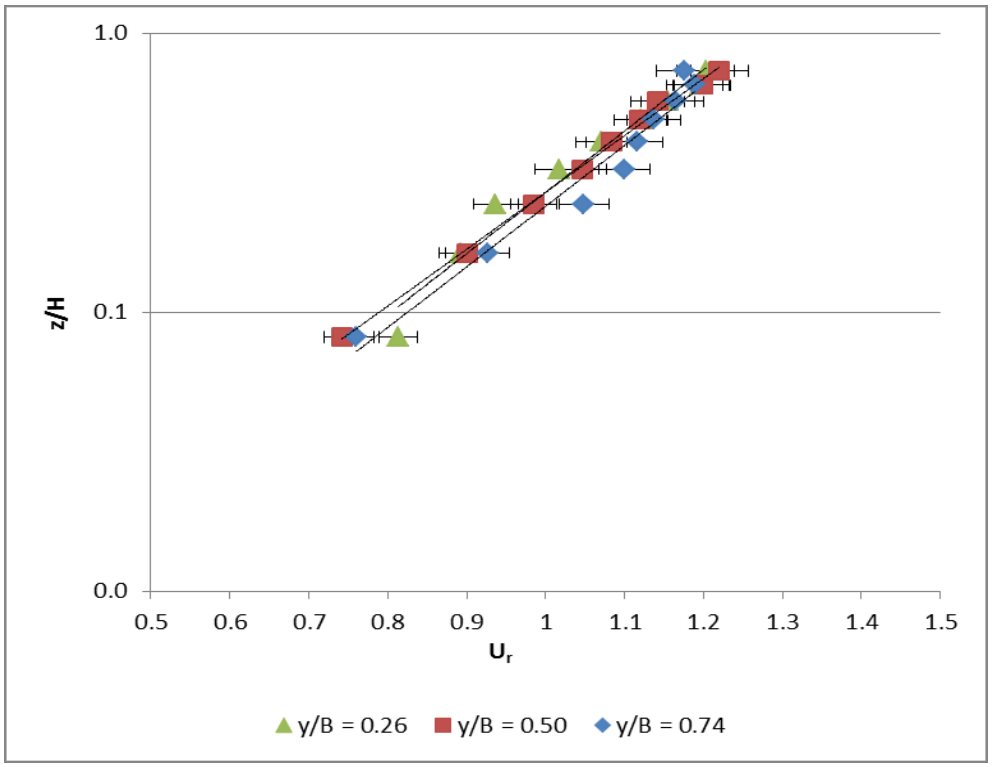

Figure 85: Vertical Ur Distribution at the Primary Sections (BC2 F1 CS2)

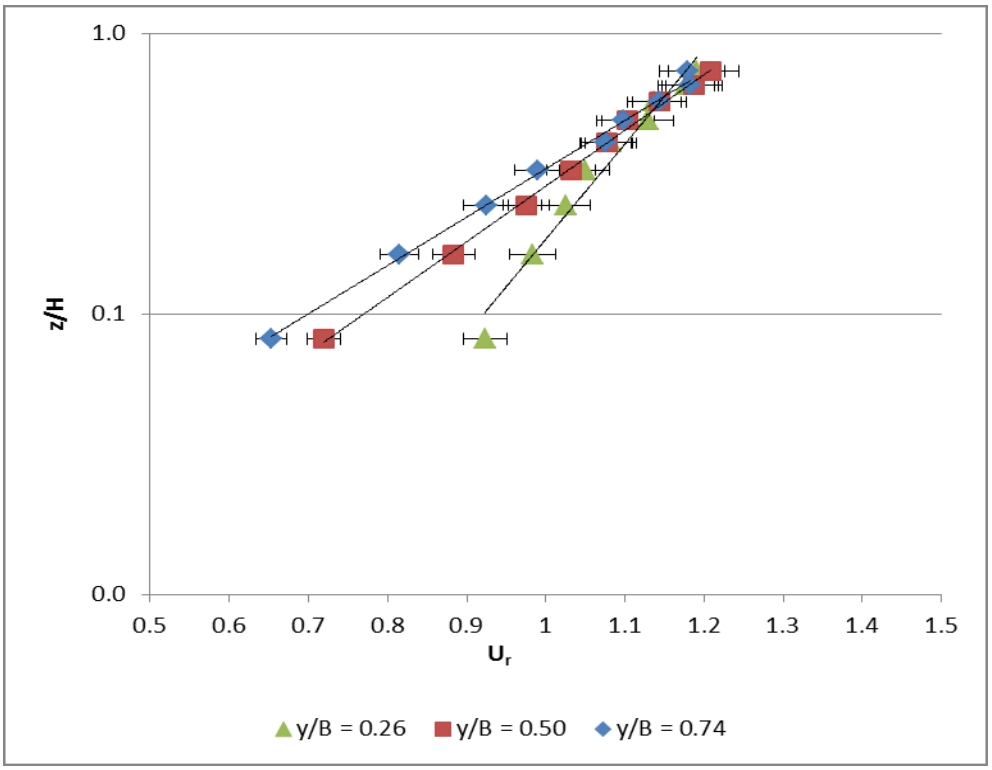

Figure 86: Vertical Ur Distribution at the Primary Sections (BC2 F1 CS4)

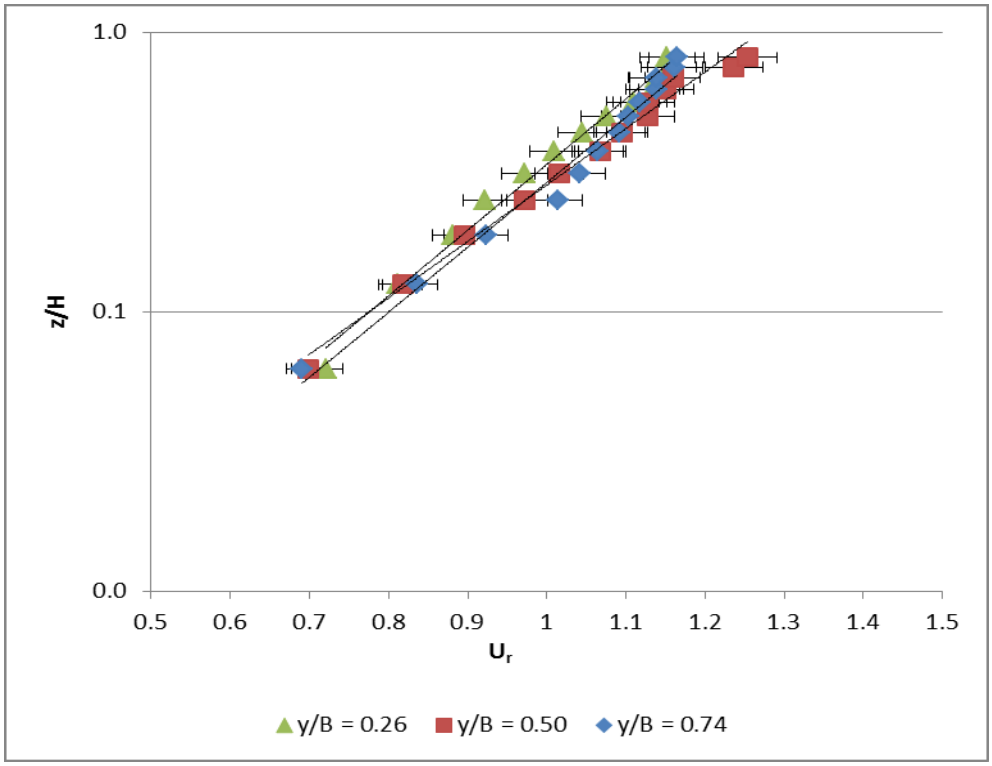

Figure 87: Vertical Ur Distribution at the Primary Sections (BC2 F2 CS2)

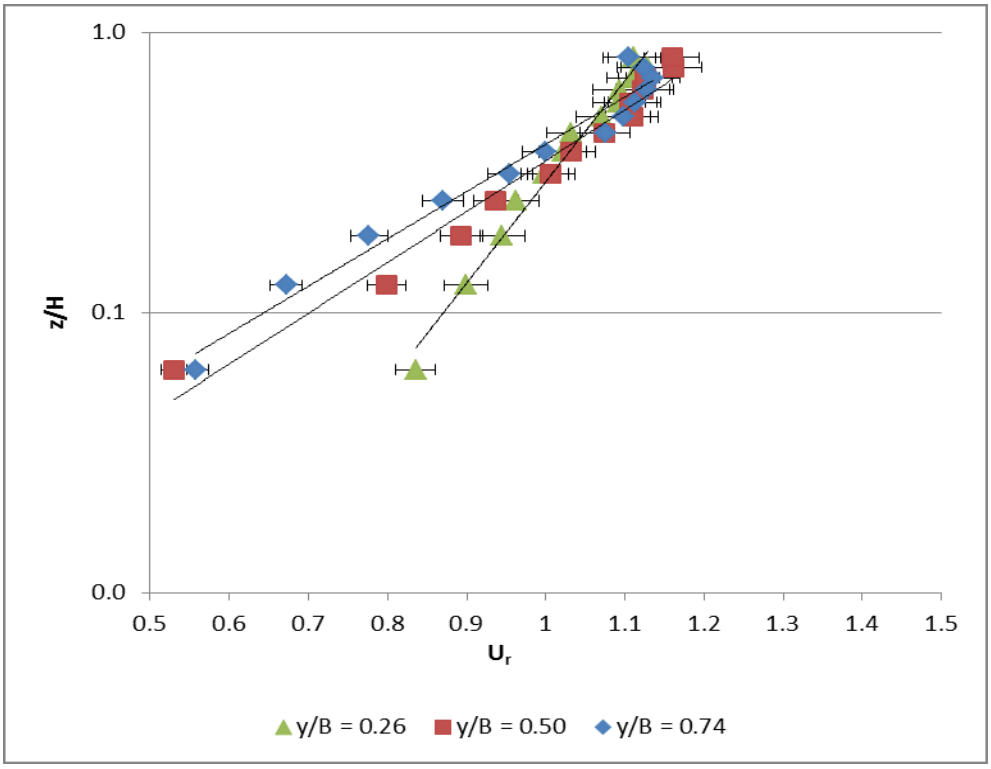

Figure 88: Vertical Ur Distribution at the Primary Sections (BC2 F2 CS4)

8.4.2 Lateral Velocities

Transverse and vertical point-mean velocities, V and W, were calculated at each point and combined to produce lateral velocity vectors (Figure 89 to Figure 92). The integrated channel means of these velocities were found to be close to zero, with RMS values of less than 3% of U_i for all data sets (generally less than 1%), as shown in Table 14.

Data Set	$V_i\ (\times 10^{-3})$	$V_{rms}\ (\times 10^{-3})$	$W_i\ (\times 10^{-3})$	$W_{rms}\ (\times 10^{-3})$
BC1 F1	0.5	8.3 (2%)	1.7	17 (3%)
BC1 F2	0.6	5.5 (1%)	1.3	5.3 (1%)
BC2 F1 CS2	0.6	4.2 (1%)	0.09	3.3 (1%)
BC2 F1 CS4	0.3	3.9 (1%)	0.25	2.8 (1%)
BC2 F2 CS2	0.6	4.6 (1%)	1.9	6.7 (1%)
BC2 F2 CS4	0.6	5.2 (1%)	0.2	5.3 (1%)

Table 14: Lateral Velocity Magnitudes and RMS Values

These mean values are as would be expected by conservation of mass considerations and are consistent with the literature (for example, (Nezu et al., 1993)).

For BC1, the lateral velocity vectors show two secondary flow cells on the smooth side of the channel for both flows. However, there are marked differences – for F1 the central flow cell extends over the RSB, while for F2 a third cell is evident over the RSB. Notwithstanding this, the position and direction of these cells, in relation to the rough and smooth regions, matches those seen by both Wang and Cheng (2006) and Vermaas (2009), with downflow occurring over the rough bed and upflow over the smooth. The clockwise central cells contribute to a transfer of slower water near

the bed moving from the rough side to the smooth, and a corresponding transfer of faster water in the opposite direction at $z/H = 0.5$. Comparison of Figure 70 and Figure 89 shows that the position of these cells coincides with a distortion of the streamwise isovels, an effect noted previously by Nezu et al. (1993), while there is evidence of similar (though less distinct) contour bulges for F2 (at $y/B \cong 0.15$; Figure 71), coinciding with the secondary flow cells shown in Figure 90

F2 shows two other secondary flows cells not evident in F1 – the first lies on the smooth side of the RSB, and its existence in F1 was suggested by continuity; the second is a corner flow cell at $y/B \cong 0.90$.

For BC2, examination of the lateral velocities (Figure 91) shows an asymmetrical distribution for CS2, unlike the U distribution. A region of strong upflow exists at the lower levels on the rough side of the RSB. This appears in the CS1 measurements, taken at the point of the bed change.

By CS3, at the streamwise centre of the section, the lateral velocities are of low magnitude, though there is some evidence of the upflow having been replaced by downflow. By CS4 there is clear downflow on the rough side of the RSB and upflow on the smooth side, matching the secondary flow cells seen for BC1. Assuming that the flow pattern at the end of the section is the mirror of CS1, the strong upflow at the bed change may be seen as an exaggeration of the existing secondary flow cell.

The bulges in the U contours are consistent with the lateral velocities vectors. In the case of F2 CS3, in which the lateral velocities form no distinct pattern near the bed but are consistently upward for upper measurements, there is no bulge evident near the bed but a distinct one coinciding with the upflow.

Bearing in mind the low velocities being measured, and the somewhat subjective nature of examining the lateral flows, the development of lateral velocities is consistent between BC2 F1 and BC2 F2. In the latter case, there is stronger downward flow on the smooth side of the RSB for CS1 and CS2. This is similar to the BC1 case, where central secondary flow cells were better defined for F2 than F1.

The strong, upper-level upflow seen in BC2 CS2 and BC2 CS3 is not seen for BC2 CS4. However, from comparison with BC1 and noting the position of the cells developing in BC2, it may be that these upper layers are (in terms of secondary flows and the rotation correction procedure) independent of the lower flow. Since these regions are 'incomplete' in the sense that there are no ADV measurements for the near-surface region, they may affect the zero velocity assumptions of the rotation correction. To test for this the BC2 F2 CS2 rotation correction was applied to a subset of the data, excluding the upper two layers – the lateral velocities seen in the lower regions were negligibly different, showing that the results are reliable for the lower half of the flow.

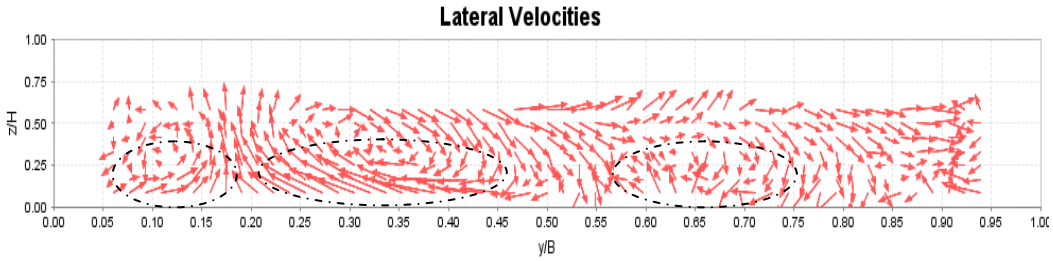

Figure 89: Lateral Velocity Distribution (BC1 F1)

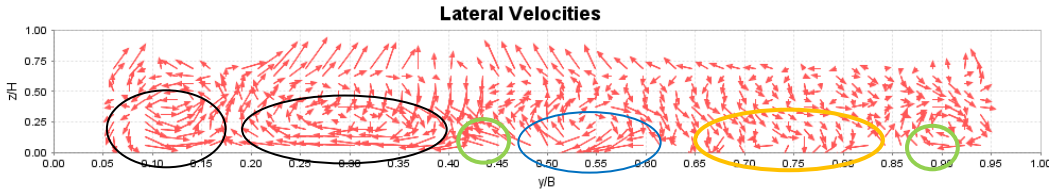

Figure 90: Lateral Velocity Distribution (BC1 F2)

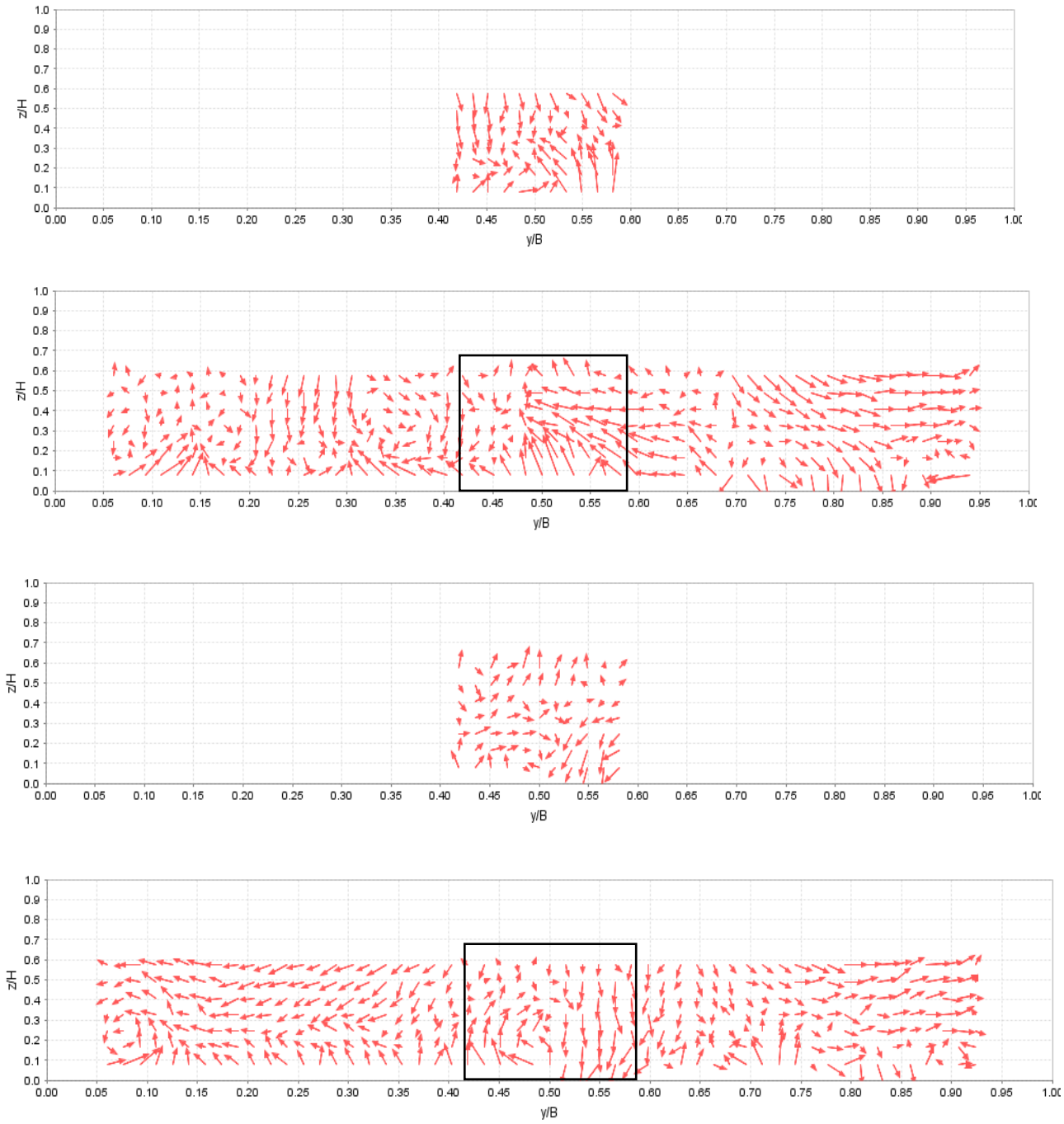

Figure 91: Lateral Velocity Vectors. CS1 (top) to CS4 (bottom). The rectangle marked on CS2 and CS4 indicates position of the CS1 and CS3 measurements (BC2 F1)

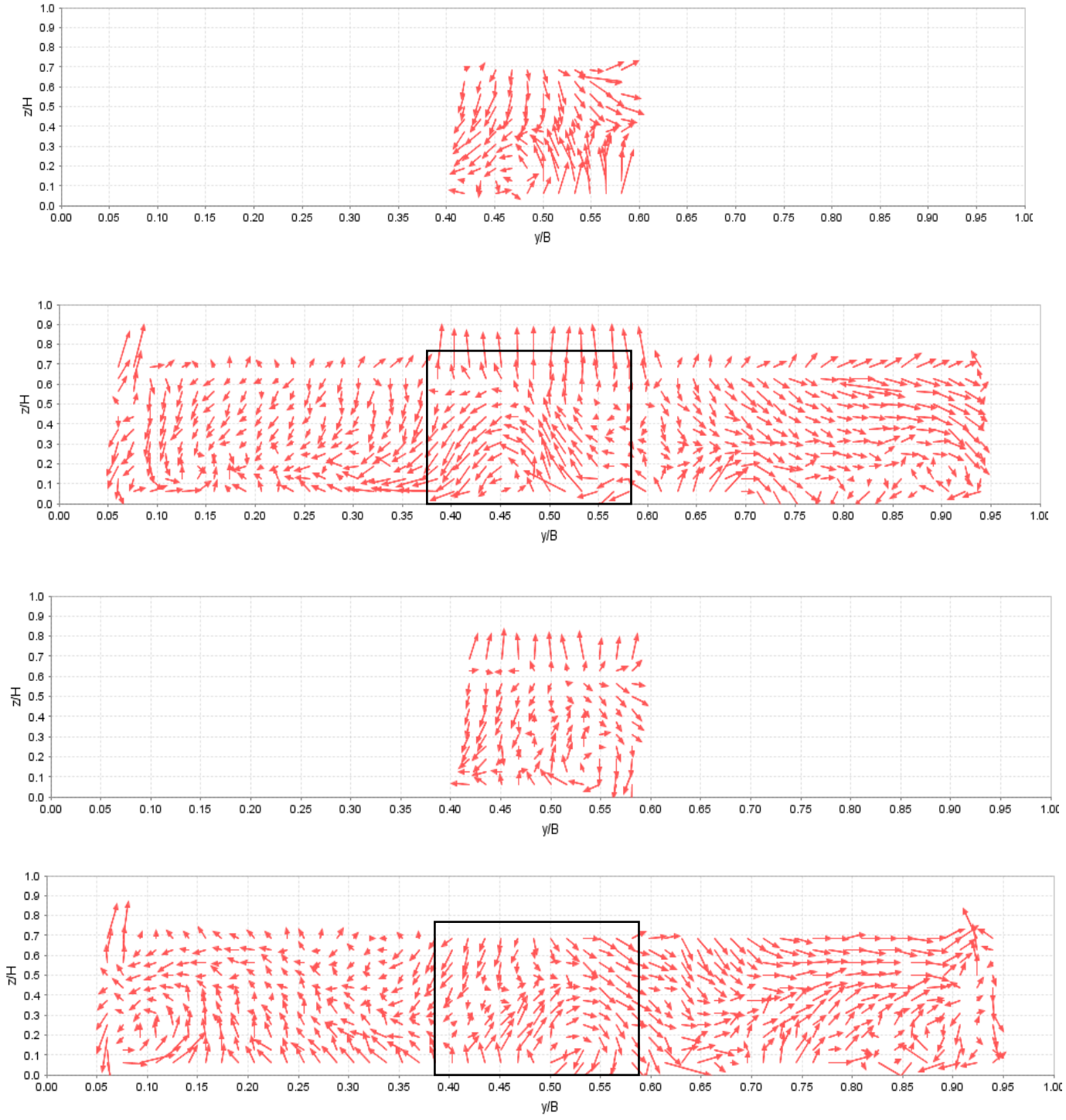

Figure 92: Lateral Velocity Vectors. CS1 (top) to CS4 (bottom). The rectangle marked on CS2 and CS4 indicates position of the CS1 and CS3 measurements (BC2 F2)

8.4.3 Reynolds Stress Distributions

In the following discussion of the vertical and horizontal Reynolds stresses (τ_V^R and τ_H^R respectively) the results are presented in a dimensionless form by scaling with the channel-mean boundary shear stress, $\overline{\tau_b} \equiv \rho g R S_0$. Thus, for example, $(\tau_V^R)_{nd} \equiv -\rho\overline{u'w'}/\overline{\tau_b}$. The estimation of $\overline{\tau_b}$ is presented in Section 9.1. The mean boundary shear stress and integrated channel mean Reynolds stresses are shown in Table 15:

Data Set	$\overline{\tau_b}$ (Nm^{-2})	$(-\rho\overline{u'w'})_i$ (Nm^{-2})	$(-\rho\overline{u'v'})_i$ (Nm^{-2})
BC1 F1	1.05	0.75	-0.29
BC1 F2	1.27	0.48	-0.23
BC2 F1 CS2	1.06	0.49	-0.10
BC2 F1 CS4	1.06	0.50	0.07
BC2 F2 CS2	1.27	0.61	-0.05
BC2 F2 CS4	1.27	0.59	0.04

Table 15: Estimated Mean Boundary Shear Stress and Integrated Mean Reynolds Stresses

The cross-sectional distributions of $(\tau_V^R)_{nd}$ are shown in Figure 93 to Figure 98. Figure 99 to Figure 104 show the mean vertical distribution over the rough and smooth sides of the channel. For both BC1 F1 and F2, smooth side $(\tau_V^R)_{nd}$ decreases with z except for the region $z/H < \sim 0.2$, where $(\tau_V^R)_{nd}$ is approximately constant (F1) or decreasing (F2) This range of z/H matches Nezu and Nakagawa's definition of the wall region, $z/H < (0.15 - 0.2)$ (Nezu and Nakagawa, 1993), the open-channel equivalent to the inner layer of the boundary region. In this region the τ_V^R decreases towards the channel bed as the viscous stress increases, with their sum remaining constant (Davidson, 2004), and so the "hook" in the F2 data matches the theory – it would be anticipated that, if it were possible to make them, τ_V^R measurement closer to

the bed would show this distribution more clearly for both F1 and F2. In contrast, rough side $(\tau_V^R)_{nd}$ decreases linearly with z, including the lowest measured points. This near-bed linearity appears to contradict the wall region discussion above. However, it should be noted that, while the top of the gravel on the rough side is nominally at the same height $(z \equiv 0)$ as the smooth bed, in the case of a rough bed the effective bed position lies somewhat below the top of the roughness elements (Salih Kirkgoz, 1989, Nezu and Nakagawa, 1993). Thus the inner region will be moved downwards and the wall region will start closer to the $z = 0$ datum, resulting in the “hook” being below the measured region of the flow.

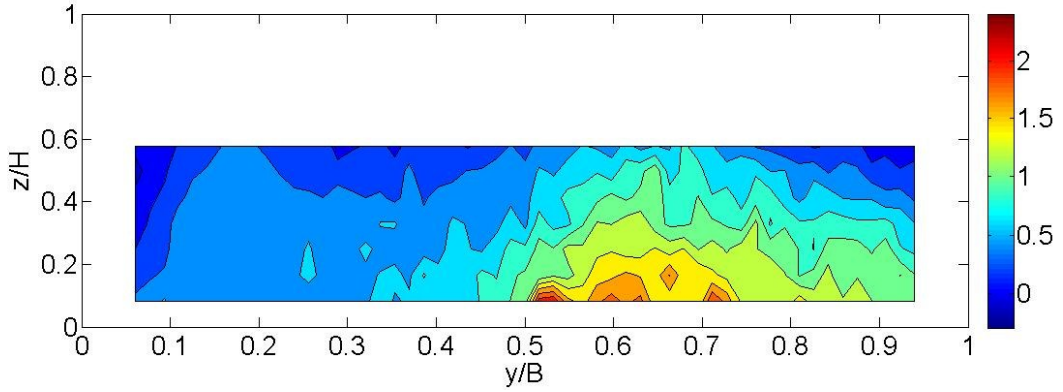

Figure 93: Dimensionless τ_V^R Distribution (BC1 F1)

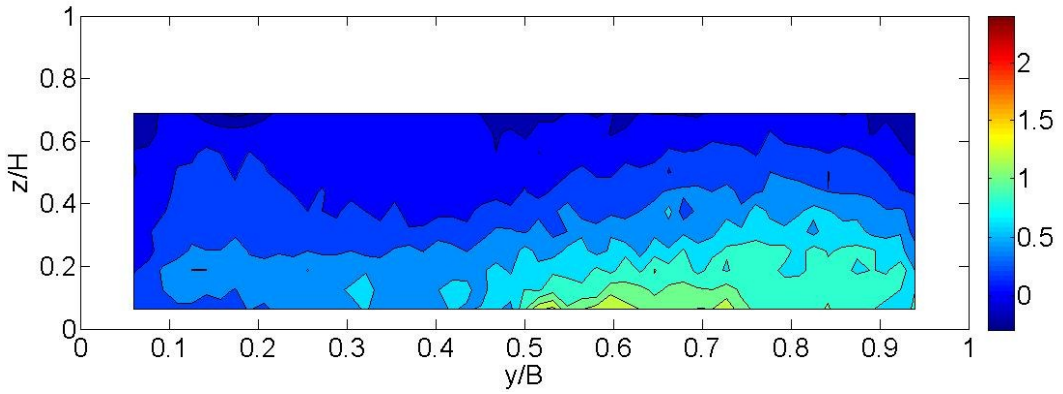

Figure 94: Dimensionless τ_V^R Distribution (BC1 F2)

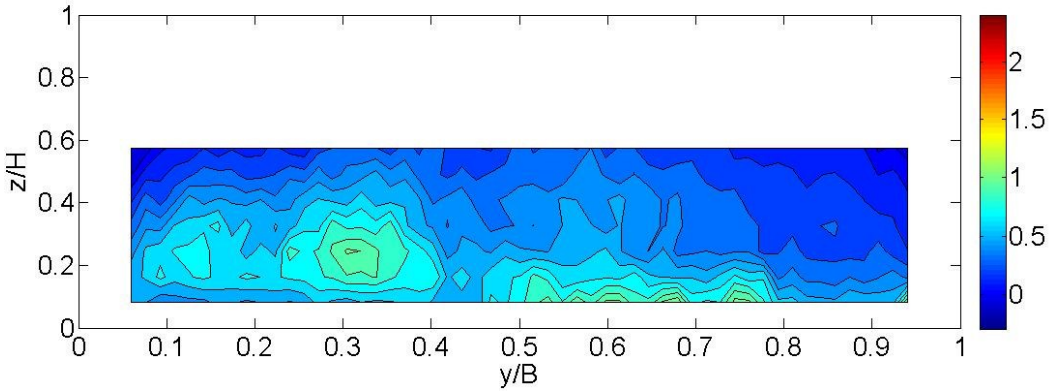

Figure 95: Dimensionless τ_V^R Distribution (BC2 F1 CS2)

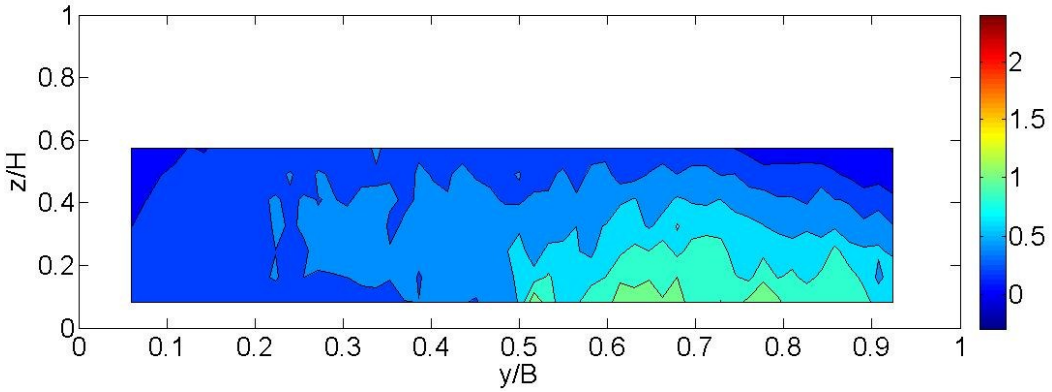

Figure 96: Dimensionless τ_V^R Distribution (BC2 F1 CS4)

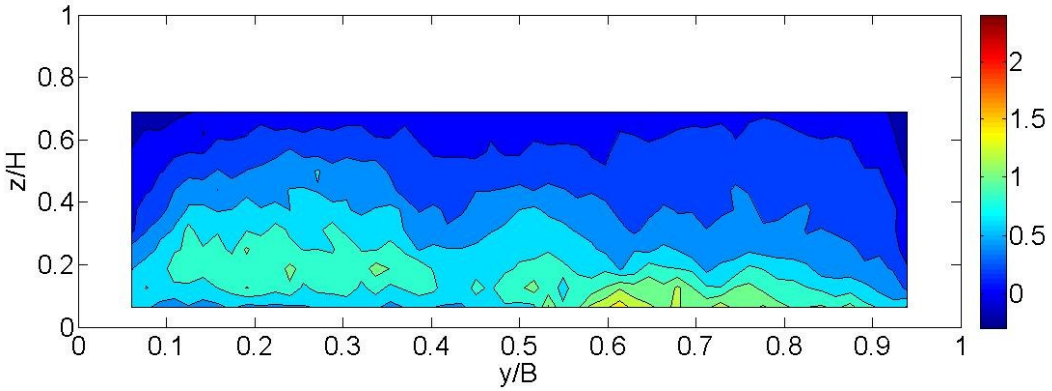

Figure 97: Dimensionless τ_V^R Distribution (BC2 F2 CS2)

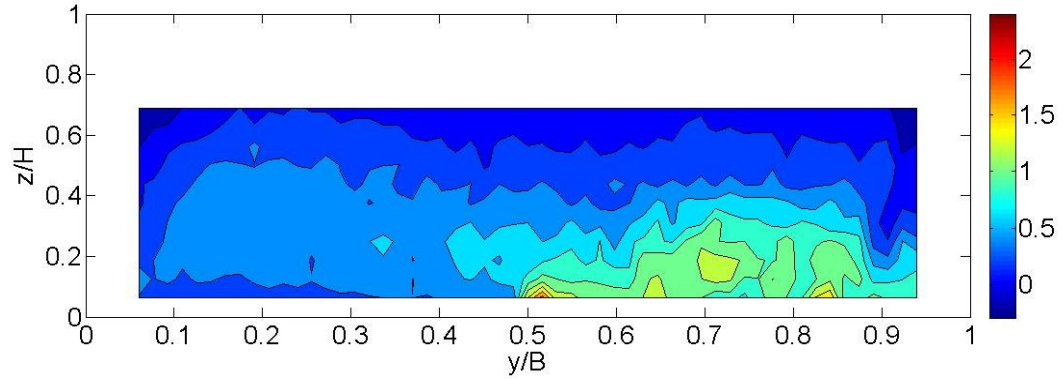

Figure 98: Dimensionless τ_V^R Distribution (BC2 F2 CS4)

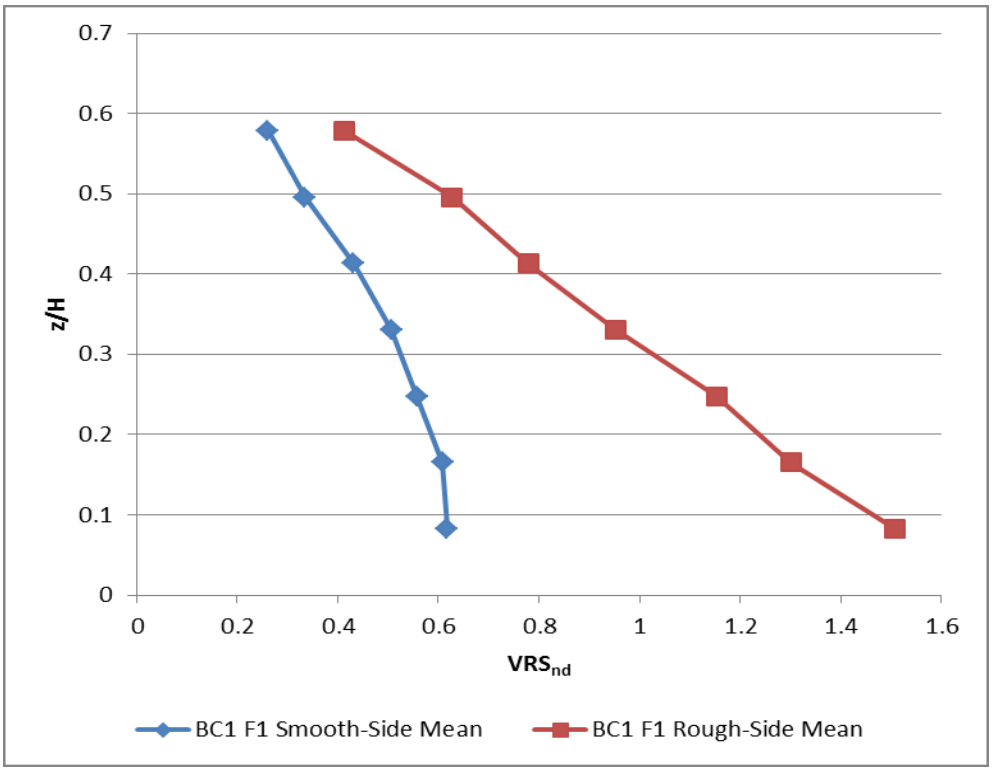

Figure 99: Mean Vertical Distribution of Relative τ_V^R (labelled VRS in Figure) by Channel Side (BC1 F1)

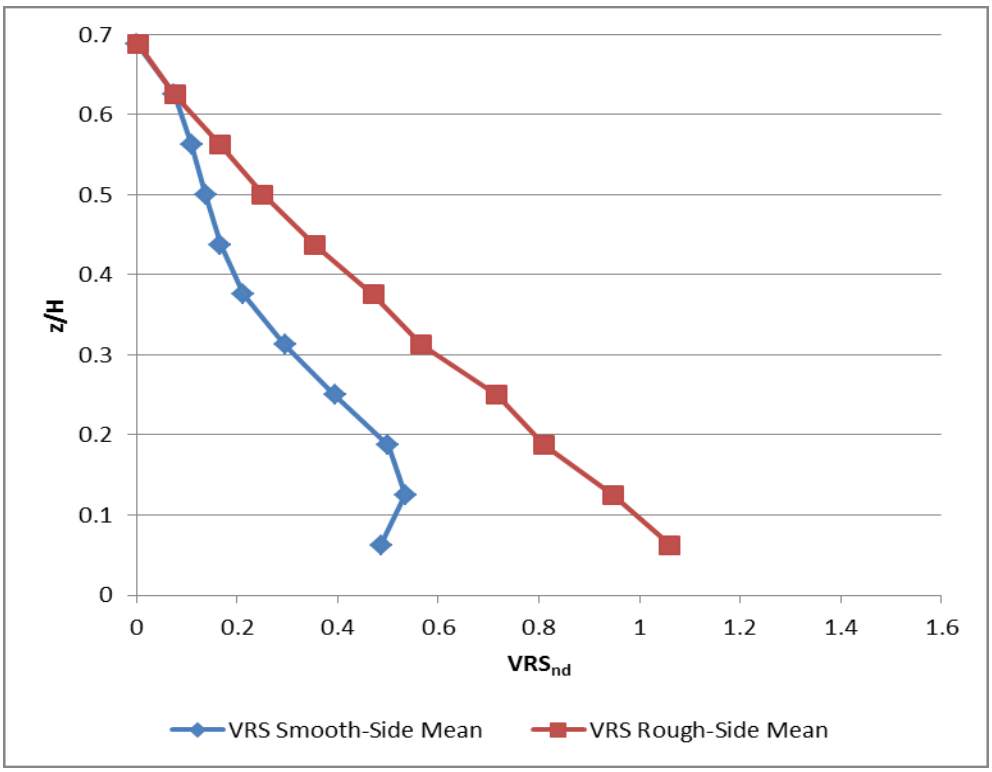

Figure 100: Mean Vertical Distribution of Relative τ_V^R (labelled VRS in Figure) by Channel Side (BC1 F2)

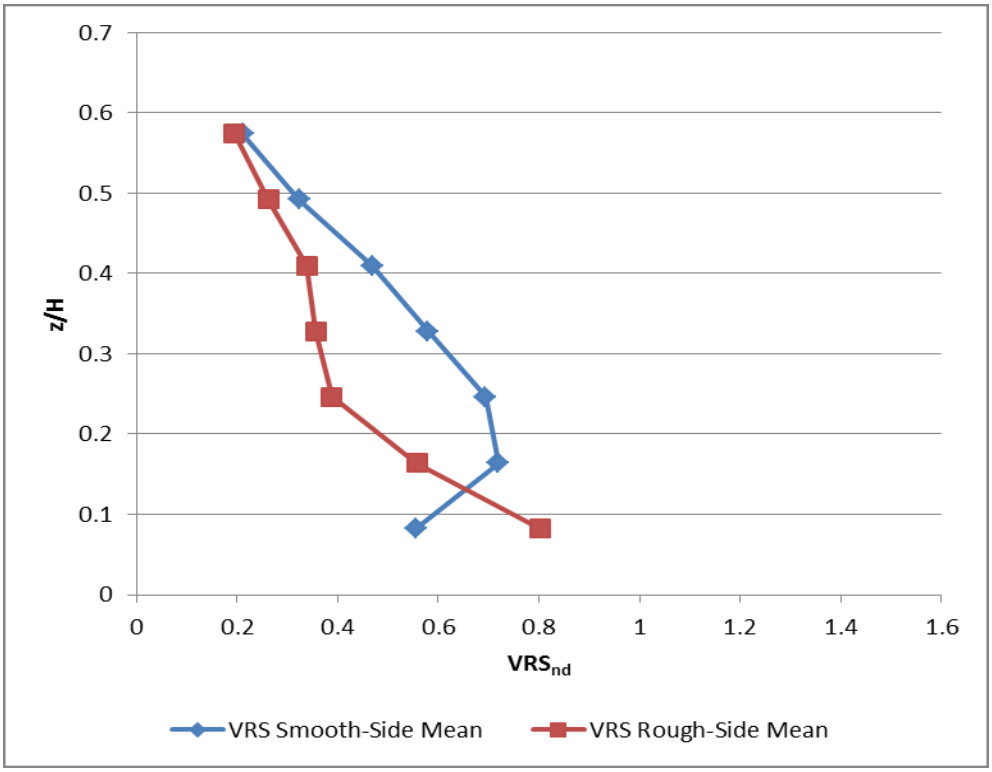

Figure 101: Mean Vertical Distribution of Relative τ_V^R (labeled VRS in Figure) by Side (BC2 F1 CS2)

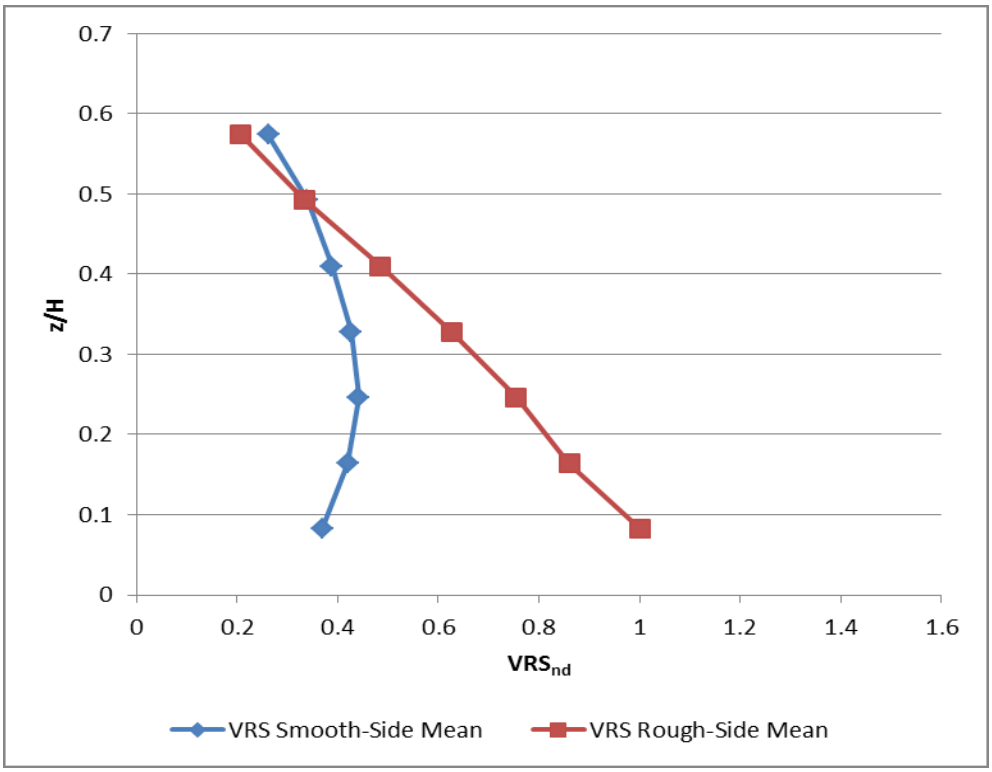

Figure 102: Mean Vertical Distribution of Relative τ_V^R (labelled VRS in Figure) by Side (BC2 F1 CS4)

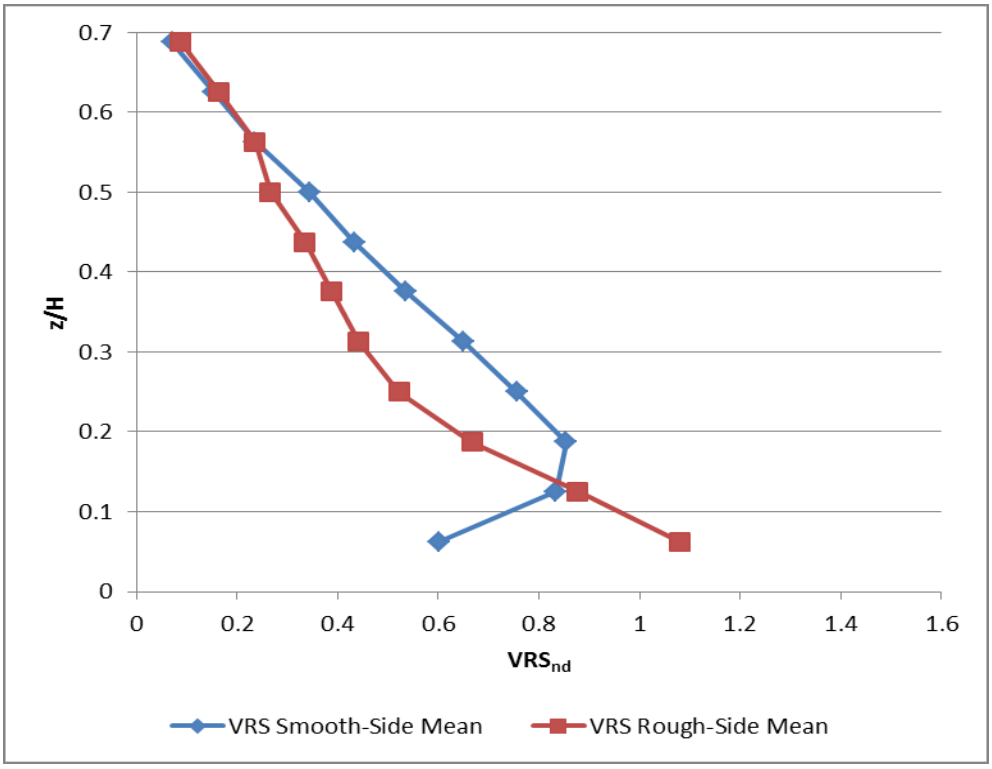

Figure 103: Mean Vertical Distribution of Relative τ_V^R (labelled VRS in Figure) by Side (BC2 F2 CS2)

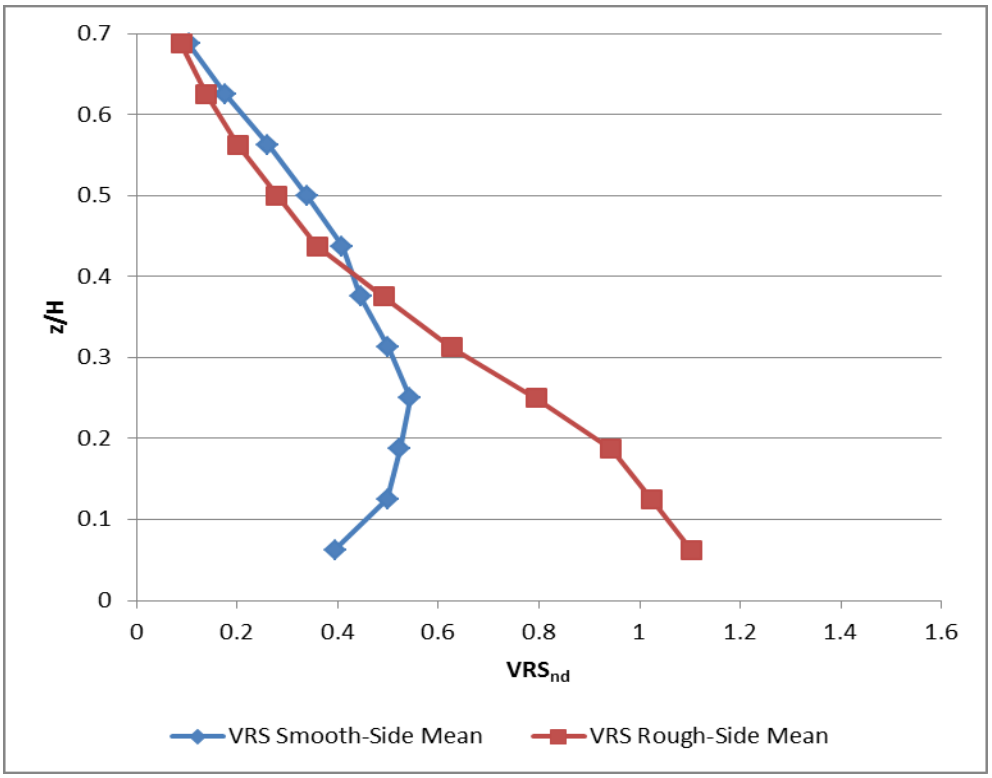

Figure 104: Mean Vertical Distribution of Relative τ_V^R (labelled VRS in Figure) by Side (BC2 F2 CS4)

For both BC1 flows the maximum $(\tau_V^R)_{nd}$ occurs in the region $0.50 < y/B < 0.75$, though the relative magnitudes differ - ~2.5 for F1 and ~1.2 for F2. Additionally, the magnitudes of $(\tau_V^R)_i$ for BC1 F1 and BC1 F2 are very different, with that for BC1 F2 being ~35% lower. Closer examination of the distribution shows that, in the F2 case, there is a large region of negative τ_V^R in the upper levels of flow which reduces the channel mean value. If this data set is truncated at $z = 70mm$ (i.e. the same absolute depth range as covered by the F1 data), this difference reduces to ~9%. While this is hardly conclusive (with only two flow depths examined) it does suggest that the range of influence of the bed is depth independent.

For BC2 the magnitude of $(\tau_V^R)_i$ varies negligibly (2%) along the channel section, though the distribution develops from the roughness switch. At CS2 (Figure 95) the τ_V^R increases close to the rough bed. On the newly smooth side the opposite happens, with τ_V^R decreasing close to the smooth bed. However, a region $(0.1 < z/H < 0.4,\ 0.1 < y/B < 0.4)$ of higher τ_V^R remains over the smooth bed. As this τ_V^R is a direct result of turbulent fluctuation, this shows that the smooth bed is damping the turbulence in its close proximity – the high τ_V^R region corresponds to the area where TKE is dissipated through heat dissipation only, reducing at a lower rate than in the damped region. By CS4 (Figure 96) the τ_V^R distribution is qualitatively as for BC1, though $(\tau_V^R)_d$ magnitudes (particularly in the near-bed region) are lower.

The mean-by-side vertical distribution of τ_V^R show a distinct “hook” on the smooth side at CS2 (Figure 101 and Figure 103), an exaggeration of that seen for BC1. This has flattened by CS4 (Figure 102 and Figure 104). Such a distribution would normally be associated with a shear layer near the boundary, as discussed above, but this

explanation does not fit with the exaggerated hook seen here. Rather, it is thought that damping of w' by the bed discussed above would lead to a similar distribution, with τ_V^R reducing more rapidly close to the bed than at greater z – by CS4 the smooth side τ_V^R has also reduced away from the bed and a distribution similar to that seen for BC1 has been achieved.

Figure 105 to Figure 110 show the cross-sectional distribution of relative τ_H^R. It should be noted that the sign of the shear stress is dependent on the coordinate system used – τ_V^R is positive when it "acts" upwards from the bed, and similarly τ_H^R is negative when it acts from the rough (low U) to the smooth (high U) side. For BC1 F1 the τ_{RH}, which peaks close to the RSB, is clearly acting from rough to smooth side at the RSB, as would be anticipated. For BC1 F2 the τ_H^R is of a lower peak magnitude than for BC1 F1, with a relative value of 0.4 rather than 0.5. In the central region, around the RSB, the distribution appears markedly different from that seen for F1, with two distinct vertical lines, one of negative ("rough-to-smooth") τ_H^R on the smooth side (and slightly over) the RSB, and one of positive ("smooth-to-rough") τ_H^R on the rough side. However, the positive region is of low magnitude in comparison with the negative region (Figure 106), to such an extent that it may be considered negligible – if this is accepted then the distribution approximates that for F1.

There are two additional peaks in magnitude for F1. On comparison with Figure 89, it may be seen that these correspond to regions of upward flow (with positive τ_H^R at $y/B \cong 0.25$) and downward flow (with negative τ_H^R at $y/B \cong 0.80$). The former of these clearly matches the meeting point of two secondary flow cells, while there is some evidence of a similar occurrence at the latter. Similarly, the peak $(\tau_H^R)_d$ near the

bed for F2 (at $y/B \cong 0.46$) corresponds to the meeting of the central secondary flow cells shown in Figure 90, while the y position of these vertical lines matches the meeting of fast and slower regions of flow shown in Figure 71

As would be anticipated due to the more symmetrical U distribution, the magnitude of the τ_H^R is much reduced with BC2, with mean magnitudes of 34% (F1 CS2), 25% (F1 CS4), 16% (F2 CS2) and 13% (F2 CS4) of that for BC1 F1. The τ_H^R distribution around the RSB is similar to that seen for BC1 F2, with positive and negative vertical bands (Figure 107 to Figure 110). However, these bands are less clear than for BC1 F2 due to the lower magnitudes involved and the less uniform distribution of the shear stress.

From Figure 109 and Figure 110 it may be seen that peaks in the τ_H^R appear near the bed at the RSB for both CS2 and CS4, though these peaks are approximately 50% and 30% of the magnitude of the peaks seen for BC1.

From these figures the concentration of Reynolds stress near the intersection of the bed and RSB is apparent, with retardation of the upper flow (by τ_V^R between the slower moving water at the bed) and of the smooth side flow (by τ_H^R between the faster moving water on the smooth side of the channel and slower moving water on the rough side).

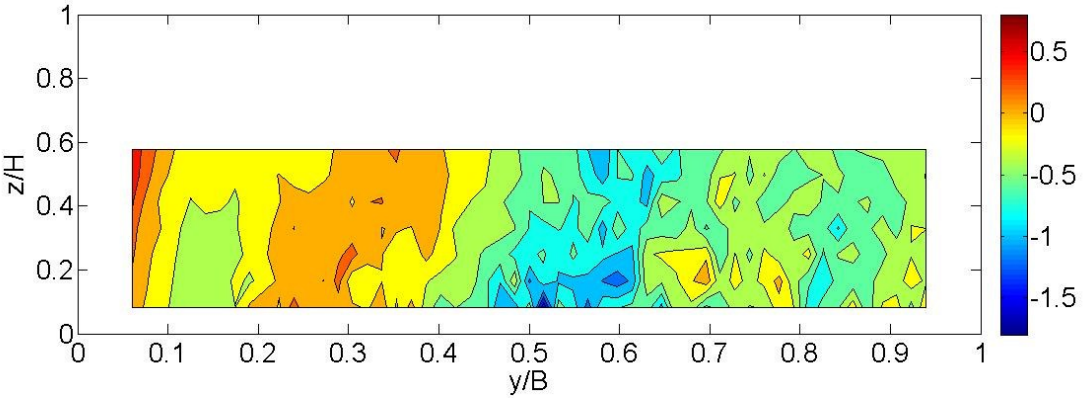

Figure 105: Dimensionless τ_H^R Distribution (BC1 F1)

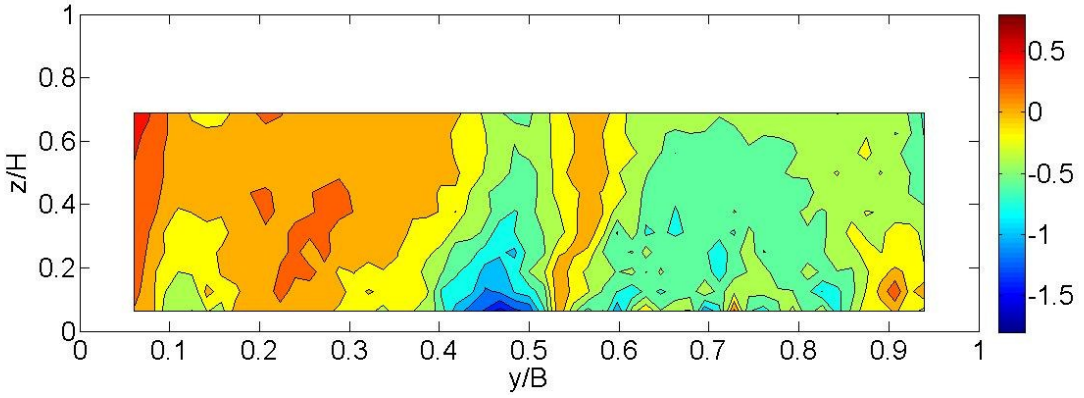

Figure 106: Dimensionless τ_H^R Distribution (BC1 F2)

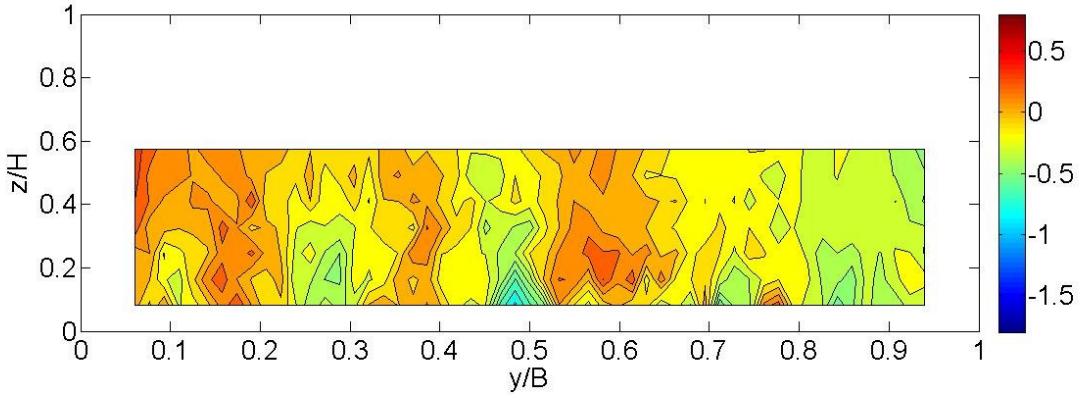

Figure 107: Dimensionless τ_H^R Distribution (BC2 F1 CS2)

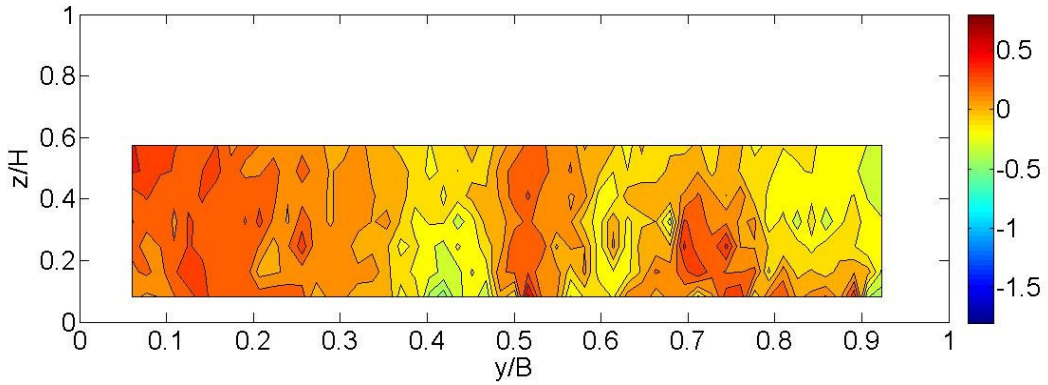

Figure 108: Dimensionless τ_H^R Distribution (BC2 F1 CS4)

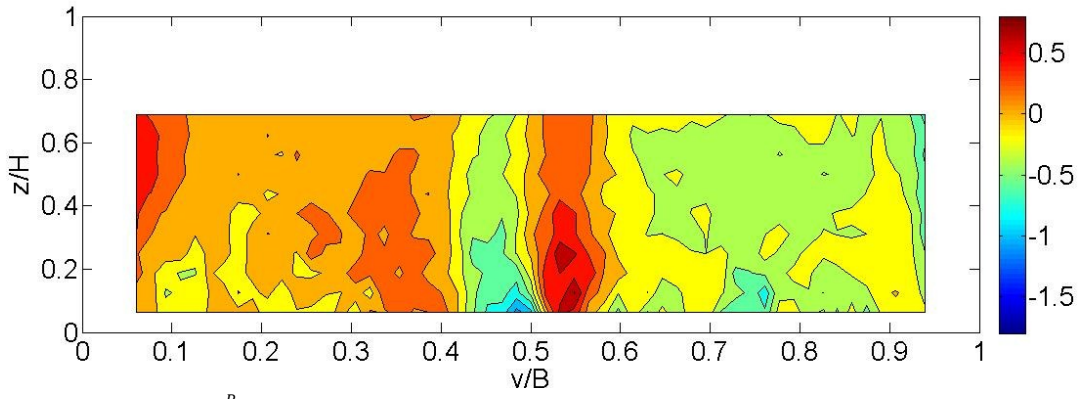

Figure 109: Dimensionless τ_H^R Distribution (BC2 F2 CS2)

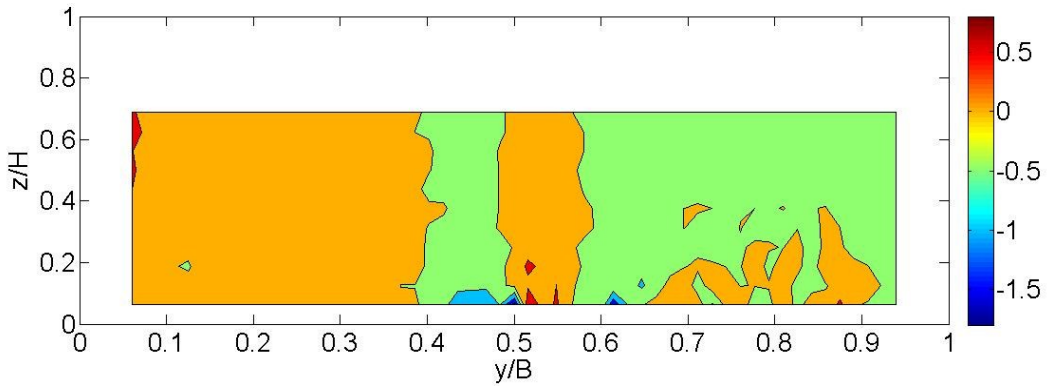

Figure 110: Dimensionless τ_H^R Distribution (BC2 F2 CS4)

8.4.4 Turbulence Intensity, Turbulent Kinetic Energy and its Flux

The distribution of turbulence intensity between the streamwise, transverse and vertical directions is remarkably consistent over the data sets (Table 16), with $\left(TI_y\right)_i \cong 0.75(TI_x)_i$ and $(TI_z)_i \cong 0.45(TI_x)_i$. The reduced TI in the z-direction may be due to boundary damping of vertical turbulent fluctuations by the channel bed and free surface. In conjunction with the equality of the integrated mean values, the equivalence of the cross-sectional (Figure 111 to Figure 128) and vertical (Figure 129 and Figure 130) distributions enables TI_x to be discussed here as representative of all three components. By CS4 the BC2 flow distributions are as for BC1 and BC2 CS4 – separation from the bed on the newly smooth side (as seen for the τ_V^R) is seen for BC2 CS2.

$(TI_x)_i$ appears to be independent of bed configuration but dependent on flow (and thus water depth) (Table 16). Despite the differences in the cross-sectional distribution of $(TI_x)_r$ at BC2 CS2 and CS4, $(TI_x)_i$ is independent of cross-section. This implies that the generation and dissipation of turbulence are balanced along the channel sections, at least between C2 and CS4. As noted earlier, Vermaas (2009) measured increases in water depth at the roughness switch, which (by continuity) must signify reduced U and reduced kinetic energy. Measurements of TI over a full section at CS1 might therefore be expected to show a greater TI, though these are not available with the data collected for this research.

Data Set	$(TI_x)_i$	$(TI_y)_i$	$(TI_z)_i$
BC1 F1	0.124 (100%)	0.093 (75%)	0.055 (44%)
BC1 F2	0.103 (100%)	0.080 (77%)	0.048 (47%)
BC2 F1 CS2	0.120 (100%)	0.091 (76%)	0.052 (43%)
BC2 F1 CS4	0.119 (100%)	0.091 (76%)	0.052 (43%)
BC2 F2 CS2	0.102 (100%)	0.076 (75%)	0.049 (48%)
BC2 F2 CS4	0.102 (100%)	0.075 (74%)	0.048 (47%)

Table 16: Integrated Channel Mean TI by Direction (Percentage of x-direction value in brackets)

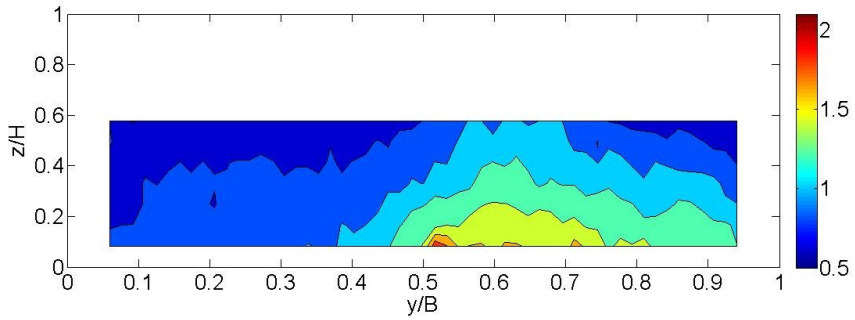

Figure 111: Streamwise Relative Turbulence Intensity (BC1 F1)

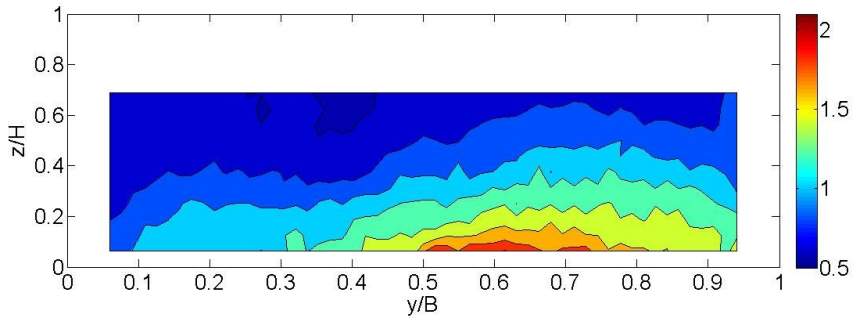

Figure 112: Streamwise Relative Turbulence Intensity (BC1 F2)

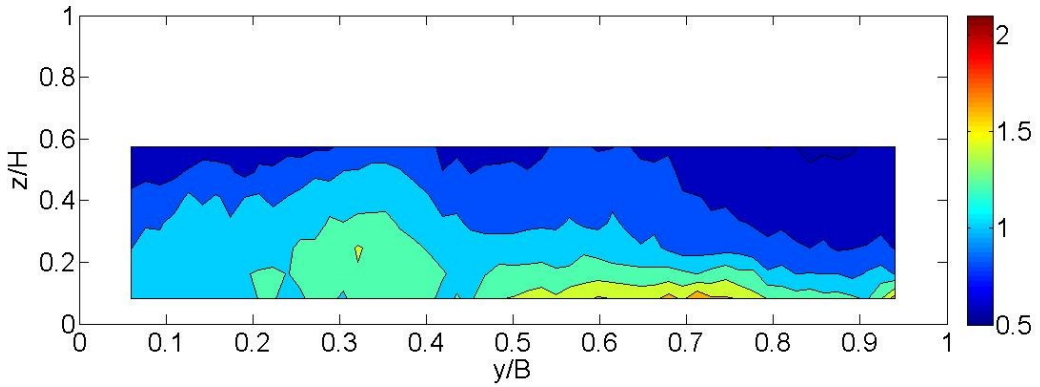

Figure 113: Streamwise Relative Turbulence Intensity (BC2 F1 CS2)

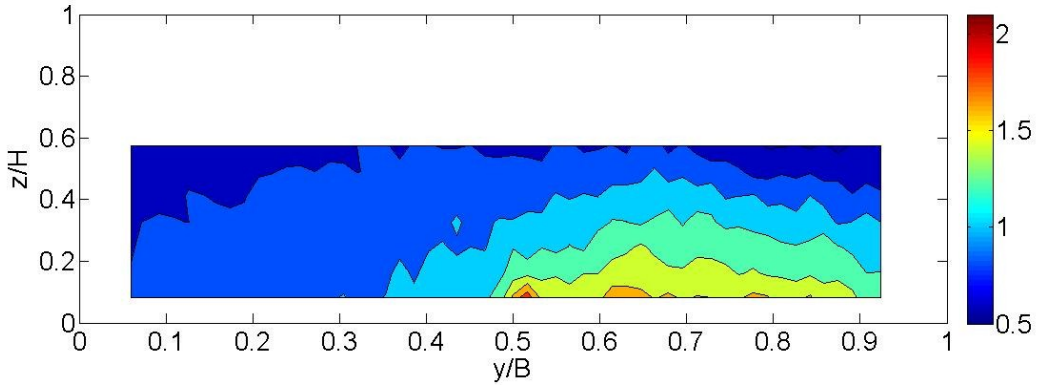

Figure 114: Streamwise Relative Turbulence Intensity (BC2 F1 CS4)

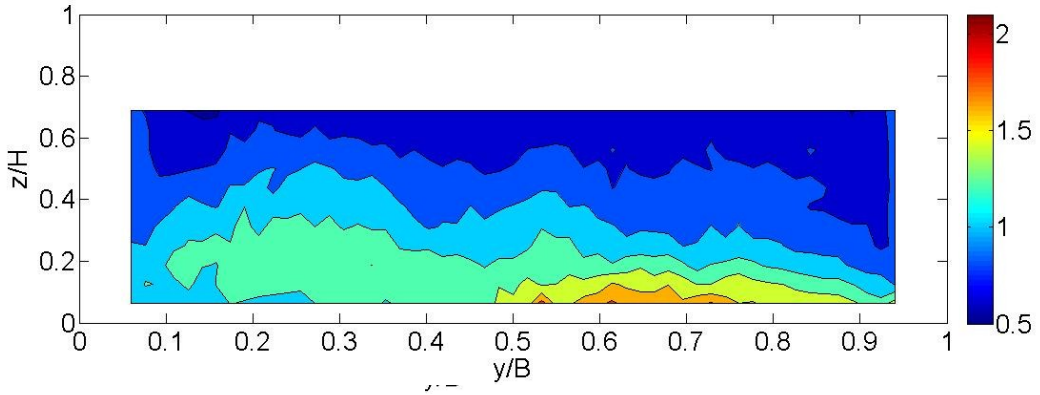

Figure 115: Streamwise Relative Turbulence Intensity (BC2 F2 CS2)

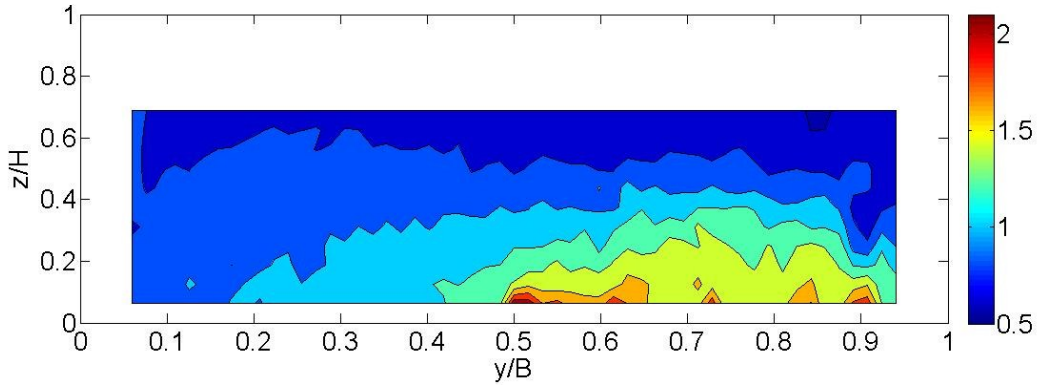

Figure 116: Streamwise Relative Turbulence Intensity (BC2 F2 CS4)

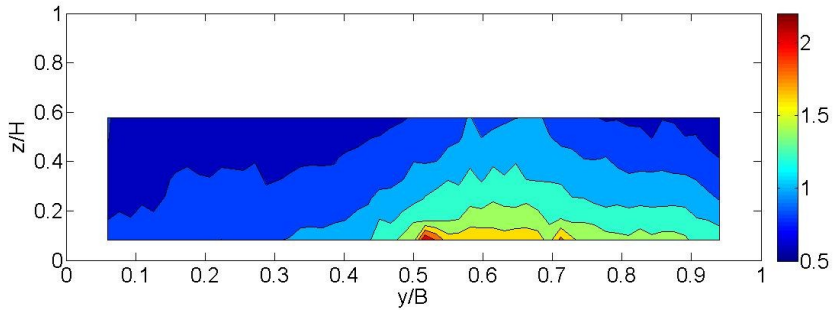

Figure 117: Transverse Relative Turbulence Intensity (BC1 F1)

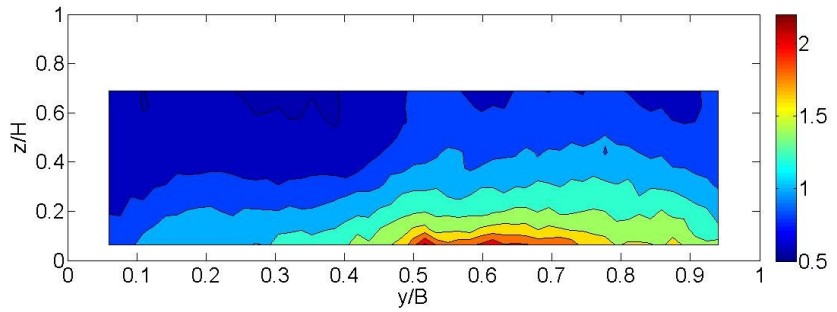

Figure 118: Transverse Relative Turbulence Intensity (BC1 F2)

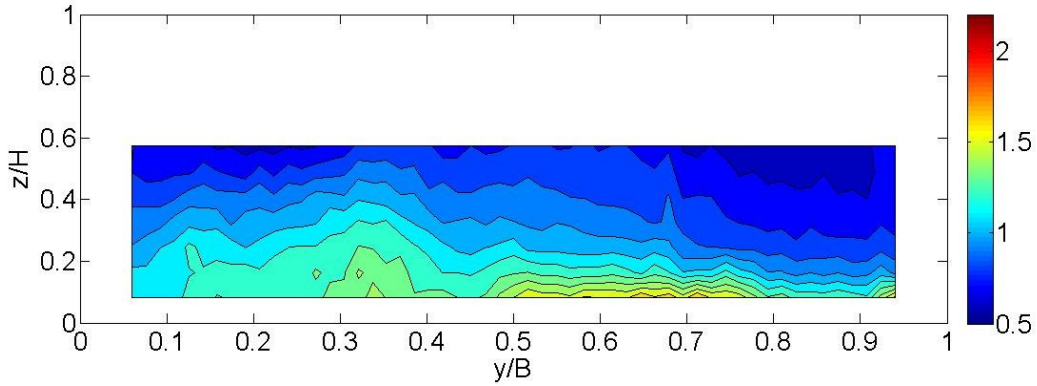

Figure 119: Transverse Relative Turbulence Intensity (BC2 F1 CS2)

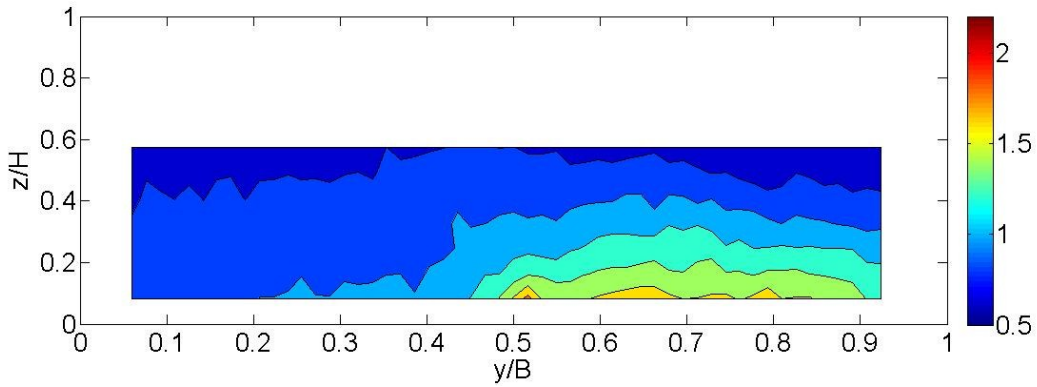

Figure 120: Transverse Relative Turbulence Intensity (BC2 F1 CS4)

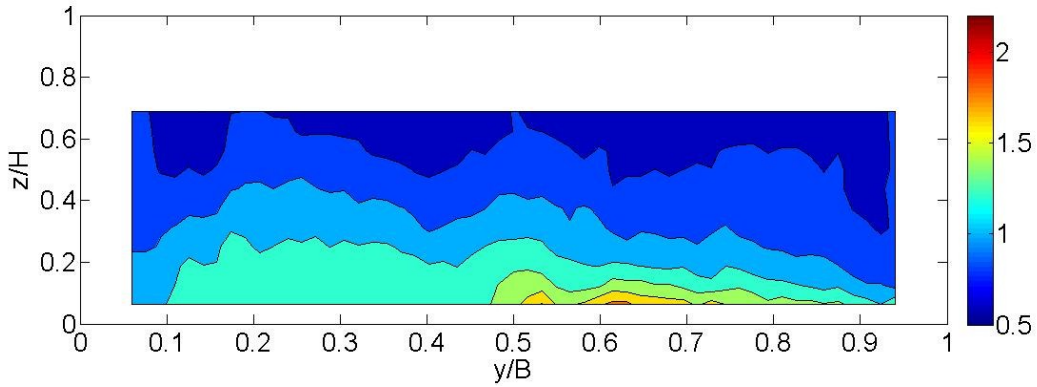

Figure 121: Transverse Relative Turbulence Intensity (BC2 F2 CS2)

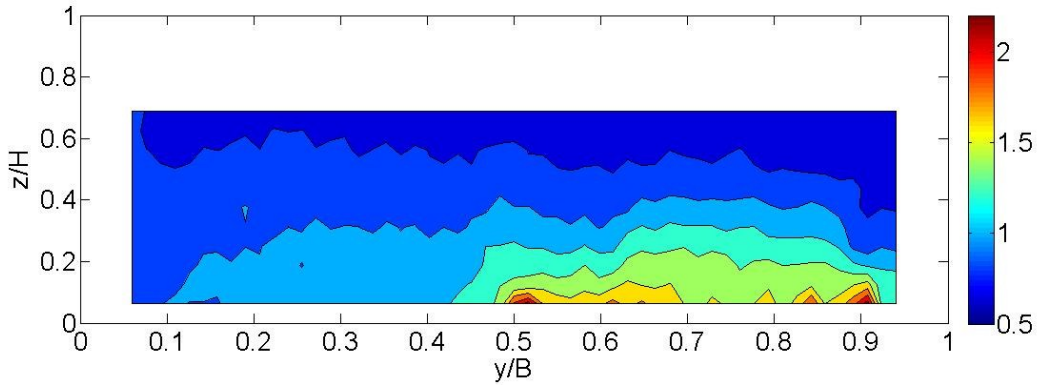

Figure 122: Transverse Relative Turbulence Intensity (BC2 F2 CS4)

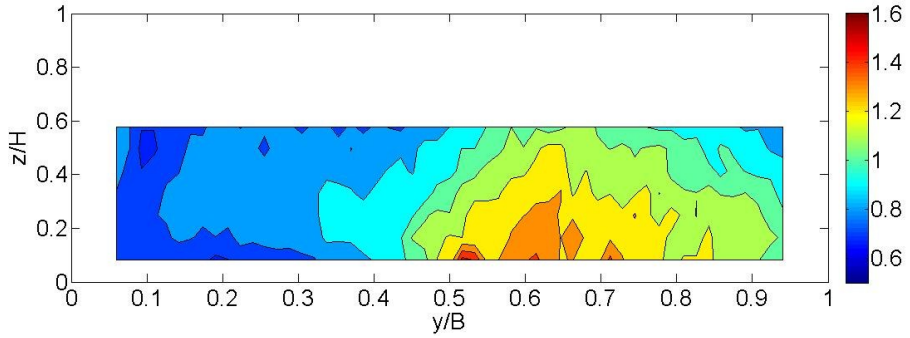

Figure 123: Vertical Relative Turbulence Intensity (BC1 F1)

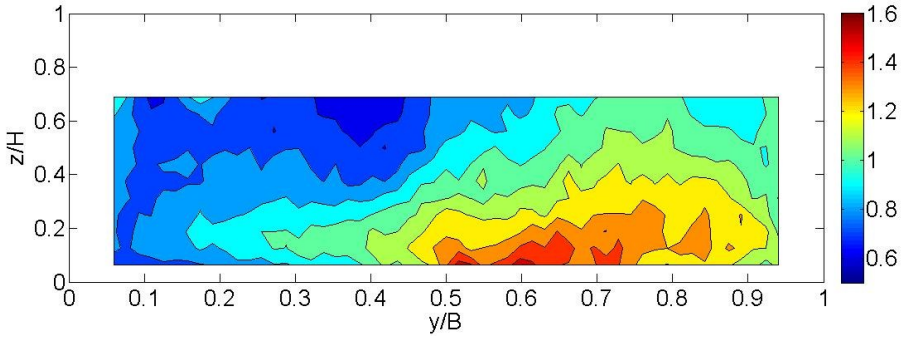

Figure 124: Vertical Relative Turbulence Intensity (BC1 F2)

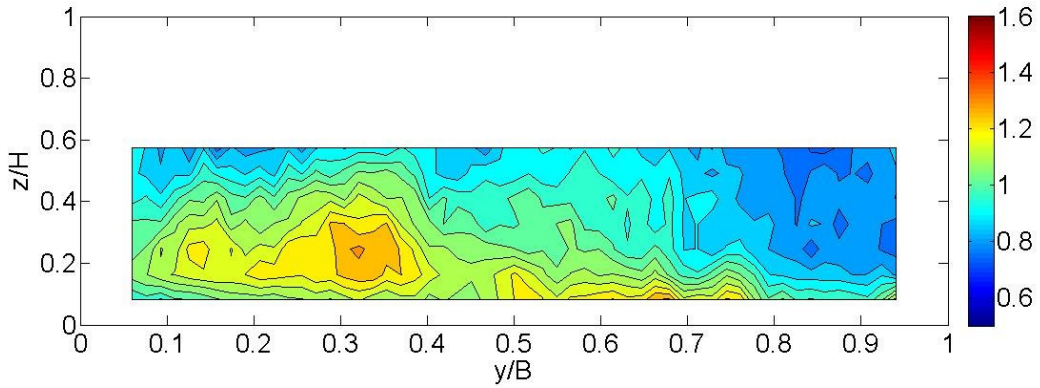

Figure 125: Vertical Relative Turbulence Intensity (BC2 F1 CS2)

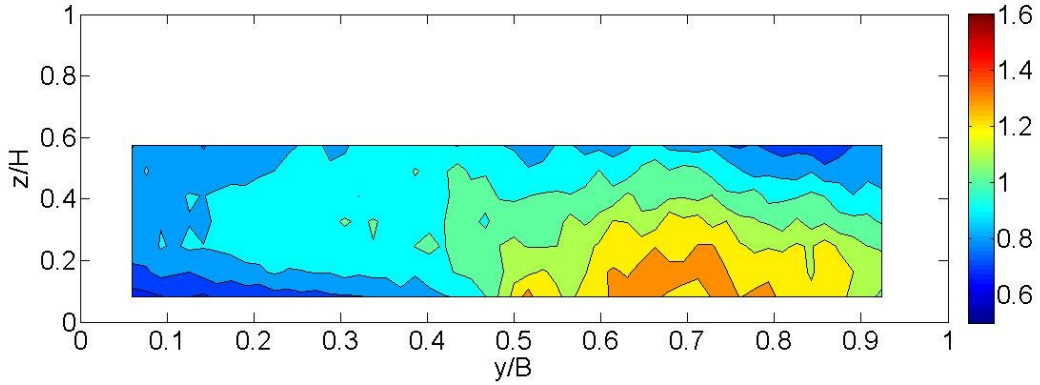

Figure 126: Vertical Relative Turbulence Intensity (BC2 F1 CS4)

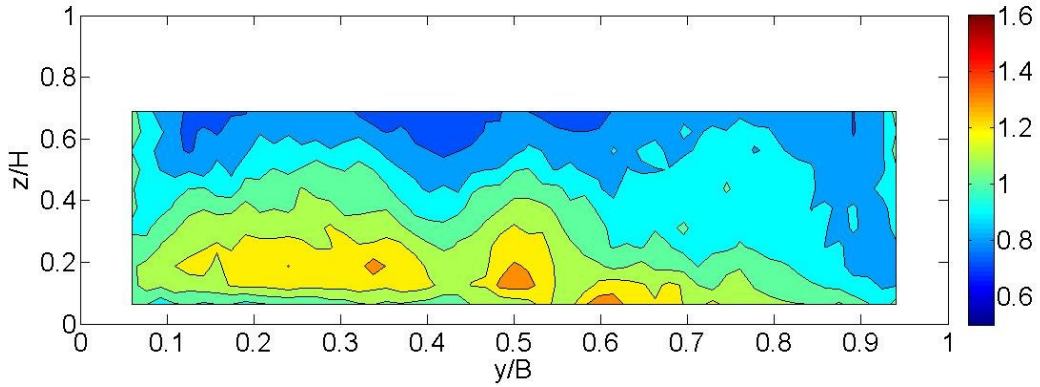

Figure 127: Vertical Relative Turbulence Intensity (BC2 F2 CS2)

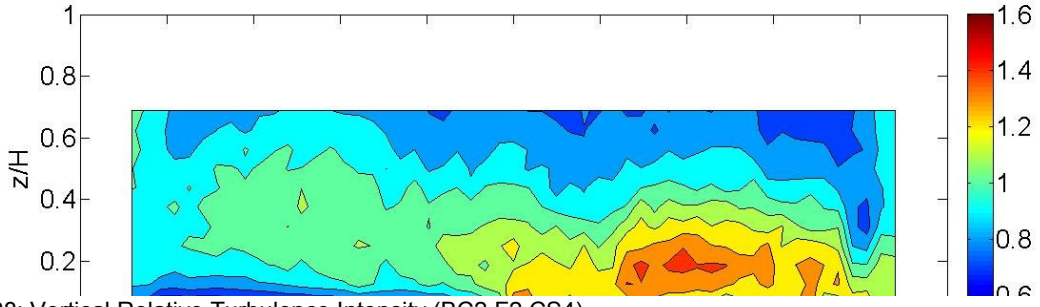

Figure 128: Vertical Relative Turbulence Intensity (BC2 F2 CS4)

y/B

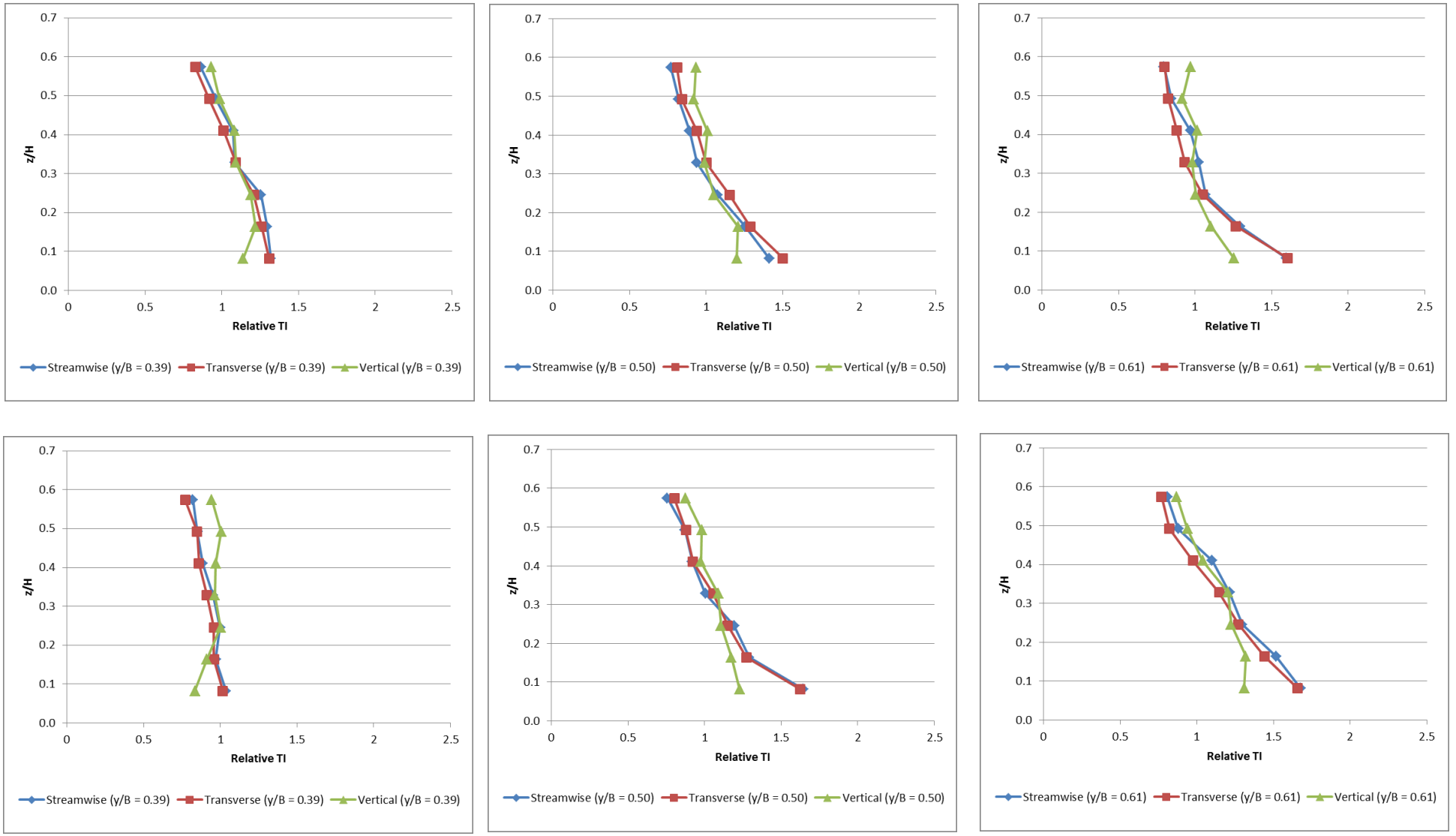

Figure 129: Vertical Distribution of Streamwise, Transverse and Vertical Relative and Absolute Turbulence Intensity at $y/B = 0.39$ (left), $y/B = 0.50$ (middle) and $y/B = 0.61$ (right) (BC2 F1 CS2 (top) and CS4 (bottom)

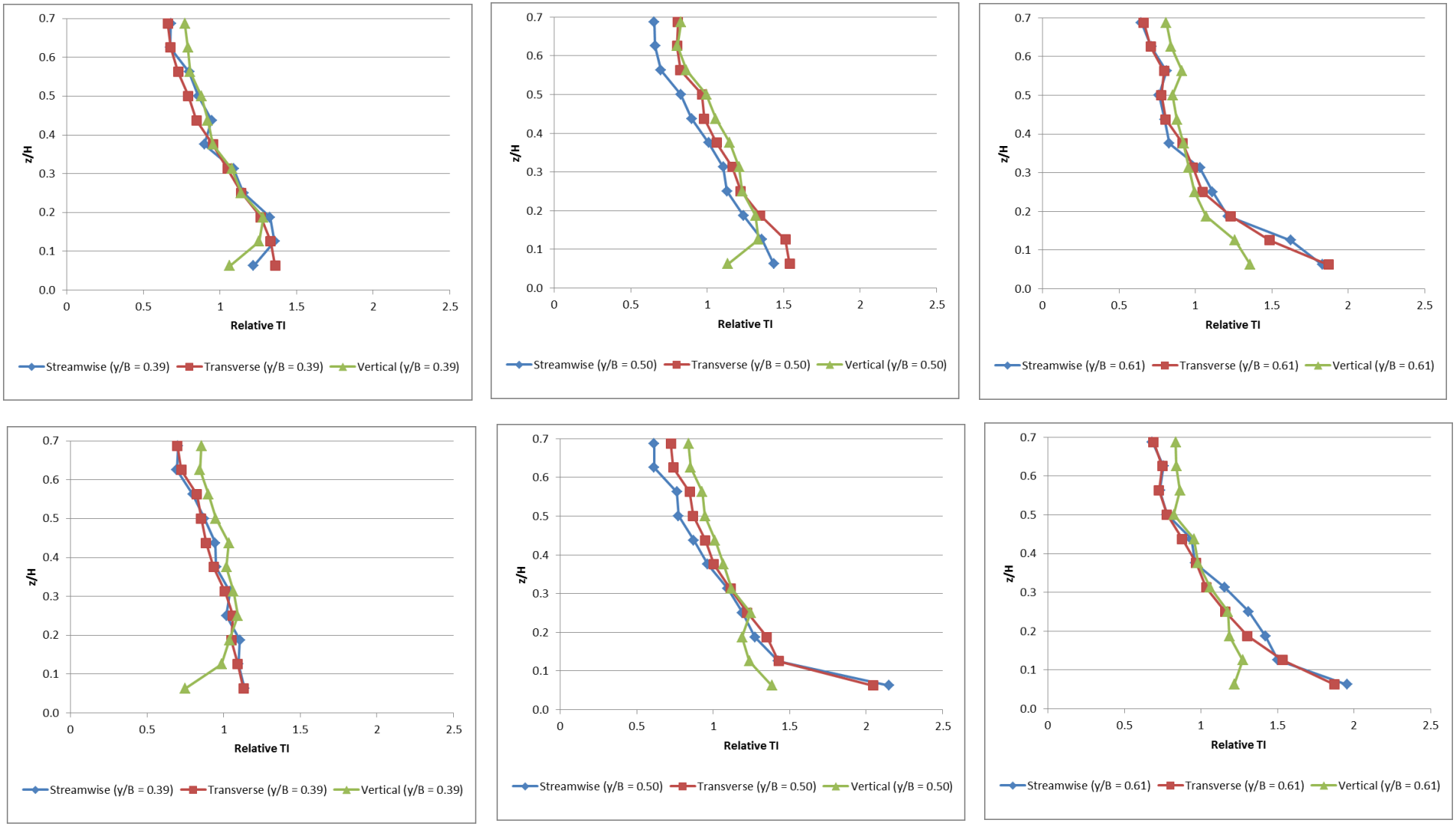

Figure 130: Vertical Distribution of Streamwise, Transverse and Vertical Relative and Absolute Turbulence Intensity at $y/B = 0.39$ (left), $y/B = 0.50$ (middle) and $y/B = 0.61$ (right) (BC2 F2 CS2 (top) and CS4 (bottom)

In all cases the vertical distribution of TI is linear above $z/H = 0.2$ for all three components, with the relative value distributions collapsing onto one another. Below this point, in the wall region where viscous stresses start to become significant, differences occur between the three components. $(TI_x)_r$ and $\left(TI_y\right)_r$ remain linear over the smooth side of the channel (though a reduction in $(TI_x)_r$ is seen in one case, BC2 CS2), while $(TI_z)_r$ reduces by ~25%. Over the rough side of the channel, and at the RSB, $(TI_z)_r$ remains approximately linear while $(TI_x)_r$ and $\left(TI_y\right)_r$ increase logarithmically. At this point distinctions must be made between F1 and F2, and also BC2 CS2 and CS4 – for F2 the change to a logarithmic distribution is more marked, with near bed $(TI_x)_r$ and $\left(TI_y\right)_r$ values exceeding those of F1 by ~15% - ~30%, while at the RSB, for CS2, $(TI_z)_r$ decreases near the bed.

With turbulence being generated by the rough bed, the TKE flux shows the dispersion of the TKE through the flow. Figure 131 to Figure 136 show the lateral flux vectors. The transmission of TKE from the rough bed is evident, as is the flux from the rough to the smooth side at the RSB in the BC1/BC2 CS4 cases. This cross-RSB flux is not evident for BC2 CS2, though in these cases (Figure 133 and Figure 135) the separation of the turbulent region from the bed on the newly smooth side is once again evident, with negligible TKE flux near the smooth bed but significant flux above. The opposite is seen over the newly rough side, with TKE flux developing and increasing by CS4.

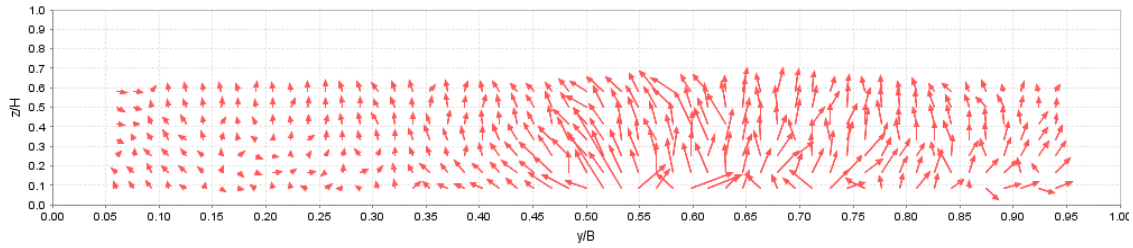

Figure 131: Lateral Flux of TKE (arrow length relative but not to fixed scale)

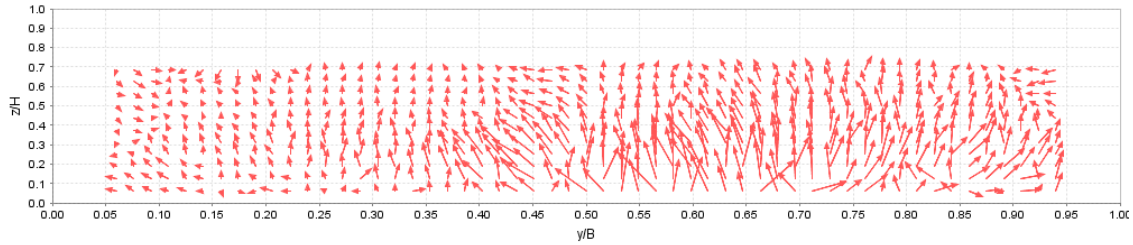

Figure 132: Lateral Flux of TKE (arrow length relative but not to fixed scale) (BC1 F2)

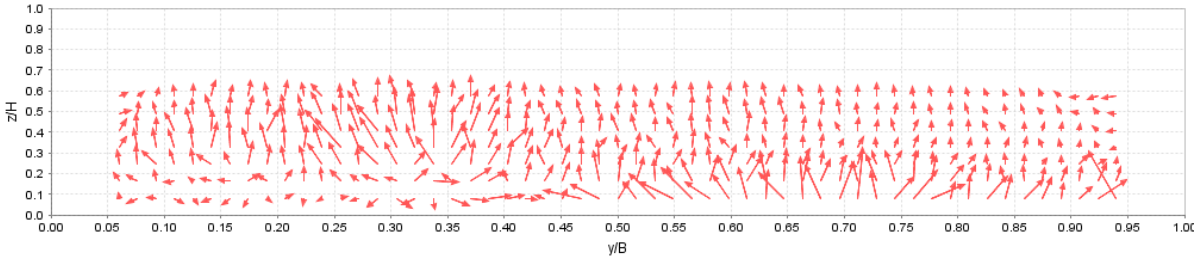

Figure 133: Lateral Flux of TKE (arrow length relative but not to fixed scale) (BC2 F1 CS2)

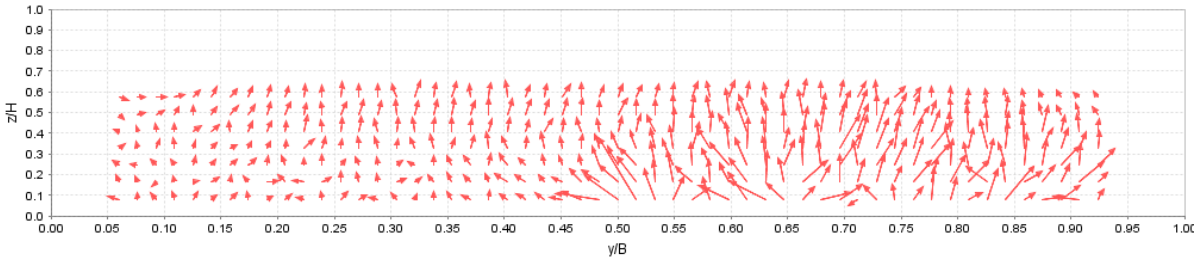

Figure 134: Lateral Flux of TKE (arrow length relative but not to fixed scale) (BC2 F1 CS4)

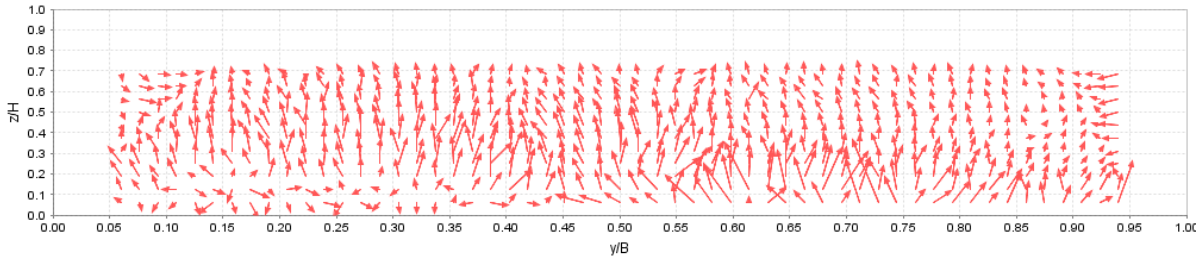

Figure 135: Lateral Flux of TKE (arrow length relative but not to fixed scale) (BC2 F2 CS2)

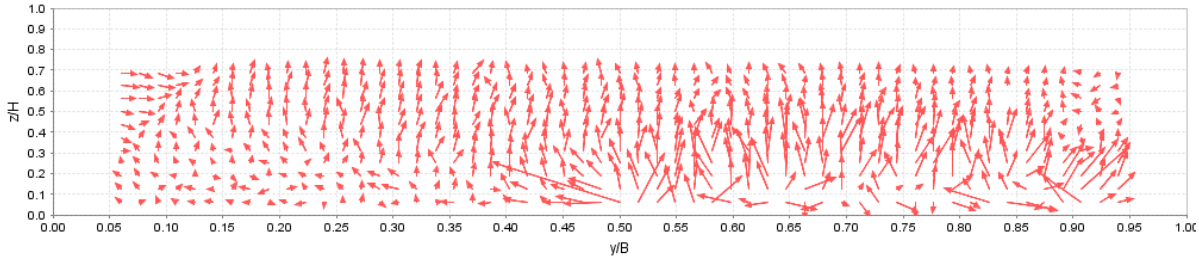

Figure 136: Lateral Flux of TKE (arrow length relative but not to fixed scale) (BC2 F2 CS4)

8.4.5 Q-H Analysis

Henceforth, “other events” is used to mean all events which are neither ejections nor sweeps.

8.4.5.1 *Vertical* $(u'w')$

Quadrant-Hole analysis examines the structure of turbulence by splitting the Reynolds stress into four components and comparing their relative magnitudes (see Section 4.4). In their wind tunnel experiments, Lu and Willmarth (1973) found that the proportion of total shear stress from ejections $\left(P_2 \equiv S_{2,0}/\overline{u'w'}\right)$ was approximately constant through the boundary layer, with a value of 0.77. The equivalent value for sweeps $\left(P_4 \equiv S_{4,0}/\overline{u'w'}\right)$ was 0.55, with P_1 and P_3being negative such that the sum $\sum_{i=1}^{4} P_i = 1$. P_1, P_2, P_3 and P_4 have been calculated for all data sets in the current work and are presented in the following figures (Figure 137 to Figure 154). The interpretation of these figures is somewhat unintuitive:

(i) With P_1 and P_3 being negative, the sum of P_2 and P_4 must be ≥ 1 (P_2 and P_4 were both found to be > 0.5 and of comparable magnitude).

(ii) As a guide, the lower (closer to 0.5) P_2 and P_4 are the more disproportionately large the magnitudes of P_2 and P_4 are in comparison to P_1 and P_3, and the more dominate ejections and sweeps are. Again, this is an artefact of the negative sign of P_1 and P_3 and the condition $\sum_{i=1}^{4} P_i = 1$ – if the total Reynolds stress is constant, an increase in P_2 and P_4 necessitates a relatively larger increase in the magnitude of P_1 and P_3, reducing the dominance of the ejections and sweeps.

(iii) In the preparation of these figures it was necessary to limit values to the range ± 1 due to the existence of extreme values in regions of low shear stress due to the division in the definition of P_i. Values of greater magnitude than this limit only appeared remote from the bed, where both TI and Reynolds stress is negligible in comparison to the near bed region, and so this limit may be imposed without affecting discussion of the results.

(iv) Due to the use of relative magnitudes the P_i values do not differentiate between regions of high and low τ_H^R and so the figures are, in the sense of showing propagation of turbulence, misleading without cross-reference to the Reynolds stress distribution (Figure 93 to Figure 98).

While the entire cross-section is shown in these figures, the following discussion concentrates on the regions of high τ_H^R, i.e. over the rough side. This limitation is applied partly due to (iii) and (iv) above, and partly to make the discussion of a manageable length. However it is worth noting that:

(i) For BC1, where there is upflow due to the convergence of two secondary flow cells $(y/B \cong 0.15 \rightarrow 0.20)$ P_2 is approximately equal to the value seen close to the rough bed. This region of low P_2 extends upwards to a greater extent than on the rough side. There is a matching increase at $y/B \cong 0.40 \rightarrow 0.50$, corresponding to the downflow at the right-hand edge of the central secondary flow cell. Similarly, P_4 increases at $y/B \cong 0.15 \rightarrow 0.20$, though an equivalent increase at $y/B \cong 0.40 \rightarrow 0.50$ is not evident. This would suggest that secondary flow cells not only contribute to momentum transfer, but also to the

propagation of turbulence by expanding the region over which ejections and sweeps are dominant.

(ii) For BC2, P_4 shows clear separation from the newly smooth bed – this is not evident for P_2, though the development of the reduction over the newly rough bed is apparent.

(iii) The P_3 distribution was found to be identical to that for P_1 for all data sets and so is not shown. P_1 is approximately constant over the high τ_V^R region, with a value of ~ -0.2.

When compared to the findings of Lu and Willmarth, the current research shows more variation in P_2 and P_4. $P_2 \cong 0.65$ adjacent to the bed, though values as low as $P_2 \cong 0.5$ are seen, particularly for BC2 F2. In all cases, P_2 increases with height above bed, having a value ~ 1 above $z/H \cong 0.5$. Unlike P_2, P_4 initially decreases rapidly from the near bed value of ~ 0.75 to a value of ~ 0.6. The high P_4 is exaggerated for BC2 F1, though not for BC2 F2. Strangely, the opposite occurs for BC1, though to a much smaller degree – the BC1 F1 low P_4 region extends to the lowest measurements while for BC1 F2 there is a clear, near bed region of increased P_4. The region of low $P_4 (\cong 0.6)$ covers the majority of the channel, extending beyond the high τ_V^R region, up to $z/H \cong 0.60$. While data from closer to the bed would be beneficial in drawing conclusions, it would appear that sweeps (P_4) form a greater proportion of the total Reynolds stress near the bed, and a constant proportion over the majority of the channel. Conversely, the contribution of ejections increases linearly with depth (Figure 155).

Nakagawa and Nezu (1977) examined the ratio P_4/P_2 in channels of varying bed roughness, finding that this ratio increases as the wall is approached. While this appears to support the findings of the current research, it should be noted that the data examined by Nakagawa and Nezu was for the region $30 < z^+ < 1000$ – only the very upper limit of this region overlaps with the current research. Additionally, Nakagawa and Nezu found that $P_4/P_2 \cong 0.7$ at $z^+ \cong 1000$ whereas the current research gives $P_4/P_2 \cong 1.0$ at the lowest measured points. From Figure 155 it is evident that this ratio must decrease with depth, with a value of ~ 0.65 at the upper levels. Nakagawa and Nezu and Lu and Willmarth (1973) give a value of ~ 0.7 for this ratio.

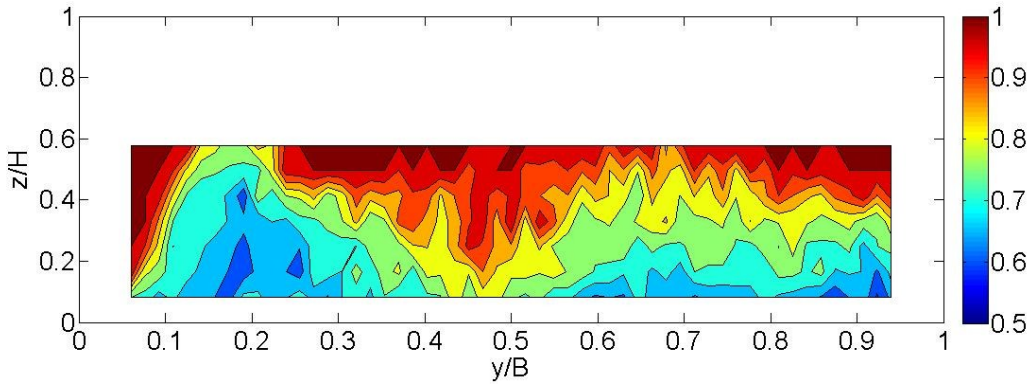

Figure 137: $u'w'$ Proportion of Total Shear Stress from Ejections (BC1 F1)

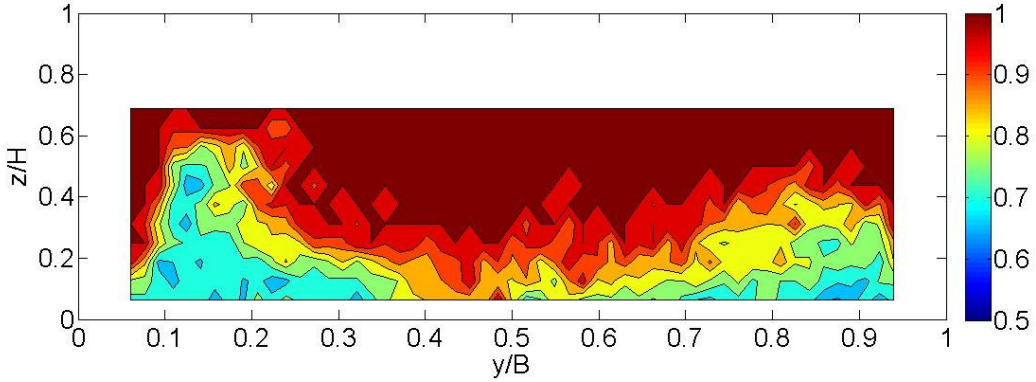

Figure 138: $u'w'$ Proportion of Total Shear Stress from Ejections (BC1 F2)

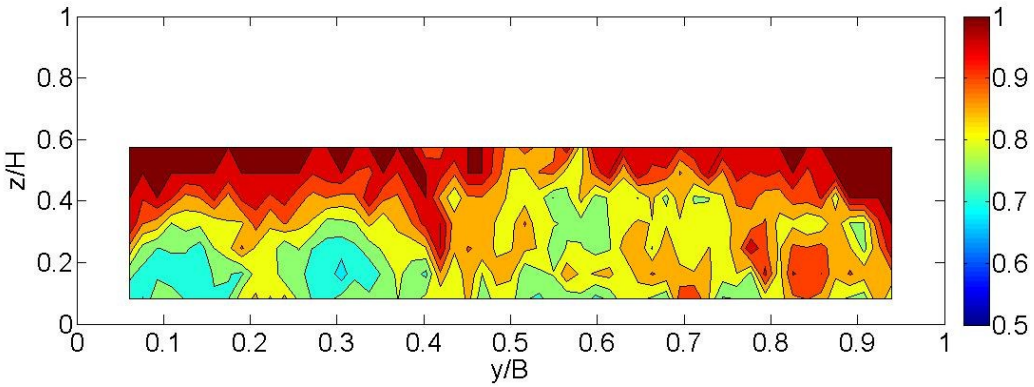

Figure 139: $u'w'$ Proportion of Total Shear Stress from Ejections (BC2 F1 CS2)

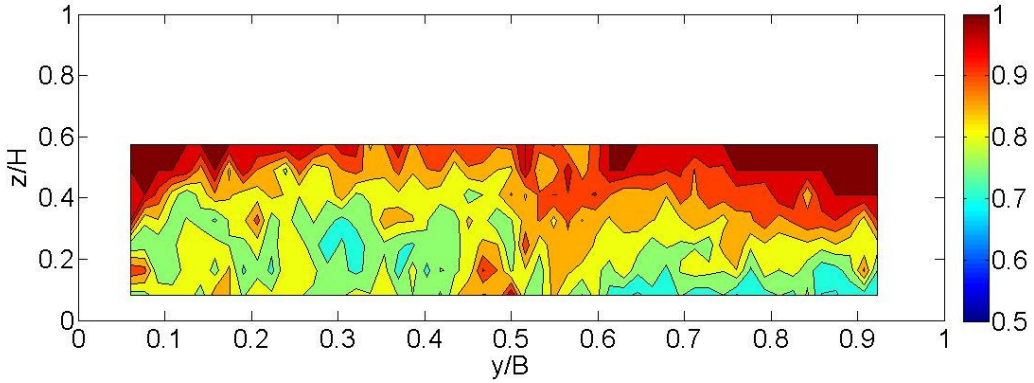

Figure 140: $u'w'$ Proportion of Total Shear Stress from Ejections (BC2 F1 CS4)

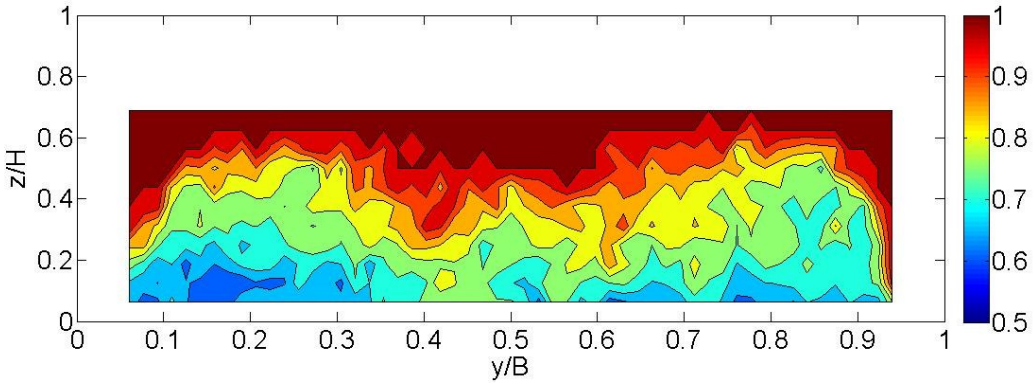

Figure 141: $u'w'$ Proportion of Total Shear Stress from Ejections (BC2 F2 CS2)

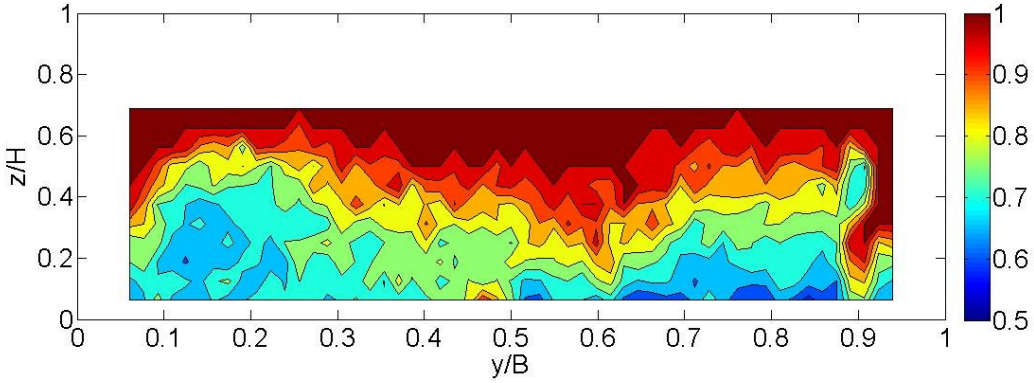

Figure 142: $u'w'$ Proportion of Total Shear Stress from Ejections (BC2 F2 CS4)

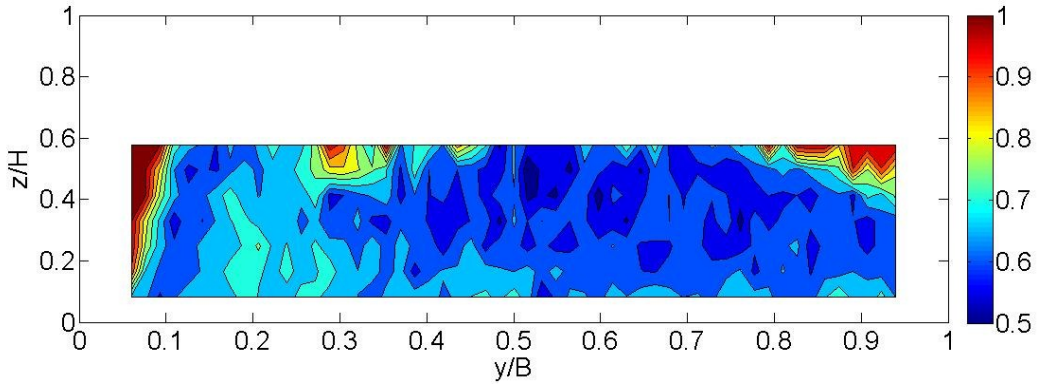

Figure 143: $u'w'$ Proportion of Total Shear Stress from Sweeps (BC1 F1)

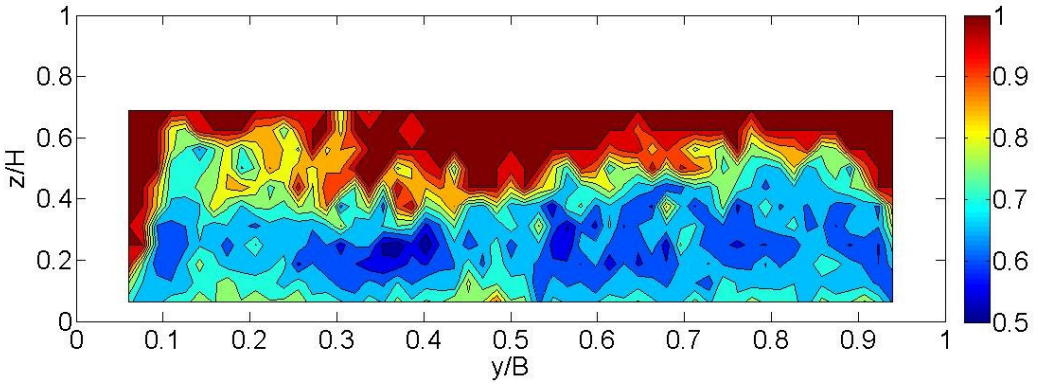

Figure 144: $u'w'$ Proportion of Total Shear Stress from Sweeps (BC1 F2)

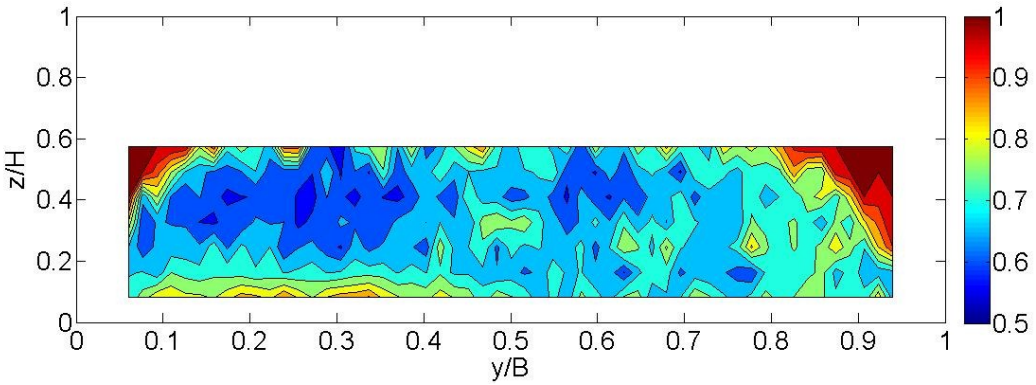

Figure 145: $u'w'$ Proportion of Total Shear Stress from Sweeps (BC2 F1 CS2)

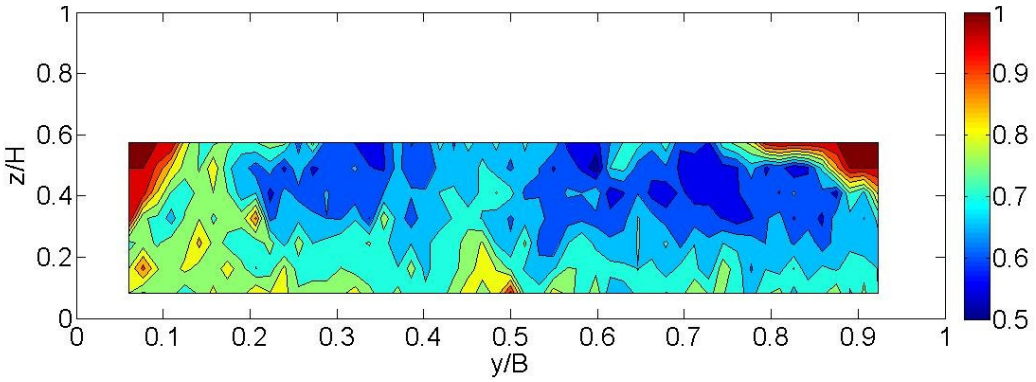

Figure 146: $u'w'$ Proportion of Total Shear Stress from Sweeps (BC2 F1 CS4)

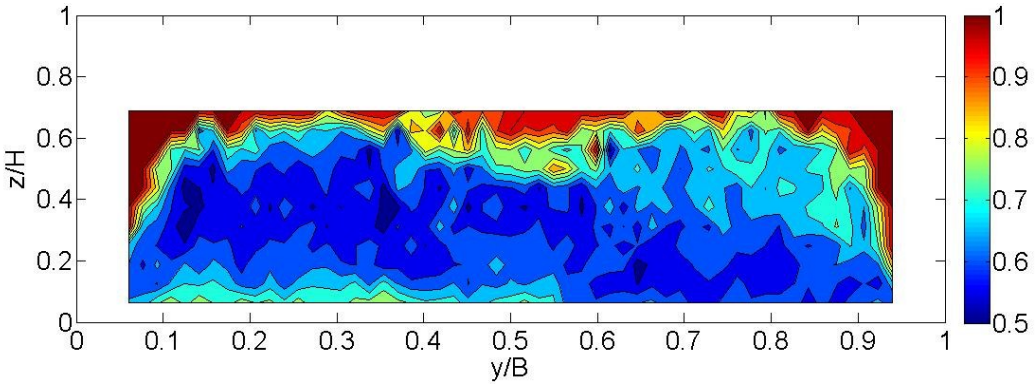

Figure 147: $u'w'$ Proportion of Total Shear Stress from Sweeps (BC2 F2 CS2)

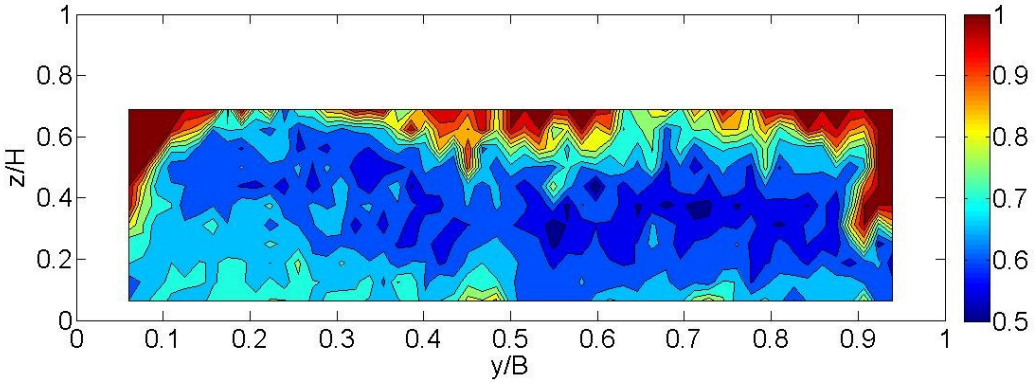

Figure 148: $u'w'$ Proportion of Total Shear Stress from Sweeps (BC2 F2 CS4)

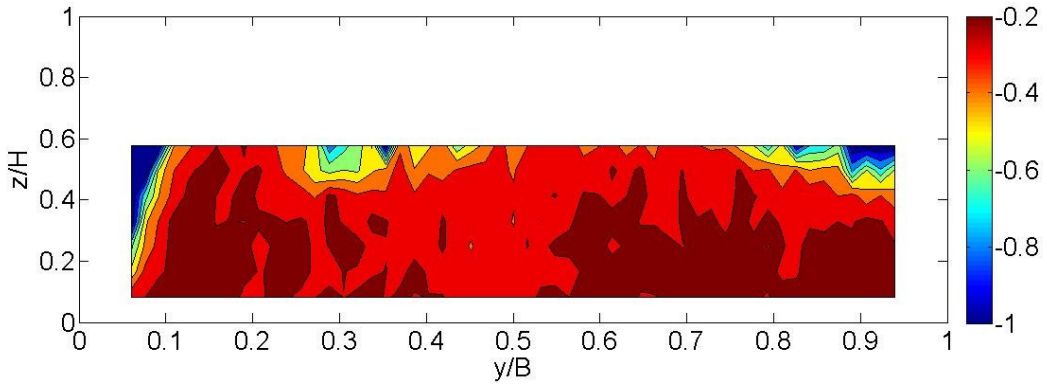

Figure 149: $u'w'$ Proportion of Total Shear Stress from P1 Events (BC1 F1)

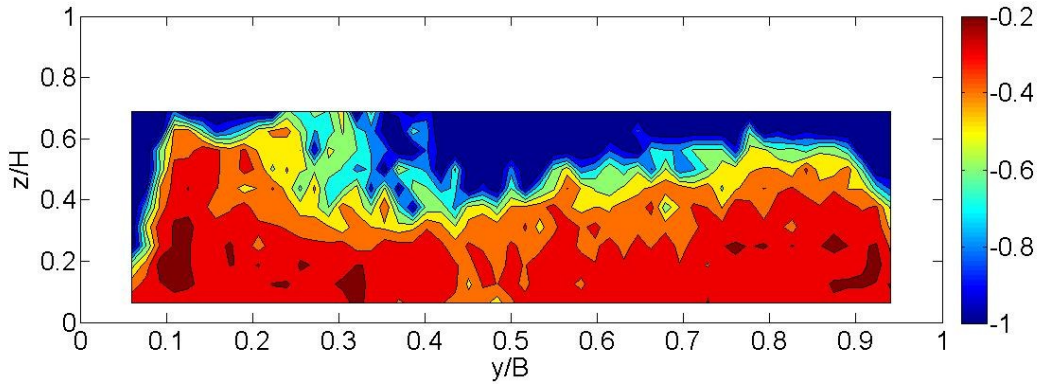

Figure 150: $u'w'$ Proportion of Total Shear Stress from P1 Events (BC1 F2)

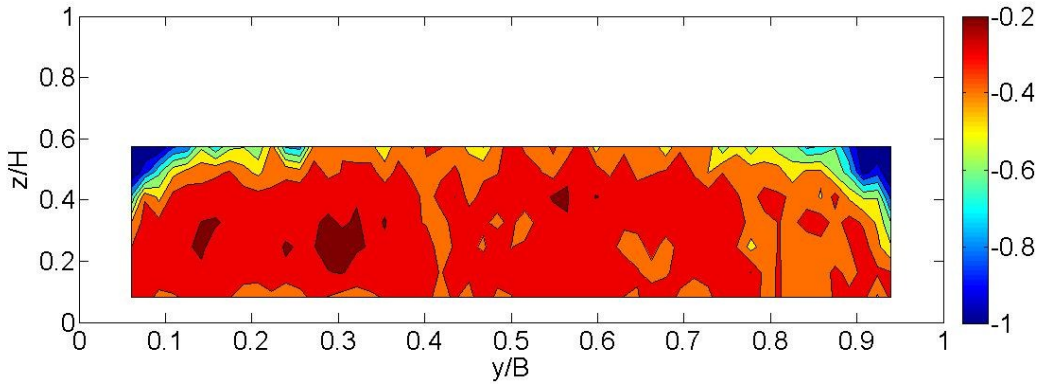

Figure 151: $u'w'$ Proportion of Total Shear Stress from P1 Events (BC2 F1 CS2)

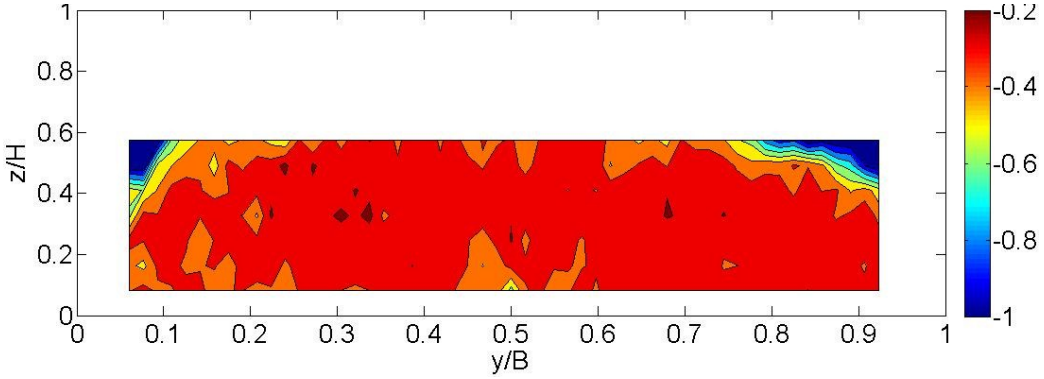

Figure 152: $u'w'$ Proportion of Total Shear Stress from P1 Events (BC2 F1 CS4)

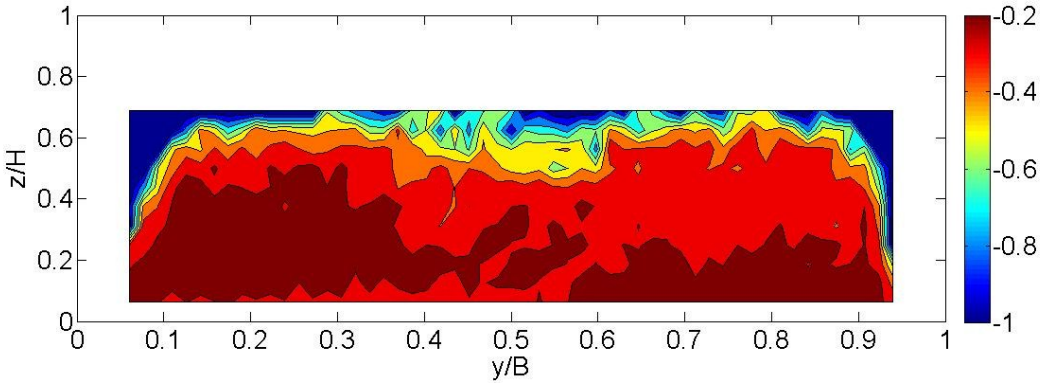

Figure 153: $u'w'$ Proportion of Total Shear Stress from P1 Events (BC2 F2 CS2)

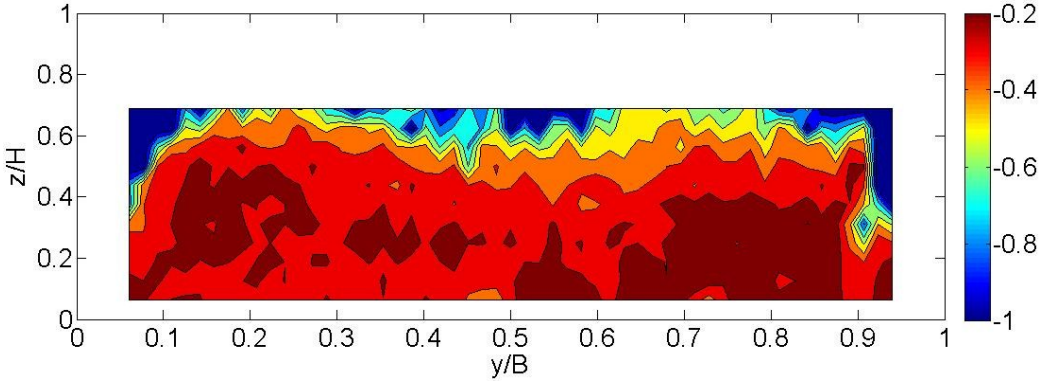

Figure 154: $u'w'$ Proportion of Total Shear Stress from P1 Events (BC2 F2 CS4)

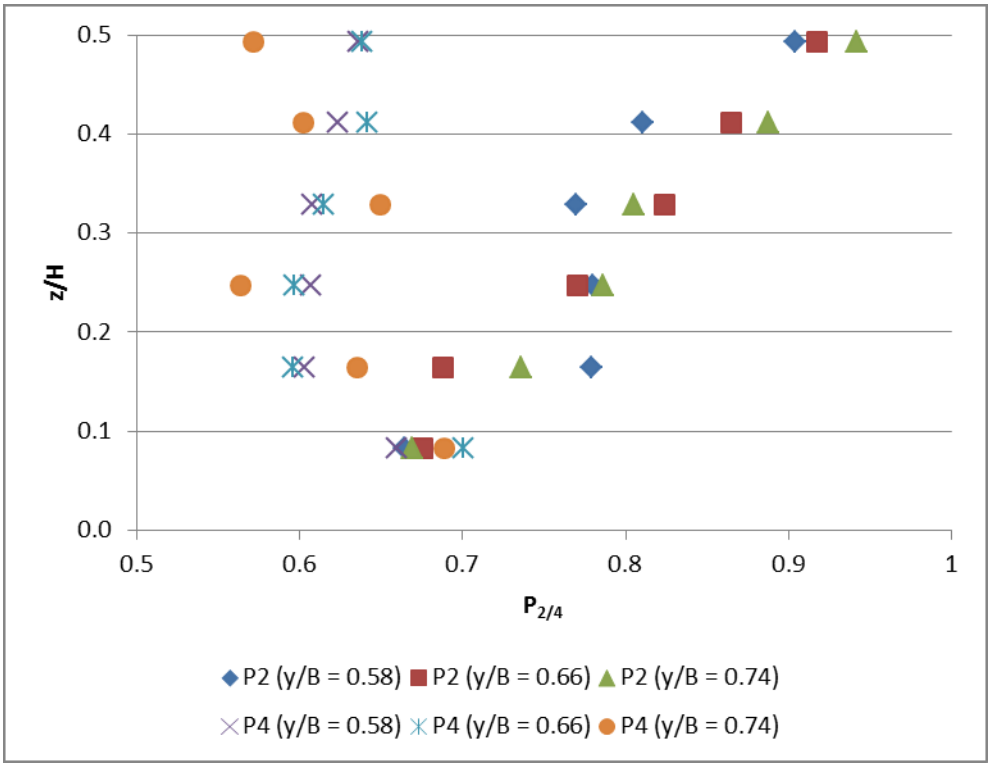

Figure 155: Depth Variation of Ejection (P_2) and Sweep (P_4) Contribution to Reynolds Stress (BC1 F1)

It is impractical to examine in detail the quadrant split of Reynolds stress for all data points due to the quantity of data. However, an examination of a number of points in the high τ_V^R region indicates that, when the variation with hole size of both percentage of total τ_V^R per quadrant and percentage time spent in each quadrant are calculated, the distributions of these quantities are near identical. This applies across data sets as well as within each data set, and so a single data point is examined as representative of the high τ_V^R region in all cases (Figure 156).

The form of these distributions matches the findings of Lu and Willmarth (1973) and Nakagawa and Nezu (1977). Quantitatively there are differences – in these previous studies the decrease of proportion of τ_V^R with hole size was smaller with, for example,

$S_{2,5} \cong 40\%$. In the current research the proportion of τ_V^R due to ejections has fallen to 33% by $J = 2$. This indicates that high energy events are of lower importance than seen by the earlier studies. However, high energy events still provide a disproportionate percentage of the τ_H^R when the duration is considered. At $J = 2$, the 33% of the τ_H^R from ejections occurs in 4% of the time, with the 18% of the τ_H^R from sweeps occurring in 3% of the time.

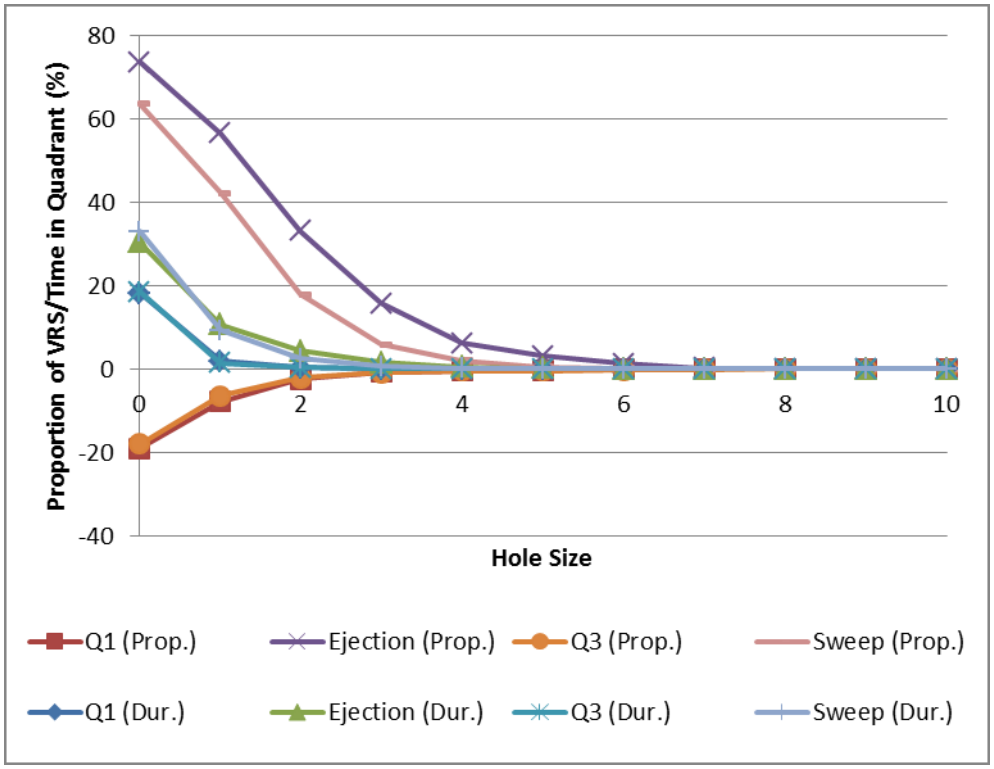

Figure 156: Variation of Proportion of τ_V^R/Time per Quadrant with Hole Size (BC1 F1; $y/B = 0.74, z/H = 0.16$; τ_V^R labelled as VRS in Figure)

8.4.5.2 *Horizontal* $(u'v')$

Before presenting the results of the Quadrant-Hole analysis, it is worth commenting on the analysis for the horizontal Reynolds stress (involving the product $u'v'$). When considering the momentum transfer due to the ejections and sweeps it is necessary

to assume a monotonic velocity distribution, which is not the case for a horizontal section (fixed z, varying y) spanning the entire channel. However, from Figure 70 it may be seen that this assumption is valid in the central region ($y/B \cong 0.4$ to $y/B \cong 0.6$) which, when considering transverse shear due to the RSB, is expected to be the region of interest. In this region $V(y)$ is monotonically decreasing and this leads to the ejection and sweep quadrants moving from the standard quadrant 2 and quadrant 4 to quadrants 3 and 1 respectively.

In the central region specified above, the ratio of ejections and sweeps to other events Figure 157 to Figure 162) is correlated to the magnitude of the τ_{RH} (Figure 105 to Figure 110). In regions of low magnitude τ_H^R the other (Q2 and Q4) events dominate (though due to the low magnitude of total τ_H^R, their magnitudes must be low), while in regions of high magnitude τ_H^R ejections and sweeps dominate. Therefore there is evidence of turbulence propagation in the parts of the central region where the τ_H^R is significant.

Taking a representative point in a high τ_H^R area (BC1 F2, $y/B = 0.47, z/H = 0.08$, Figure 163) and another in a low τ_H^R area (BC1 F2, $y/B = 0.53, z/H = 0.08$, Figure 164), the difference in structure of the turbulence is evident. In the former case, ejections and sweeps are dominant (as for the τ_V^R), while in the latter the P_is are of approximately equal magnitude.

The above results indicate that a vertical turbulent shear layer is formed at the RSB with ejection and sweep events propagating turbulence away from this boundary.

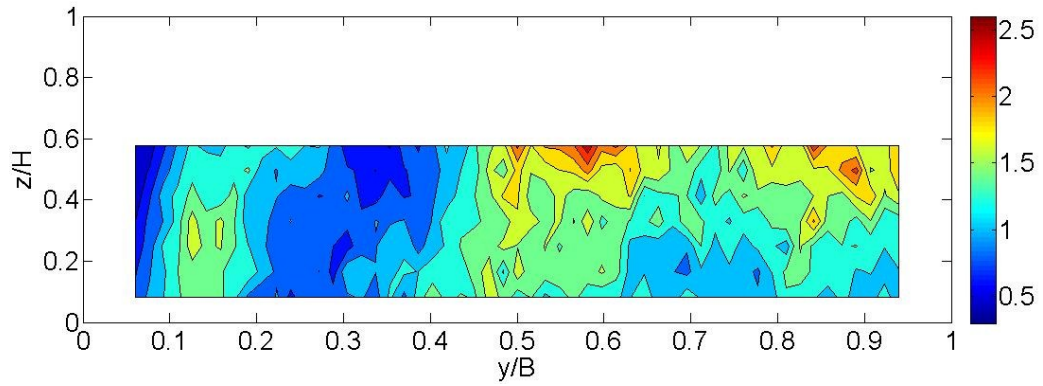

Figure 157: $u'v'$ Ejections and Sweeps to Other Events (BC1 F1)

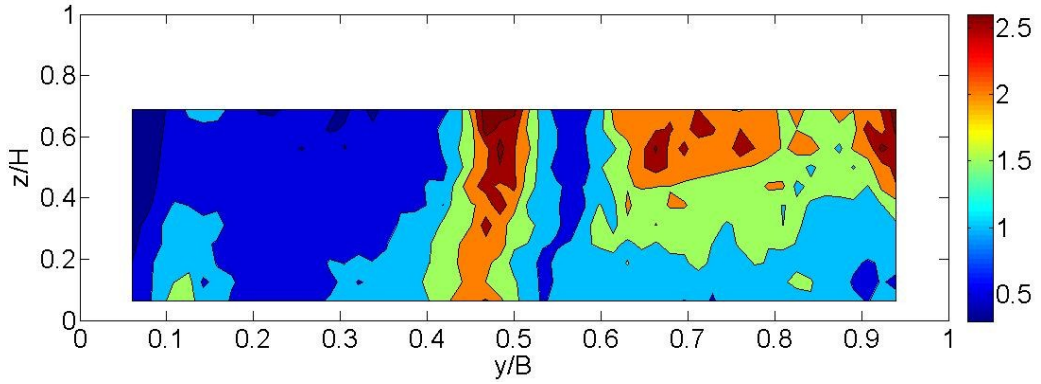

Figure 158: $u'v'$ Ejections and Sweeps to Other Events (BC1 F2)

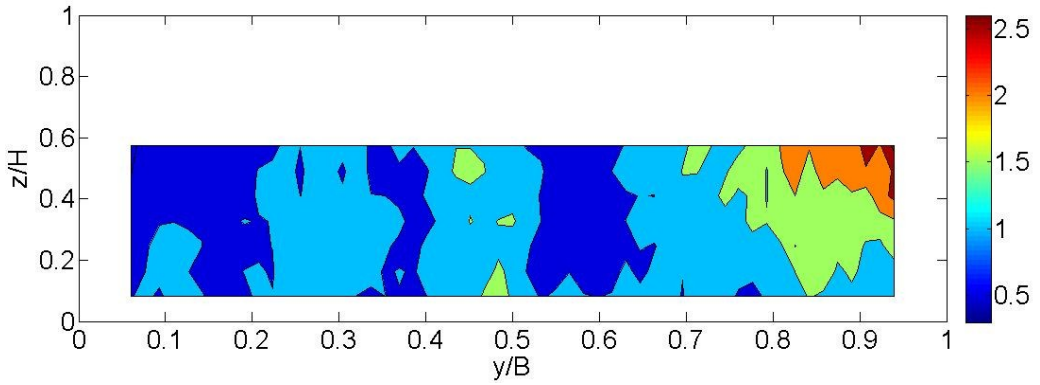

Figure 159: $u'v'$ Ejections and Sweeps to Other Events (BC2 F1 CS2)

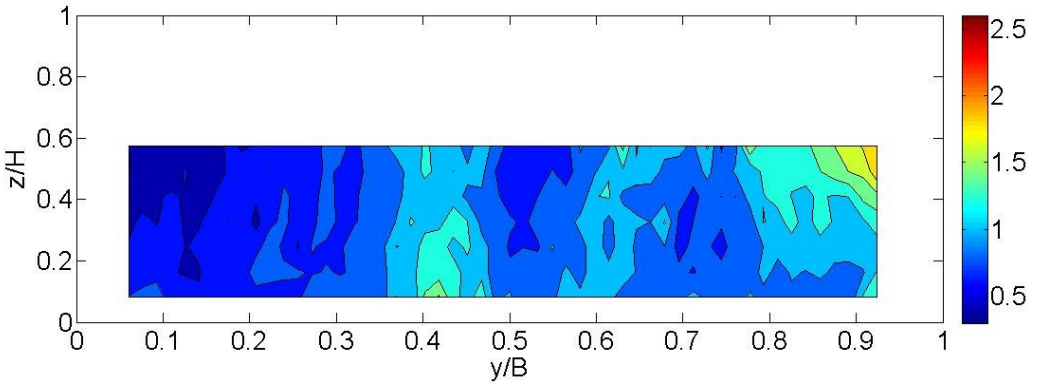

Figure 160: $u'v'$ Ejections and Sweeps to Other Events (BC2 F1 CS4)

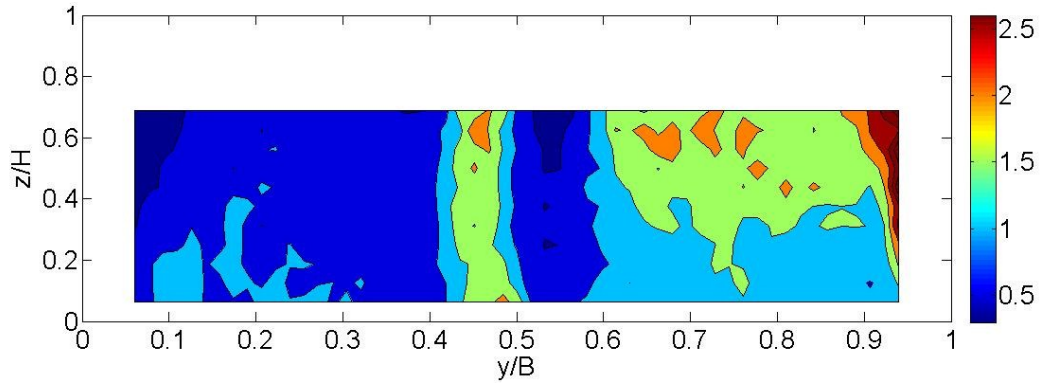

Figure 161: $u'v'$ Ejections and Sweeps to Other Events (BC2 F2 CS2)

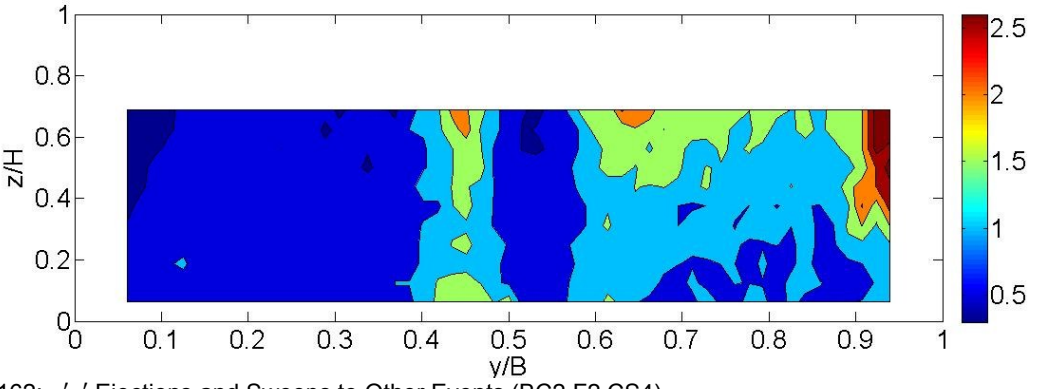

Figure 162: $u'v'$ Ejections and Sweeps to Other Events (BC2 F2 CS4)

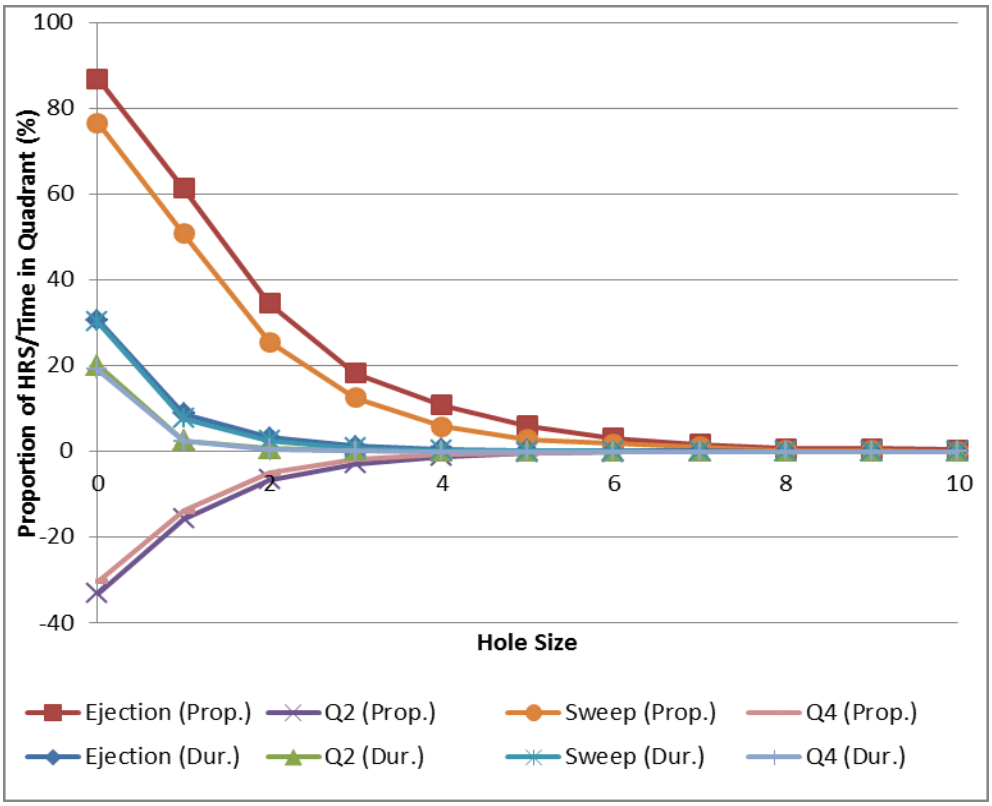

Figure 163: Variation of Proportion of τ_H^R/Time per Quadrant with Hole Size (BC1 F2; $y/B = 0.47, z/H = 0.08$; τ_H^R labelled as HRS in Figure)

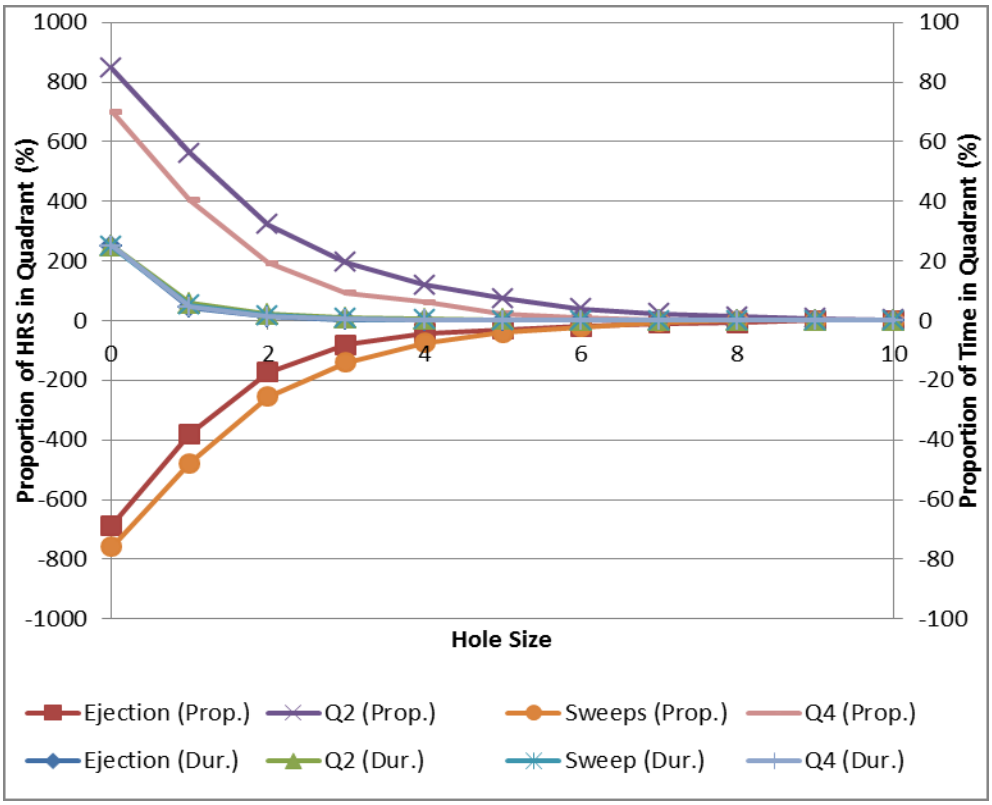

Figure 164: Variation of Proportion of τ_H^R/Time per Quadrant with Hole Size (BC1 F2; $y/B = 0.53, z/H = 0.08$; τ_H^R labelled as HRS in Figure)

8.4.6 Conditional Time-Series

A discrete conditional time-series analysis (as described in Section 4.5) was performed on selected data points in order to examine the coherence between the turbulent fluctuations in the velocity components. The continuous conditional series selection function, $I(t)$, was mimicked by determining which u measurements fell within the upper 2% of all measurements (termed peak measurements). For each velocity component, an ensemble of 8 second long ($-4 < \Im < +4$) time series of the normalised turbulent fluctuations (i.e. u'/σ_u, v'/σ_v or w'/σ_w) were then extracted from the full time-series, each centred on one of these peak u measurements, and the ensemble-mean series calculated. As mentioned in Section 4.5, the bounding value (in this case the extreme 2% of measurements) is somewhat arbitrary, though justifiable as it is the extreme ejection and sweep events which are of particular interest. An identical approach was used to detect trough measurements, those in the lowest 2% of u measurements.

Over the smooth side of the channel ($y/B = 0.26$, Figure 165 to Figure 172) and the RSB ($y/B = 0.50$, Figure 173 to Figure 180) there is a clear relationship between u and w for peak u events for $z/H \leq 0.25$, with peaks in u' appearing simultaneously with troughs in w'. It is evident, therefore, that such peaks are associated with sweep events, the downward motion of faster (streamwise) water. Above this level, while there is some evidence of coherence, the magnitude of the w' trough is insignificantly greater than that of other fluctuations seen in the w' series. Over the rough bed ($y/B = 0.74$, Figure 181 to Figure 188) the coherence remains evident throughout the water column, though (as in the previous cases) the magnitude of the w' trough

reduces significantly with depth (from approximately 50% of the u' peak magnitude at $z/H = 0.08$ to approximately 25% at $z/H = 0.25$).

Similarly, the minima of u', the u' troughs, are in step with maxima of w'. Such troughs are therefore associated with ejections of slower (streamwise) water upwards, away from the bed. Unlike the peak u' case, this coherence continues at all depths across the entire channel. For $z/H \geq 0.25$ the trough u' and w' time-series also seem to exhibit anti-phase coherence throughout the series (as also noted by Nezu and Nakagawa (1993), with synchronised u' troughs and w' peaks. Close to the bed, at $z/H = 0.08$, the coherence is limited to the time of the u' trough. This may be due to ejections of varying magnitude u' dissipating as they move upwards from the bed into the upper layers of the flow. While all such ejections may be of sufficiently high magnitude u' to fall within the 2% detection limit at the bed, higher in the flow u would increase (lower magnitude u') due to interaction with the main flow and so these ejections would not be detected directly under the 2% detection limit. If the ejections were periodic, these low magnitude ejections would occur at regular intervals with respect to the high magnitude ejections which are still detected in the upper regions of the flow, and would therefore be retained in the ensemble-mean averaging process, producing the ensemble-mean time series seen.

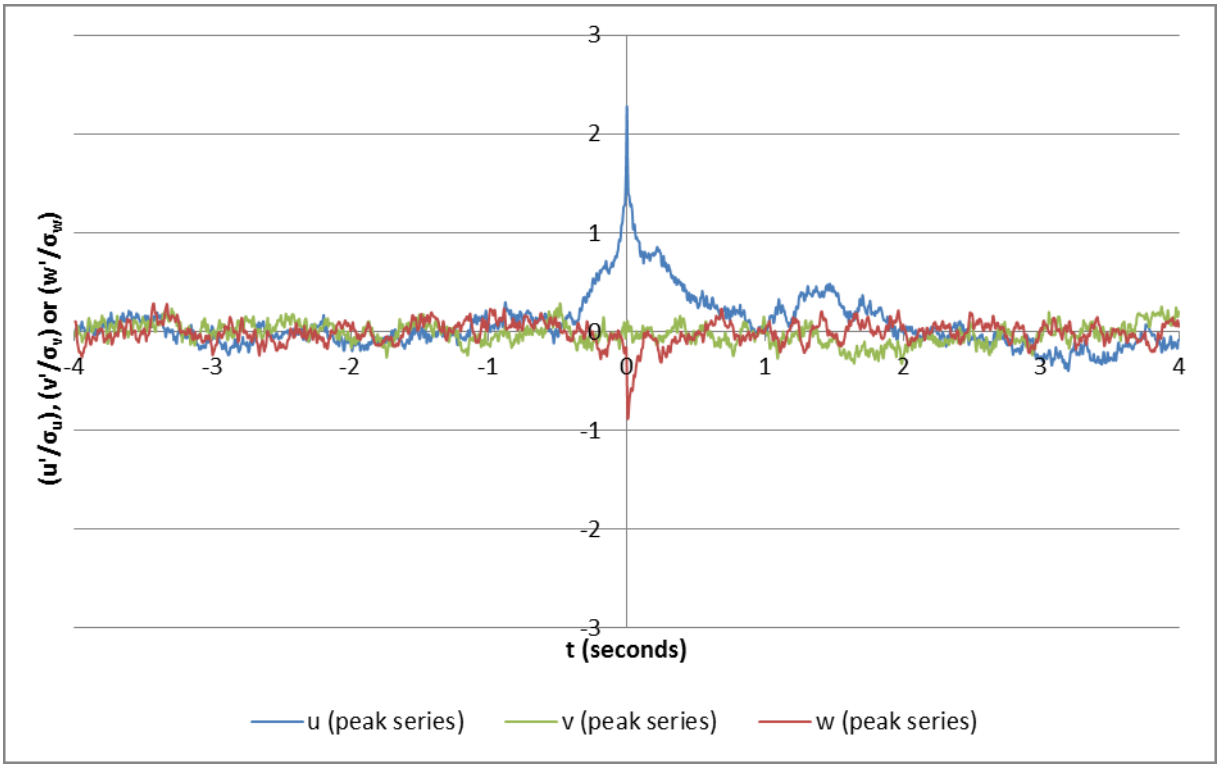

Figure 165: Peak Measurement Ensemble-Mean Time Series (BC1 F1, $y/B = 0.26, z/H = 0.08$)

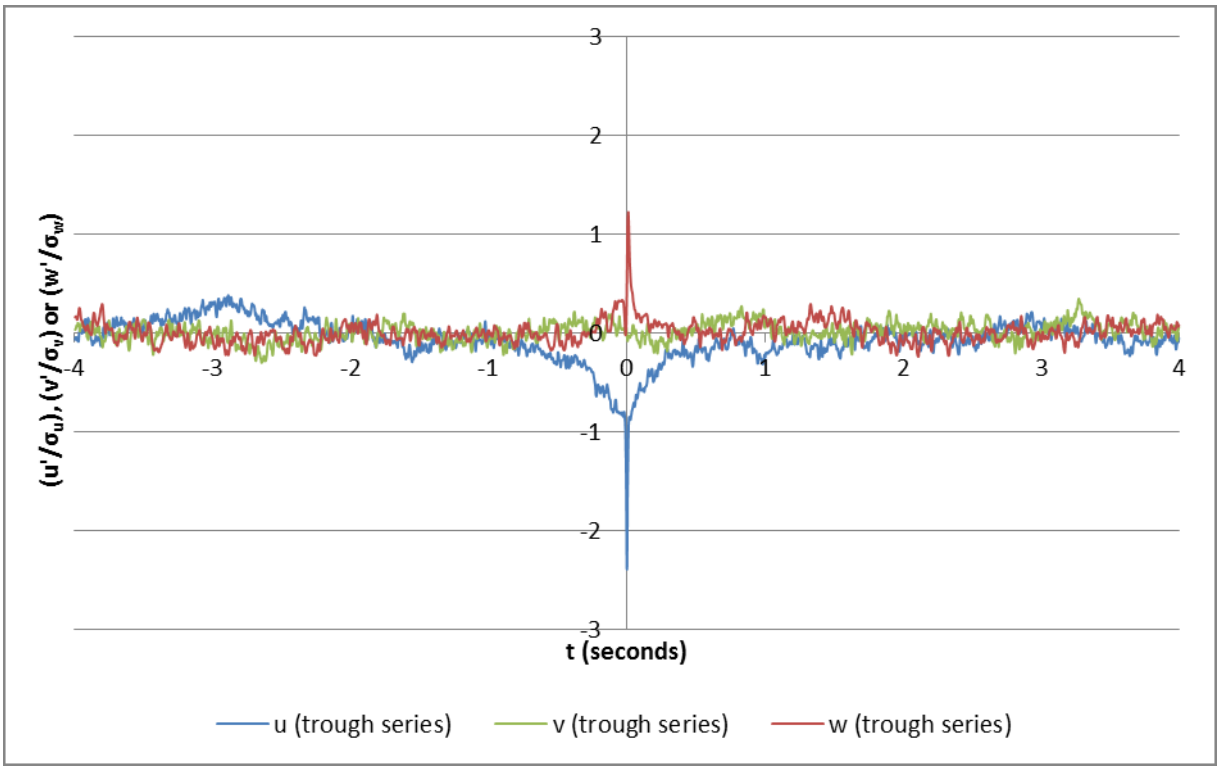

Figure 166: Trough Measurement Ensemble-Mean Time Series (BC1 F1, $y/B = 0.26, z/H = 0.08$)

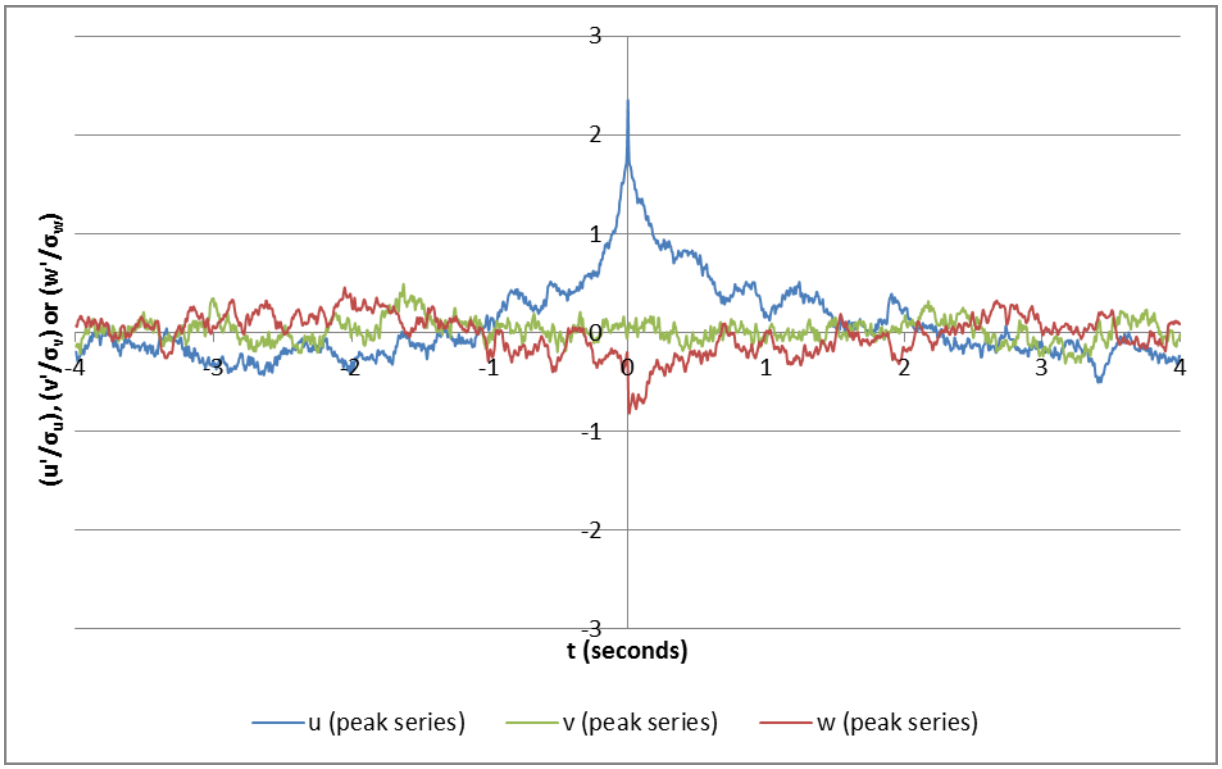

Figure 167: Peak Measurement Ensemble-Mean Time Series (BC1 F1, $y/B = 0.26, z/H = 0.25$)

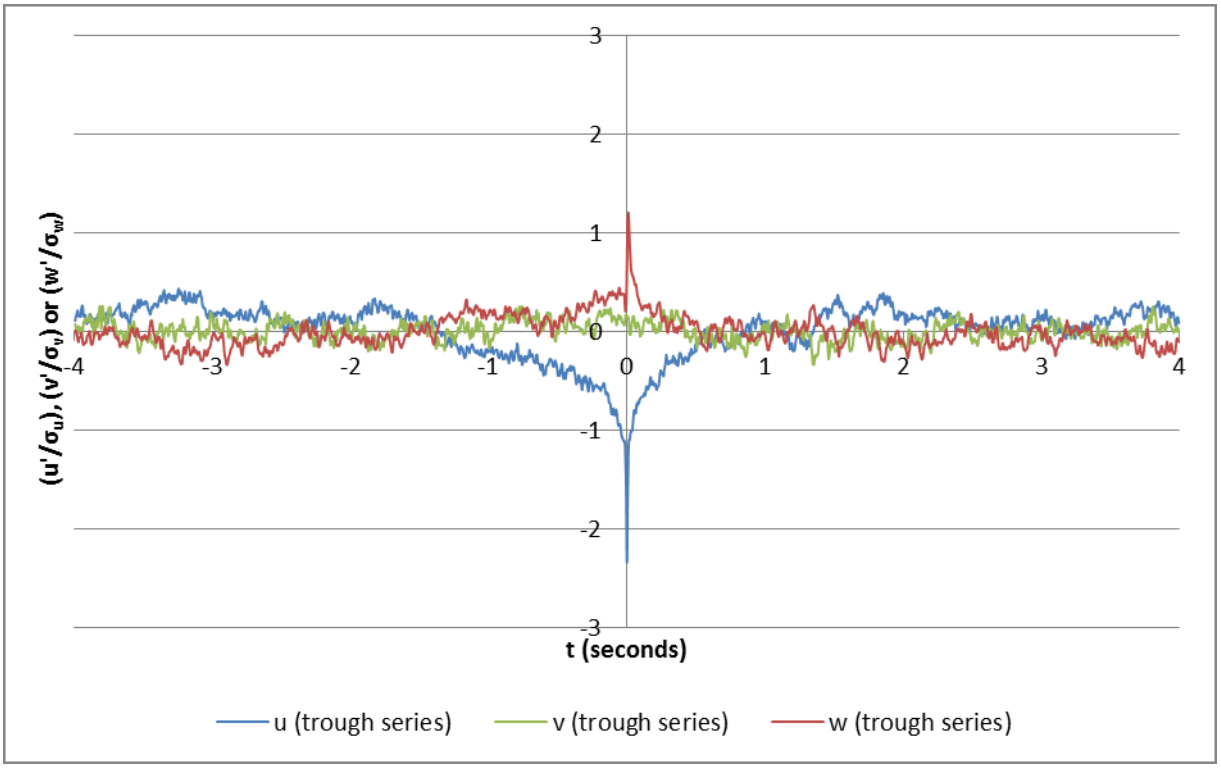

Figure 168: Trough Measurement Ensemble-Mean Time Series (BC1 F1, $y/B = 0.26, z/H = 0.25$)

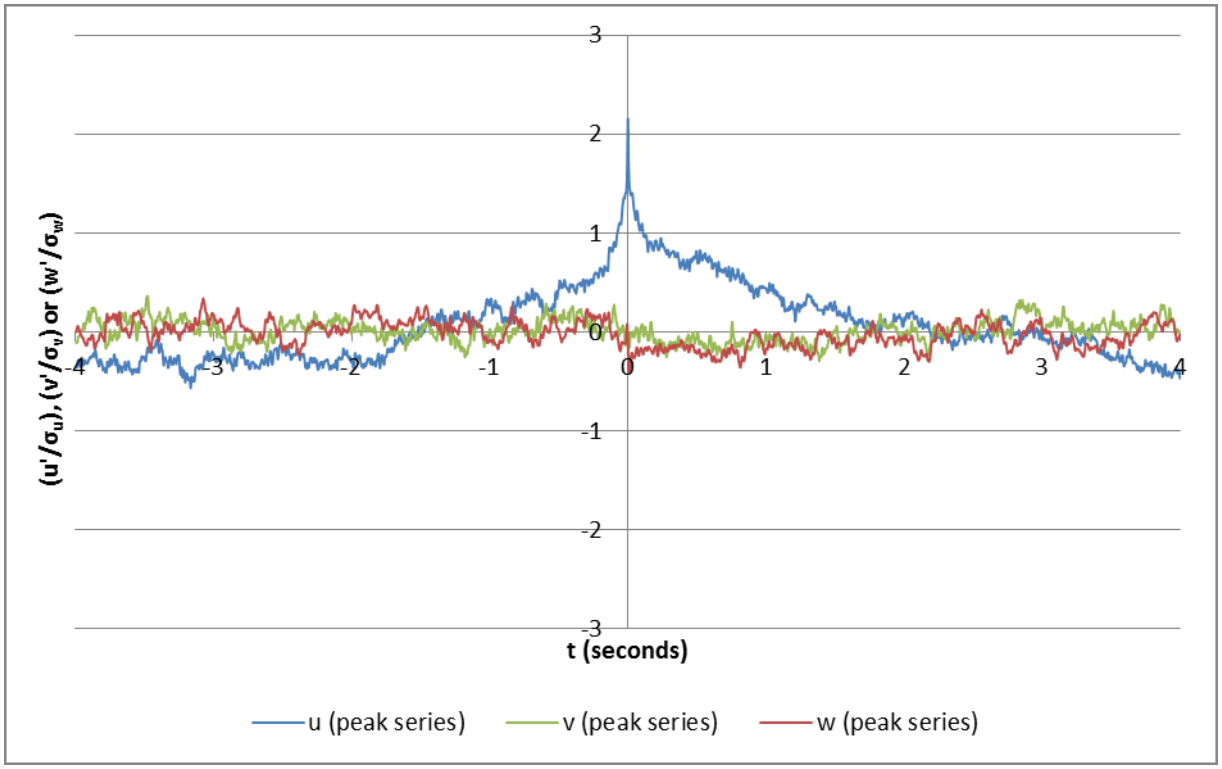

Figure 169: Peak Measurement Ensemble-Mean Time Series (BC1 F1, $y/B = 0.26, z/H = 0.41$)

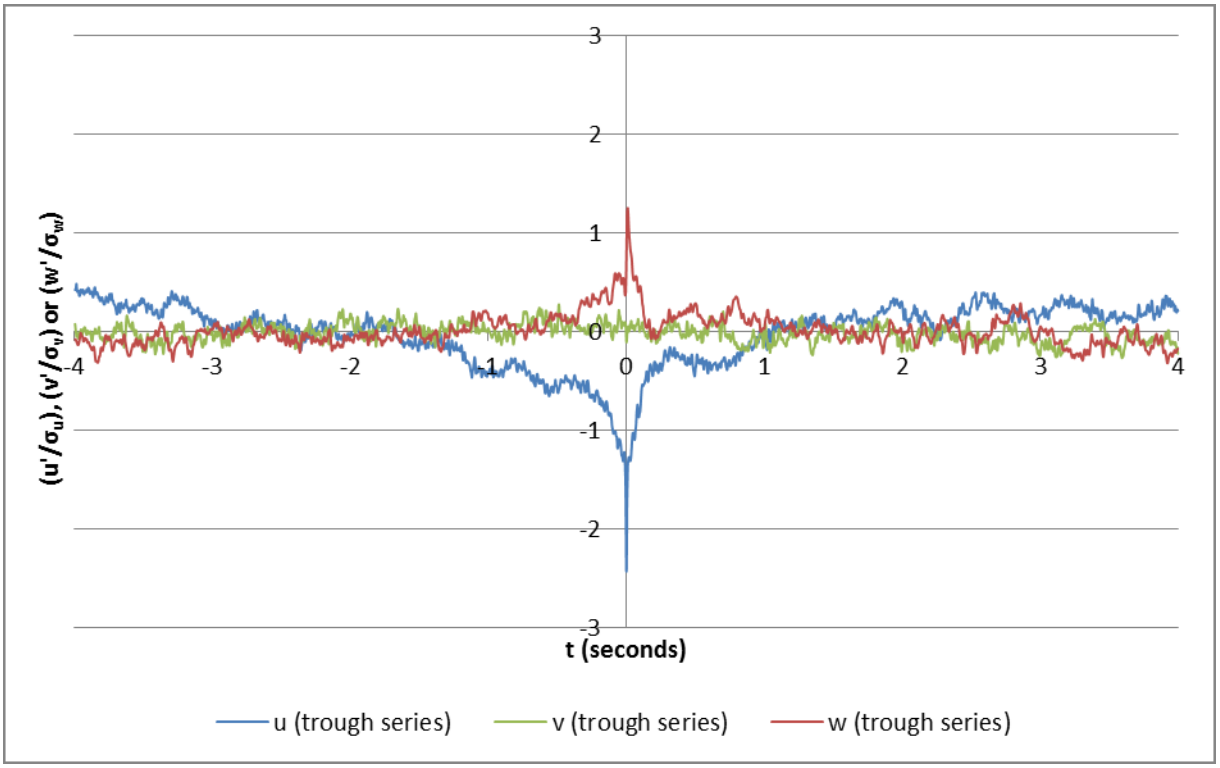

Figure 170: Trough Measurement Ensemble-Mean Time Series (BC1 F1, $y/B = 0.26, z/H = 0.41$)

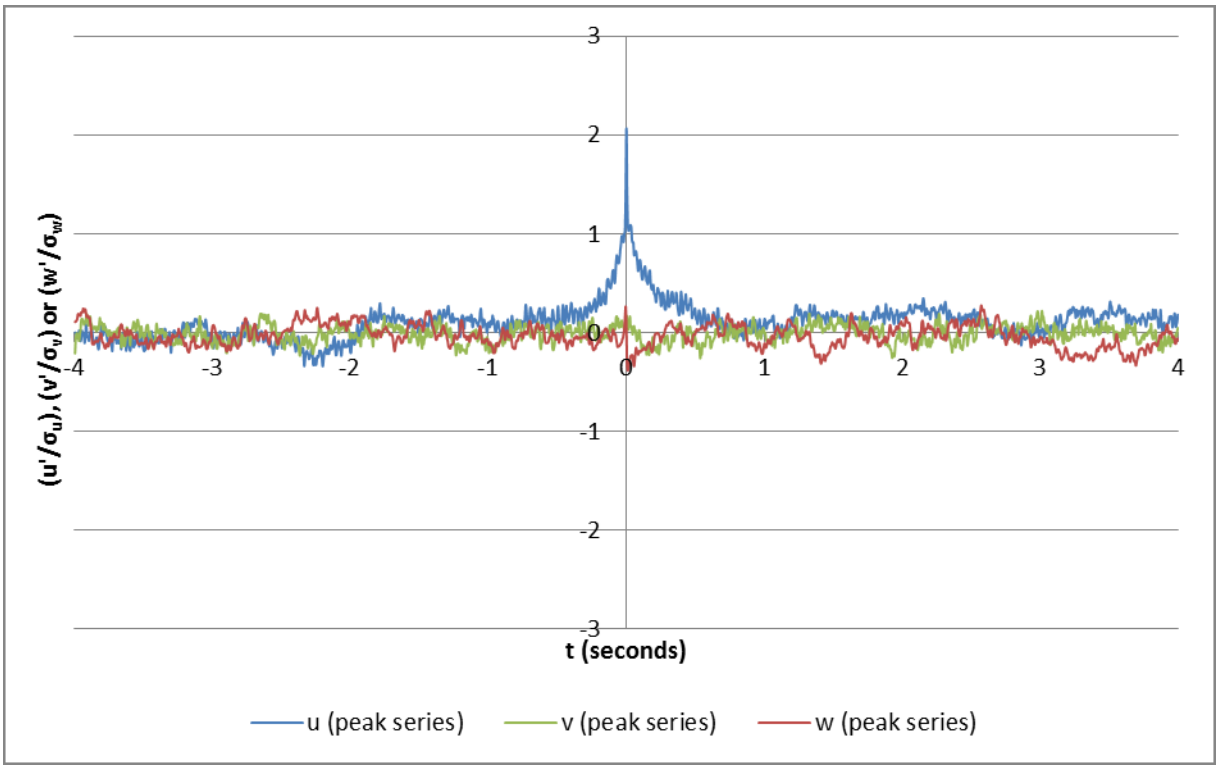

Figure 171: Peak Measurement Ensemble-Mean Time Series (BC1 F1, $y/B = 0.26, z/H = 0.57$)

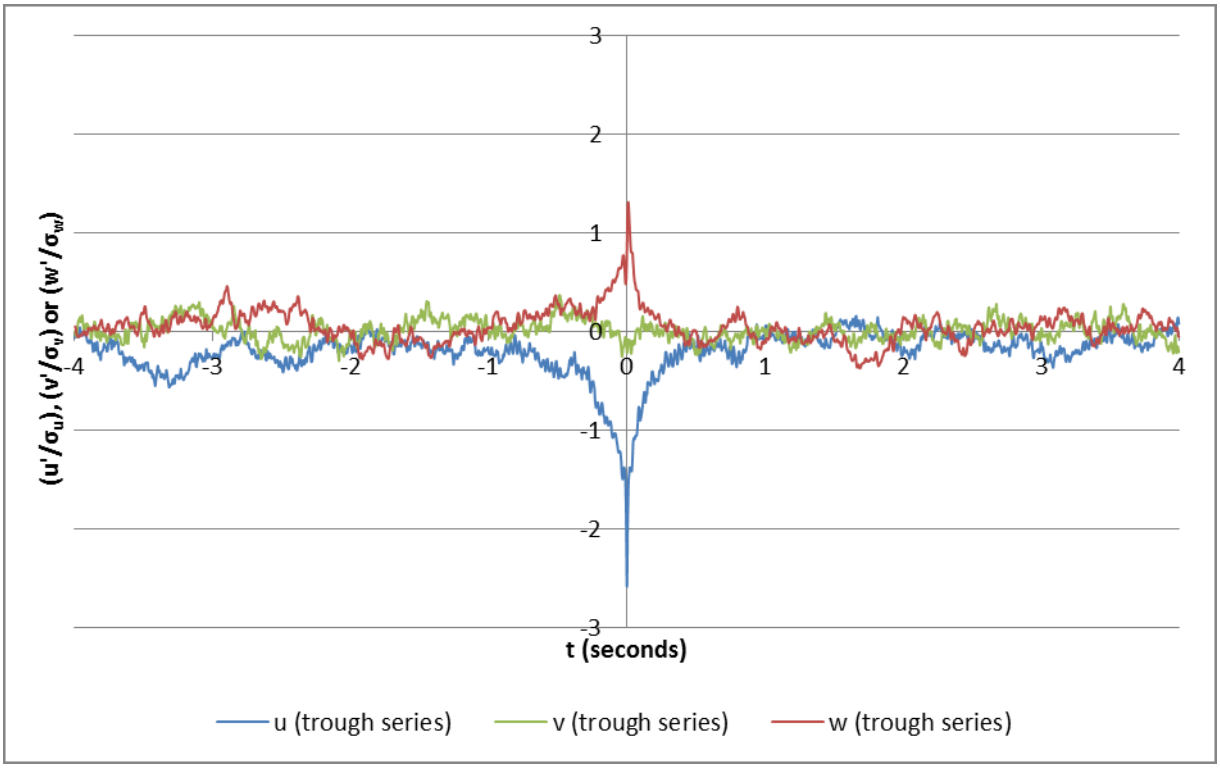

Figure 172: Trough Measurement Ensemble-Mean Time Series (BC1 F1, $y/B = 0.26, z/H = 0.57$)

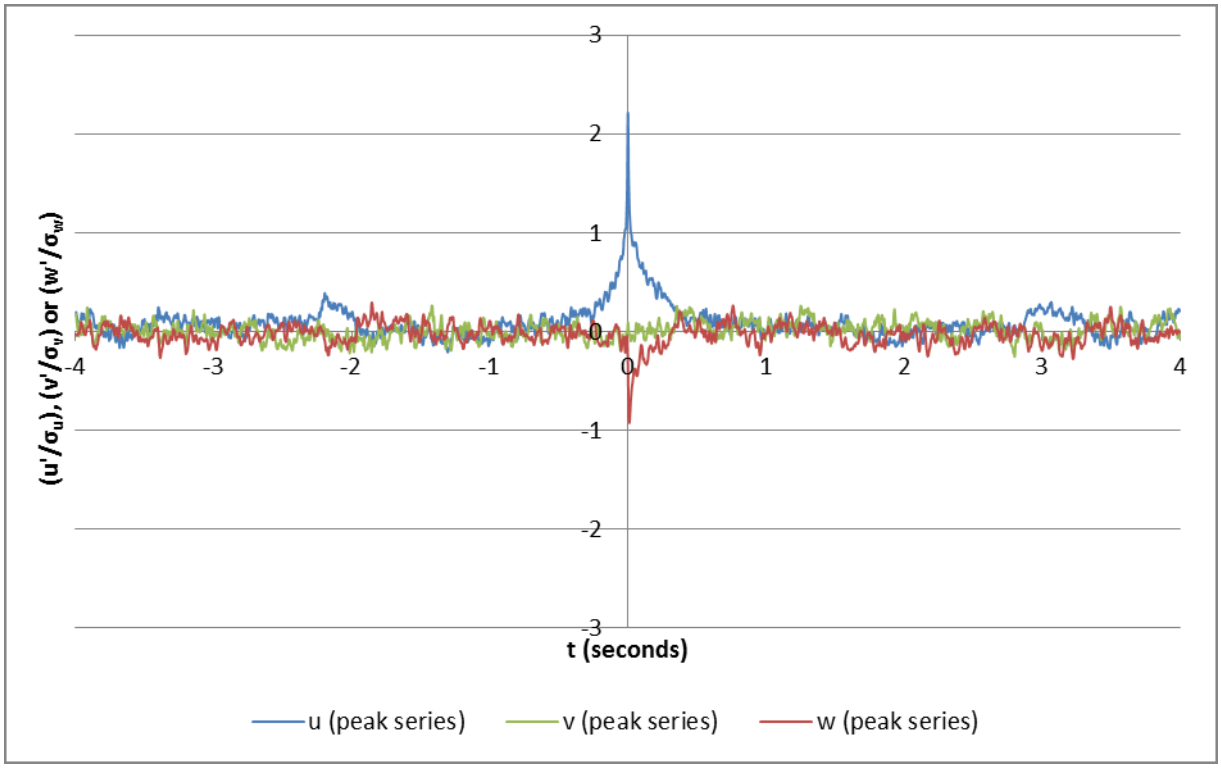

Figure 173: Peak Measurement Ensemble-Mean Time Series (BC1 F1, $y/B = 0.50, z/H = 0.08$)

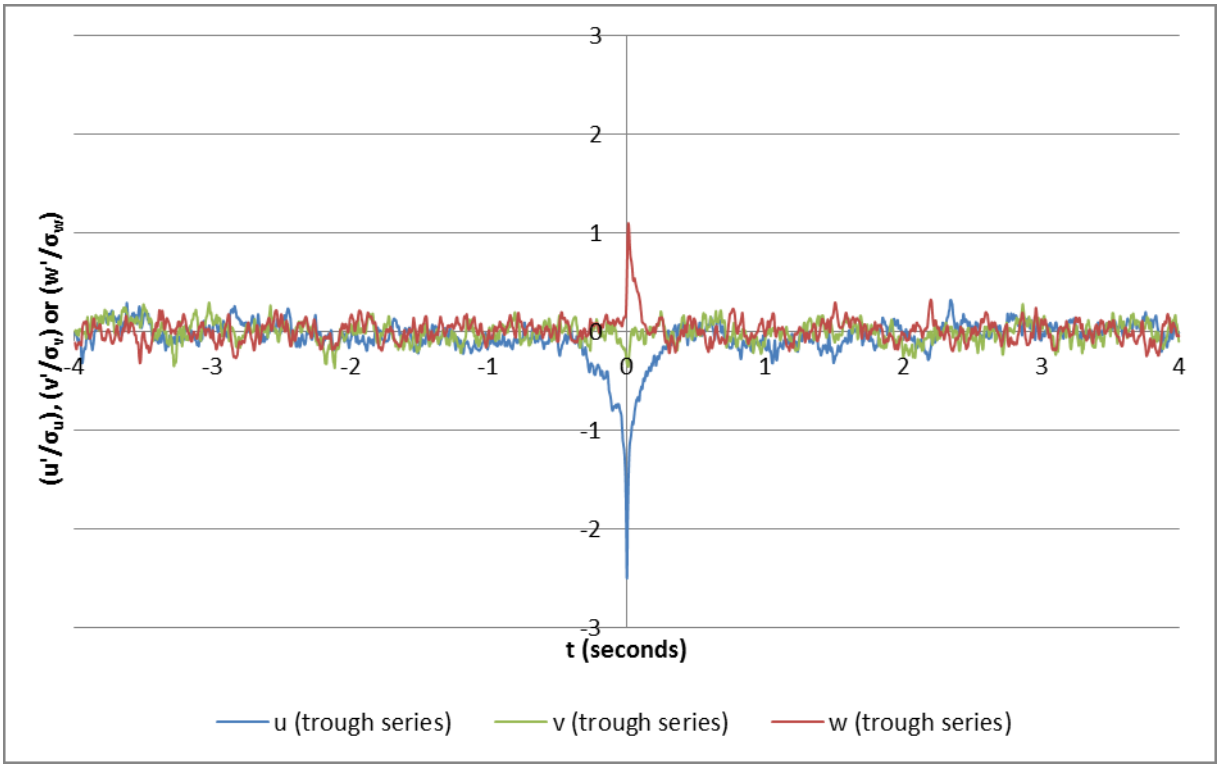

Figure 174: Trough Measurement Ensemble-Mean Time Series (BC1 F1, $y/B = 0.50, z/H = 0.08$)

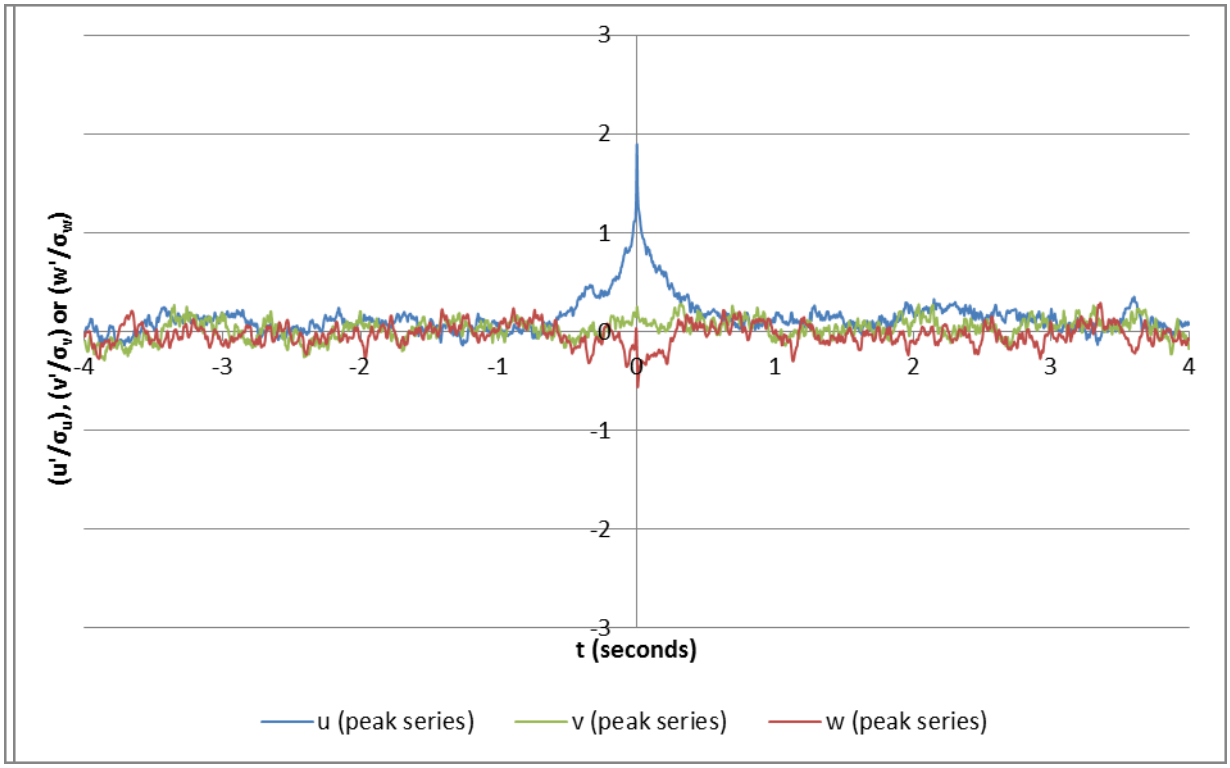

Figure 175: Peak Measurement Ensemble-Mean Time Series (BC1 F1, $y/B = 0.50, z/H = 0.25$)

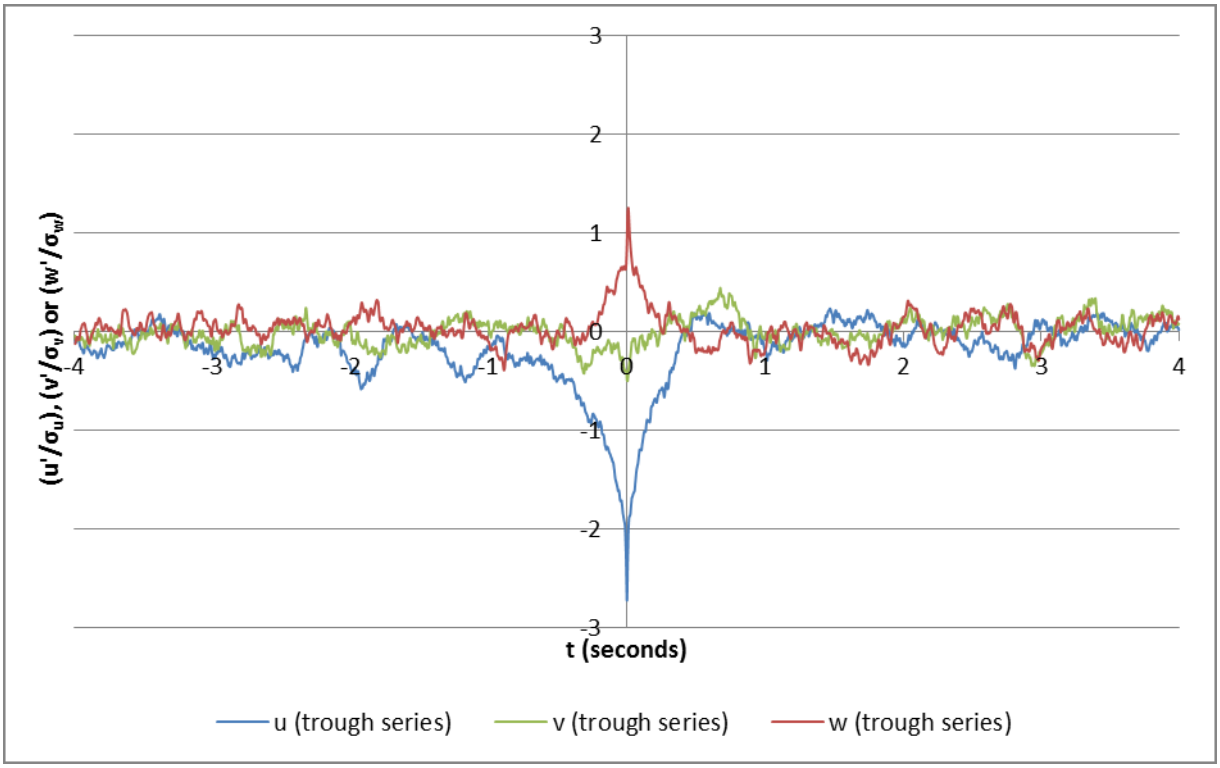

Figure 176: Trough Measurement Ensemble-Mean Time Series (BC1 F1, $y/B = 0.50, z/H = 0.25$)

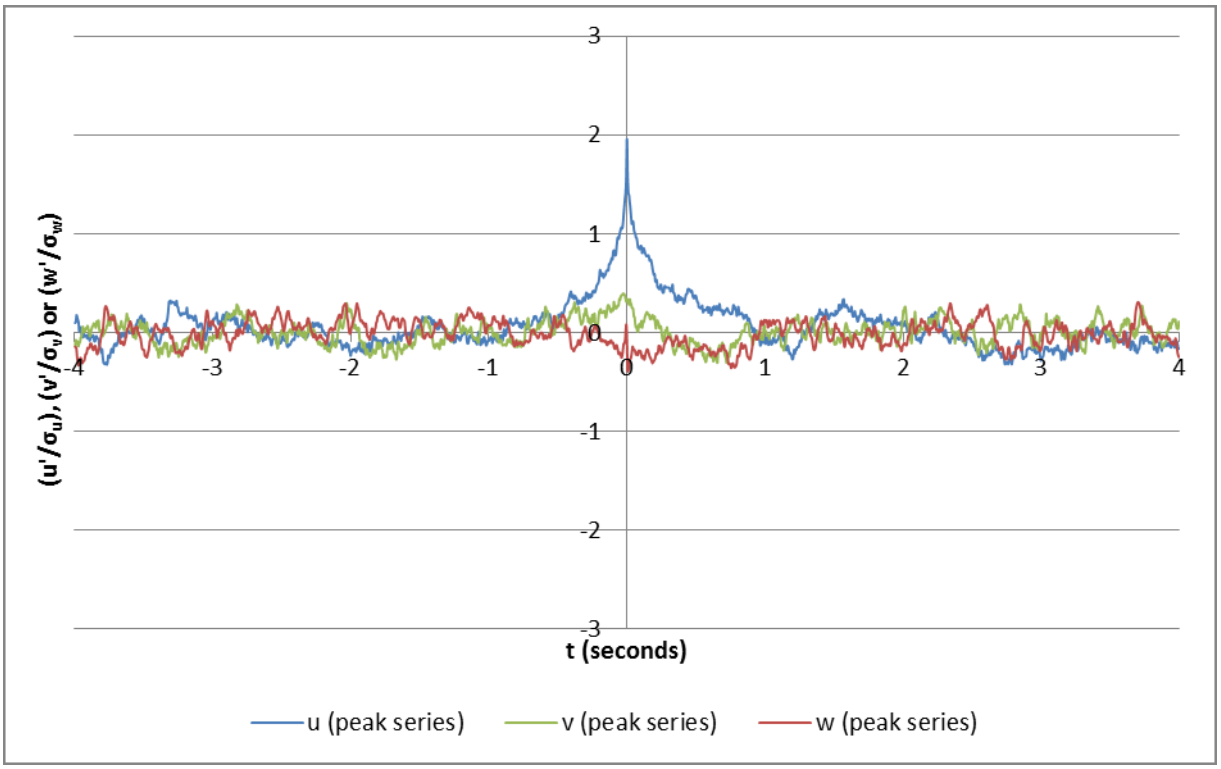

Figure 177: Peak Measurement Ensemble-Mean Time Series (BC1 F1, $y/B = 0.50, z/H = 0.41$)

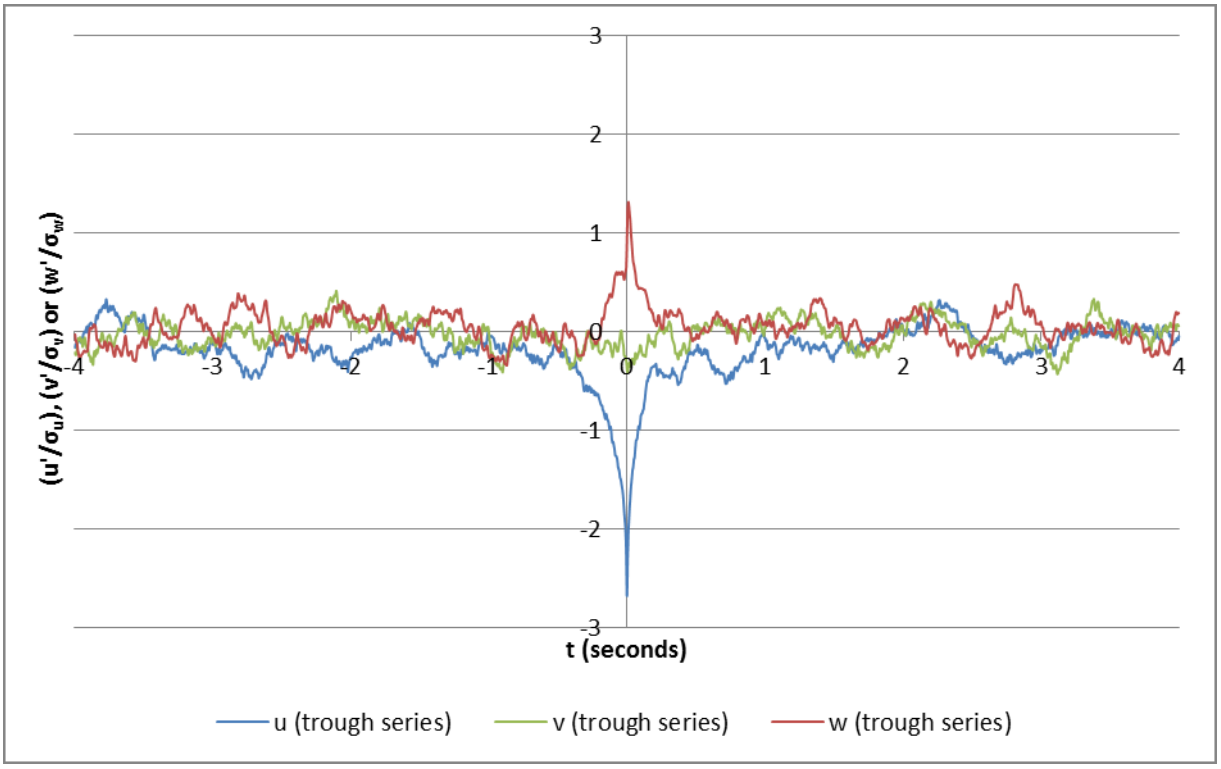

Figure 178: Trough Measurement Ensemble-Mean Time Series (BC1 F1, $y/B = 0.50, z/H = 0.41$)

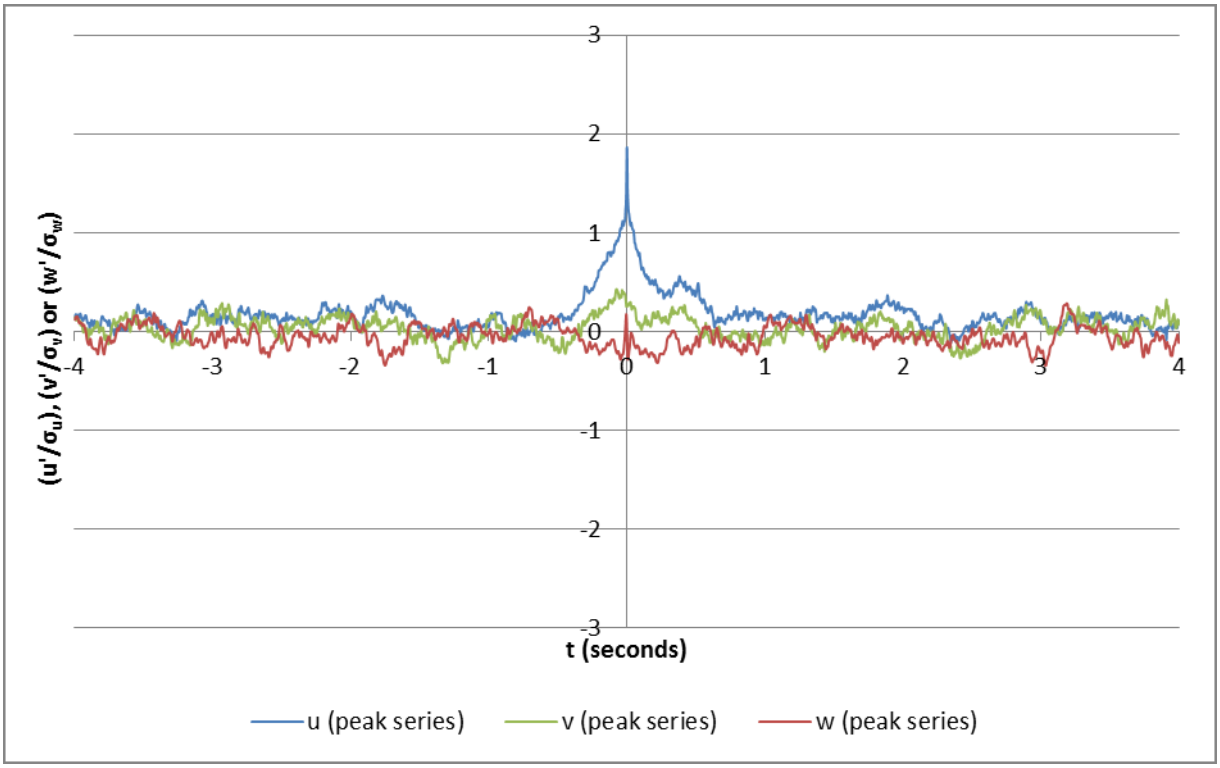

Figure 179: Peak Measurement Ensemble-Mean Time Series (BC1 F1, $y/B = 0.50, z/H = 0.57$)

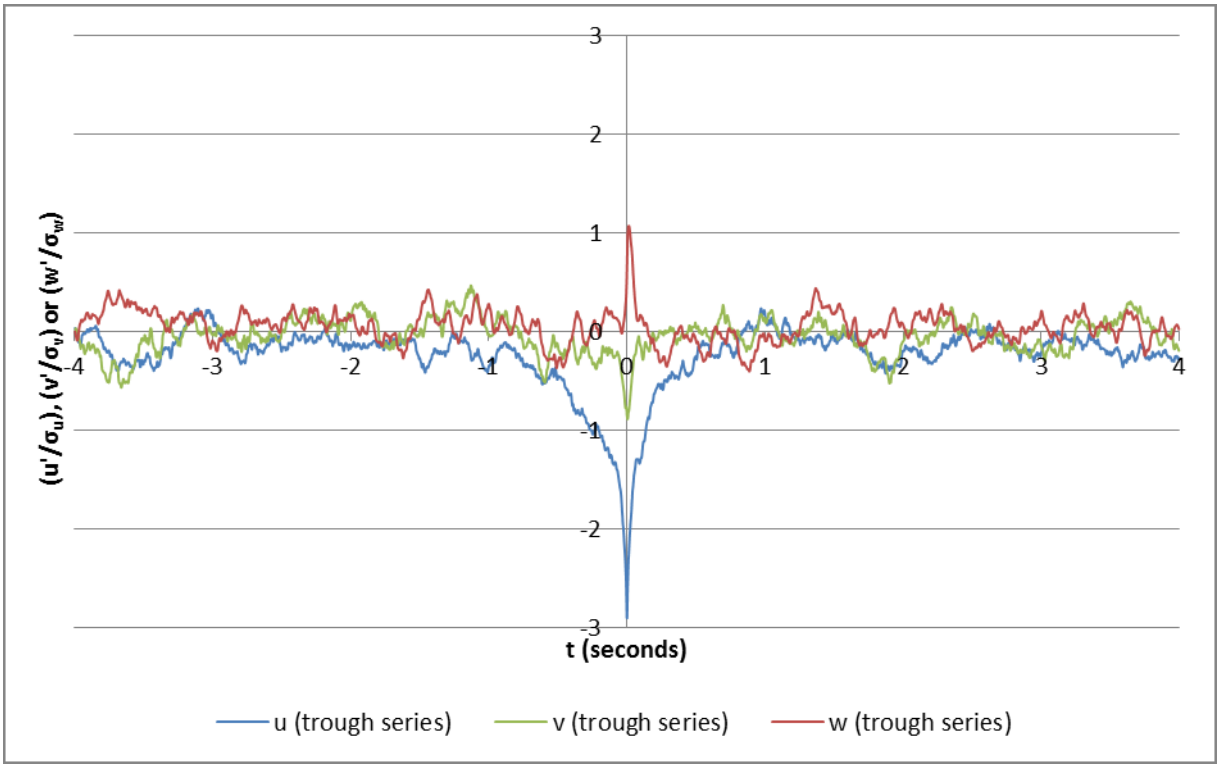

Figure 180: Trough Measurement Ensemble-Mean Time Series (BC1 F1, $y/B = 0.50, z/H = 0.57$)

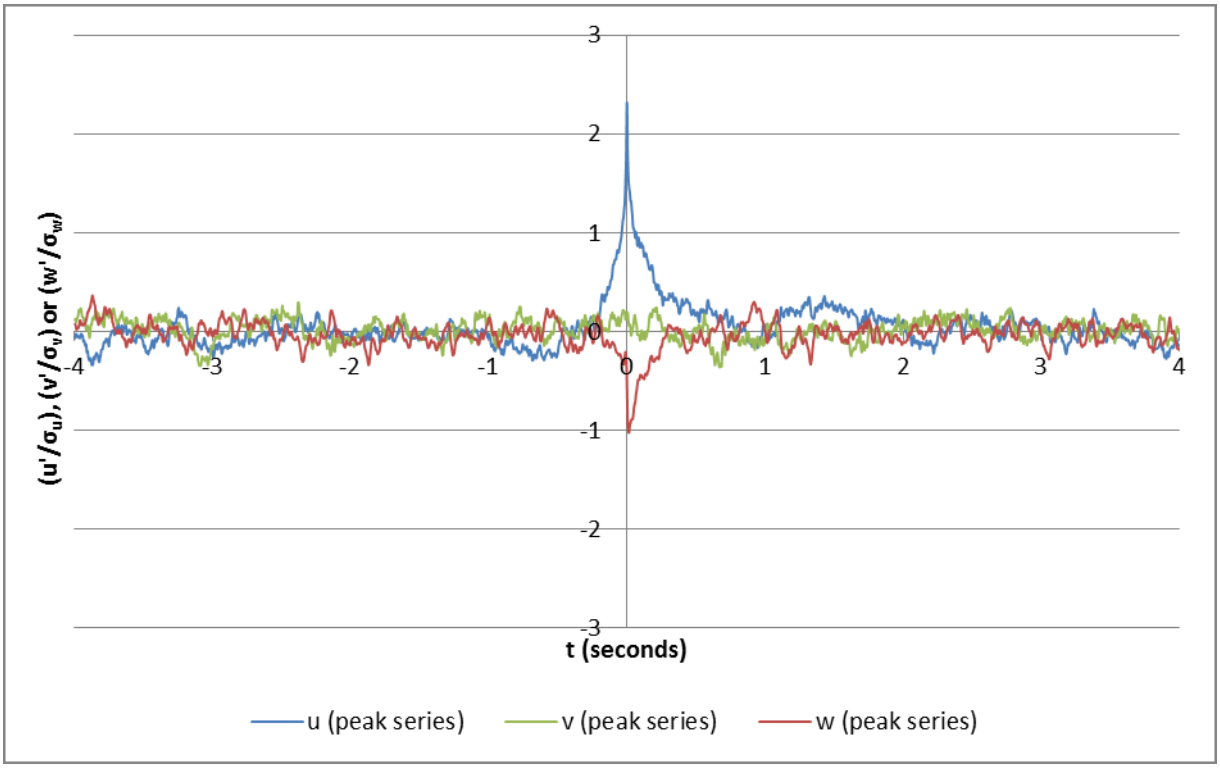

Figure 181: Peak Measurement Ensemble-Mean Time Series (BC1 F1, $y/B = 0.74, z/H = 0.08$)

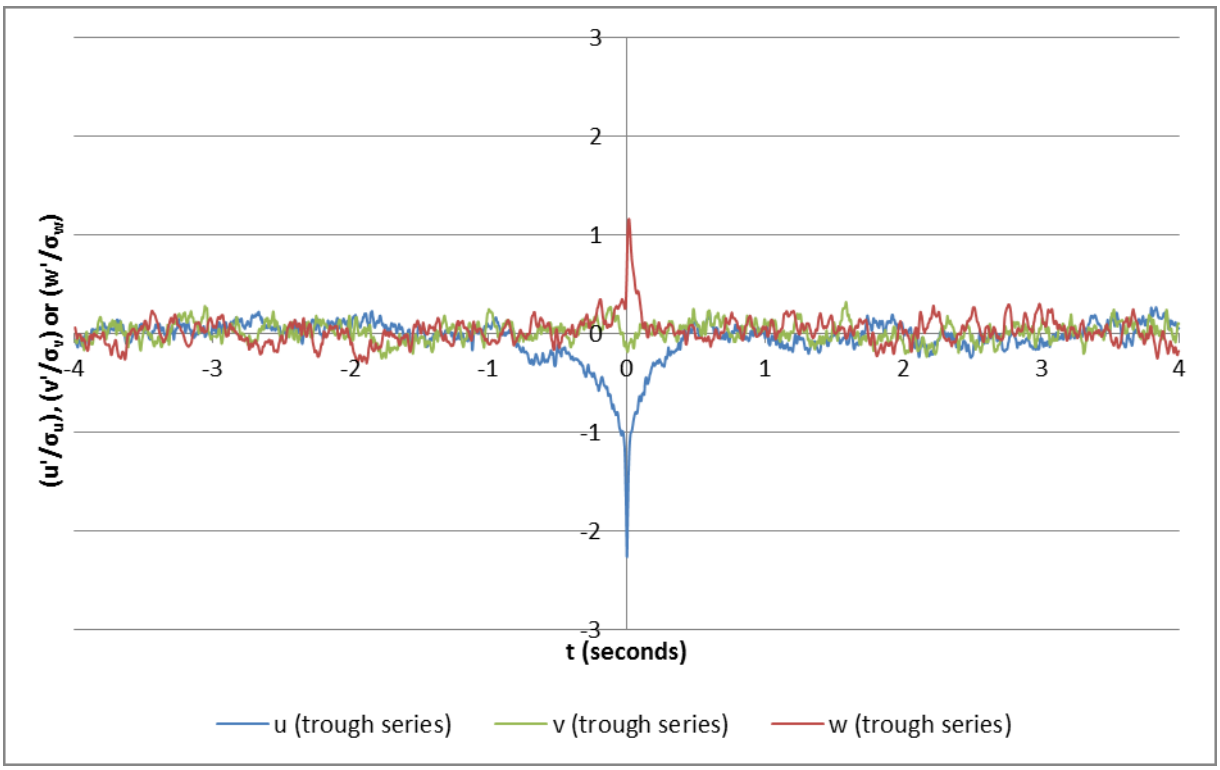

Figure 182: Trough Measurement Ensemble-Mean Time Series (BC1 F1, $y/B = 0.74, z/H = 0.08$)

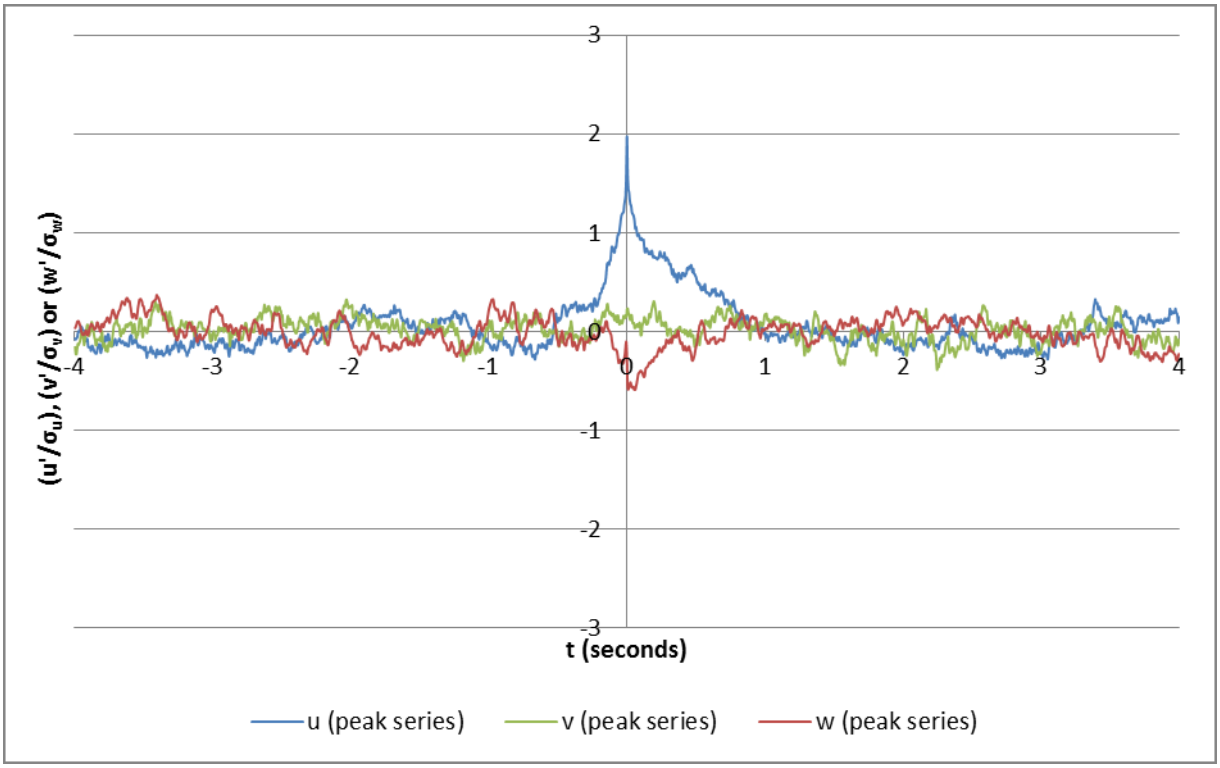

Figure 183: Peak Measurement Ensemble-Mean Time Series (BC1 F1, $y/B = 0.74, z/H = 0.25$)

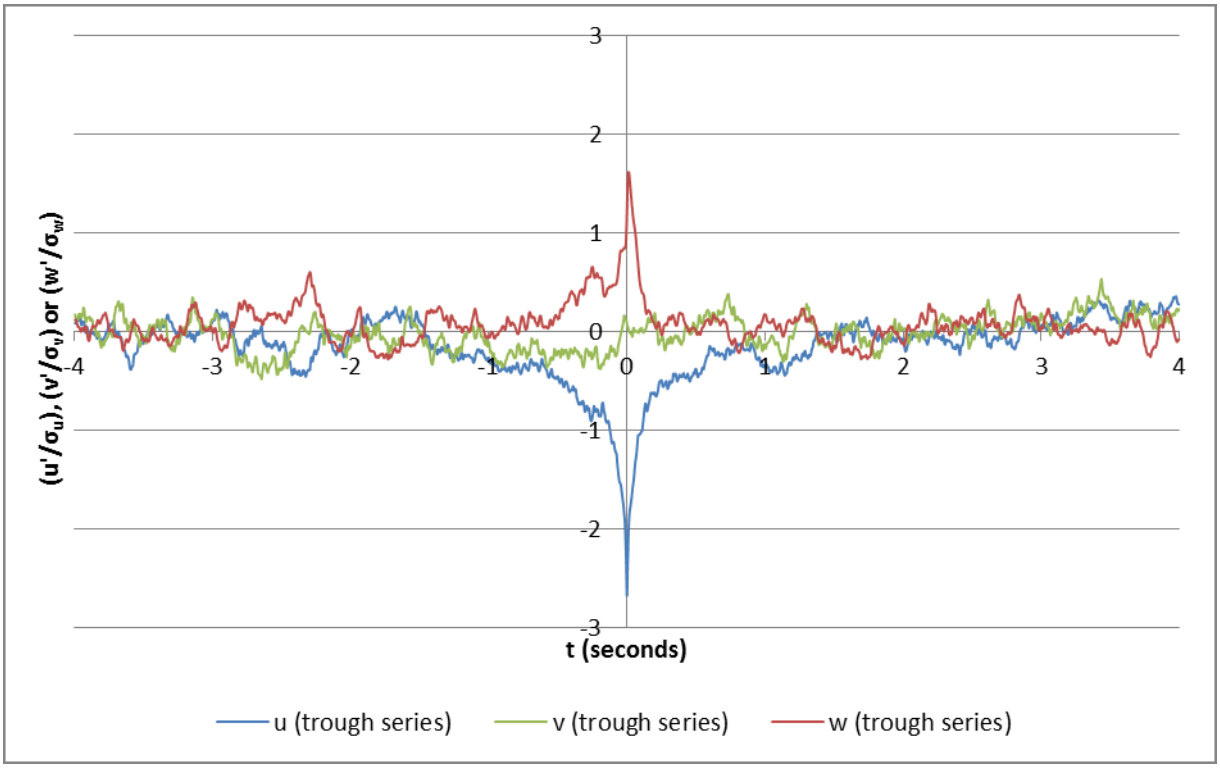

Figure 184: Trough Measurement Ensemble-Mean Time Series (BC1 F1, $y/B = 0.74, z/H = 0.25$)

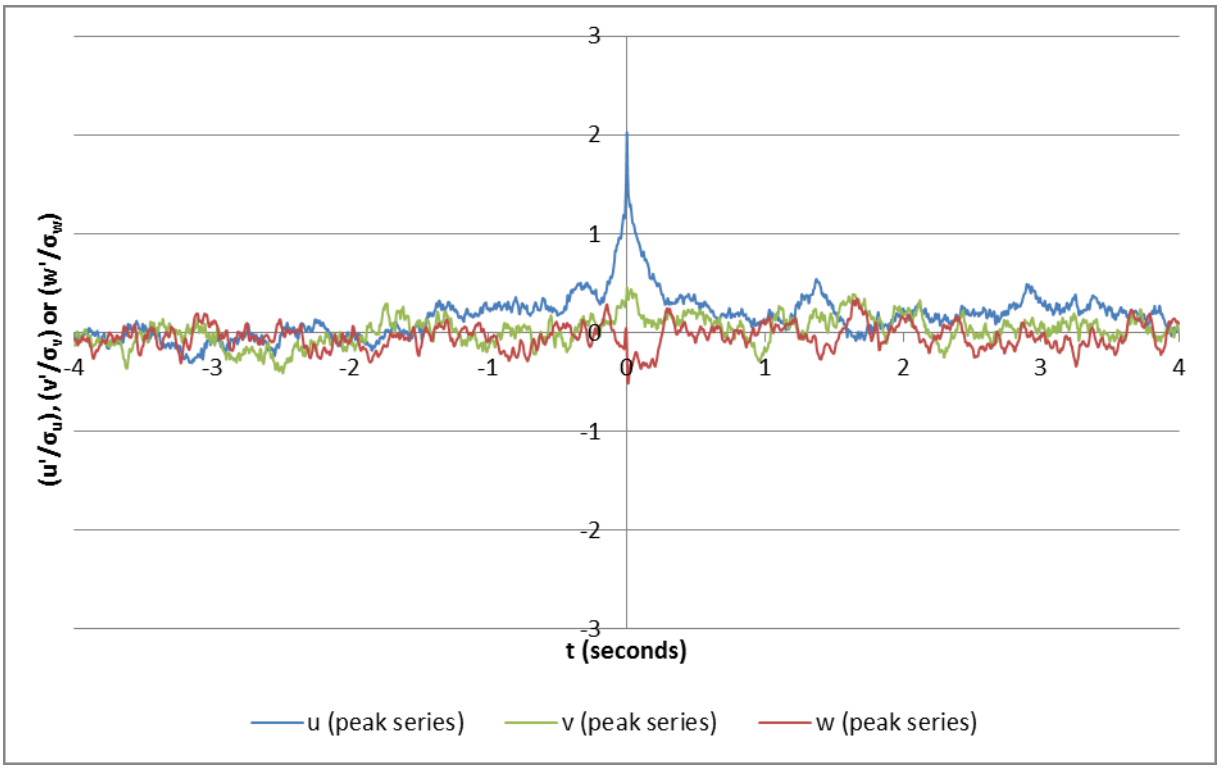

Figure 185: Peak Measurement Ensemble-Mean Time Series (BC1 F1, $y/B = 0.74, z/H = 0.41$)

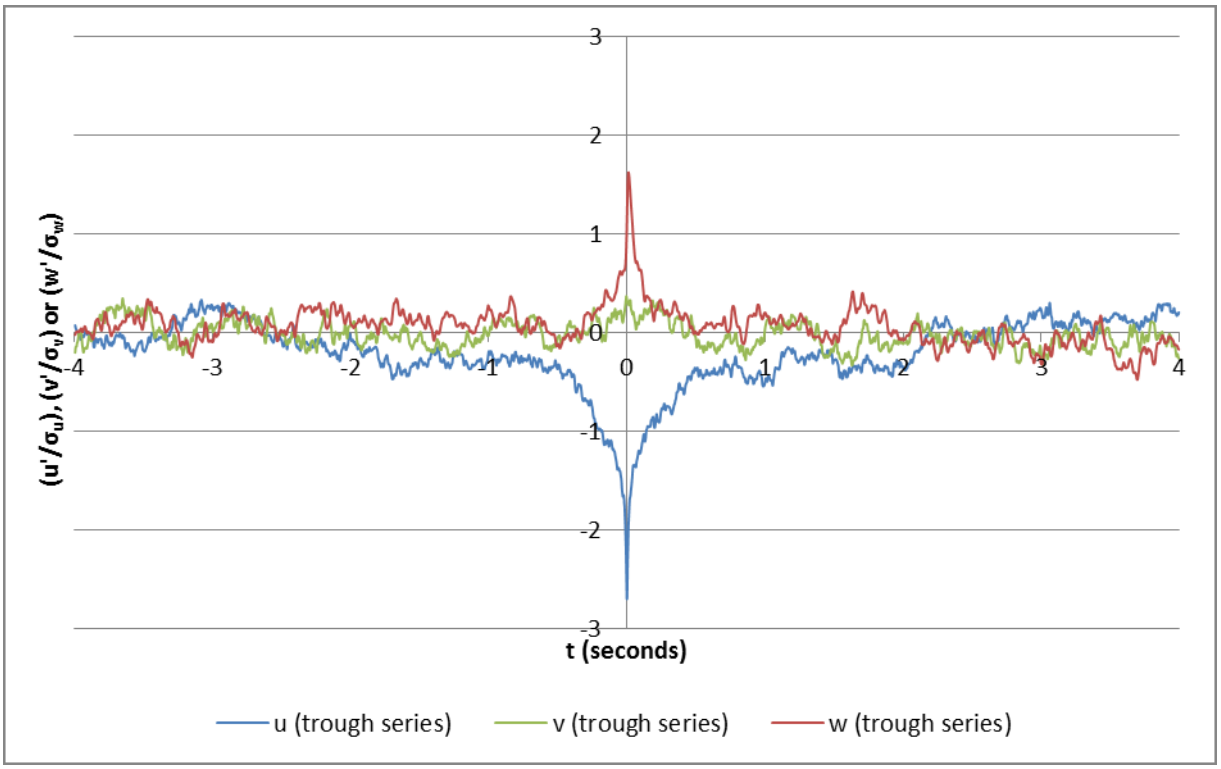

Figure 186: Trough Measurement Ensemble-Mean Time Series (BC1 F1, $y/B = 0.74, z/H = 0.41$)

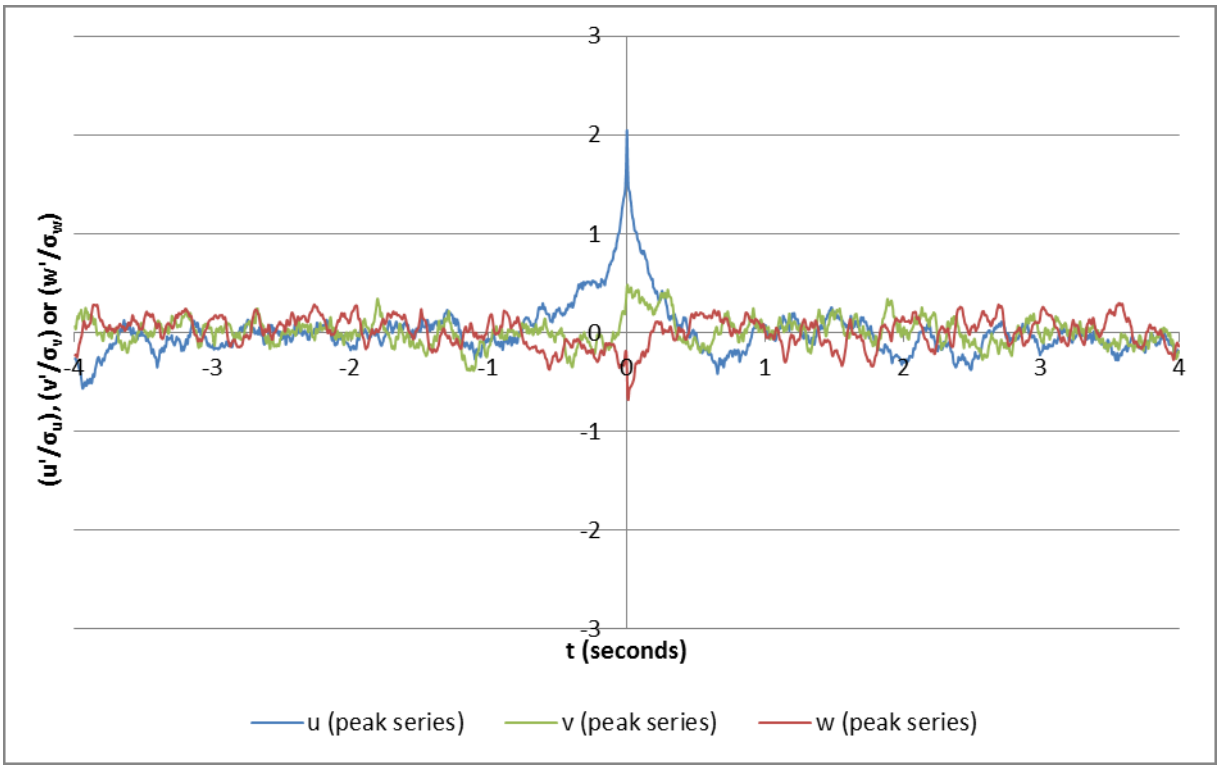

Figure 187: Peak Measurement Ensemble-Mean Time Series (BC1 F1, $y/B = 0.74, z/H = 0.57$)

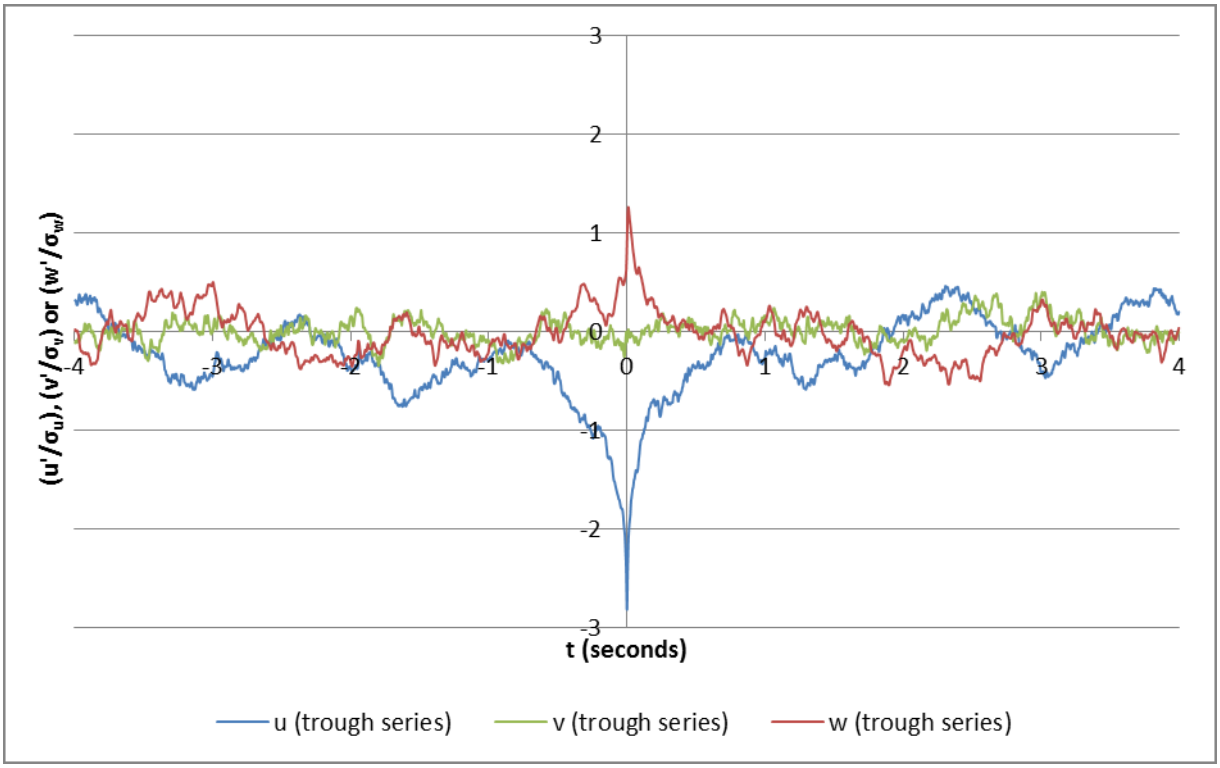

Figure 188: Trough Measurement Ensemble-Mean Time Series (BC1 F1, $y/B = 0.74, z/H = 0.57$)

For the horizontal case (u', v') coherence is only evident at the RSB (as would be expected) and there only at the uppermost measured level, $z/H = 0.57$. Conditional time-series analysis of other data points in the upper levels close to the RSB (not shown) reveal similar results to those seen here for the $y/B = 0.50$, $z/H = 0.57$ case – slight peaks in v' corresponding to peaks in u' and sharp, higher magnitude troughs in v' corresponding to troughs in u'. Bearing in mind the quadrant switch when analysing the horizontal Reynolds stress, these are evidence of horizontal ejections and sweeps at the RSB, albeit of a much lower magnitude than in the case of the vertical Reynolds stress.

The above analysis is made from a detailed study of the data from BC1 F1 – inspection of a selection of corresponding data points indicates that it is equally valid for BC1 F2 (see Appendix A for a selection of figures for other data sets). For the BC2 data sets, the results near the bed match those for BC1. However, differences are apparent at the $z/H \cong 0.57$ level for the peak u case, where the coherence is reduced (as for the smooth side for BC1) for both the rough and the smooth sides. Interestingly, when both CS2 and CS4 are examined (for both F1 and F2) the differences between the two cross-sections are negligible. Also noteworthy is that for BC2 F1 CS2 and CS4 u' and w' maintain their coherence at $y/B \cong 0.50$-$z/H \cong 0.57$ to a much higher degree than on either the rough side or smooth side, or at the RSB for any other data sets (Figure 189). More data would be required to investigate this further, though an examination of the data point at the same absolute depth ($z = 70mm$) for BC2 F2 indicates that this is not related to absolute depth rather than relative depth.

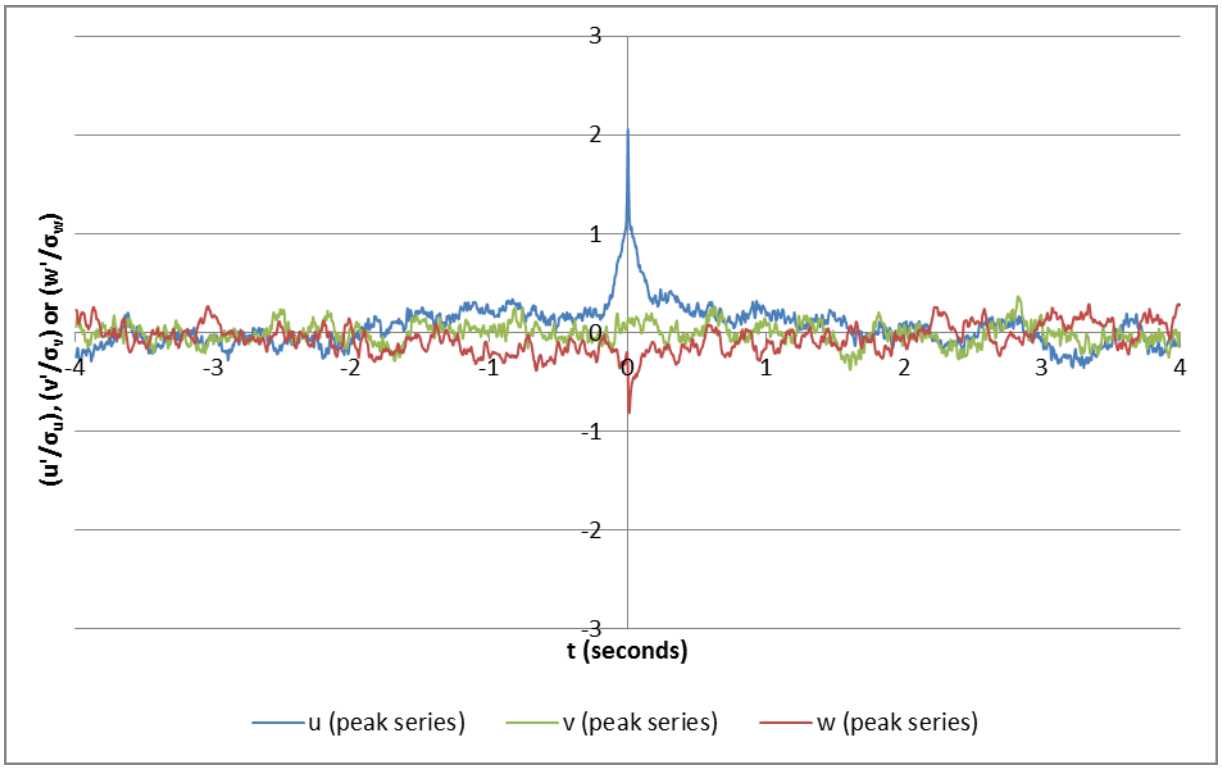

Figure 189: Peak Measurement Ensemble-Mean Time Series (BC2 F1 CS4, $y/B = 0.50, z/H = 0.57$)

9 BOUNDARY SHEAR STRESS

9.1 Measurement and Estimation

As discussed in Section 5.3.6, the boundary shear stress was measured directly over the smooth bed using a Preston tube and associated static-pressure tube. These measurements are subject to an experimental error of approximately $0.05Nm^{-2}$, as discussed in Section 5.3.6. As illustrated by Figure 190, where the boundary shear stress was measured twice for a cross-section the two sets of measurements were, for a high proportion of points, equal to within this experimental error.

The boundary shear stress, τ_b, can also be estimated in a number of ways (see Section 3.8), and similar methods have been applied to the experimental data, with the combined results presented here.

The methods used to estimate τ_b are:

A. Linear extrapolation of the vertical distribution of τ_V^R
B. Linear extrapolation of the τ_V^R at the two points nearest the bed
C. Mean value of the three points nearest the channel bed
D. For the smooth side, application of the log-law of the wall, calculating U_* by iteration using (76) and taking the mean of the valid values (i.e. those for which $26 < \frac{zU_*}{\upsilon} < 0.2\frac{HU_*}{\upsilon}$ (Nezu et al., 1993, Nezu and Nakagawa, 1993))

$$U = U_*\left[\frac{1}{\kappa} ln\left(\frac{zU_*}{\upsilon}\right) + 5\right] \tag{76}$$

The equivalent rough-side equation to (76):

$$U = U_* \left[\frac{1}{\kappa} ln\left(\frac{z}{k_s}\right) + 8.5\right] \tag{77}$$

could not be applied since the Nikuradse equivalent sand-roughness, k_s, is unknown for the channel. However, k_s was estimated using shear velocity values calculated from the τ_b estimates made using methods A to C.

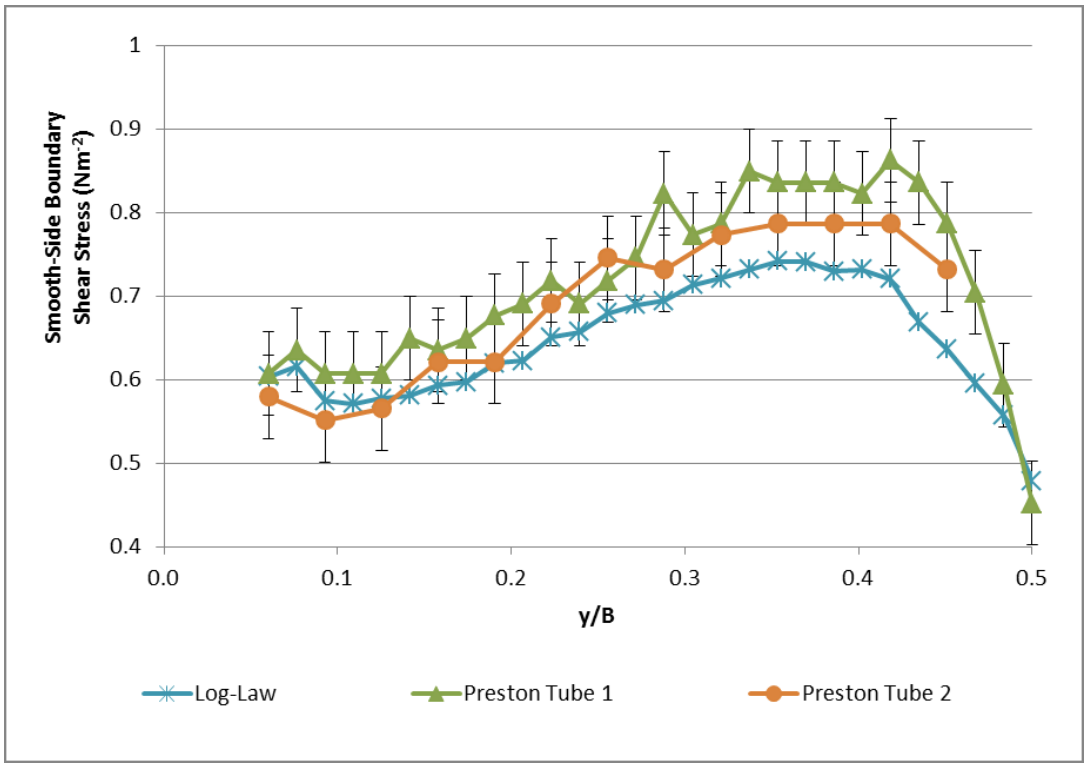

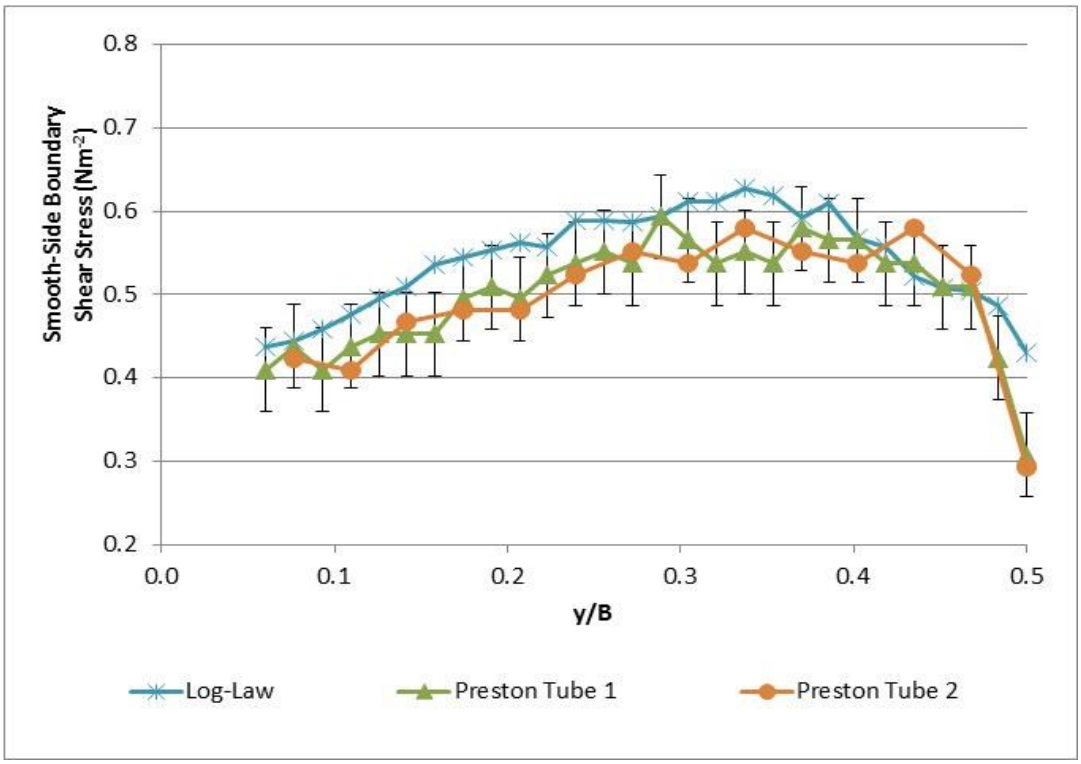

Figure 190: Experimental Errors in Boundary Shear Stress Measurement

For each data set, method D is seen to give good results over the smooth side of the channel (Table 17 and Figure 191 to Figure 196). This table shows the percentage difference in the mean shear stress value over the smooth side of the channel. However, method D is not applicable for the rough-side of the channel. In order to identify the preferred method of estimating the rough-side boundary shear stress, method D is ignored for the following discussion. For BC2, CS2 linear extrapolation (LE) from the bottom two points provides significantly better results than full series LE and three-point mean. For BC1 and BC2, CS4 full series extrapolation gives boundary shear stress within a mean error magnitude of 8% of the measured value.

	LE (Full Series)	LE (Bottom 2 Points)	Mean (Bottom 3 Points)	Log-law
BC1 F1	-16	-31	-30	-2
BC1 F2	-8	-32	-22	-11
BC2 F1 CS2	97	-3	62	9
BC2 F1 CS4	-9	-37	-18	8
BC2 F2 CS2	104	-21	64	1
BC2 F2 CS4	7	-49	-16	-10

Table 17: Percentage Difference in Mean Boundary Shear Stress from Estimated and Measured Values

All of the methods which are based on the measured Reynolds stress are susceptible to large errors. As seen in Section 4.2.5.3, the choice of filtering and replacement method used with the ADV data can affect the point τ_V^R measurements by almost 10%. The variation by cross-section of the estimation methods may be partially explained from a graphical representation of the distribution with depth of side-mean τ_V^R (i.e. the mean τ_V^R value calculated for each z, split by rough and smooth side of the channel) shown in Figure 197. For BC2 CS2, this distribution shows as sharp “hook” in the near-bed region – extrapolation using the bottom two points would be expected to give a very different estimation in this case. BC1 and BC2 CS4 also show this phenomenon but to a lesser extent. Such a reduction in τ_V^R in this region would be

anticipated from the theory of the wall region (see Section 3.5.1), which states that the total shear stress in this region remains constant, with the Reynolds stress component decreasing linearly as the viscous stress increases, although the exaggeration of this effect for BC2 CS2 (in comparison with the other datasets) is thought to be due to other, as yet unclear, factors. While the link between side-mean τ_V^R distribution and preferred estimation method are not as clear (over the smooth side) as may be hoped, what is evident from Figure 197 is the high linearity of this distribution over the rough side. Based on this, the full series LE may be expected to give a reasonable estimate of the rough-side boundary shear stress distribution. From Figure 191 to Figure 196 it may be seen that these two methods give similar mean results, though (due to its greater susceptibility to experimental error) the two-point LE method produces a far spikier distribution. For these reasons the full-series LE method is used for the rough-side boundary shear stress estimation.

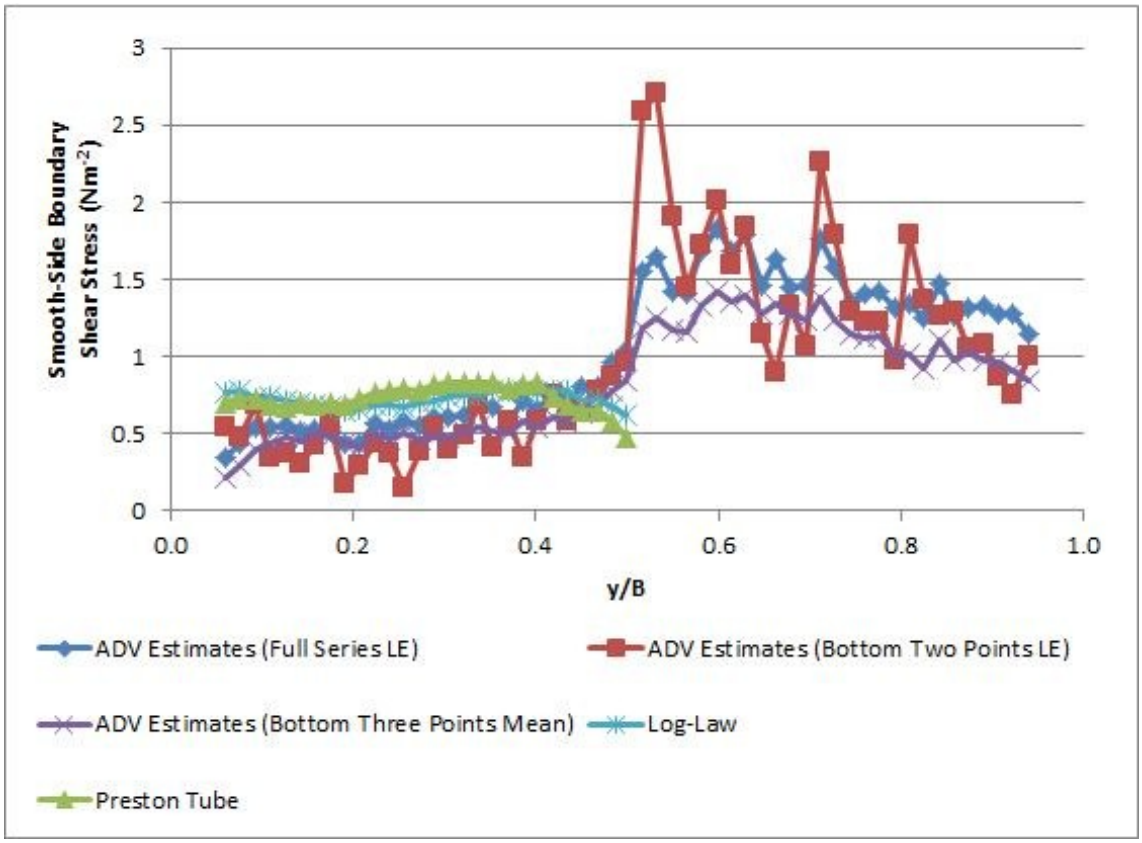

Figure 191: Measured and Estimated Boundary Shear Stress (BC1 F1)

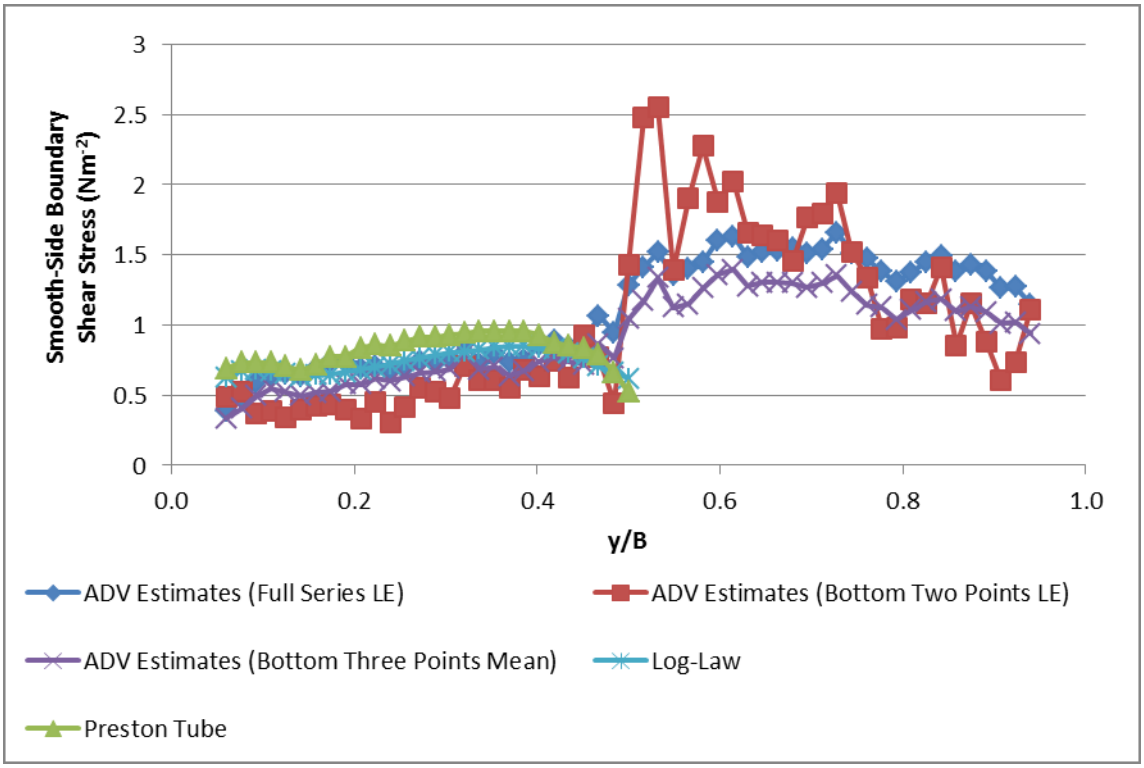

Figure 192: Estimated Boundary Shear Stress (BC1 F2)

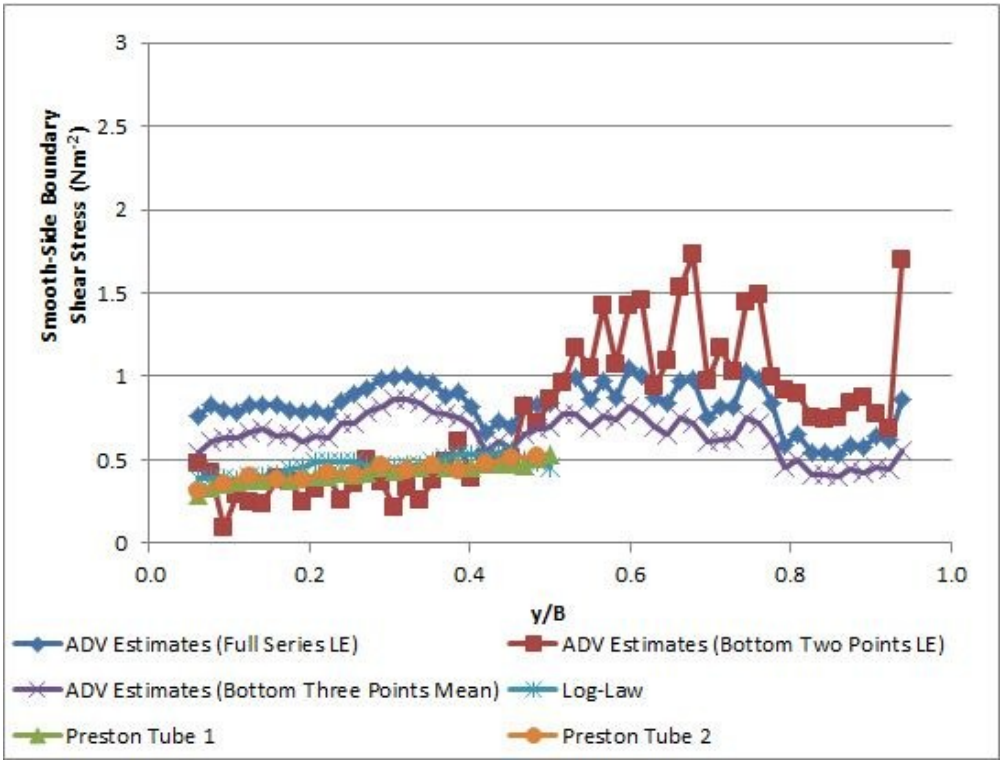

Figure 193: Measured and Estimated Boundary Shear Stress (BC2 F1 CS2)

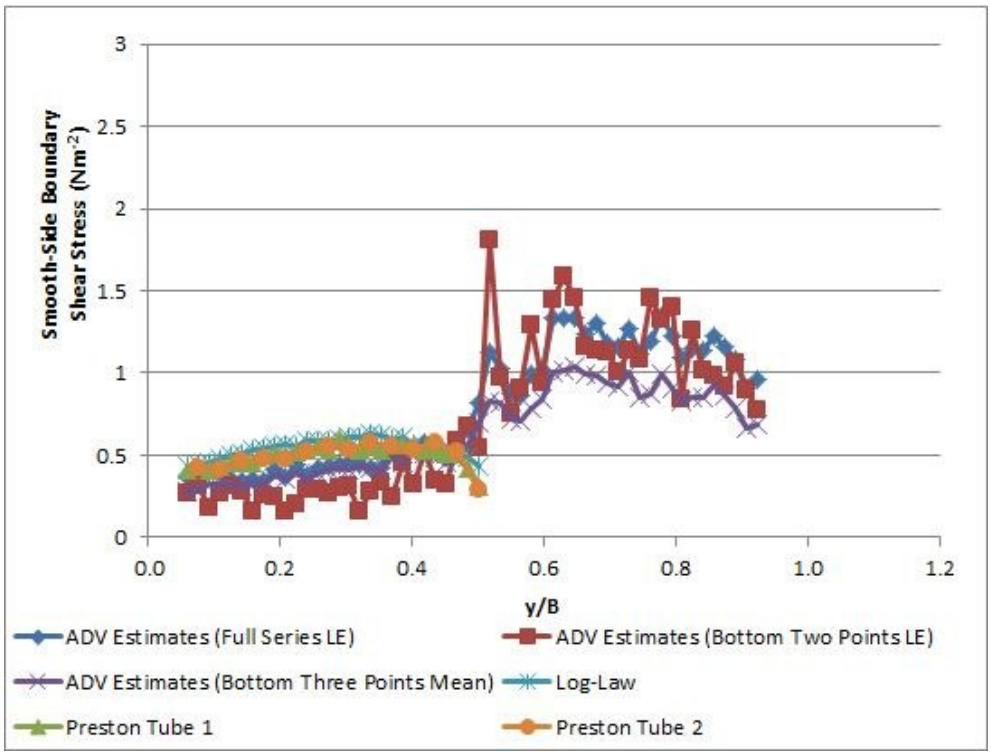

Figure 194: Measured and Estimated Boundary Shear Stress (BC2 F1 CS4)

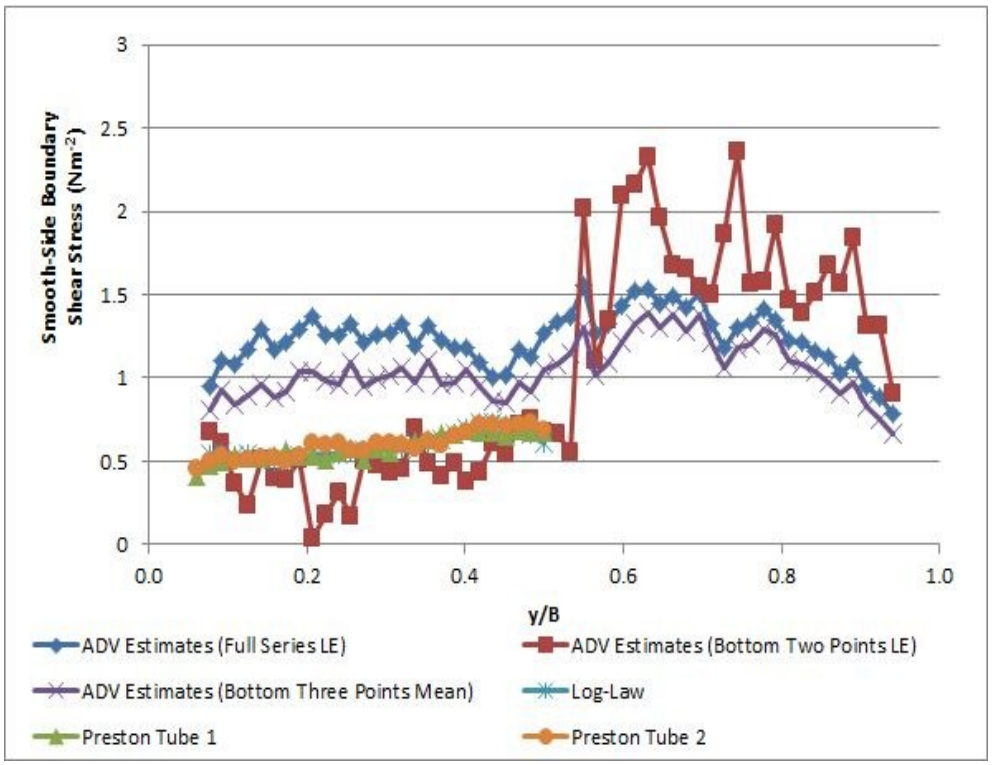

Figure 195: Measured and Estimated Boundary Shear Stress (BC2 F2 CS2)

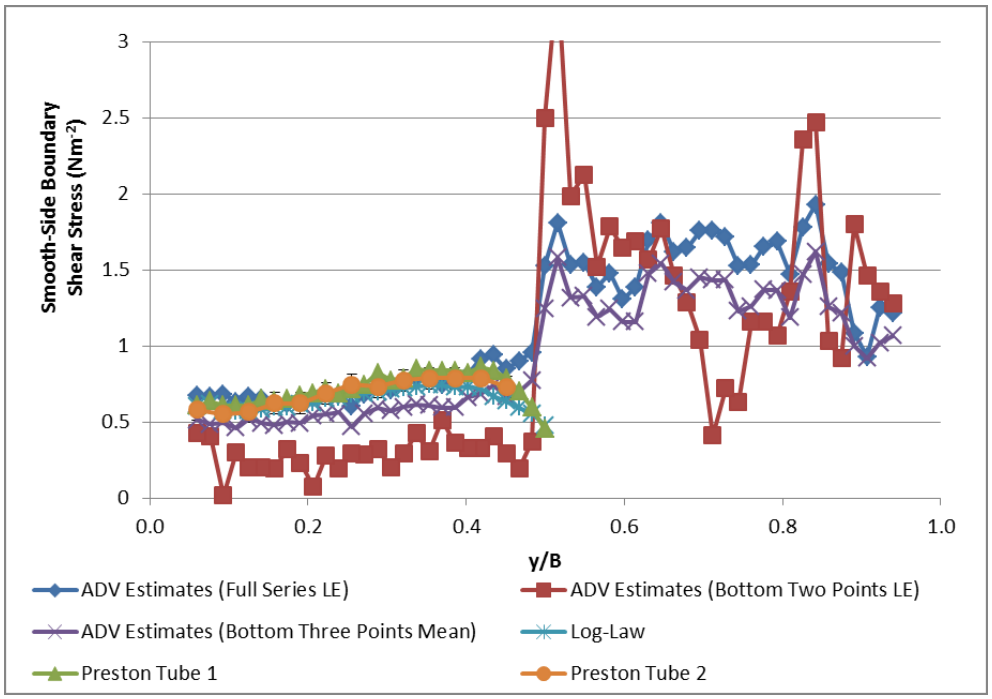

Figure 196: Measured and Estimated Boundary Shear Stress (BC2 F2 CS4)

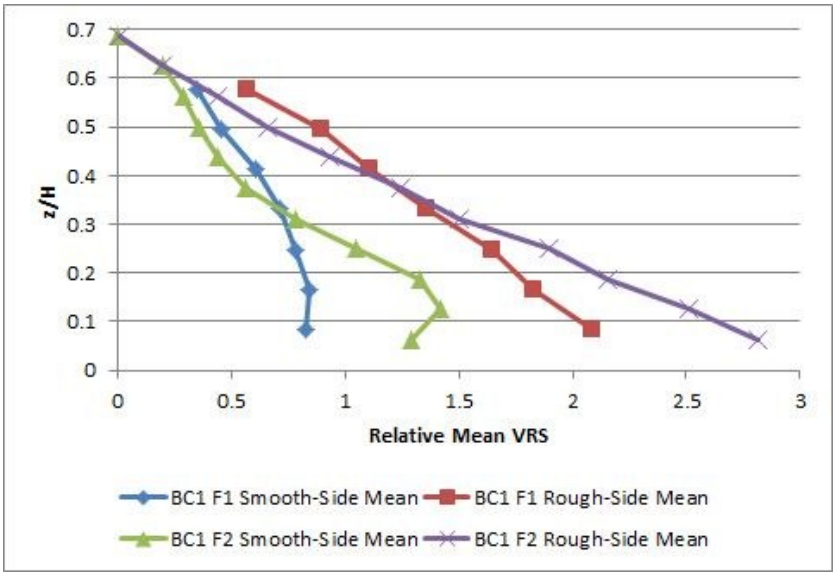

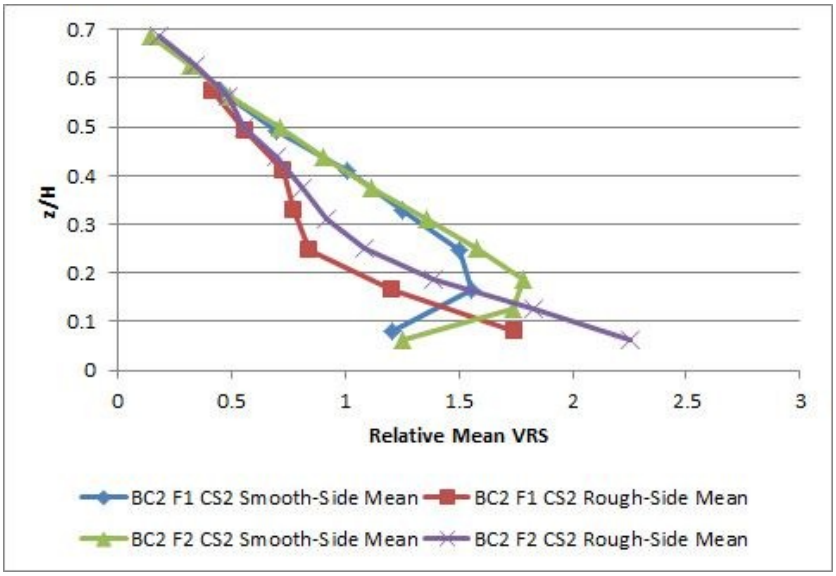

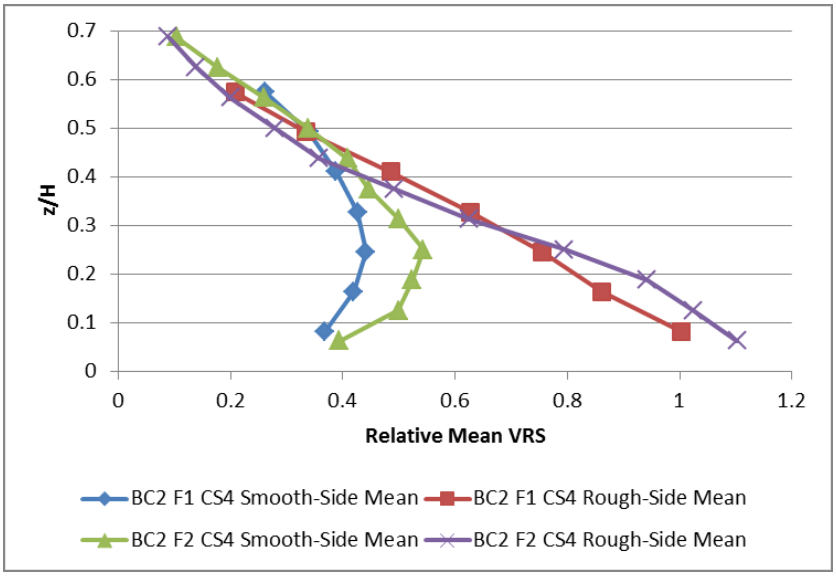

Figure 197: Mean Relative τ_{RV} by Side of Channel

A merged boundary shear stress distribution for each measured cross-section was constructed from the measured data (for the smooth-side) and the full series LE (for the rough-side) and is shown in Figure 198. Mean values have been calculated using these merged distributions ($\overline{\overline{\tau_b}}$) and the mean value calculated from $\overline{\tau_b} = \rho g R S_0$.

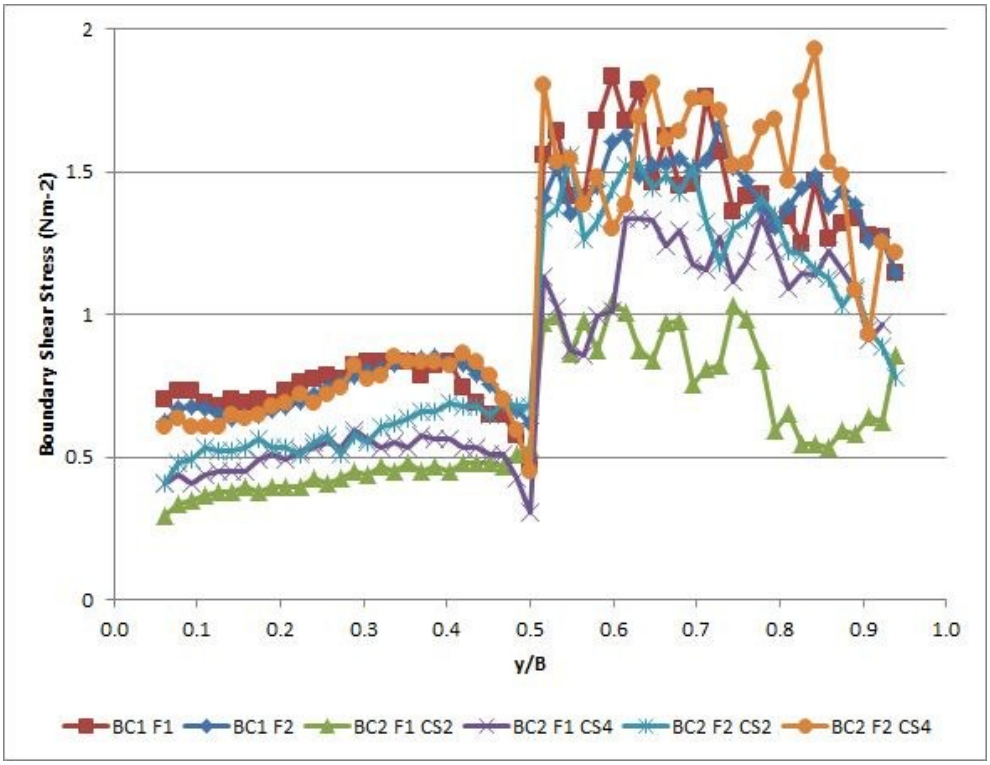

Figure 198: Transverse Boundary Shear Stress Distributions from Measurement ($y/B \leq 0.5$) and Estimate ($y/B > 0.5$)

	$\overline{\overline{\tau_b}}$	$\overline{\tau_b}$	% Diff
BC1 F1	1.09	1.05	4
BC1 F2	1.08	1.27	-15
BC2 F1 CS2	0.61	1.06	-42
BC2 F1 CS4	0.81	1.06	-24
BC2 F2 CS2	0.93	1.27	-27
BC2 F2 CS4	1.12	1.27	-12

Table 18: Mean Boundary Shear Stress Values

9.2 Discussion

As previously shown in Section 8, the flow for BC2 CS4 has developed sufficiently to be comparable with the BC1 flow, while the BC2 CS2 flow (just downstream of the roughness switch) has different characteristics. This pattern is seen in the boundary shear stress distributions – for BC1 and BC2 CS4 the boundary shear stress is seen to decrease as the RSB is approached from the smooth side, while for BC2 CS2 the boundary shear stress is approximately constant over this region.

In all cases the boundary shear increases sharply as the RSB is crossed, though it is acknowledged that the immediacy of this change may well be a feature of the transition from measured to estimated values. On both the rough and smooth sides the boundary shear stress increases with discharge and, in the BC2 case, with distance from the roughness switch.

For the BC1 F1 case, $\overline{\overline{\tau_b}} \cong \overline{\tau_b}$ (Table 18). In the BC1 F2 case there is a larger difference, though this may, in part, be due to interference from the fixed probe, an issue rectified for the other cross-sections. Interestingly, $\overline{\overline{\tau_b}}$ is significantly (~40% for BC2 F1 CS2) lower than $\overline{\tau_b}$ for BC2, and increases with distance from the roughness switch. There is evidence (see Section 8.4.1) that the flow for a checkerboard channel bed, as BC2, is non-uniform around the roughness switch, i.e. $\frac{\partial H}{\partial x} \neq 0$ For steady, non-uniform flow, $\overline{\tau_b} = \rho g R S_f$ where:

$$S_f = S_0 - \frac{\partial H}{\partial x} - \frac{U}{g}\frac{\partial U}{\partial x} \tag{78}$$

S_f is related to the Froude number, Fr, by:

$$\frac{\partial H}{\partial x} = \frac{S_0 - S_f}{1 - Fr^2} \tag{79}$$

and so for sub-critical flow $\frac{\partial H}{\partial x} > 0 \Longrightarrow S_0 > S_f$ and vice versa. However, streamwise variations in flow depth seem unlikely to be a cause of the discrepancies seen in Table 18 for two reasons. Firstly, the water profile measurements of Vermaas reported in Section 8.4.1 show a rapid depth variation in $\frac{\partial H}{\partial x}$ at the roughness switch, which reverts quickly to the constant value seen throughout the majority of the channel. Thus it is reasonable to assume that $\frac{\partial H}{\partial x} \cong 0$ at CS2 and CS4, and so $S_f \cong S_0$. Secondly, $\frac{\partial H}{\partial x}$ would have opposite sign at BC2 and BC4, implying that at one section $\overline{\tau_b} = \rho g R S_0$ would over-estimate $\overline{\tau_b}$ while at the other it would under-estimate it - for both cross-sections the experimental data gives $\overline{\overline{\tau_b}} < \overline{\tau_b}$. It should also be noted that both $\overline{\tau_b}$ and $\overline{\overline{\tau_b}}$ are subject to experimental error through the measurement of R, S_0 and the manometer readings used for the smooth-side shear stress calculations. The latter two are the most influential, with errors from these sources estimated as $\pm 5\%$ and $\pm 7\%$ respectively.

10 SKM MODELLING OF THE EXPERIMENTAL CHANNEL

As shown in Section 3.7.3, the Shiono Knight Method splits the channel cross-section into a number of panels, and gives an analytical solution for the depth-mean velocity, U_d, in each. It is worth repeating the pertinent equations of the SKM here for ease of reference. In the (rectangular) experimental channel, all regions are constant depth and hence the streamwise flow in each panel is described by:

$$U_d = [\mathrm{A_{i1}} e^{\gamma y} + \mathrm{A_{i2}} e^{-\gamma y} + k]^{\frac{1}{2}} \tag{47}$$

where:

$$\gamma = \left(\frac{2}{\lambda}\right)^{\frac{1}{2}} \left(\frac{f}{8}\right)^{\frac{1}{4}} \frac{1}{H} \tag{49}$$

$$\beta = \frac{\Gamma}{\rho g S_0 H}$$

$$k = \frac{8 g S_0 H}{f}(1 - \beta) \tag{80}$$

where λ represents the shear stress, f is the Darcy-Weisbach friction factor,H is the water depth, Γ the secondary flow term, ρ the water density, g is gravitational acceleration and S_0 the bed slope. A_{i1} and A_{i2} are constants (note that each panel has its own A values, with panel 1 having A_{11} and A_{12}, panel 2 having A_{21} and A_{22}, and so on).

From Equations (42), (44) and (45), the mean τ_H^R, $\bar{\tau}_{yx}$, is given by:

$$\bar{\tau}_{yx} = \frac{1}{H}\int_0^H (-\rho\overline{u'v'})\,dz = \rho\lambda H U_* \frac{\partial U}{\partial y} \tag{81}$$

allowing the calculation of λ from the experimental data:

$$\lambda = \frac{\bar{\tau}_{yx}}{\rho H U_* \frac{\partial U}{\partial y}} \tag{82}$$

Similarly, Γ may be calculated using:

$$\Gamma = \frac{\partial H(\rho UV)_d}{\partial y} \tag{83}$$

and f from:

$$f = \frac{8\tau_b}{\rho U_d^2} \equiv \frac{8U_*^2}{U_d^2} \tag{84}$$

Hence all terms may be calculated from the gathered data except for the A_i constants, which must be calculated for each panel by solution of a set of simultaneous equations and associated panel boundary conditions. These boundary conditions are the continuity of U_d and the continuity of the modified gradient of U_d, $\mu\left(\frac{\partial U_d}{\partial y}\right)$ where $\mu = \lambda\sqrt{f/8}$ (see (Omran, 2005)), along with known values of U_d at the outermost points of the edge panels. This last condition is usually specified as a no-slip condition at the channel walls (i.e. $U_d(y=0) = U_d(y=B) \equiv 0$). However, following previous research (e.g. (Omran and Knight, 2006)) the outermost panels extend to the outermost measured points ($y = 10mm$ and $y = 604mm$), with a linear approximation used from these points to the channel walls, where $U_d = 0$. This approach avoids underestimation of the near-wall U_d seen by Chlebek and Knight (2006).

Considering panel 1 and its boundary with panel 2, these boundary conditions are represented mathematically by (85), (86) and (87), in which y_1 is the left-most measured point and y_2 is the position of the panel 1/panel 2 boundary. Other subscripts reference the panel number.

$$A_1 e^{\gamma y_2} + A_2 e^{-\gamma y_2} - A_3 e^{\gamma y_2} - A_4 e^{-\gamma y_2} = k_2 - k_1 \tag{85}$$

$$\mu_1 \gamma_1 A_1 e^{\gamma y_2} - \mu_1 \gamma_1 A_2 e^{-\gamma y_2} - \mu_2 \gamma_2 A_3 e^{\gamma y_2} + \mu_2 \gamma_2 A_4 e^{-\gamma y_2} = 0 \tag{86}$$

$$A_1 e^{\gamma y_1} + A_2 e^{-\gamma y_1} = (U_d(y = y_1))^2 - k_1 \tag{87}$$

Equation (85) is derived simply from the equality of (47) when applied to panel 1 and panel 2 at $y = y_2$. Similarly, (86) is derived from differentiation of (47) with respect to y and equality of the resulting expressions scaled by μ, noting that the denominator in each case is equal to $U_d(y = y_2)$ and therefore may be cancelled.

When applied to all panel boundaries, these boundary conditions may be expressed in matrix form:

$$O\boldsymbol{A} = \boldsymbol{k} \tag{88}$$

Where $\boldsymbol{A}$ is the vector of A constants, $\boldsymbol{k}$ is the vector of the RHSs of (85), (86) and (87) and O is the matrix of the co-efficients of the As.

A detailed analysis of the solution of these equations is available in (Omran, 2005), with a discussion of methods to solve them. Within the context of this thesis, it is sufficient that γ and β are calculated to adequate precision, that O is non-singular

(i.e. the inverse, O^{-1}, may be calculated) and that the inverse is calculated to "adequate" precision. In order to maintain the precision of the calculation of γ and β, the calculations were performed using an application written in Java, using the BigDecimal class (which allows high-precision calculation of very large or very small numbers; see (Oracle, 2010)) with twenty significant figures. If these conditions hold then A may be calculated since $O^{-1}OA = A = O^{-1}\tilde{k}$. The latter two conditions may be verified by the existence of E^{-1} and back-calculation of OA_c (where A_c is the calculated vector A) and comparison with $\tilde{k}$. Once the A constants have been calculated for each panel the U_d distribution over the entire channel may be calculated. From this, a theoretical stage-discharge curve may be calculated.

One important decision in modelling using the SKM is the number of panels used. In previous work, such as (Knight et al., 2007), this has been determined by channel geometry (e.g. the existence of variable depth regions over the side slope of a trapezoidal channel) and the pattern of secondary flow cells within the channel. Thus each panel represents a region of constant Γ. Such work has focused on symmetrical channels, in which only one half of the channel need be modelled and a symmetrical flow assumption applied, and in which the secondary flow cells meet at their boundaries. In the case of the heterogeneous channel such symmetry obviously cannot be assumed and would (as shown in the results above) be incorrect. Additionally, on both the rough and (for BC2) the smooth sides of the channel regions of negligible secondary flow exist. Based on the secondary flow cells seen in Figure 89 and Figure 90, for BC1 the smooth side of the channel would be split into three panels. The rough side would be more complex, with regions of negligible secondary flow requiring additional panels (Figure 199).

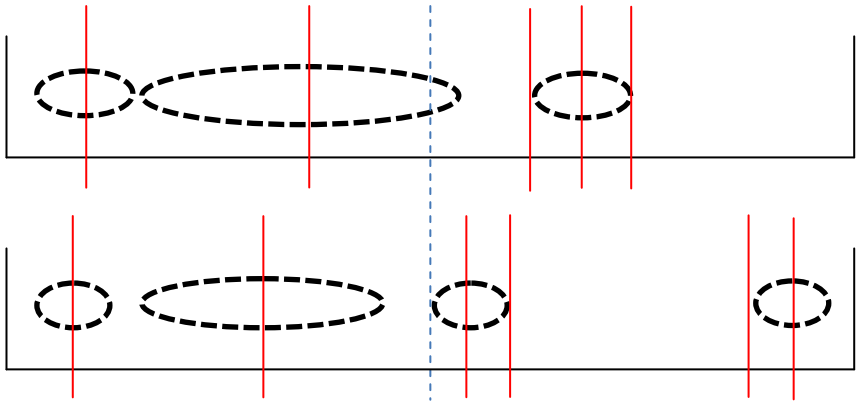

Figure 199: Schematic of SKM Panels for BC1 Based on the Observed Secondary Flow Cells. Dashed vertical line represents $y/B = 0.5$ (one panel boundary), red lines represent additional panel boundaries.

However, splitting the channel based purely on the secondary flow cells assumes that the other SKM parameters, f and λ, are constant over constant depth regions (see Shiono and Knight (1991), for example). This assumption has been shown to be invalid for the "best" solution (Sharifi et al., 2008), where "best" means the most accurate without consideration of the physical meaning of the parameters. With the horizontal variation of U_d seen in the current research, and the high τ_H^R near the RSB, it is reasonable to expect that this assumption is also invalid for a heterogeneous bed. In order to determine the correct number of panels for the modelling of a heterogeneous channel, the relevant flow parameters have been plotted and the distributions examined. Each flow parameter is discussed in one of the following sections. In addition to the SKM parameters, the form of the U_d distribution also places constraints on the panels as each panel may contain only a single point of inflection, or a maximum, or a minimum. How the panel boundaries are arranged based on U_d is somewhat subjective, though a correspondence with the variation of the SKM parameters seems appropriate where possible.

10.1 Determination of Panel Boundaries and Parameter Values

10.1.1 Lateral Shear, λ

The distribution of the SKM λ (calculated from (82)) is shown for each data set in Figure 200 to Figure 205. These figures also include the depth-averaged relative streamwise velocity, $\widehat{U_d}(y) \equiv U_d(y)/U_{Q/A}$, and approximate positions of secondary flow cells are shown where applicable.

The F1 data shows greater scatter than that for F2. The physical reasons for this are unclear and it may be a consequence of the calculation method used. Considering the smooth side for simplicity (over the smooth side U_* is approximately constant and so $\lambda \propto \bar{\tau}_{yx}/\frac{\partial U}{\partial y}$), λ will spike where $\left|\frac{\partial U}{\partial y}\right| \approx 0$. Due to the central difference method used for the discrete approximation $\left(\frac{\partial U_d}{\partial y} \cong \frac{U_d(y_{i+1})-U_d(y_{i-1})}{y_{i+1}-y_{i-1}}\right)$, the appearance of such spikes is highly dependent on the surrounding values (i.e. $\left|\frac{\partial U_d}{\partial y}\right| \approx 0$ may not be captured even at a local maximum/minimum unless $U_d(y_{i+1}) \approx U_d(y_{i-1})$). For BC1, F1 peaks and troughs of $\overline{\overline{U}}_r(y)$ are generally broader than for F2, increasing the chances of $U_d(y_{i+1}) \approx U_d(y_{i-1})$. This also applies somewhat to BC2 and, in addition, the BC2 F1 $\widehat{U_d}(y)$ distribution is less smooth than that for BC2 F2, increasing the chances of a "mini-plateau" such as that seen at $y/B \cong 0.15$ for BC2 F1 CS2. While such spikes may appear to complicate the process of determining λ values for the SKM panels, inspection of the $\widehat{U_d}(y)$ distribution reveals that these spikes are an indicator of potential panel boundaries. For BC1 the position of these spikes is consistent with the location of the secondary flow cells, while (as an example) for BC2 the mini-plateau at $y/B \cong 0.15$ for BC2 F1 CS2 is matched for BC2 F2 CS2, as is the one at

$y/B \cong 0.80$. Certainly the former of these corresponds to a weak secondary flow cell seen in the lateral velocity vectors (Figure 91 and Figure 92). Interestingly, by CS4 this secondary flow cell is stronger but its effect on $\widehat{U_d}(y)$ appears negligible. This indicates that these cells lead to local maxima and minima of the $\widehat{U_d}(y)$ distribution, which fits with the concept of isovel distortion by secondary flows.

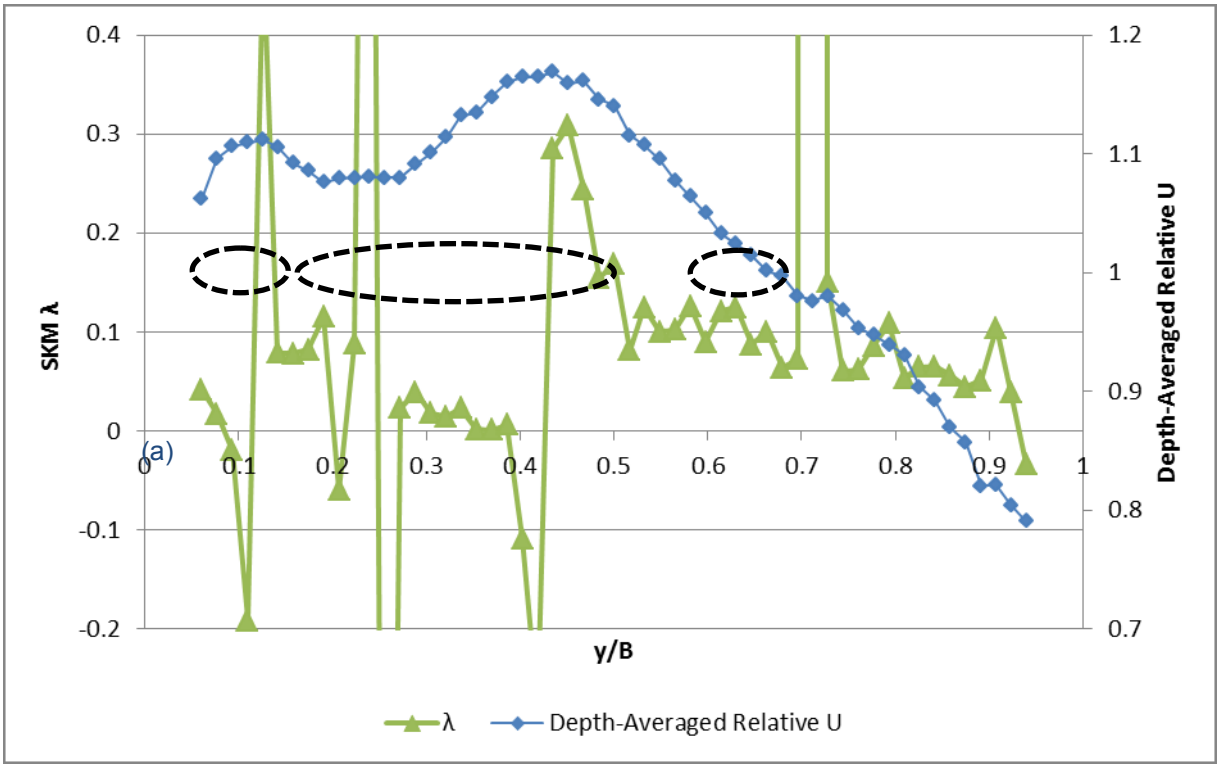

Figure 200: Distribution of $\overline{U_r}$ (BC1 F1)

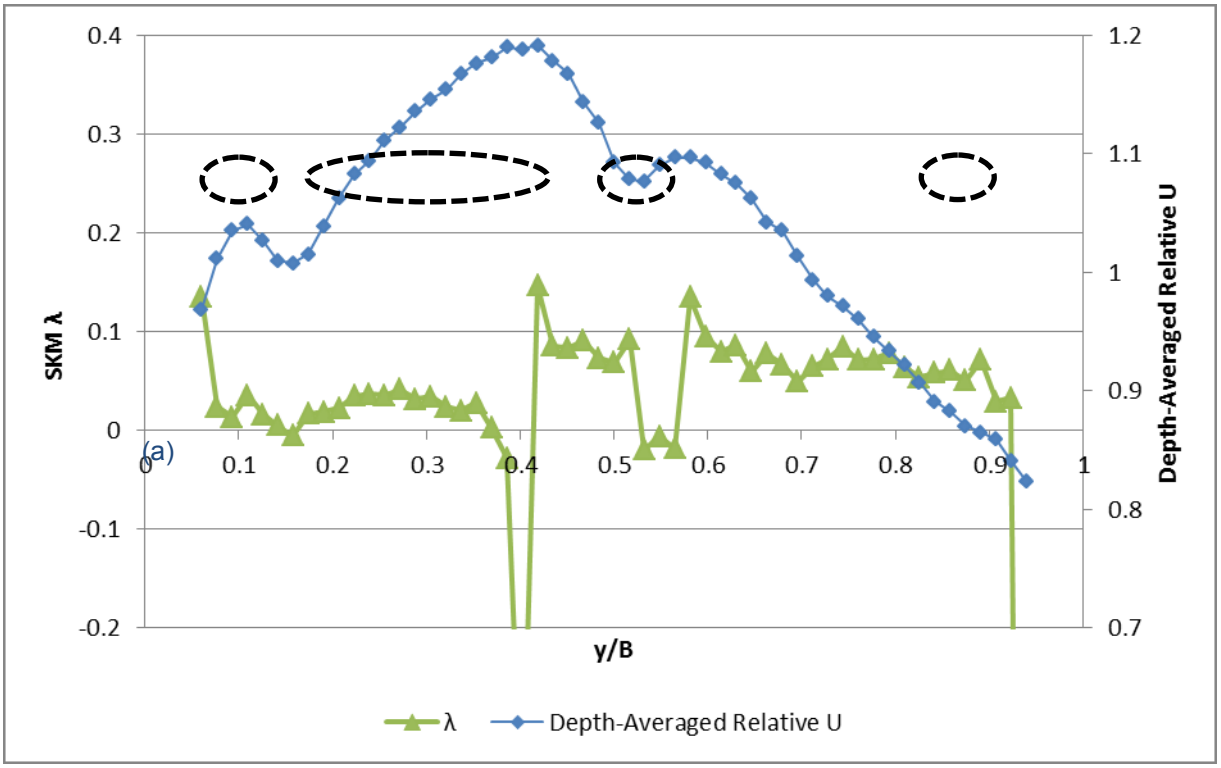

Figure 201: Distribution of $\overline{U_r}$ (BC1 F2)

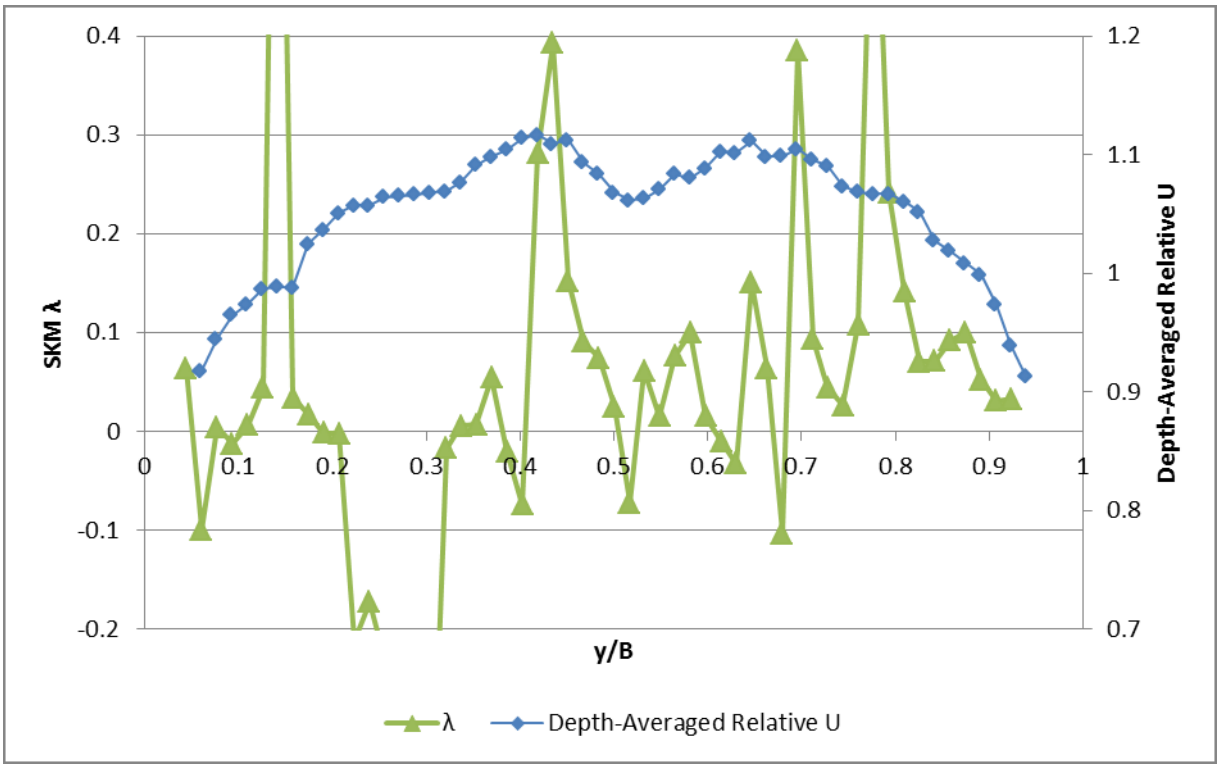

Figure 202: Distribution of $\overline{\overline{U_r}}$ (BC2 F1 CS2)

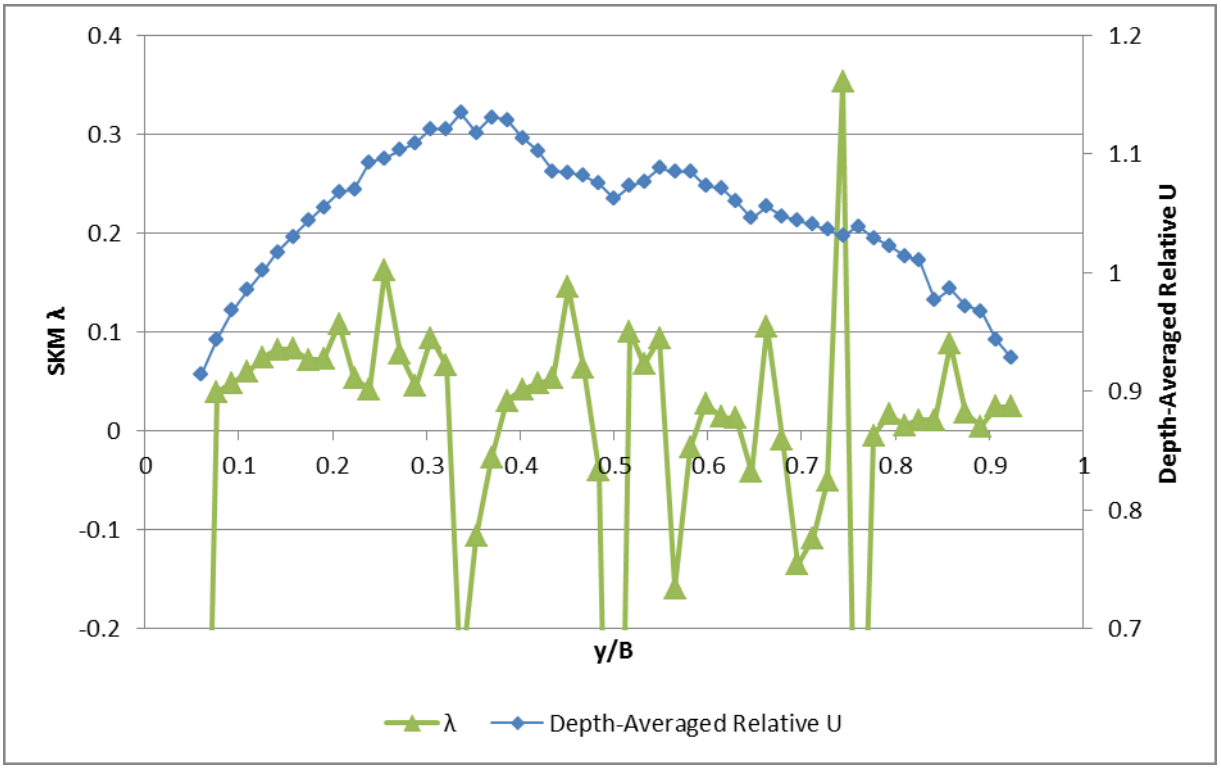

Figure 203: Distribution of $\overline{\overline{U_r}}$ (BC2 F1 CS4)

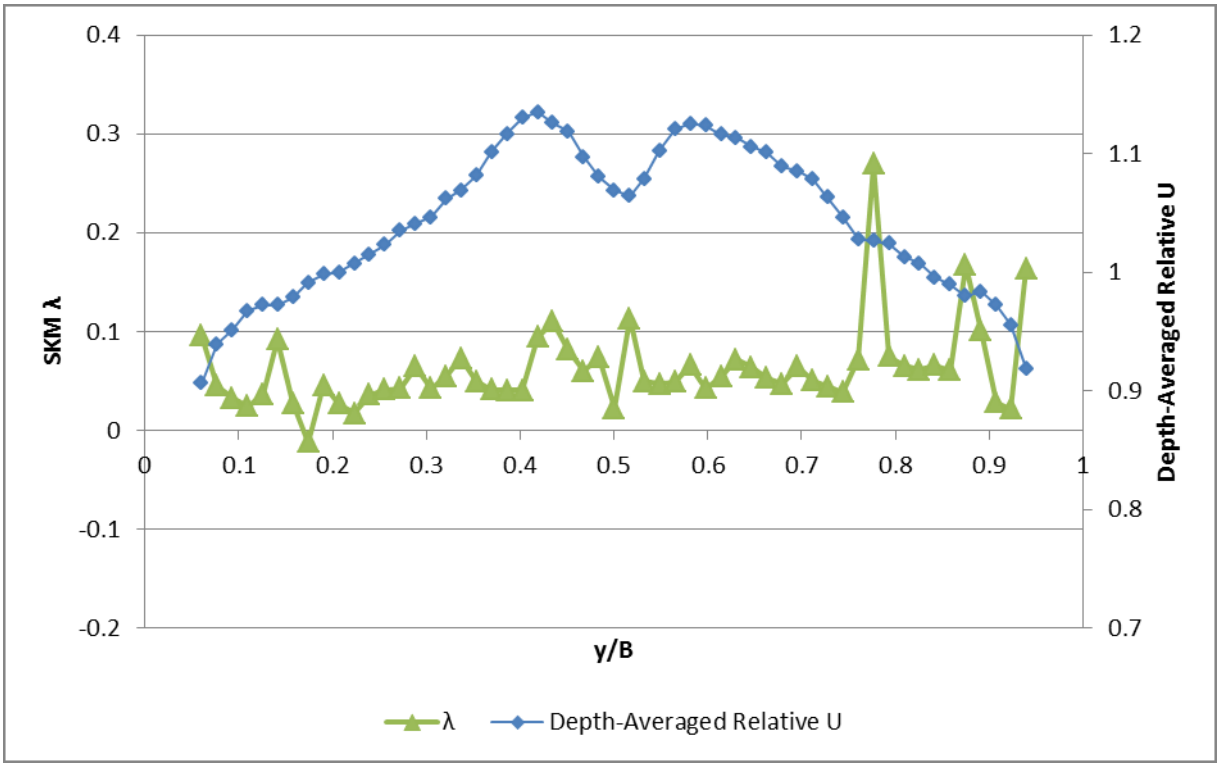

Figure 204: Distribution of $\overline{\overline{U_r}}$, (BC2 F2 CS2)

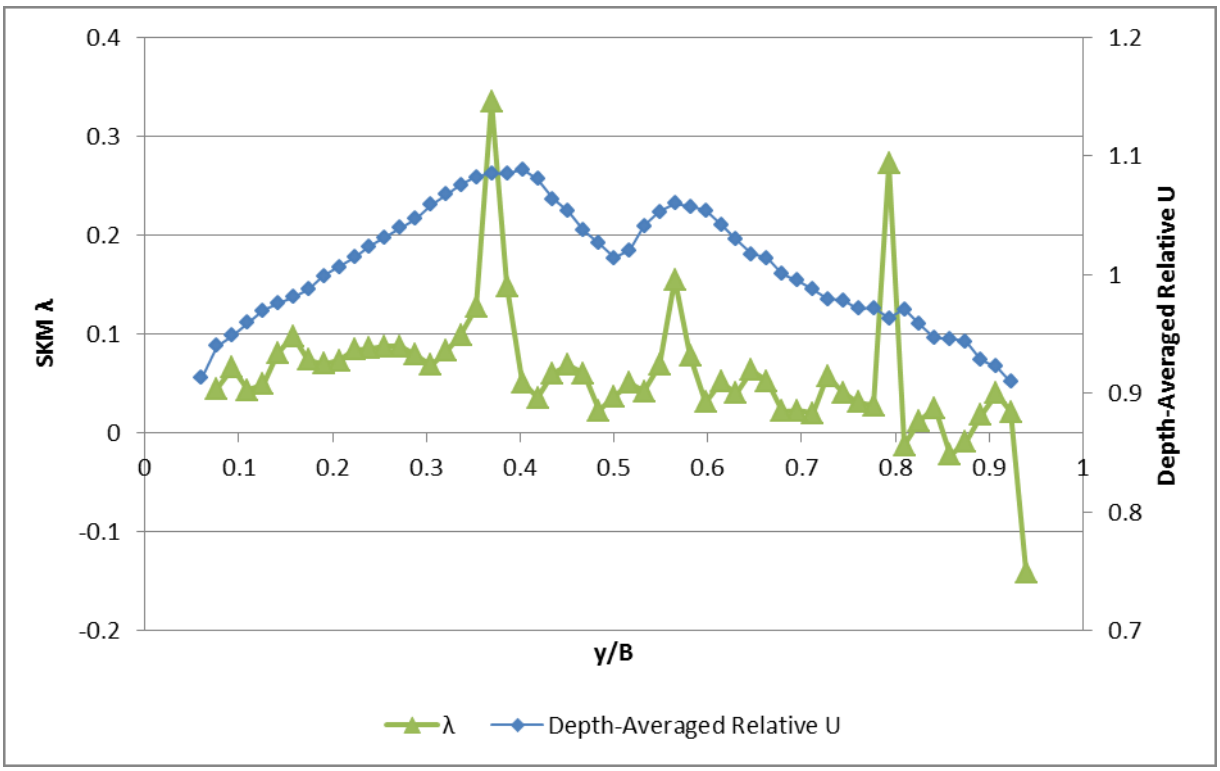

Figure 205: Distribution of $\overline{\overline{U_r}}$, (BC2 F2 CS4)

10.1.2 Friction Factor, f

As mentioned earlier, previous work has generally assumed f to be constant over regions of constant depth. A linear variation over each panel was evaluated by Omran and Knight (2006) in an attempt to eradicate discontinuities in boundary shear stress, though such a discontinuity may be expected in heterogeneous channel. Taking the mean of the $\overline{\tau_b}$ errors from Table 18 (20%) as the best estimation of the experimental error value in the τ_b values, error bars have been added to Figure 206 to Figure 211, which show the calculated f distributions for each of the datasets. It may be seen that the assumption that f is constant on the rough side of the channel and constant (through with a different value to the rough side) on the smooth side is valid in the majority of cases, with some noteworthy discrepancies. Close to the RSB, the more developed flows of BC1 and BC2 CS4 show a reduction in f on both the rough and smooth sides. This suggests that additional panels, with lower f values in comparison to the "main" value of that side, may be required. Additionally, reductions in f near the right-hand wall are evident in three of the four BC2 cases (with BC2 F1 CS4 the exception); conversely, BC1 does show some evidence of f increasing towards the wall, though this is insignificant within the bounds of experimental error. As will be seen later, these variations were found to be inconsequential within the scope of the SKM modelling, and were ignored for the sake of simplicity. Further investigation of the apparent reduction in f near the RSB may be worthwhile, but is not attempted here. The only panel position condition implied by the friction factor is the existence of a panel boundary at the RSB, $y/B = 0.50$.

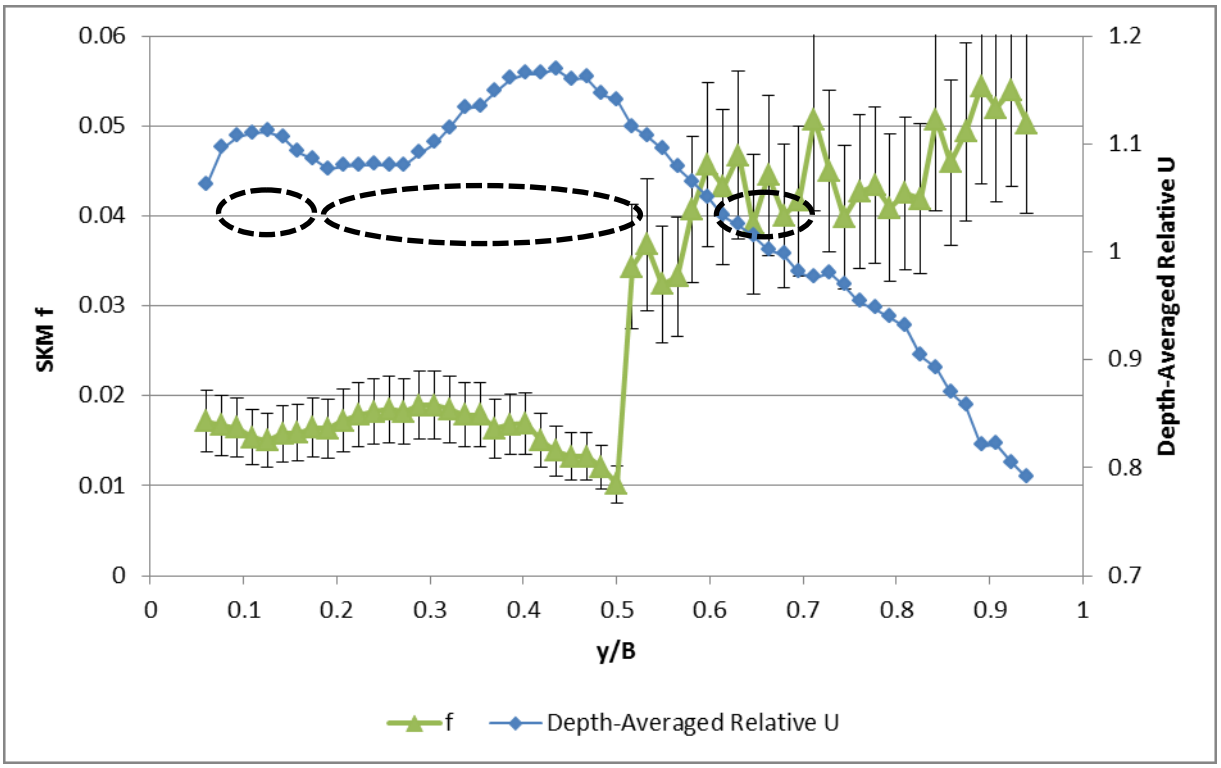

Figure 206: Distribution of f (BC1 F1)

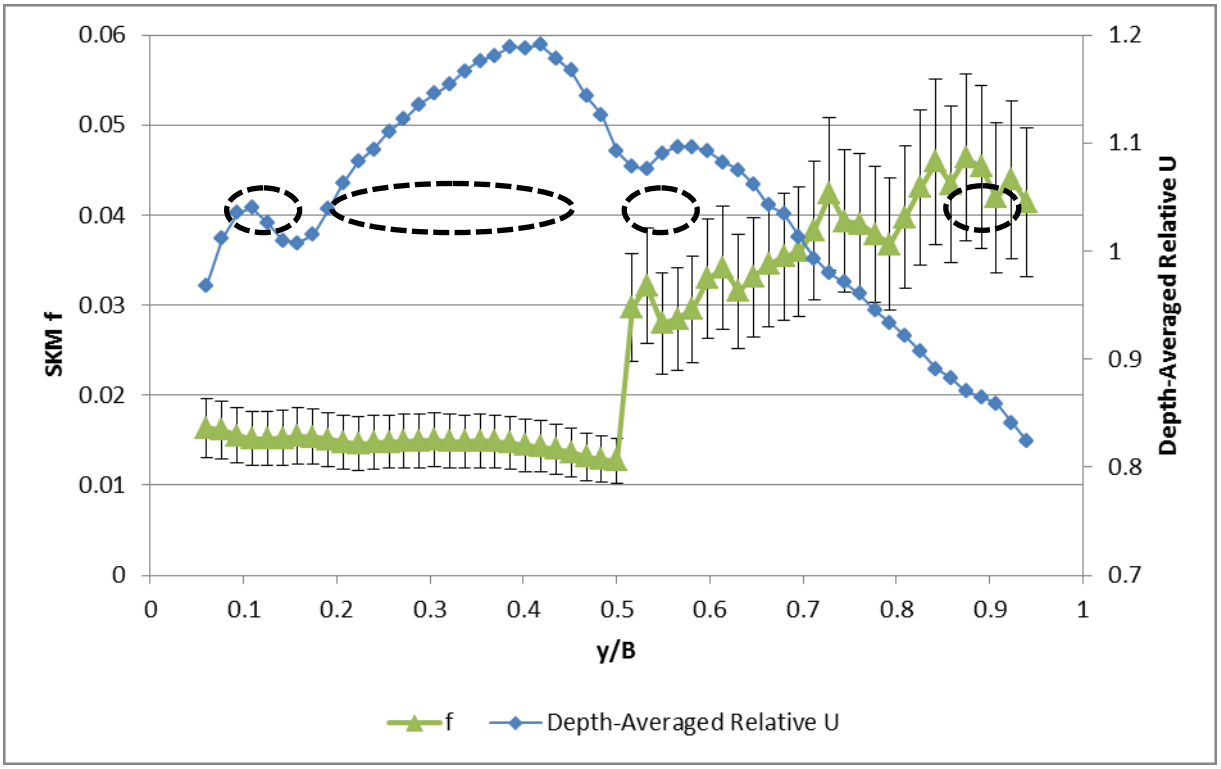

Figure 207: Distribution of f (BC1 F2)

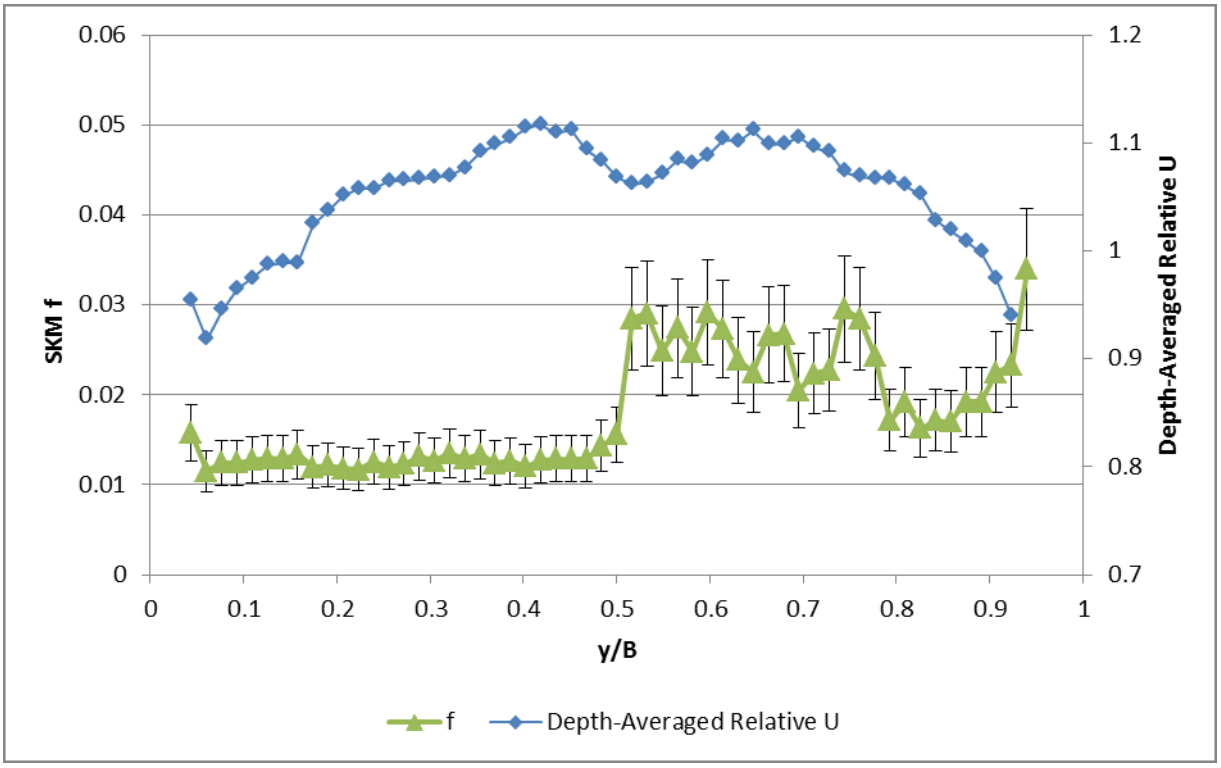

Figure 208: Distribution of f (BC2 F1 CS2)

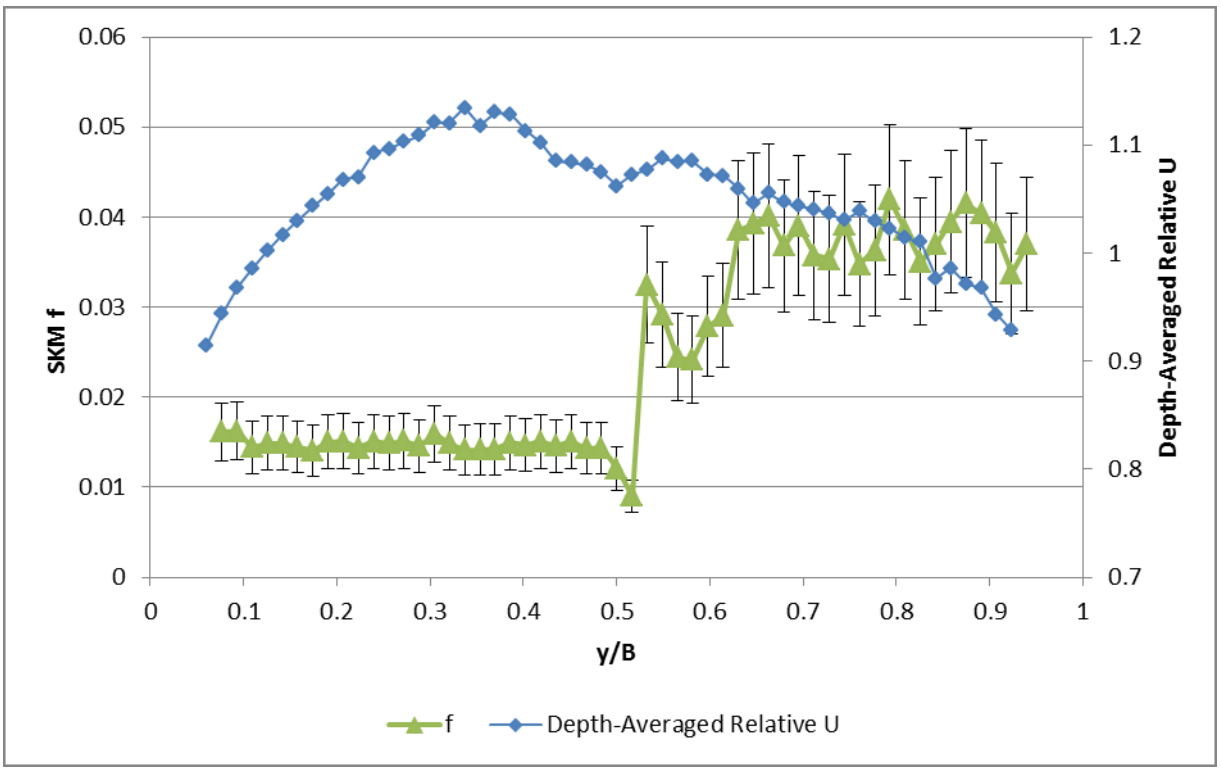

Figure 209: Distribution of f (BC2 F1 CS4)

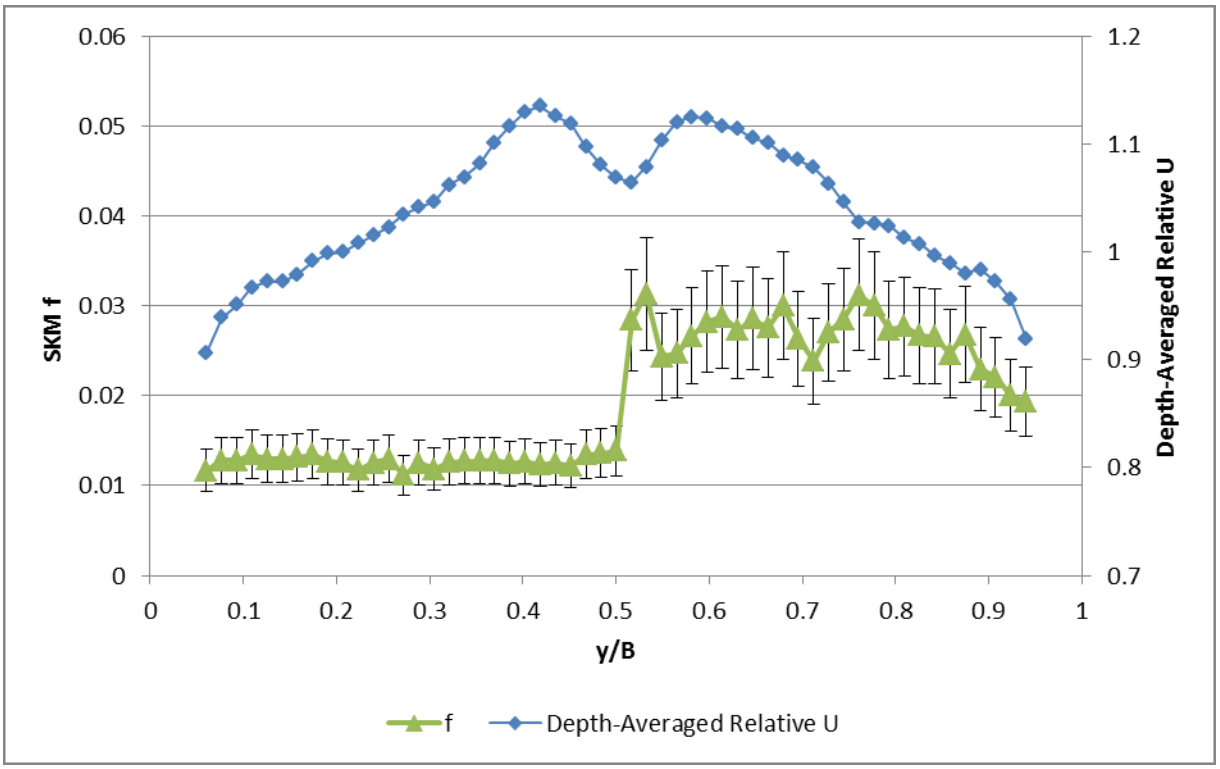

Figure 210: Distribution of f (BC2 F2 CS2)

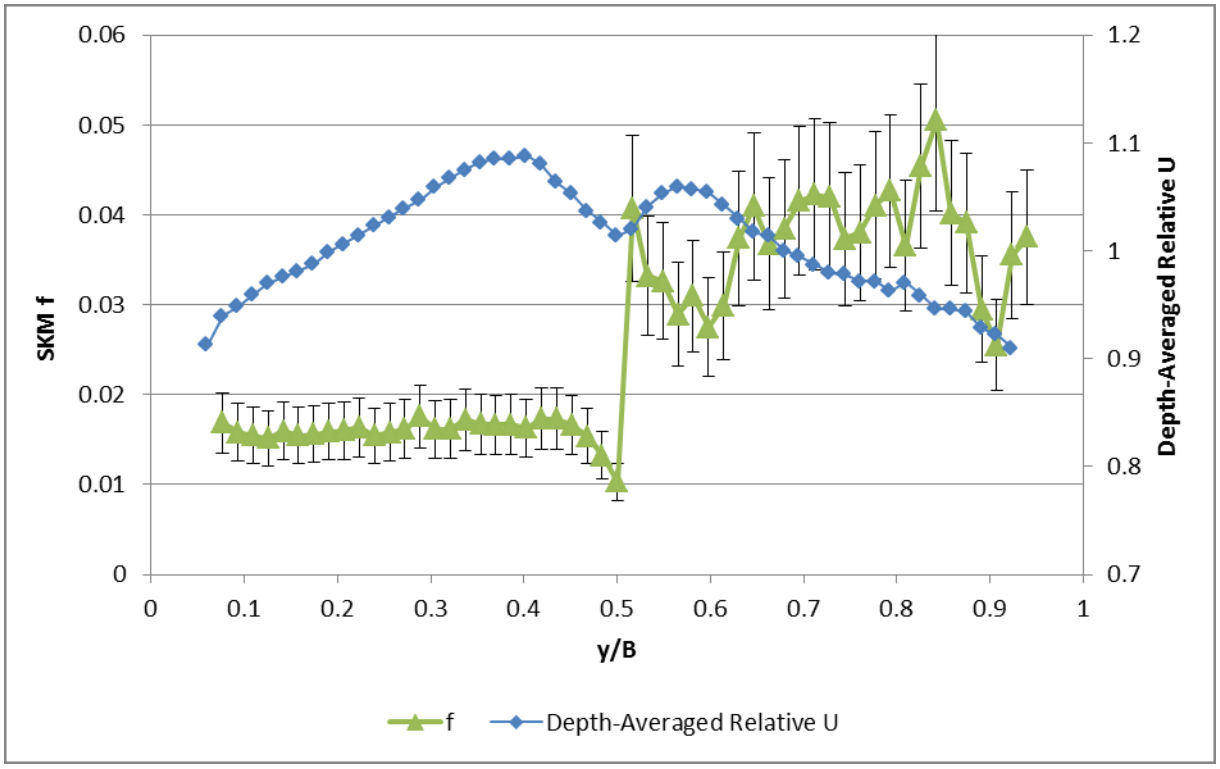

Figure 211: Distribution of f (BC2 F2 CS4)

10.1.3 Secondary Flows, Γ

The secondary flow term has been calculated from the experimental data. However, the values obtained far exceed (by a couple of orders of magnitude) the values seen in previous research and are considered invalid for modelling. This is unsurprising based on the secondary flow cell structures seen both in this research and in the research detailed in Section 3.6. With the 3-D velocity data not covering the entire water depth, and the presence of vertically stacked flow cells (see Figure 11), the calculation of $(UV)_d$ is not achievable. More importantly, the experimental result of Shiono and Knight that $\Gamma = constant$ (Shiono and Knight, 1991) is based on single, full-depth secondary flow cells. It would therefore seem that Γ should be used as a calibration parameter, as a sink for unmeasured physical interactions. While not entirely satisfying, this is consistent with previous applications of the SKM.

10.1.4 Panel Boundaries and Parameter Values

The division of the channel into panels is based on the transverse variation of the SKM parameters (effectively the variation of λ along with the condition of a panel boundary at the RSB imposed by f) and the U_d distribution, as discussed above. The precise location of the panel boundaries is somewhat subjective – where two or more conditions imply boundaries in close proximity, these are merged as a single boundary. Not only does this simplify the model, eliminating extremely narrow panels, but it has some intuitive physical basis if the SKM parameters and U_d are all considered to be linked. Parameter values and panels are shown in the following figures (Figure 212 to Figure 217). Parameter values in these figures are approximations based on an estimated median value for the panel – based on the

transverse distributions shown for these parameters, and the experimental errors inherent in the distributions, it was considered unlikely that a rigorous mathematical calculation of an “average” value is would be preferable to an estimation “by eye”, an assumption supported by calculation of a selection of mean f values.

As will be shown later (Section 10.2), the standard value of $\lambda = 0.07$ was used across all panels, for all datasets. The estimated friction factors (Table 19) appear to vary inversely with discharge (and therefore H) for BC1 – this is consistent with the results seen in Figure 62 – but for BC2 any discharge/depth dependency is overshadowed by a dependency on distance from the roughness switch. For both BC2 F1 and F2, f increases with distance from the switch and (bearing in mind the inaccuracies involved in estimating these values) are approximately equal for F1 CS2 and F2 CS2, and for F1 CS4 and F2 CS4. It should be noted, as a limitation of the experimental data, that both discharges fall into regions of low dependency of f on H (see Figure 62 and Figure 63) and so arguments for f being independent of H for BC2 are invalid, particularly when the inaccuracies of estimating f from the flow data are considered.

Dataset	f (smooth)	f (rough)
BC1 F1	0.018	0.045
BC1 F2	0.015	0.040
BC2 F1 CS2	0.013	0.025
BC2 F1 CS4	0.015	0.035
BC2 F2 CS2	0.013	0.027
BC2 F2 CS4	0.016	0.036

Table 19: Estimated Friction Factors for the Rough and Smooth Sides of the Channel

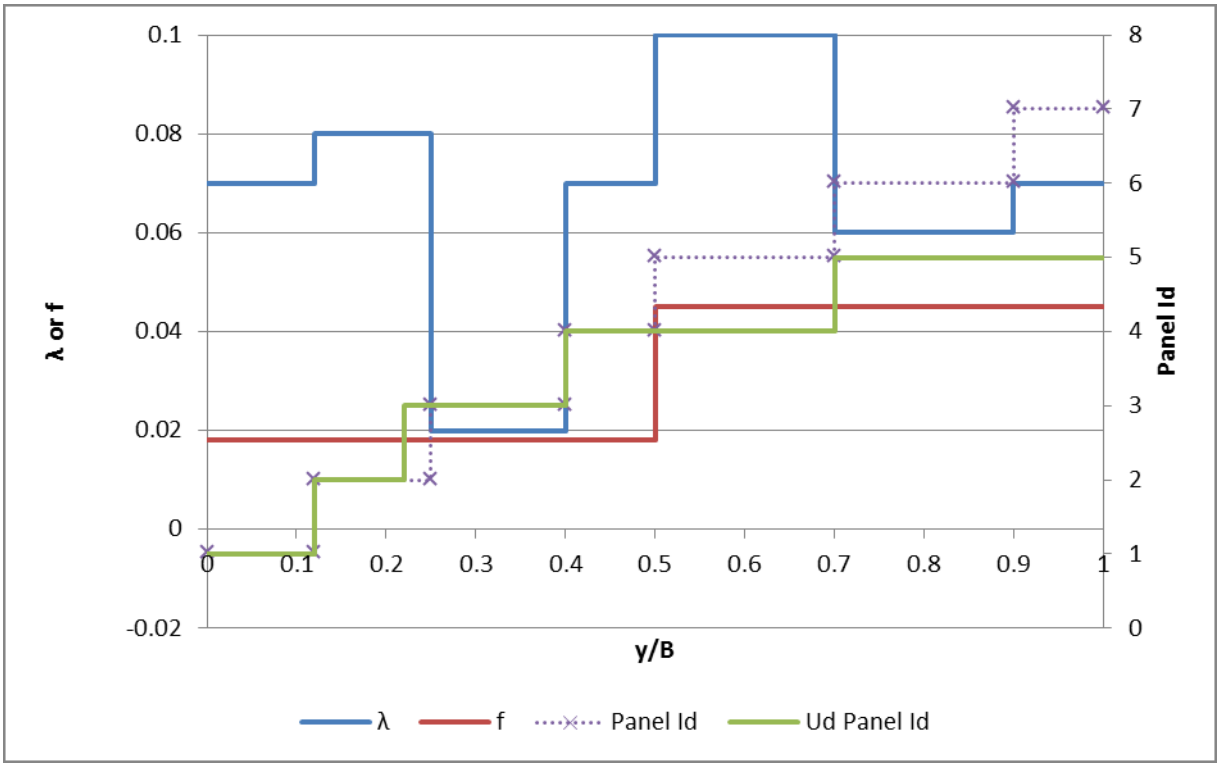

Figure 212: SKM Parameter Values By Panel (BC1 F1)

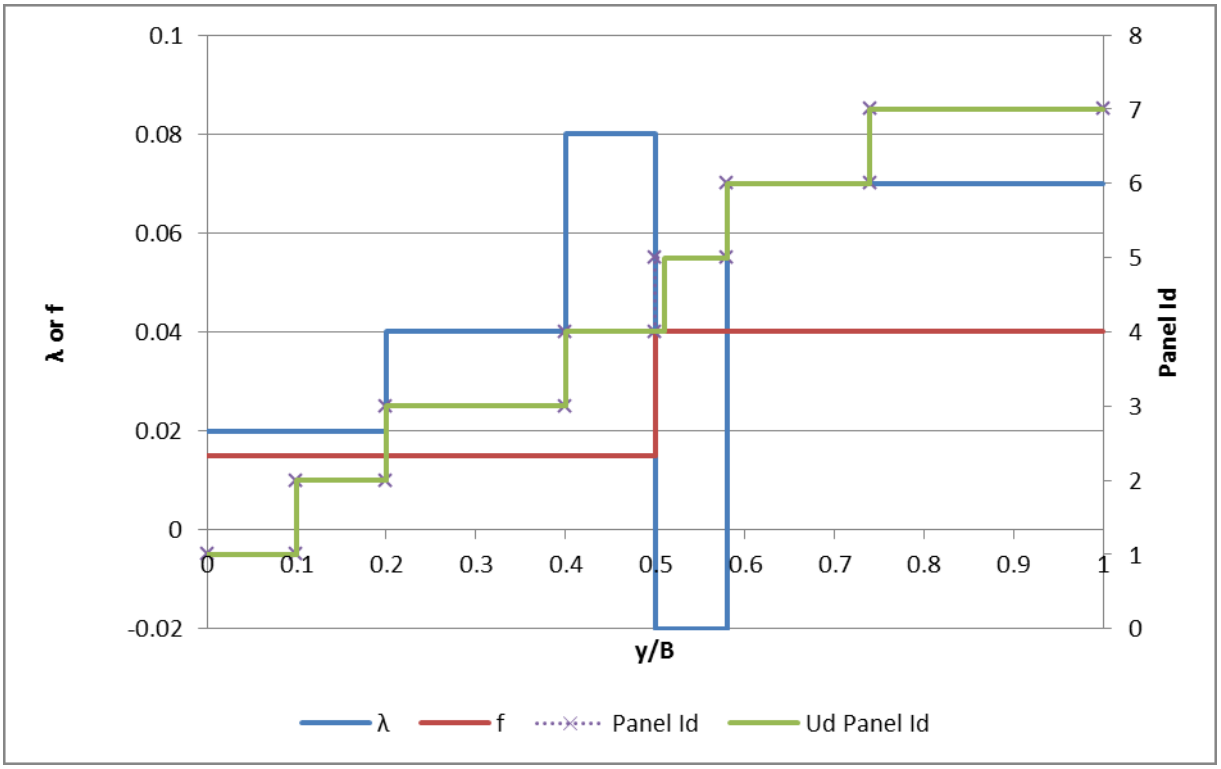

Figure 213: SKM Parameter Values By Panel (BC1 F2)

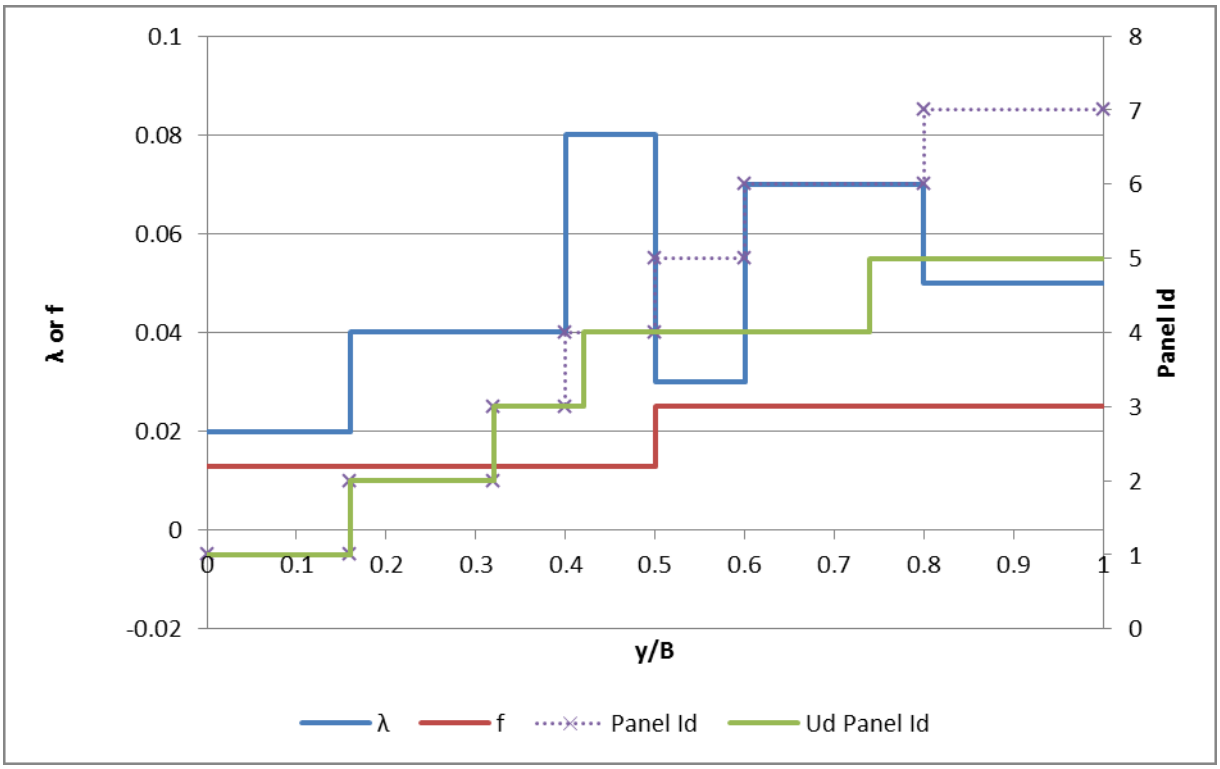

Figure 214: SKM Parameter Values By Panel (BC2 F1 CS2)

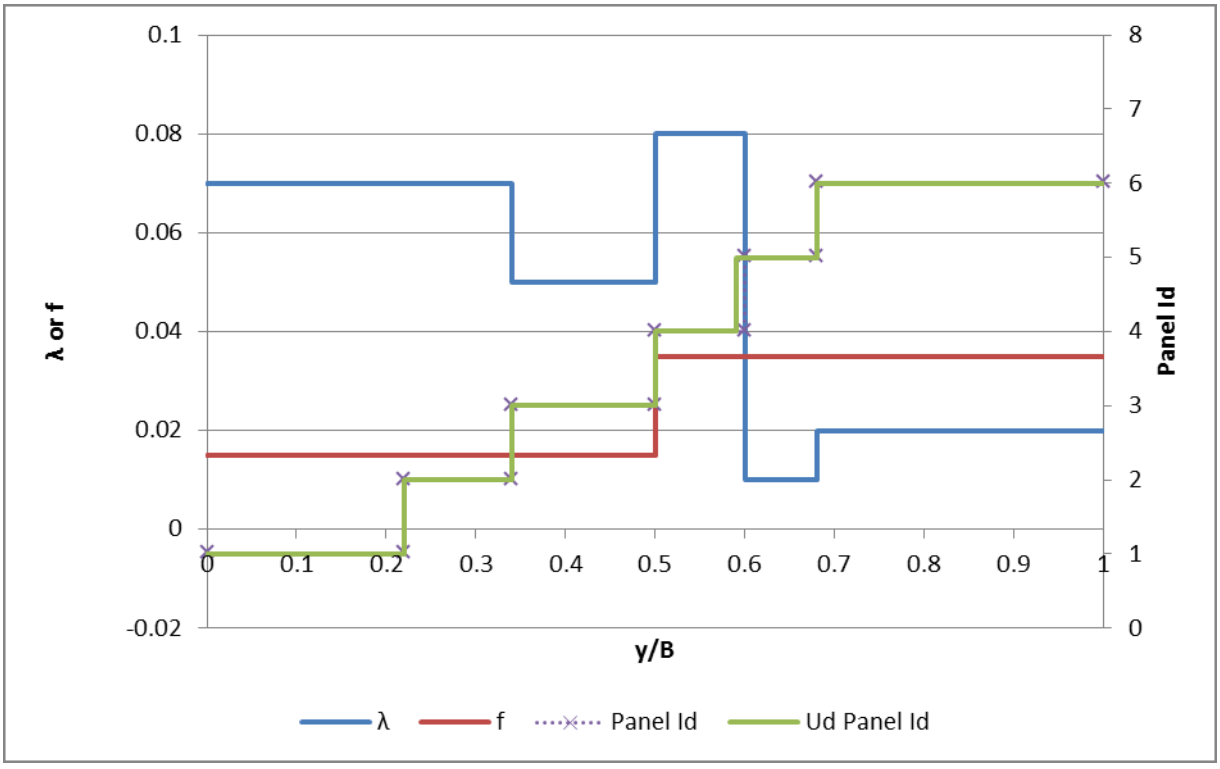

Figure 215: SKM Parameter Values By Panel (BC2 F1 CS4)

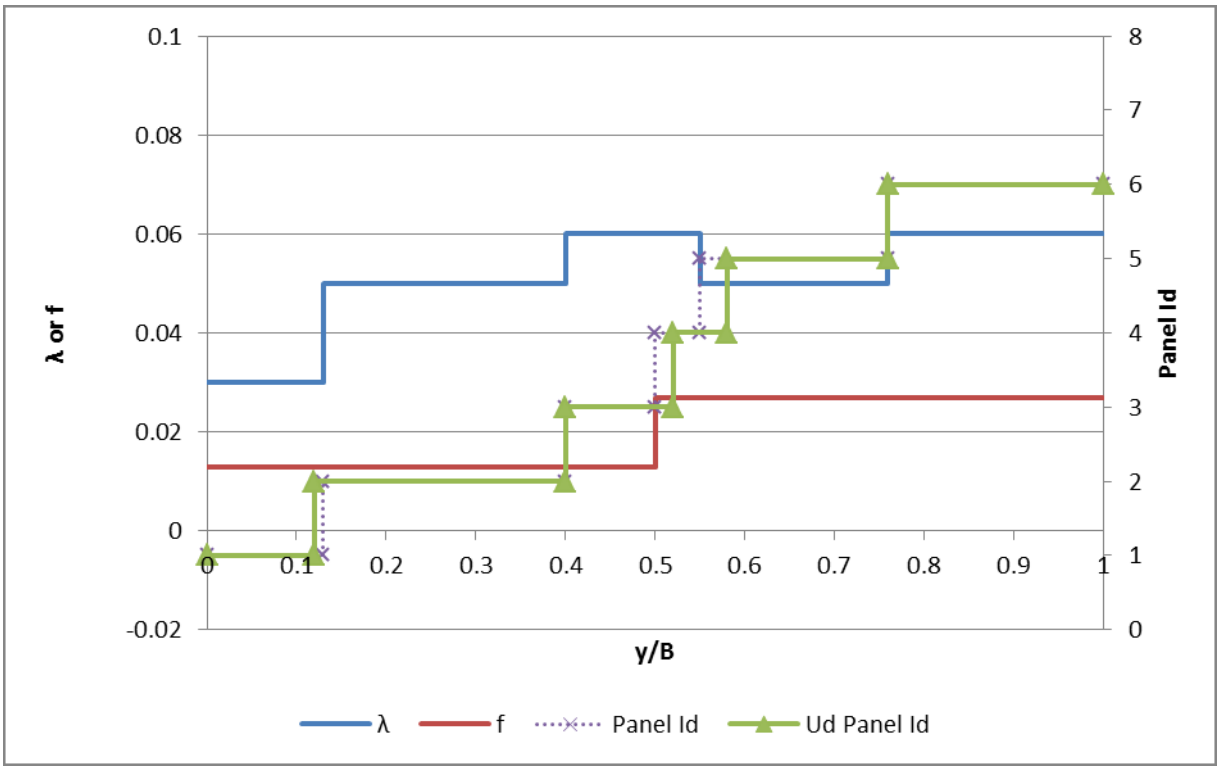

Figure 216: SKM Parameter Values By Panel (BC2 F2 CS2)

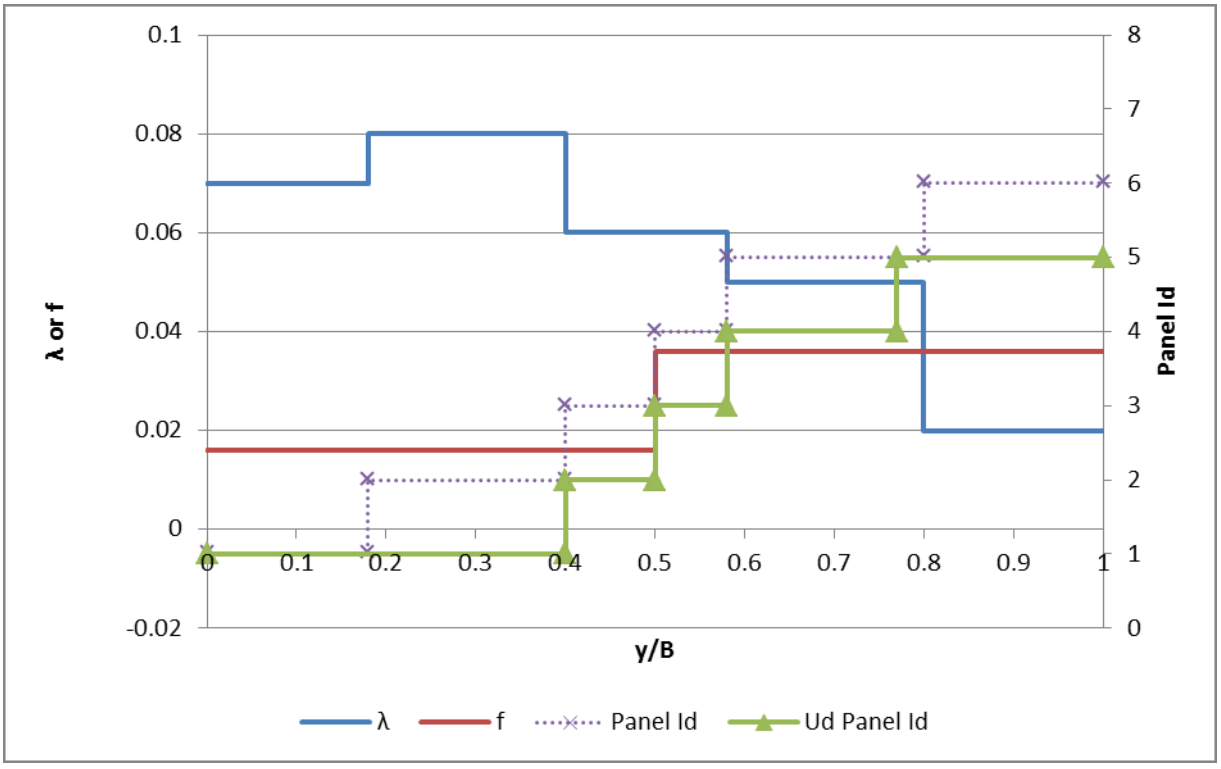

Figure 217: SKM Parameter Values By Panel (BC2 F2 CS4)

10.2 Dataset Specific SKM Modelling

It is instructive to examine the output of the SKM when applied to each data set using the panel boundaries and parameter values derived in Section 10.1 and without tuning (through Γ). The SKM has been applied in three ways:

(i) Using the λ values obtained from the experimental data and the panel boundaries obtained from examination of the transverse distribution of all parameters

(ii) Using the "standard" λ value of 0.07 for all panels and the panel boundaries obtained from examination of the transverse distribution of all parameters (as in (i))

(iii) Using the "standard" λ value of 0.07 for all panels (as in (ii)) but neglecting the λ distribution from the estimation of panel boundaries (termed "min. panels" in the accompanying figures)

The results of these methods are shown in Figure 218 and Figure 219 for BC1 F1 and BC2 F1 CS2 only, though the conclusions drawn are equally applicable for all datasets. The predictions using the calculated and standard λ values are negligibly different, except for regions where the calculated values are small $\lambda < \sim 0.05$, where the standard value improves the results. Whilst this simplifies the modelling somewhat, supporting the use of a single λ value across the channel, it is somewhat disappointing to find that the calculation of λ actually worsens the SKM modelling. However, if the definition of λ (see (82)) is examined then it is clear that calculations are hindered by the use of the (estimated) shear velocity and the (discrete approximation to) $\frac{\partial U}{\partial y}$. Additionally, while method (3) above does appear to give

poorer results than when panel boundaries are estimated from the λ distribution, estimating panel boundaries from this distribution while ignoring the calculated values in favour of the standard value is somewhat contradictory. Hence the following method for applying the SKM was used from this point on:

(i) $\lambda = 0.07$ for all panels

(ii) Panel boundaries estimated from the U_d distribution only

(iii) Tuning via Γ

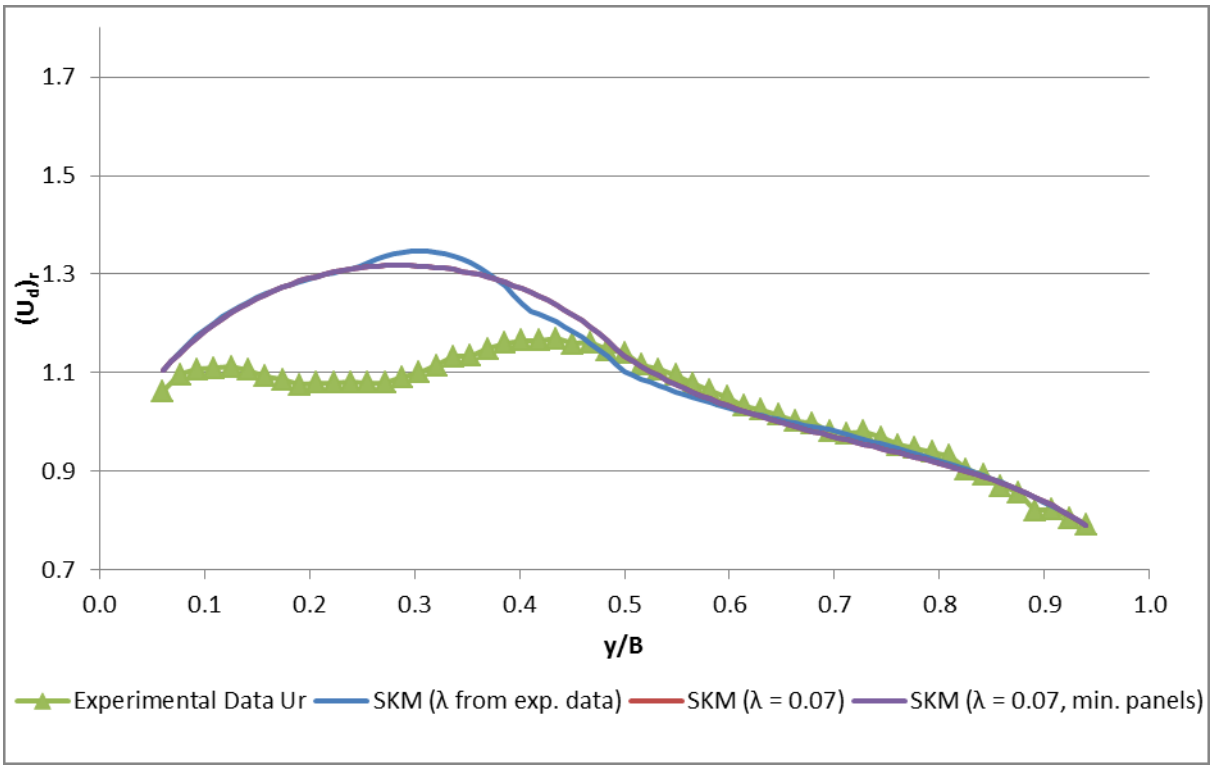

Figure 218: Initial SKM Predictions Using Different Panel Parameter Setting Methods (BC1 F1)

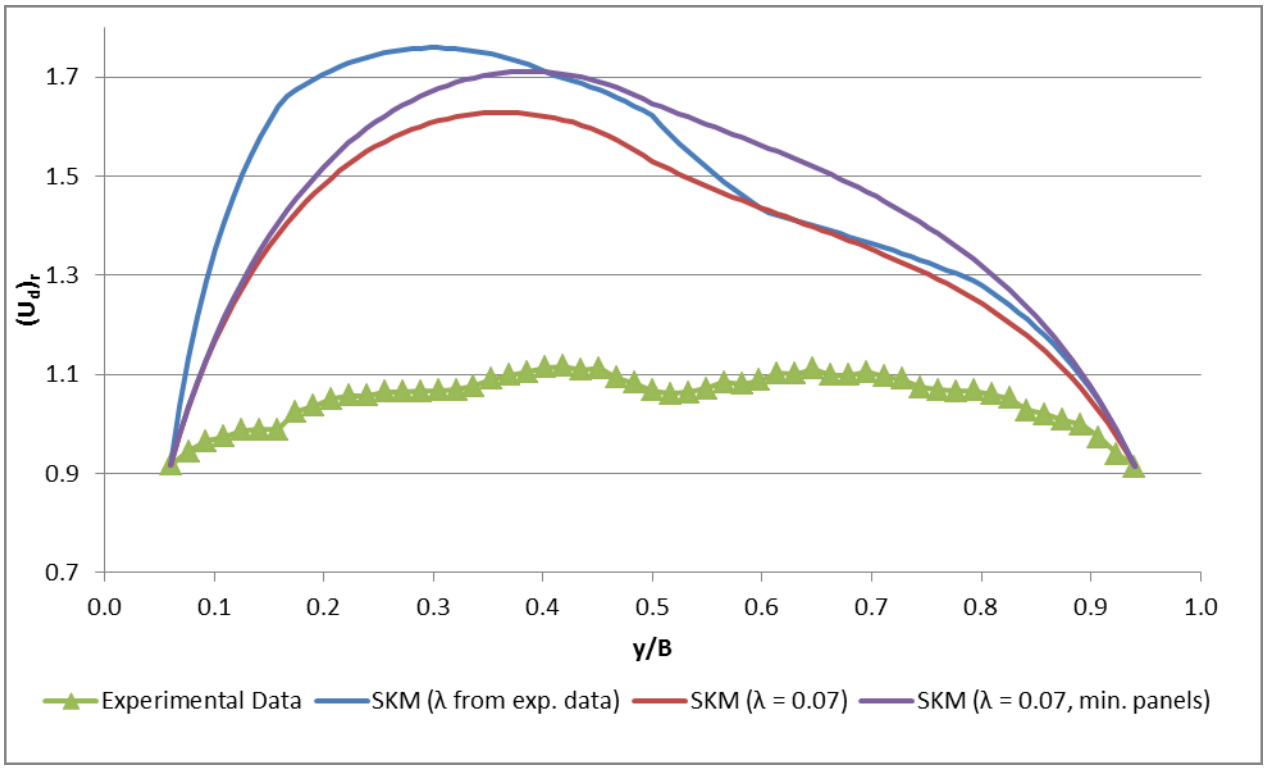

Figure 219: Initial SKM Predictions Using Different Panel Parameter Setting Methods (BC2 F1 CS2)

10.3 Generic Heterogeneous Channel SKM Modelling

In order to provide useful guidance to river modellers applying the SKM, it is necessary to determine (if possible) a suitable panel strategy for such a channel. The channel boundaries identified above are summarised in Figure 220. While this figure shows no definitive, shared panel boundary positions, certain positions are suggested which may give acceptable results for all datasets:

(i) $y/B = 0.20$

(ii) $y/B = 0.40$

(iii) $y/B = 0.50$ (RSB)

(iv) $y/B = 0.60$

(v) $y/B = 0.75$

This gives a total of six panels, three on each side. It should be mentioned that the panel boundary positions for BC1 and BC2 may reasonably be expected to differ, with BC1 having its own set of boundaries and similarly for BC2. However, this distinction is unclear from Figure 220 and so a common panel set is assumed valid at this point. These common panel boundaries were tested (for the U_d distribution – boundary shear stress will be considered later) against the experimental data using $\lambda = 0.07$ and $\Gamma = 0$ (no tuning) (Figure 221 to Figure 226), with the common boundaries showing better agreement with the experimental data, though the disparity between these untuned analytical results and the experimental results is noted.

In order to tune the SKM Γ was varied. The difficulty in doing this in a multi-panel SKM is that changes in Γ for one panel also affect the adjoining panels, making

manual tuning very difficult. An automated approach has been used by Sharifi et al. (2008, 2009) but such an algorithm is excessively complex for the single variable tuning required here. A brute force method has thus been applied (with some subtleties as described below), with Γ varied in the range $-2.0 \leq \Gamma \leq 2.0$ for each panel, in increments of $\Delta\Gamma = 0.1$. A larger Γ range was tried, but resulted in complex values of U_d in some cases; $\Delta\Gamma = 0.1$ was shown to give sufficient resolution, with smaller values having a negligible effect on the results. For each combination of panel Γ values the square of the difference between the analytical solution and the experimental data was calculated at each y position. These were then summed over the cross-section to give a representation of the error for that combination of Γs, with the combination which minimised the error used for the tuned SKM.

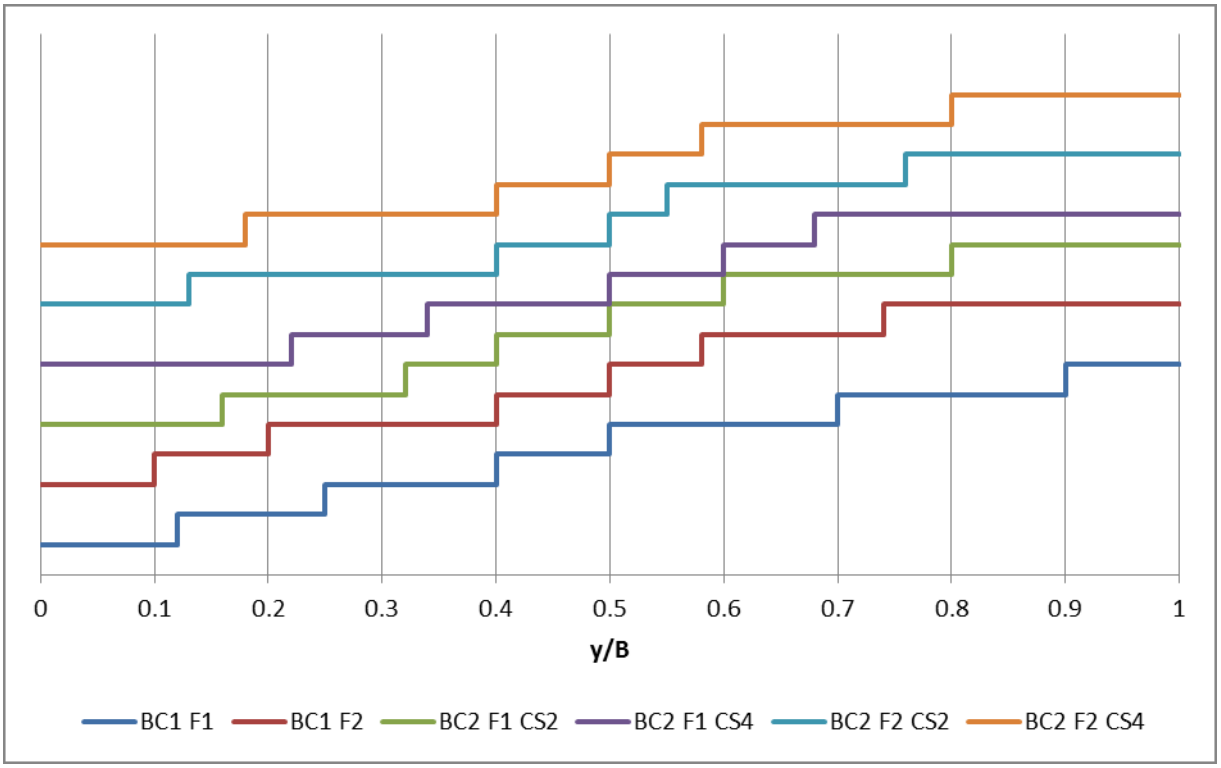

Figure 220: The Panel Boundaries Identified for Each Dataset (each horizontal section represents a single panel)

With n panels, a range of Γ of magnitude $\overleftrightarrow{\Gamma}$ and a resolution of magnitude $\Delta\Gamma$, there are $\left[\left(\overleftrightarrow{\Gamma}/\Delta\Gamma\right)+1\right]^n$ combinations of Γ per data set. With six panels and the values specified above, this results in $41^6 \cong 5\times10^9$ combinations of Γ for each data set, which is computationally prohibitive. A simple algorithm was therefore applied. Denoting the value of Γ for panel i in the minimising Γ combination as Γ_m^i, the following iterative procedure was performed:

1. Initialise $\Gamma_m^i = 0\ \forall\ i$, $\Delta\Gamma = 1$, $\overleftrightarrow{\Gamma}^i = \Gamma_m^i \pm 2\Delta\Gamma \equiv \pm 2\Delta\Gamma$ (being the $-2.0 \le \Gamma \le 2.0$ range).
2. Calculate the new Γ_m^i
3. Reduce $\Delta\Gamma$ by a factor of 2 and recalculate the ranges, $\overleftrightarrow{\Gamma}^i$ (these may now be different for each panel, being centred on the new Γ_m^i)

4. Repeat (2) and (3) until $\Delta\Gamma < 0.1$

This procedure reduces the number of calculations to $\sim 6 \times 10^4$ calculations (4 iterations with $5^6 \cong 1.6 \times 10^4$ calculations per iteration).

The tuned SKM results are included in Figure 221 to Figure 226. The common panels appear suitable to model the heterogeneous channel once appropriate tuning has been performed using Γ, though certain features of the U_d are not accurately modelled. For BC1 F2, the local minimum at $y/B \cong 0.15$ is not apparent in the SKM results, though it should be recalled that this dip is thought to be (at least in part) due to interference from the fixed ADV probe present for this dataset. For BC2, in particular for F2 for which they are more pronounced, the maxima and minimum around the RSB are not modelled by the SKM. This does not appear to be an issue with the common panels themselves, as tuning the custom panel versions of the SKM does not improve the modelling in this region (see Figure 227). As shall be seen below, the implications of this mis-modelling of the fine detail of U_d at the RSB on the discharge calculation are negligible. The tuned values of Γ are presented in Table 20.

Panel	BC1 F1	BC1 F2	BC2 F1 CS2	BC2 F2 CS2	BC2 F1 CS4	BC2 F2 CS4
1	0.3	1.4	0.9	1.3	0.9	1.1
2	1.0	1.0	1.0	1.3	0.8	0.9
3	-0.9	-0.4	0.8	1.0	1.0	1.3
4	0.0	0.9	1.0	0.5	0.1	0.0
5	-0.1	-0.5	0.3	0.3	0.4	0.4
6	0.0	1.0	0.5	0.1	0.1	0.3

Table 20: Variation of Γ

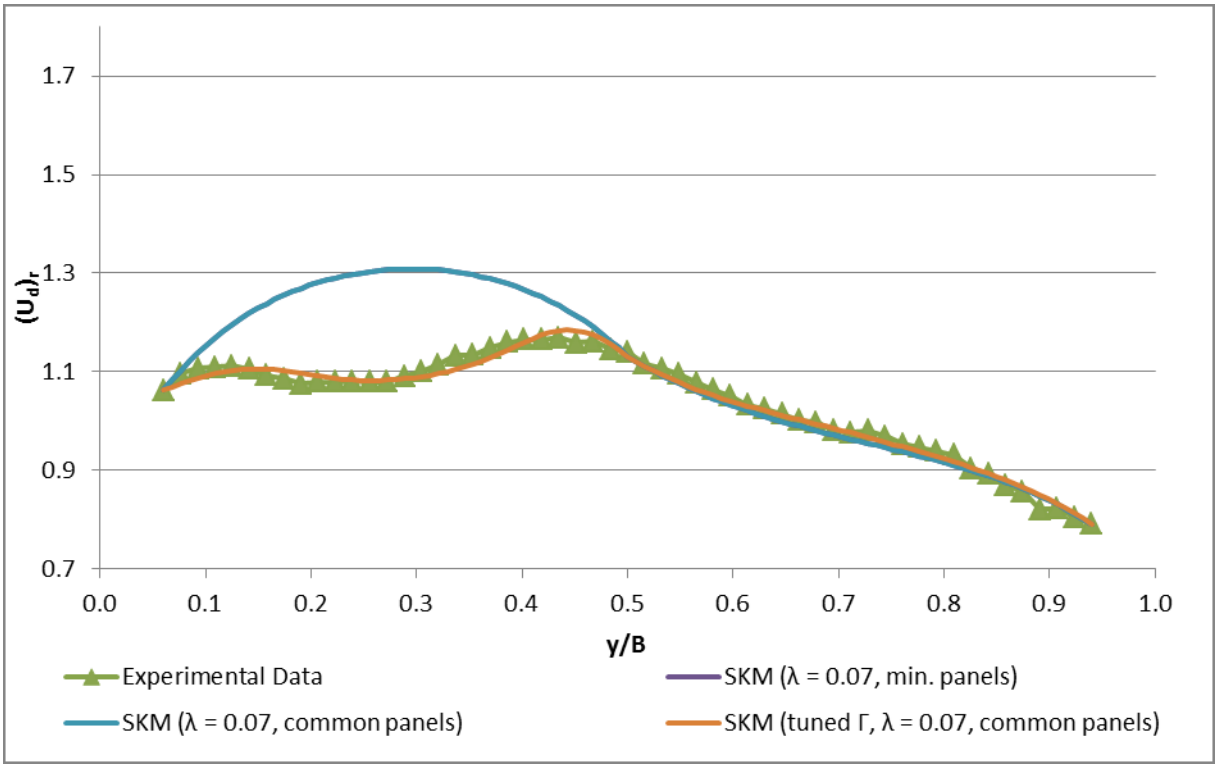

Figure 221:U_d Distribution Using a Common Set of SKM Panels (BC1 F1)

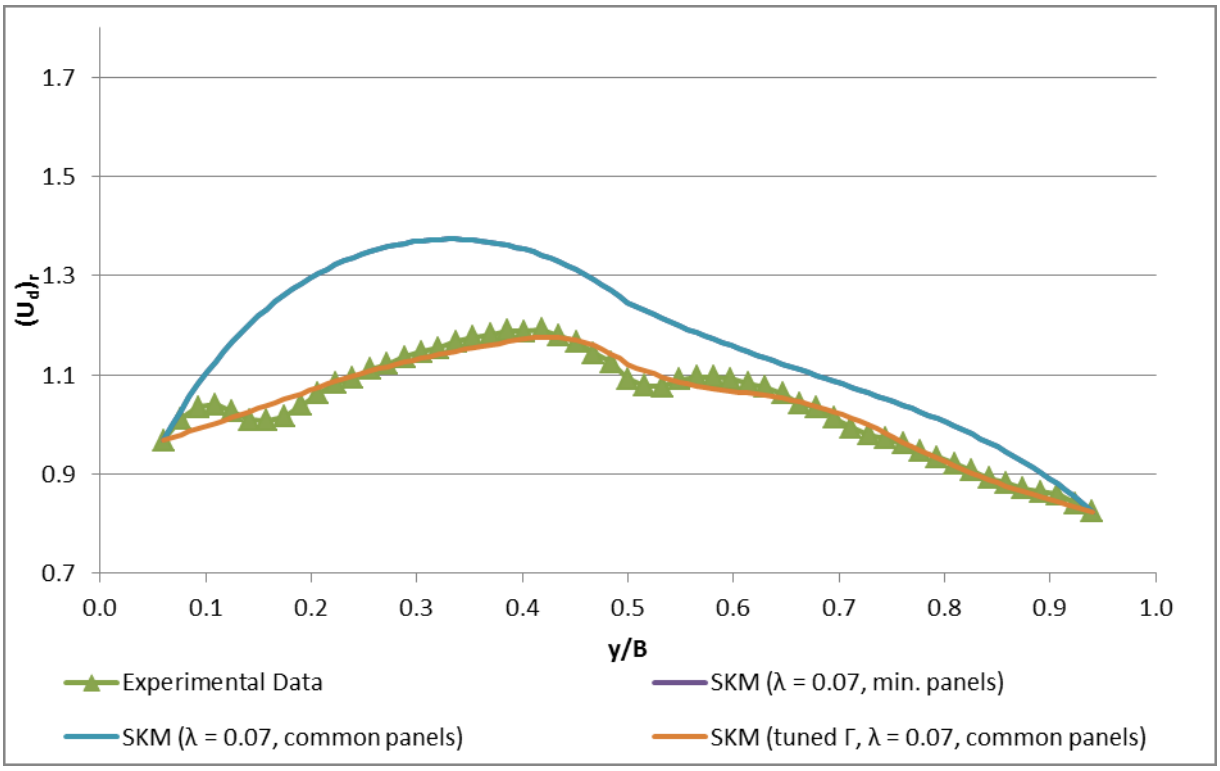

Figure 222:U_d Distribution Using a Common Set of SKM Panels (BC1 F2)

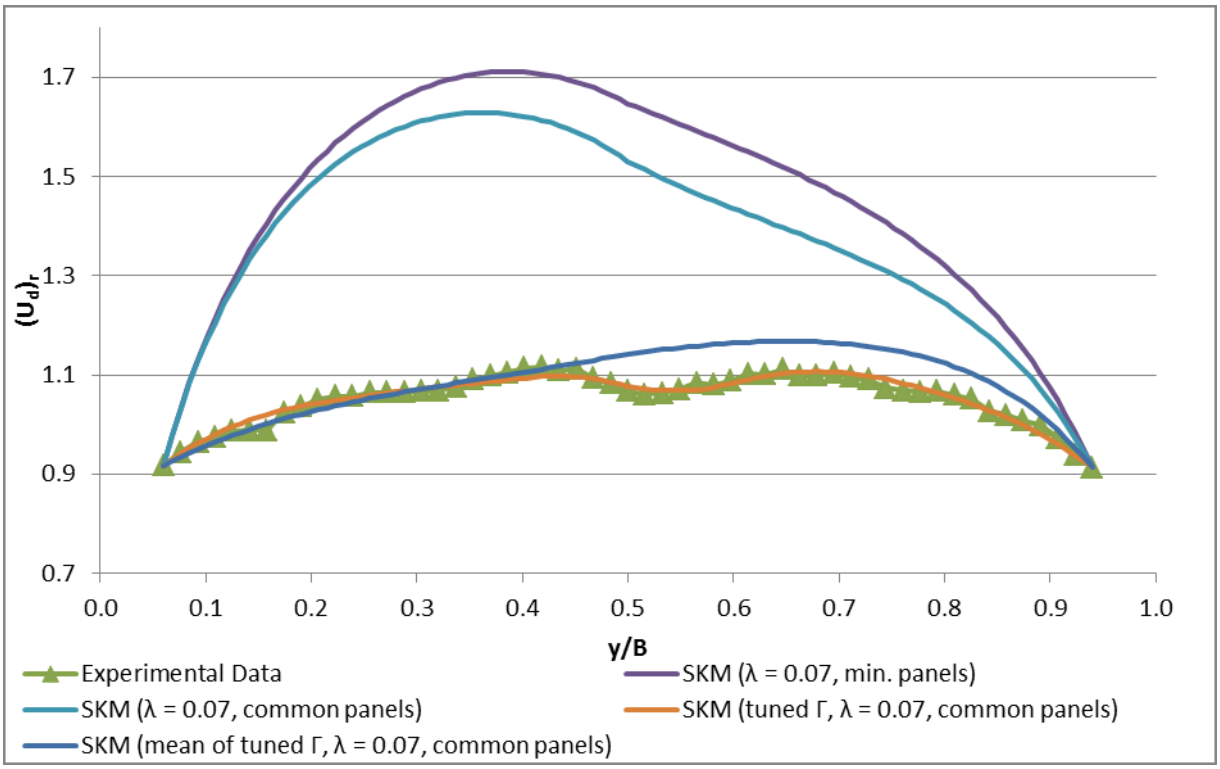

Figure 223:U_d Distribution Using a Common Set of SKM Panels (BC2 F1 CS2)

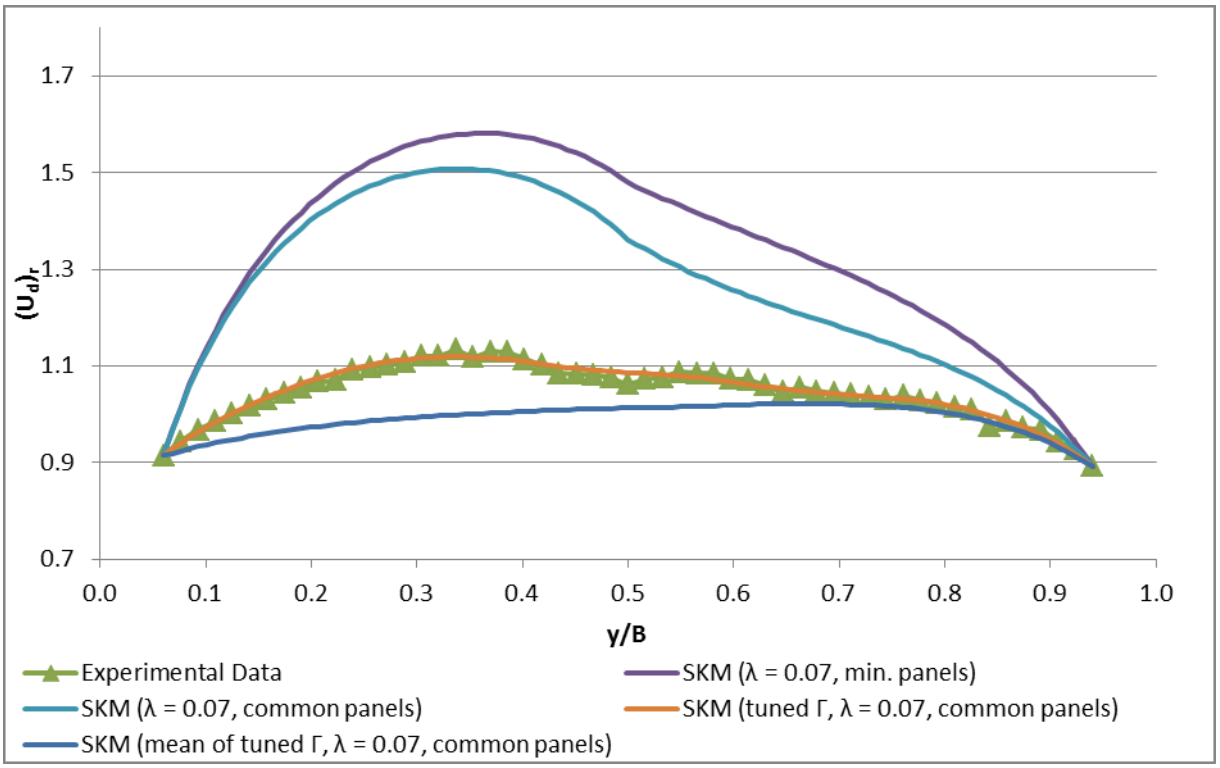

Figure 224:U_d Distribution Using a Common Set of SKM Panels (BC2 F1 CS4)

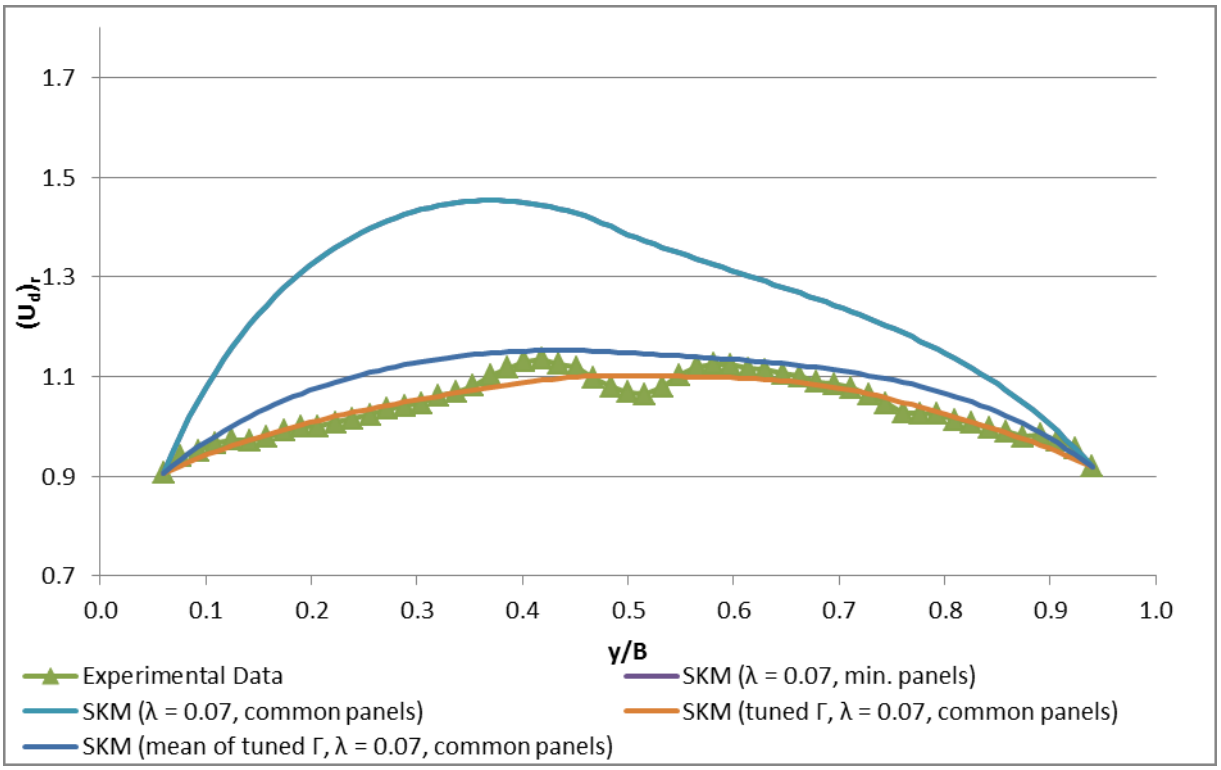

Figure 225:U_d Distribution Using a Common Set of SKM Panels (BC2 F2 CS2)

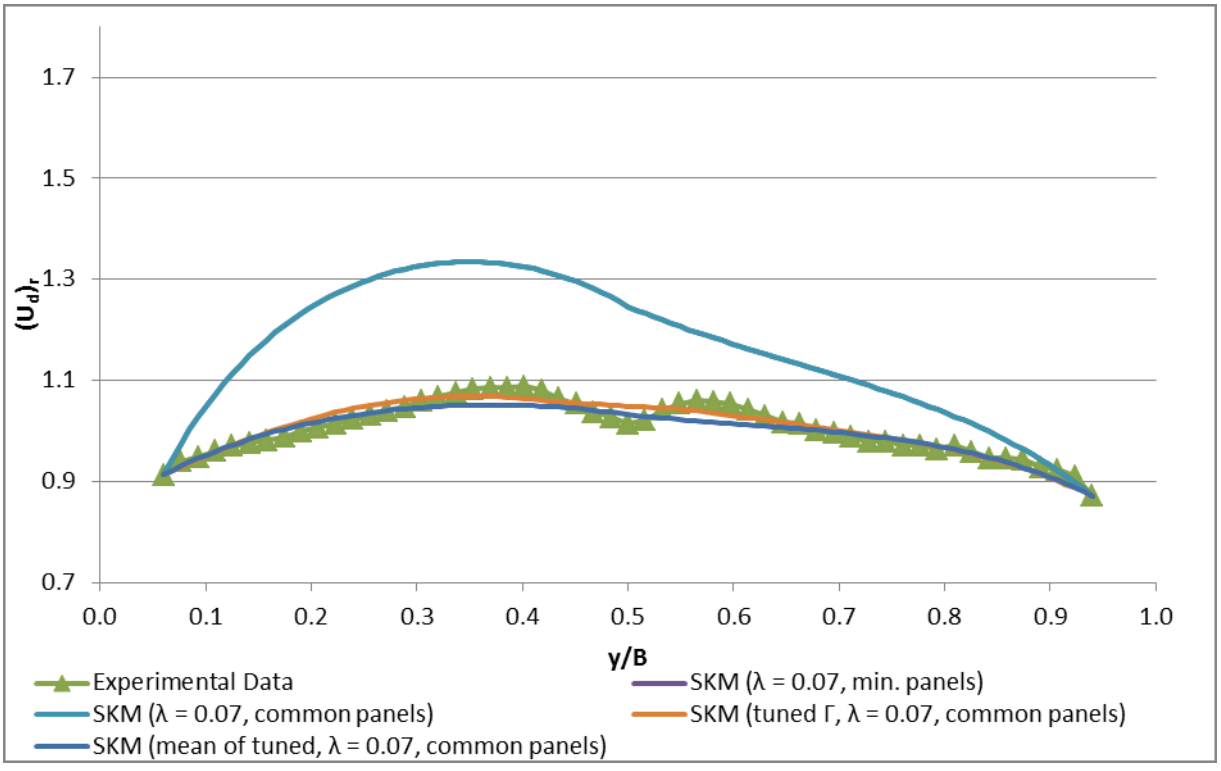

Figure 226:U_d Distribution Using a Common Set of SKM Panels (BC2 F2 CS4)

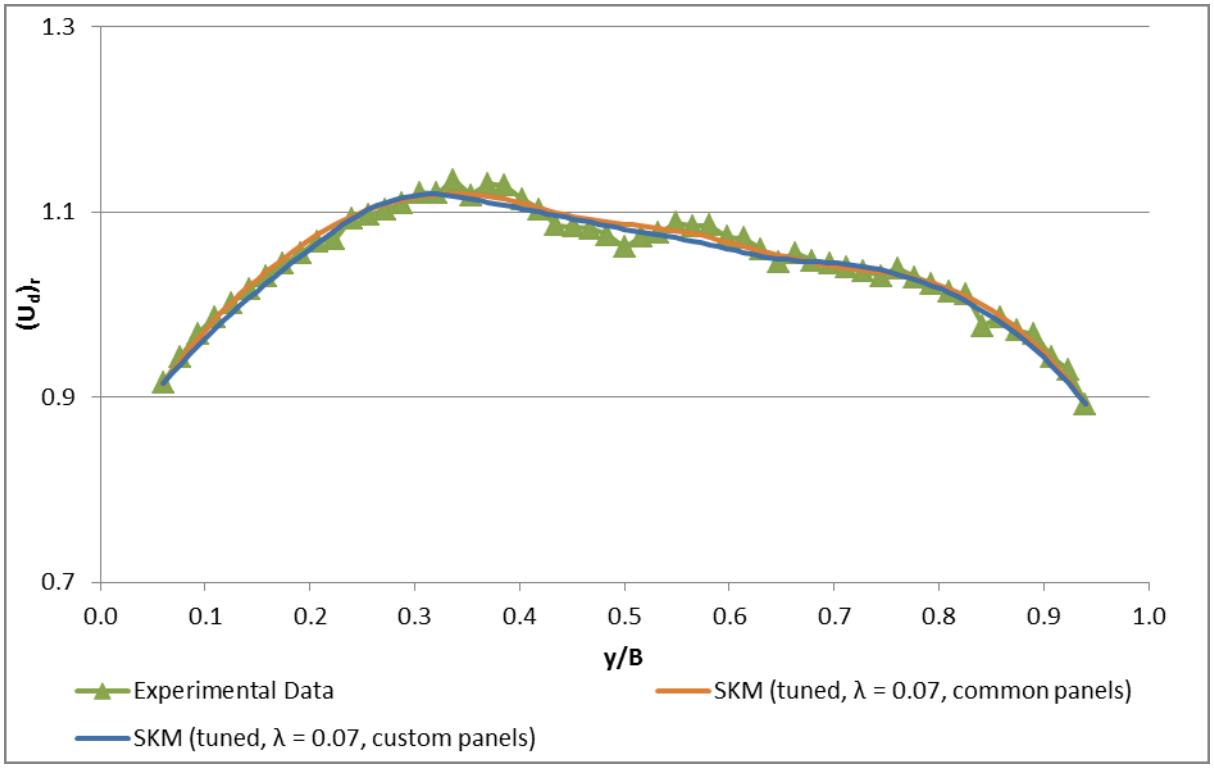

Figure 227: U_d Distribution with the Tuned SKM Using Common and Custom Panels (BC2 F1 CS4)

The discharge was calculated using the trapezium rule scaled by H ($\Delta Q(y) = U_d(y)(\Delta y)H \equiv U_d(y)(\Delta A)$, where $\Delta Q(y)$ is the discharge through the section $y_i < y < y_{i+1}$ and $\Delta y \equiv y_{i+1} - y_i$).

Dataset	% Deviation from Experimental Data Q					
	Q SKM (λ from exp. data)	Q SKM (λ = 0.07)	Q SKM (λ = 0.07, min. panels)	Q SKM (λ = 0.07, Common panels)	Q SKM (tuned, λ = 0.07, common panels)	Q SKM (mean of tuned Γ, λ = 0.07, common panels)
BC1 F1	5.6	5.6	5.6	5.6	-0.2	N/A
BC1 F2	10.6	12.1	12.1	12.1	-0.3	N/A
BC2 F1 CS2	40.3	32.1	39.0	32.1	-0.1	2.9
BC2 F1 CS4	33.2	28.4	28.4	21.2	0.1	-5.5
BC2 F2 CS2	27.0	21.4	21.4	21.4	-0.4	4.0
BC2 F2 CS4	18.2	15.5	15.5	15.5	0.1	-0.8

Table 21: Experimental and Modelled Discharge by SKM Panel Scheme

While the results tabulated above show that the SKM can be applied accurately to the experimental data using customised values of Γ, it is desirable to identify a pattern in the values to allow recommendations to be made for wider use of the SKM. With only two discharges measured it is evident that any such pattern will be imprecise at best. However, if the data sets are split by bed configuration and, in the

BC2 case, by cross-section (Table 20), then some conclusions may be drawn. Overall the Γ values are comparable to those found by Chlebek (2009) for rectangular channels of comparable aspect ratio.

For BC1, Γ shows much variation with H for the edge panels, 1 and 6 with $\Gamma \leq 0.3$ in these panels for F1, increasing to ≥ 1 for F2; this direct proportionality was also seen by Chlebek. Panel 2 (covering the central part of the smooth side) takes a value $\Gamma = 1.0$ for both flows; the equivalent rough side panel (panel 5) has a negative Γ whose magnitude increases for F2. Γ switches sign at the RSB, being negative for panel 3 and positive for panel 4. For panel 3, the magnitude decreases with H, while for panel 4 it increases from 0 (F1) to 0.9 (F2). In the theoretical development of the SKM the gamma term represents the effects of both (horizontal) secondary flow cells and (vertical) interface vortices. However, while it is tempting to ascribe this gamma sign reversal to such interface vortices, with only two data sets this would be highly speculative and, with gamma acting as a sink term, the signs are incorrect since such vortices would be expected to decrease U on the smooth and increase U on the rough side.

For BC2 the Γ values are more consistent across flows and cross-section, to the extent that the variation seen is inconclusive. With this consistency it is an obvious step to try using common values for all the BC2 data sets, and this has been done using the mean value of Γ for each panel, calculated from the four BC2 data sets. The output from the SKM using these “mean of tuned” Γ values is include in Figure 223 to Figure 226, and the predicted discharge included in Table 21. The discharge

prediction is within 6% of the true value in all cases, although (as may be seen from the figures) the modelling of the U_d distributions is unsatisfactory.

Knight et al (2007) identified discontinuities in the boundary shear stress distribution when using constant values of f for the SKM panels, and attempted to solve this by using a varying f, with constant values at the panel boundaries and a linear variation between. This improved the results as shown in Figure 228. However, the experimental data for the heterogeneous channel, in which an abrupt, large change in f occurs at the RSB, shows a discontinuity in τ_b (Figure 229 to Figure 234). Using a constant f models this change reasonably well, though in the case of BC1 the boundary shear stress is overestimated on both sides of the RSB. Using a linear f over the RSB panels 3 and 4 improves the boundary shear stress prediction on the rough side of the channel, but causes a greater overestimation on the smooth side (Figure 229 and Figure 232). For both BC2 F1 CS4 and BC2 F2 CS4 there is evidence of a spike in τ_b at the RSB followed by a dip at $0.5 < y < 0.65$. While the spike is modelled by neither the constant f nor linear f SKM, this dip is better modelled using the latter. Whilst giving a smoother τ_b distribution, the U_d distribution (also shown in Figure 229 and Figure 232) is less smooth, showing sharp peaks at the boundaries of the panels for which f is varied linearly.

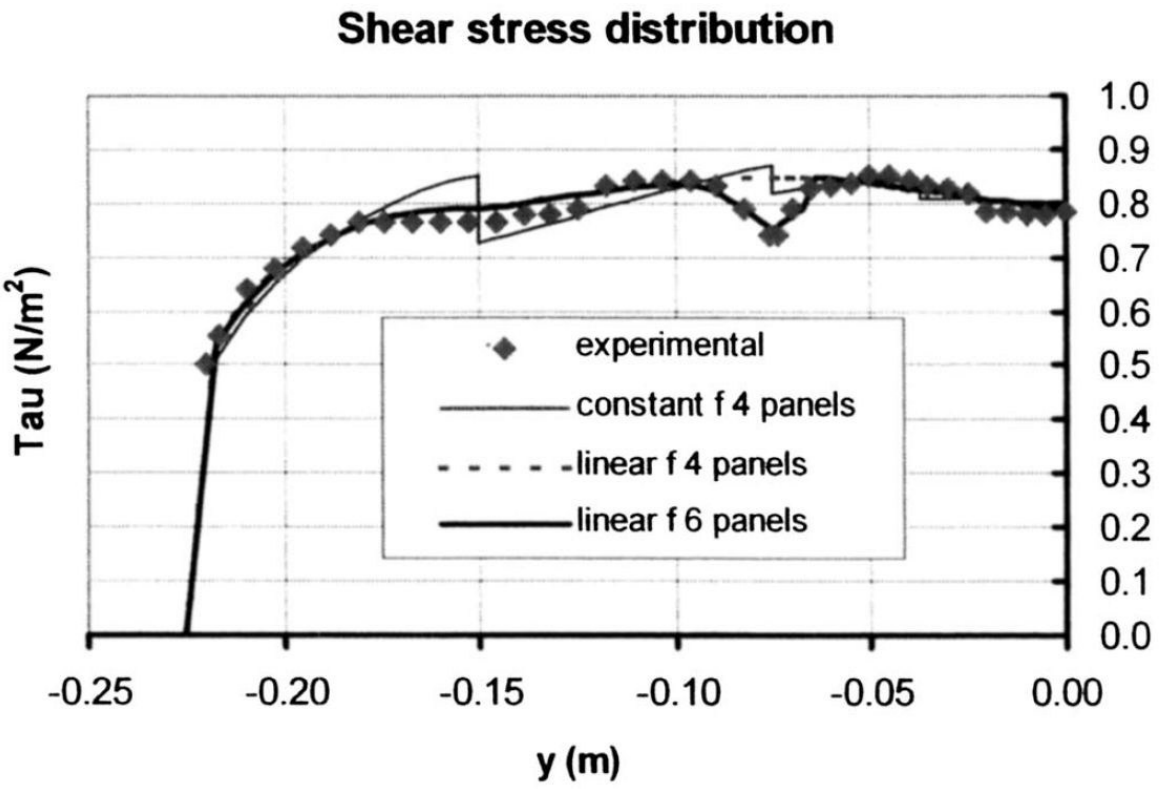

Figure 228: SKM Modelling of Boundary Shear Stress with Linearly Varying f (Knight et al., 2007)

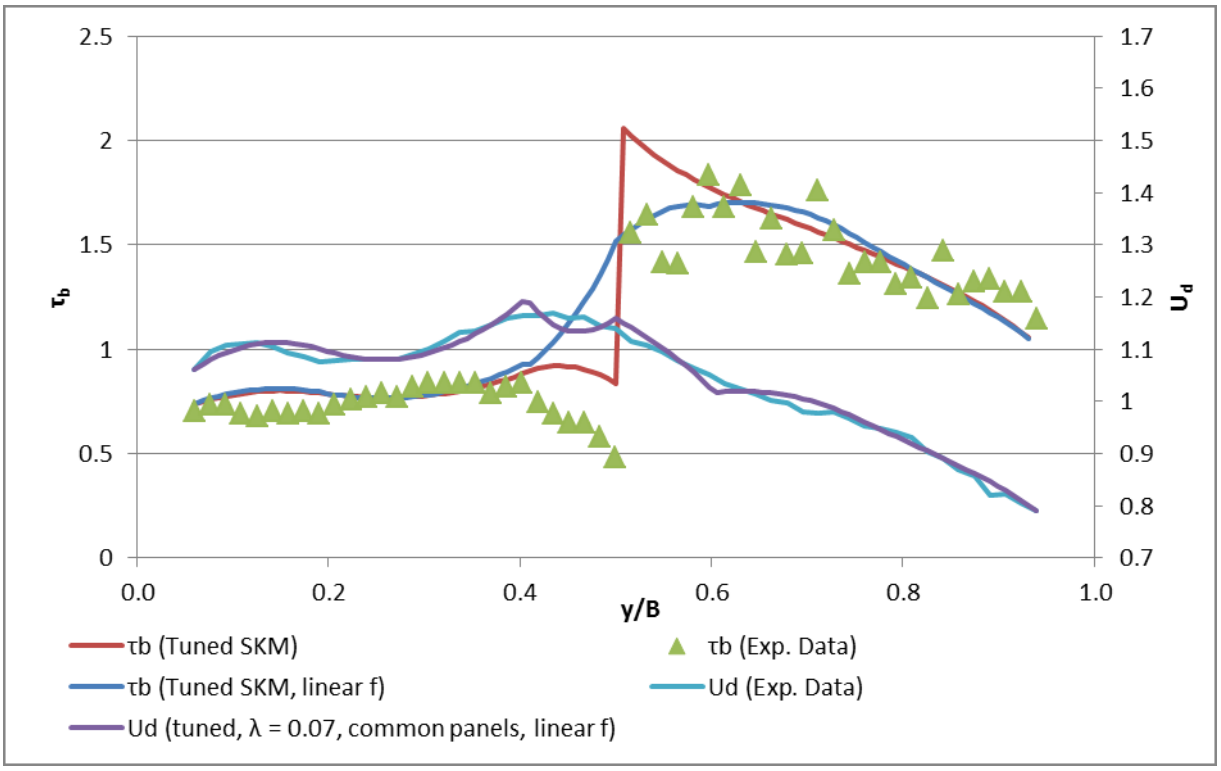

Figure 229: Boundary Shear Stress Distribution (BC1 F1)

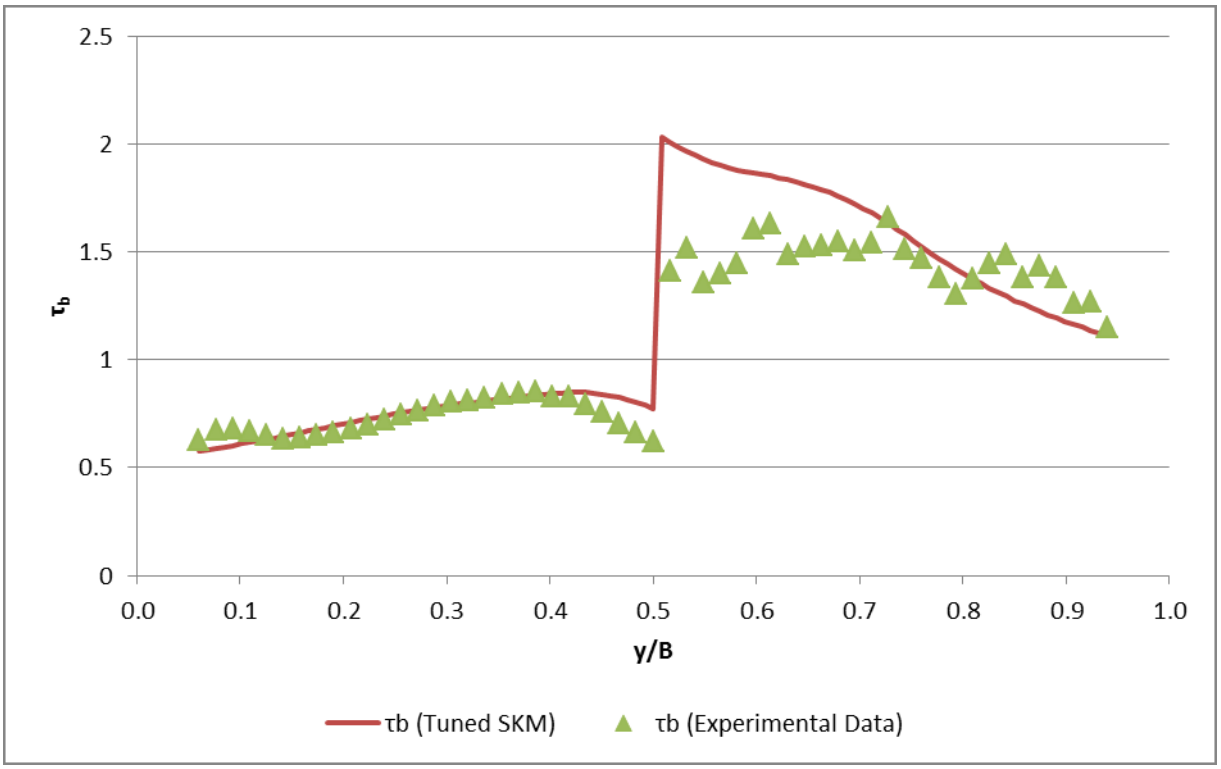

Figure 230: Boundary Shear Stress Distribution (BC1 F2)

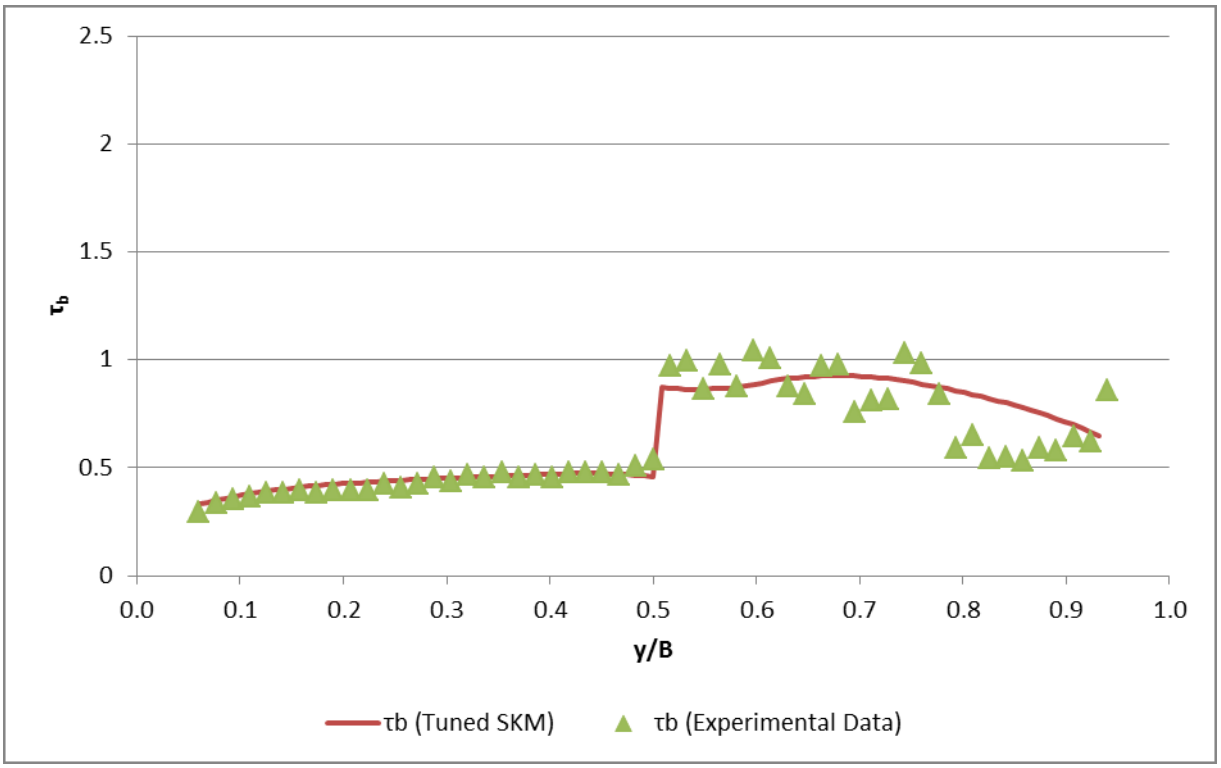

Figure 231: Boundary Shear Stress Distribution (BC2 F1 CS2)

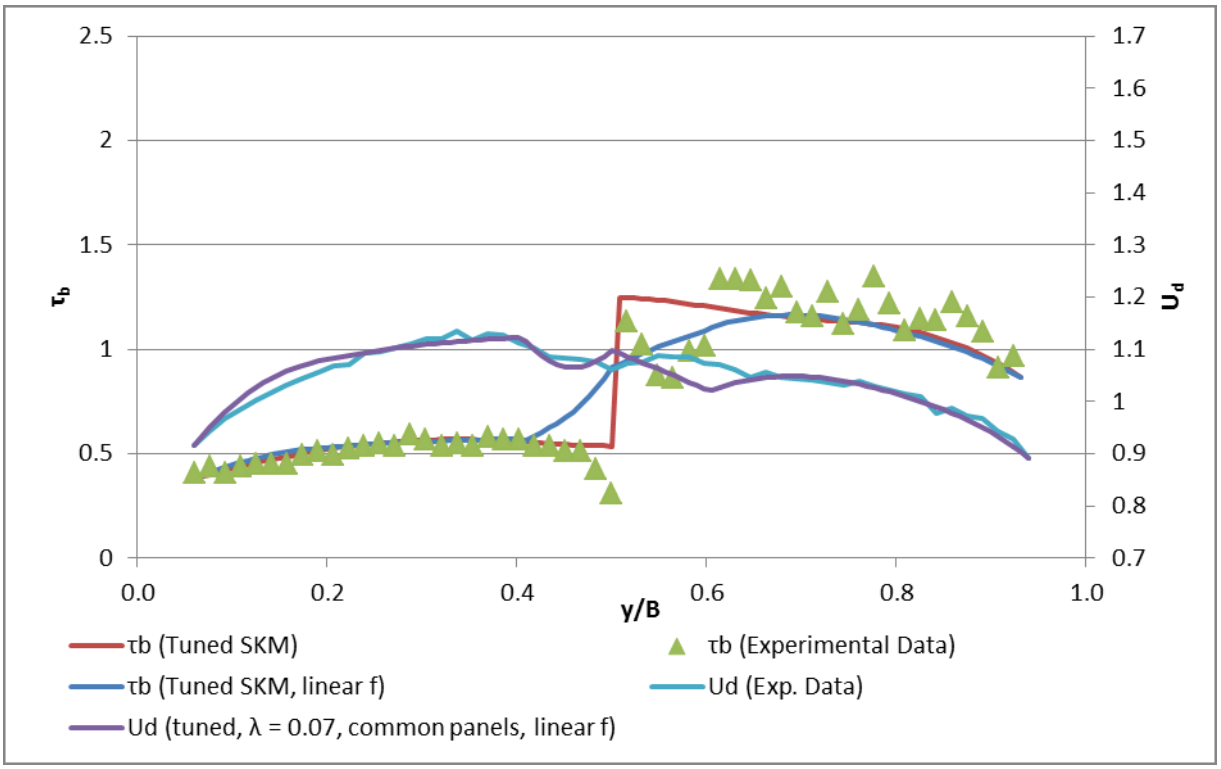

Figure 232: Boundary Shear Stress Distribution (BC2 F1 CS4)

Figure 233: Boundary Shear Stress Distribution (BC2 F2 CS2)

Figure 234: Boundary Shear Stress Distribution (BC2 F2 CS4)

11 CONCLUSIONS AND RECOMMENDATIONS

11.1 Conclusions

This thesis examined a little researched, yet extremely common, open-channel flow system – the laterally horizontal, heterogeneous channel – in order to better understand the physical processes occurring within such a system, and how to model such a system using the Shiono-Knight Method. Two bed configurations were used, one of full-length, longitudinal strip roughness ("BC1", allowing fully-developed, uniform flow to be examined) and another of alternating sections of rough and smooth bed in a "checkerboard" pattern ("BC2", more closely mimicking the bed variation in a natural river). From the stage-discharge and high-frequency, 3-D velocity measurements made the following conclusions may be drawn (the hypotheses and objectives referenced below are defined in Section 2):

11.1.1 Stage-Discharge

(i) Stage-discharge curves constructed using standard divided channel methods (DCMs) have been compared with experimental stage-discharge curves for a heterogeneous channel constructed to meet Objective (i). These DCM curves do not accurately model a heterogeneous channel, underestimating discharge by $\sim 5\%$ at very low flow rates and $> 15\%$ at medium and high flow rates.

(ii) For a given flow depth, H, discharge differences of $\sim 15\%$ are seen between the BC1 and BC2 for low flow rates, while at medium to high flow rates the difference between the two stage-discharge curves is approximately $\sim 4\%$.

Along with (i), this proves the latter part of the first hypothesis (see Section 2), that a heterogeneous bed will significantly affect the channel conveyance.

(iii) The overall channel friction factor and Manning's n are highly dependent on H, decreasing monotonically with depth, though this variation reduces as H increases. For BC2 the friction factor and n tend towards the values for a homogeneously rough channel for small H (low flow rates).

11.1.2 Mean Velocity Characteristics

The second objective of this research (Objective (ii)) was to map the 3-D velocity field over channel cross-sections. From the data provided by these measurements it is concluded that:

(i) For BC1 the streamwise velocity profiles show interaction between the rough side and smooth side flow. In the BC2 case, the streamwise velocity profile develops from the point at which the roughness switches sides, with a profile resembling that of BC1 by a distance approximately $2.5B$ downstream of the roughness switch. A clear streamwise velocity difference is evident, particularly near the channel bed, as hypothesised in Section 2.

(ii) Vertical U distributions are logarithmic throughout the channel, for all data sets. For BC2, the streamwise velocity reacts quickly to the roughness switch – at positions below $y/B \cong 0.2$, U increases (or decreases, depending on whether the channel side changes from rough to smooth or smooth to rough) within a distance $1B$ of the roughness switch.

(iii) Secondary flow cells are caused by the RSB and contribute to lateral momentum transfer, as hypothesised. In the case of BC1, clearly defined cells

are seen on the smooth side and extending over the RSB. In the case of BC2, a central secondary flow cell develops by $2.5B$ from the roughness switch; for both BC1 and BC2 these cells are upwards over the smooth bed and downwards over the rough bed. However, immediately following the roughness switch there is strong upflow over the newly rough bed near the RSB which reduces with downstream distance until it reverses as part of this central flow cell. Lateral velocities are small ($\sim 2\%$ of U).

11.1.3 Turbulence Characteristics

The examination of the turbulent part of the velocity data (Objective (ii)) and the application of Quadrant-Hole and Conditional Time-Series analyses (Objective (iii)) lead to the following conclusions, which support the first hypothesis that interaction between faster and slower moving regions of water will lead to regions of high transverse shear and turbulence:

(i) τ_V^R is at a maximum over the rough bed and, in the BC2 case, is damped by the smooth bed after the roughness switch. The τ_H^R distribution shows a vertical band of peak magnitude near the RSB, analogous to the τ_V^R near the bed with the "bed" being the slower moving water on the rough side of the channel. The magnitude of the τ_H^R is much reduced for BC2 compared to BC1, being less than approximately one-third at most (more so for certain data sets).

(ii) Quadrant-Hole analysis reveals that, in regions of high Reynolds stress, ejection and sweep events dominate, with high magnitude events contributing disproportionately to the total Reynolds stress. Conditional Time Series

analysis supports the finding of coherence between the turbulent fluctuations of the velocity components, and indicates a periodicity indicative of cycles of ejections and sweeps at regular intervals.

(iii) The TI, TKE and TKE flux data clearly show the propagation of turbulence from the rough bed and across the RSB. Mean values of the lateral TI components are $\sim 75\%$ and $\sim 45\%$ of the streamwise TI component for the y- and z-direction respectively. These percentages are consistent across all data sets.

11.1.4 Boundary Shear Stress

(i) Direct measurement of boundary shear stress (using a Preston tube) was not possible over the rough bed due to the length of the tube and size of the gravel. Estimation of the rough side boundary shear stress was attempted by a number of methods but was still subject to a large error $(\sim 20\% +)$. It is clear, however, that there is a step increase in boundary shear stress at the RSB, moving from the smooth to the rough side.

(ii) Smooth side boundary shear measurements for BC1 and BC2 CS4 show a reduction in the smooth side boundary shear near the RSB, a phenomenon not seen for BC2 CS2 (i.e. in the region where flow is undeveloped).

11.1.5 SKM Modelling

It is concluded that the second hypothesis, that the SKM can be customised to satisfactorily model a heterogeneous channel, has been proven by the customisation of the SKM performed in the meeting of Objective (iv). In particular it is concluded that:

(i) Unlike previous applications of the SKM, which have assumed channel symmetry about the centreline, both sides of the channel must be modelled.

(ii) The values of f calculated from the experimental data give good results when used in the SKM. Using a constant value over the rough side of the channel, and a second constant value over the smooth side of the channel (with, therefore, a panel boundary at the RSB) gives good agreement between the model and experimental U_d distribution, with negligible error (once the SKM has been tuned) in the calculation of Q.

(iii) Calculation of λ from the experimental data does not improve results relative to using the "standard" value of $\lambda = 0.07$ for all panels. Further, estimating panel boundaries from the λ distribution has a negligible effect when compared to estimating panel boundaries from the U_d distribution alone.

(iv) Γ cannot be calculated from the experimental data and should be used purely as a tuning parameter.

(v) A generic panel boundary scheme (see Section 10.3) may be applied to all data sets while maintaining accuracy, with a narrow panel each side of the RSB.

(vi) Modelling the boundary shear is contradictory – a linearly varying f (over the narrow panels surrounding the RSB, see (v)) improves the modelling of the rough side, while the constant f scheme used to model U_d performs better at modelling the smooth side. The two are equivalent outside these central panels.

(vii) Based on the above, and acknowledging the need for more data sets to confirm these findings, the following scheme for applying the SKM is recommended:

a. Six panels (three per side) as specified in Section 10.3;

b. f constant on each side;

c. $\lambda = 0.07$ for all panels;

d. Γ is used as a tuning parameter;

11.2 Recommendations for Future Study

As noted in the Introduction (Section 1) and the Related Research section of the Literature Review (Section 3.8), the investigation into heterogeneous channel beds is in its infancy. It is therefore important that additional experimental data be obtained to support (or refute) the conclusions of this thesis, and that this work is moved from an experimental channel in the laboratory towards modelling a natural river. In particular:

(i) More data sets of comparable detail to those obtained for this thesis are required, spanning a greater range of aspect ratios, allowing further investigation of depth-dependency of the flow characteristics.

(ii) Use of Γ purely as a tuning parameter is somewhat unsatisfactory. In order to better investigate the variation of this parameter, bearing in mind the vertical "stacking" of secondary flow cells in a rectangular channel, alternatives to the ADV should be considered, allowing the full depth of flow to be mapped.

(iii) Further examination of λ, through additional data sets, would be beneficial in order to better relate the value of this parameter to physical phenomena of the flow. While the standard value is based on the (experimentally derived)

Karman's constant and does, therefore, have a physical basis, it would (as with Γ) be preferable to understand the variation of this parameter in physical terms rather than using the standard.

(iv) A method of measuring the rough side boundary shear stress is required, or at least an improved method of estimation. Full depth, high frequency velocity measurements (reaching fully to the bed) may provide a better basis for estimation.

(v) The recommended scheme for application of the SKM should be applied to a natural river for which detailed flow data is available, in order to verify the methodology for practical application.

LIST OF REFERENCES

ABRIL, J. B. & KNIGHT, D. W. 2004. Stage-Discharge Prediction for Rivers in Flood Applying a Depth-Averaged Model. *Journal of Hydraulic Research,* 42**,** 616-629.

ALFREDSSON, P. H. & JOHNASSON, A. V. 1984. On the Detection of Turbulence-Generating Events. *Journal of Fluid Mechanics,* 139**,** 325-345.

ALHAMID, A. A. I. 1991. *Boundary Sheer Stress and Velocity Distributions in Differentially Roughened Trapezoidal Open Channels.* PhD, University of Birmingham.

BLANCKAERT, K. & LEMMIN, U. 2006. Means of Noise Reduction in Acoustic Turbulence Measurements. *Journal of Hydraulic Research,* 44**,** 3-17.

BOUSSINESQ, J. V. 1877. Essai sur la Theorie des Eaux Courantes ("Essay on the Theory of Water Flow"). *Memoires presentes par divers savants a l'Academie des Sciences,* 23**,** 1-680 (in French).

BRITISH STANDARDS INSTITUTE 1983. BS1042 : Section 2.1: Measurement of Fluid Flow in Closed Conduits, Method Using Pitot Static Tubes. British Standards Institute.

BUFFIN-BELANGER, T. & ROY, A. G. 2005. 1 Min in the Life of a River: Selecting the Optimal Record Length for the Measurement of Turbulence in Fluvial Boundary Layers. *Geomorphology,* 68**,** 77-94.

CEA, L., PUERTAS, J. & PENA, L. 2007. Velocity Measurements on Highly Turbulent Free Surface Flow Using ADV. *Experiments in Fluids,* 42**,** 333-348.

CHADWICK, A., MORFETT, J. & BORTHWICK, M. 2004. *Hydraulics in civil and environmental engineering*, Spon Press.

CHLEBEK, J. 2009. *Modellling of Simple Prismatic Channels with Varying Roungess Using the SKM and a Study of Flows in Smooth Non-Prismatic Channels with Skewed Floodplains.* PhD, University of Birmingham.

CHLEBEK, J. & KNIGHT, D. W. 2006. A New Perspective on Sidewall Correction Procedures, Based on SKM Modelling. *In:* FERREIRA, ALVES, LEAL & CARDOSO (eds.) *River Flow 2006.* London: Taylor & Francis Group.

CHOW, V. T. 1959. *Open-Channel Hydraulics,* Singapore, McGraw-Hill.

DAVIDSON, P. A. 2004. *Turbulence - an introduction for scientists and engineers*, Oxford University Press.

ENVIRONMENT AGENCY. 2007. *Review of 2007 Summer Floods* [Online]. Environment Agency, Rio House, Bristol, BS32 4UD. Available: http://publications.environment-agency.gov.uk/PDF/GEHO1107BNMI-E-E.pdf [Accessed 14/09/2011].

GARCIA, C. M., CANTERO, M. I., REHMANN, C. R. & GARCIA, M. H. 2004. New Methodology to Subtract Noise Effects from Turbulence Parameters Computed from ADV Velocity Signals. *World Water Congress.* ACSE.

GESSNER, F. B. 1973. Origin of Secondary Flow in Turbulent Corner Flow. *Journal of Fluid Mechanics,* 58**,** 1-25.

GORING, D. G. & NIKORA, V. I. 2002. Despiking Acoustic Doppler Velocimeter Data. *Journal of Hydraulic Engineering,* 128**,** 117-126.

HARVEY, G. L. & CLIFFORD, N. J. 2009. Microscale Hydrodynamics and Coherent Flow Structures in Rivers: Implications for the Characterization of Physical Habitat. *River Research and Applications,* 25**,** 160-180.

HENDERSON, F. M. 1966. *Open Channel Flow,* New York, Macmillan.

HORTON, R. E. 1933. Separate Roughness Coefficients for Channel Bottom and Sides. *Engineering News Record,* 22**,** 652-653.

IMAMOTO, H. & ISHIGAKI, T. 1992. Flow Visualization in a Transverse Cross Section of an Open-Channel Flow. *Experimental Thermal and Fluid Science,* 5**,** 268-273.

JAMES, C. S. & JORDANOVA, A. A. 2010. Reach-Scale Resistance of Distributed Roughness in Channels. *In:* DITTRICH, K., ABERLE & GEISENHANER (ed.) *River Flow 2010.* Karlsruhe, Germany: Bundesanstalt für Wasserbau (Federal Waterways Engineering and Research Institute).

JESSON, M., STERLING, M. & BRIDGEMAN, J. 2010. Turbulent Structures in Heterogenous Channels and Their Effects on Converyance. *First IAHR European Division Congress.* Heriot-Watt University, Edinburgh: IAHR.

JESSON, M., STERLING, M. & BRIDGEMAN, J. 2011a. An Experimental Study of Turbulence in a Heterogeneous Channel. *Proceedings of the Institution of Civil Engineers, Water Management*.

JESSON, M., STERLING, M. & BRIDGEMAN, J. Year. Open-Channel Discharge Characteristics and Secondary Flow Development Over a Biotope-Scale Heterogeneous Channel Bed. *In:* 6th IASME / WSEAS International Conference on Water Resources, Hydraulics and Hydrology, 23rd-25th February 2011 2011b Cambridge. WSEAS.

JOWETT, I. G. 1993. A Method for Objectively Identifying Pool, Run and Riffle Habitats from Physical Measurements. *New Zealand Journal of Marine and Freshwater Research,* 27**,** 241-248.

KAIMAL, J. C. & FINNIGAN, J. J. 1994. *Atmospheric Boundary Layer Flow*, Oxford University Press.

KNIGHT, D. W., MCGAHEY, C., LAMB, R. & SAMUELS, P. G. 2010. *Practical Channel Hydraulics,* London, CRC Press/Balkena, Taylor & Francis Group.

KNIGHT, D. W., OMRAN, M. & TANG, X. 2007. Modeling Depth-Averaged Velocity and Boundary Shear in Trapezoidal Channels with Secondary Flows. *Journal of Hydraulic Engineering,* 133**,** 39-47.

LANE, S. N., BIRON, P. M., BRADBROOK, K. F., BUTLER, J. B., CHANDLER, J. H., CROWELL, M. D., MCLELLAND, S. J., RICHARDS, K. S. & ROY, A. G. 1998. Three-Dimensional Measurement of River Channel Flow Processes Using Acoustic Doppler Velocimetry. *Earth Surface Processes and Landforms,* 23**,** 1247-1267.

LIAO, H. & KNIGHT, D. W. 2007. Analytic Stage-Discharge Formulas for Flow in Straight Prismatic Channels. *Journal of Hydraulic Engineering,* 133**,** 1111-1122.

LOHRMANN, A., CABRERA, R. & KRAUS, N. C. Year. Acoustic Doppler Velocimeter (ADV) for Laboratory Use. *In:* Fundamentals and Advancements in Hydraulic Measurements and Experimentation, 1994 Buffalo, New York. ASCE, 351-365.

LU, S. S. & WILLMARTH, W. W. 1973. Measurements of the Structure of the Reynolds Stress in a Turbulent Boundary Layer. *Journal of Fluid Mechanics,* 60**,** 481-511.

MATHIESEN, M. 2008. *Nortek AS Forum - Distance transmitter to sampling volume* [Online]. Nortek AS. Available: http://www.nortekusa.com/en/knowledge-center/forum/velocimeters/270676734#467719118 [Accessed 22nd September 2009].

MCGAHEY, C., SAMUELS, P. G. & KNIGHT, D. W. 2006. A Practical Approach to Estimating the Flow Capacity of Rivers - Application and Analysis. *In:* FERREIRA, ALVES, LEAL & CARDOSO (eds.) *River Flow 2006.* London: Taylor & Francis Group.

MCLELLAND, S. J., ASHWORTH, P. J., BEST, J. L. & LIVESEY, J. R. 1999. Turbulence and Secondary Flow Over Sediment Stripes in Weakly Bimodal Bed Material. *Journal of Hydraulic Engineering,* 125**,** 463-473.

MCLELLAND, S. J. & NICHOLAS, A. P. 2000. A New Method for Evaluating Errors in High-Frequency ADV Measurements. *Hydrological Processes,* 14**,** 351-366.

MORVAN, H., KNIGHT, D., WRIGHT, N., TANG, X. & CROSSLEY, A. 2008. The Concept of Roughness in Fluvial Hydraulics and its Formulation in 1D, 2D and 2D Numerical Simulation Models. *Journal of Hydraulic Research,* 46**,** 191-208.

NAKAGAWA, H. & NEZU, I. 1977. Prediction of the Contributions to the Reynolds Stress from Bursting Events in Open-Channel Flows. *Journal of Fluid Mechanics,* 80**,** 99-128.

NEWSON, M. D. & NEWSON, C. L. 2000. Geomorphology, Ecology and River Channel Habitat: Mesoscale Approaches to Basin-Scale Challenges. *Progress in Physical Geography,* 24**,** 195-217.

NEZU, I. 2005. Open-Channel Flow Turbulence and its Research Prospect in the 21st Century. *Journal of Hydraulic Engineering,* 131**,** 229-246.

NEZU, I. & NAKAGAWA, H. 1984. Cellular Secondary Currents in Straight Conduit. *Journal of Hydraulic Engineering,* 110**,** 173-193.

NEZU, I. & NAKAGAWA, H. 1993. *Turbulence in Open-Channel Flows,* Rotterdam, A.A. Balkema.

NEZU, I. & ONITSUKA, K. 2001. Turbulent Structures in Partly Vegetated Open-Channel Flows with LDA and PIV Measurements. *Journal of Hydraulic Research,* 39**,** 629-642.

NEZU, I. & RODI, W. 1986. Open-Channel Flow Measurements with a Laser Doppler Anemometer. *Journal of Hydraulic Engineering,* 112**,** 335-355.

NEZU, I., TOMINAGA, A. & NAKAGAWA, H. 1993. Field Measurements of Secondary Currents in Straight Rivers. *Journal of Hydraulic Engineering,* 119**,** 598-614.

NIKORA, V. I. & GORING, D. G. 1998. ADV Measurements of Turbulence: Can We Improve Their Interpretation. *Journal of Hydraulic Engineering,* 124**,** 630-634.

NIKURADSE, J. 1933. Laws of Flow in Rough Pipes (in German; Translation supplied as NACA Technical Memorandum 1292). Available: http://ntrs.nasa.gov/archive/nasa/casi.ntrs.nasa.gov/19930093938_1993093938.pdf [Accessed 09/10/2011].

NORTEK 2004. *Vectrino Velocimeter User Guide*, Nortek AS, Vangkroken 2, NO-1351 RUD, Norway.

OMRAN, M. 2005. *Modelling stage-discharge curves, velocity and boundary shear stress distributions in natural and artificial channels using a depth-averaged approach.* PhD, University of Birmingham.

OMRAN, M. & KNIGHT, D. W. 2006. Modelling the Distribution of Boundary Shear Stress in Open Channel Flows. *In:* FERREIRA, ALVES, LEAL & CARDOSO (eds.) *River Flow 2006.* London: Taylor & Francis Group.

ORACLE. 2010. *BigDecimal (Java 2 Platform SE 5.0)* [Online]. Oracle. Available: http://download.oracle.com/javase/1.5.0/docs/api/java/math/BigDecimal.html [Accessed 5th April 2011 2011].

PADMORE, C. L. 1997. *Physical Biotopes in Representative River Channels: Identification, Hydraulic Characterisation and Application.* PhD, University of Newcastle.

PARSHEH, M., SOTIROPOULOS, F. & PORTE-AGEL, F. 2010. Estimation of Power Spectra of Acoustic-Doppler Velocimetry Data Contaminated with Intermittent Spikes. *Journal of Hydraulic Engineering,* 136**,** 368-378.

PATEL, V. C. 1965. Calibration of the Preston Tube and Limitations on its Use in Pressure Gradients. *Journal of Fluid Mechanics,* 23**,** 185-208.

PAVLOVSKI, N. N. 1931. On a Design Formula for Uniform Flow Movement in Channels with Non-Homogeneous Walls (in Russian). *Transactions of All-Union Scientific Research Institute of Hydraulic Engineering,* 3**,** 157-164.

PERKINS, H. J. 1970. The Formation of Streamwise Vorticity in Turbulent Flow. *Journal of Fluid Mechanics,* 44**,** 721-740.

REYNOLDS, O. 1901. An Experimental Investigation of the Circumstances Which Determine Whether the Motion of Water Shall Be Direct or Sinuous, and of the Law of Resistance in Parallel Channels. *Papers on Mechanical and Physical Subjects.* Cambridge: The University Press (Downloaded from http://www.archive.org/details/papersonmechanic02reynrich).

RHODES, D. G. & KNIGHT, D. E. 1994. Velocity and Boundary Shear in a Wide Compound Duct. *Journal of Hydraulic Research,* 32**,** 743-764.

RICHARDSON, L. F. 1920. The Supply of Energy from and to Atmospheric Eddies. *Proceedings of the Royal Society of London. Series A, Containing Papers of a Mathematical and Physical Character,* 97**,** 354-373.

RICHARDSON, L. F. 1922. *Weather Prediction by Numerical Process*, Cambridge University Press.

SAKSENA, R. 2007. Monsoon Floods: A Recurring Hazard. *Emergency & Humanitarian Action Focus - Flood Fury, A Recurring Hazard.* World Health Organization.

SALIH KIRKGOZ, M. 1989. Turbulent Velocity Profiles for Smooth and Rough Open Channel Flows. *Journal of Hydraulic Engineering,* 115**,** 1543-1560.

SCHLICHTING, H. 1987. *Boundary Layer Theory*, McGraw-Hill.

SCHMITT, F. G. 2007. About Boussinesq's Turbulent Viscosity Hypothesis: Historical Remarks and a Direct Evaluation of its Validity. *Comptes Rendus Mecanique* [Online], 9-10. Available: http://hal.archives-ouvertes.fr/docs/00/26/43/86/PDF/Schmitt-Boussinesq-final.pdf [Accessed 21/09/2011].

SHARIFI, S. 2009. *Application of Evolutionary Computation to Open Channel Flow Modelling.* PhD, University of Birmingham.

SHARIFI, S., KNIGHT, D. W. & STERLING, M. 2008. Modelling Flow Using SKM and a Multi-Objective Evolutionary Algorithm. *In:* ALTINAKAR, KOKPINAR, DARAMA, YEGEN & HARMANCIOGLU (eds.) *River Flow 2008.* Kubaba Congress Department and Travel Services.

SHARIFI, S., STERLING, M. & KNIGHT, D. W. 2009. A novel application of a multi-objective evolutionary algorithm in open channel flow modelling. *Journal of Hydroinfomatics,* 11**,** 31-50.

SHIONO, K. & KNIGHT, D. W. Year. Two Dimensional Analytical Solution for a Compound Channel. *In:* IWASA, Y., TAMAI, N. & WADA, A., eds. 3rd International Symposium on Refined Flow Modelling and Turbulence Measurements, 1988 Tokyo. Universal Academy Press, 503-510.

SHIONO, K. & KNIGHT, D. W. 1991. Turbulent Open-Channel Flows With Variable Depth Across the Channel. *Journal of Fluid Mechanics.*

STERLING, M., BAKER, C. J., BERRY, P. M. & WADE, A. 2003. An Experimental Investigation of the Lodging of Wheat. *Agricultural and Forest Meterology,* 119**,** 149-165.

STERLING, M. & KNIGHT, D. W. 2000. Resistance and Boundary Shear in Circular Conduits with Flat Beds Running Part Full. *Proceedings of the Institution of Civil Engineers, Water & Maritime Engineering,* 142**,** 229-240.

STUDERUS, F. X. 1982. *Sekundärströmungen im offenen Gerinne über rauhen Längsstreifen, Dissertation ETH Nr. 7035.* PhD (in German with English Abstract), Eidgenössischen Technischen Hochschule.

TANG, X., STERLING, M. & KNIGHT, D. W. Year. A General Analytical Model for Lateral Velocity Distributions in Vegetated Channels. *In:* DITTRICH, K., ABERLE & GEISENHANER, ed. River Flow 2010, 2010.

TOMINAGA, A., NEZU, I., EZAKI, K. & NAKAGAWA, H. 1989. Three-Dimensional Turbulent Structure in Straight Open Channel Flows. *Journal of Hydraulic Research,* 27**,** 149-173.

VERMAAS, D. A. 2009. *Mixing Layers in Open Channel Flow with Abrupt Bed Roughness Changes.* MSc Thesis, Wageningen University/Delft University of Technology, The Netherlands.

VERMAAS, D. A., UIJTTEWAAL, W. S. J. & HOITINK, A. J. F. Year. Effect of Heterogeneous Bed Roughness on the Conveyance Capacity of Floodplains. *In:* VAN OS, A. G., ed. NCR-days 2007, 2007. Netherlands Centre for River Studies, 34-35.

VOULGARIS, G. & TROWBRIDGE, J. H. 1998. Evaluation of the Acoustic Doppler Velocimeter (ADV) for Turbulence Measurements. *Journal of Atmospheric and Oceanic Technology,* 15**,** 272-289.

WANG, H. 1972. *Response of a Turbulent Boundary Layer to Lateral Roughness Discontinuities.* PhD, Colorado State University.

WANG, Z.-Q. & CHENG, N.-S. 2005. Secondary Flows Over Artificial Bed Strips. *Advances in Water Resources,* 28**,** 441-450.

WANG, Z.-Q. & CHENG, N.-S. 2006. Time-mean Structure of Secondary Flows in Open Channel with Longitudinal Bedforms. *Advances in Water Resources,* 29**,** 1634-1649.

WHITE, B. L. & NEPF, H. M. 2007. Shear Instability and Coherent Structures in Shallow Flow Adjacent to a Porous Layer. *Journal of Fluid Mechanics,* 593**,** 1-32.

WHITE, B. L. & NEPF, H. M. 2008. A Vortex-Based Model of Velocity and Shear Stress in a Partially Vegetated Channel. *Water Resources Research,* 44.

WU, S. & RAJARATNAM, N. 2000. A Simple Method for Measuring Shear Stress on Rough Boundaries. *Journal of Hydraulic Research,* 38**,** 399-400.

YEN, B. C. 2003. On Establishing Uniform Channel Flow with Tail Gate. *Proceedings of the Institution of Civil Engineers, Water & Maritime Engineering,* 156**,** 281-283.

YUEN, W.-H. K. 1989. *A Study of Boundary Shear Stress, Flow Resistance and Momentum Transfer in Open Channels with Simple and Compound Trapezoidal Cross Section.* PhD, University of Birmingham, UK.

APPENDIX A

This appendix contains a selection of figures to support the statements in Section 8.4.6 regarding the comparability of the conditional time series across the data sets.

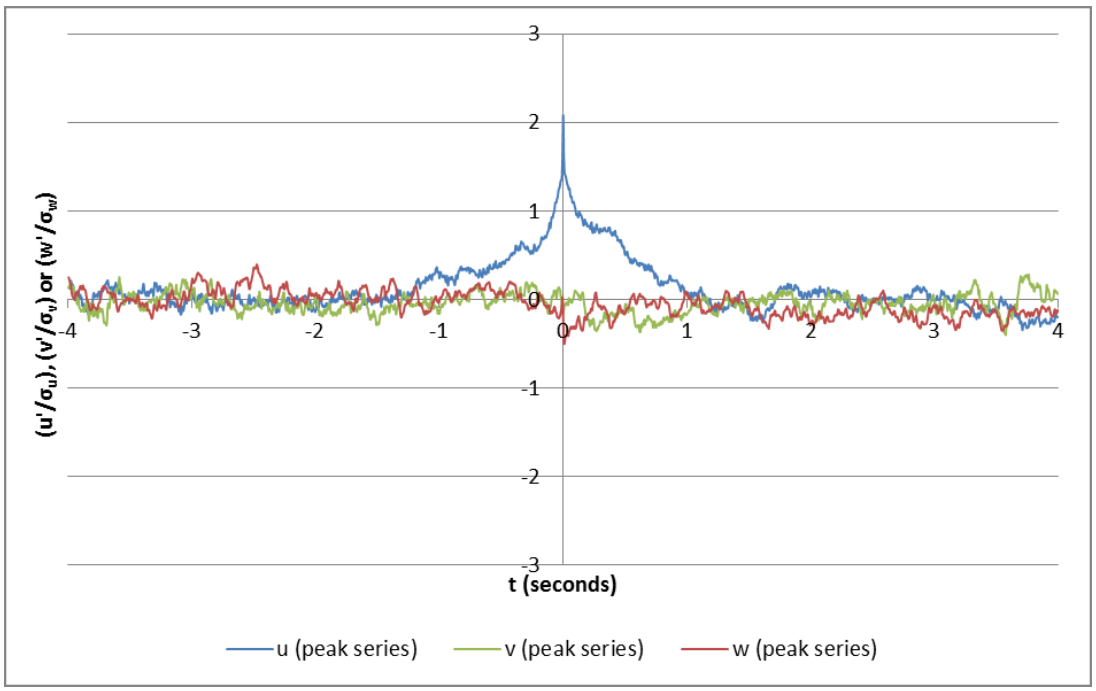

Figure 235: Peak Measurement Ensemble-Mean Time Series (BC1 F2, $y/B = 0.26, z/H = 0.57$)

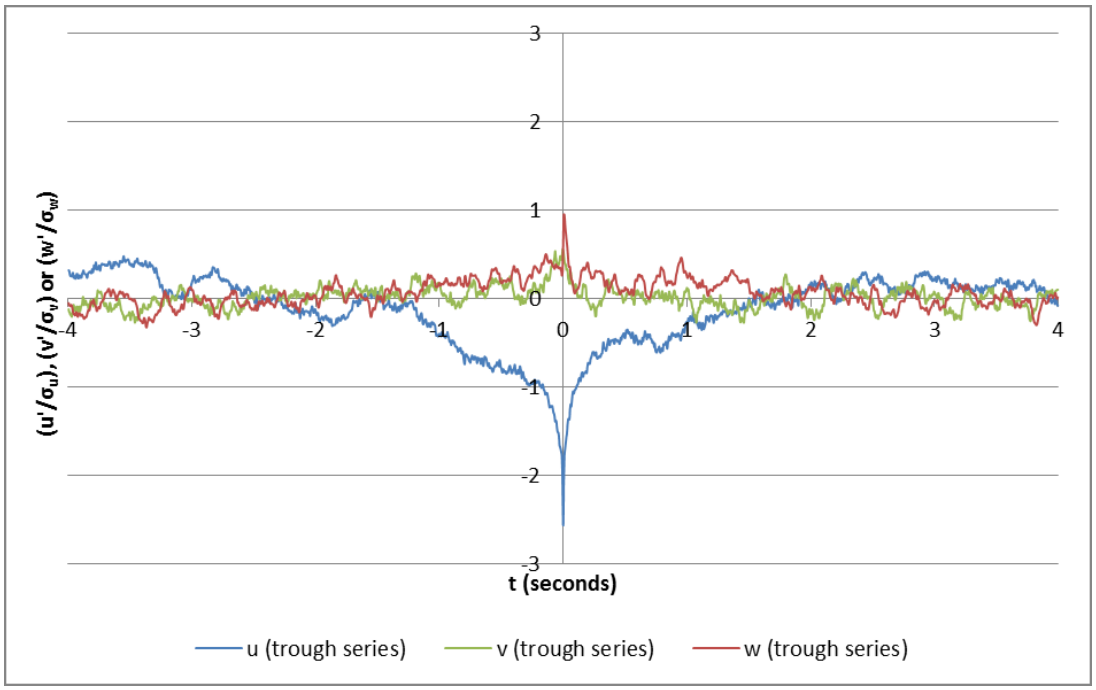

Figure 236: Trough Measurement Ensemble-Mean Time Series (BC1 F2, $y/B = 0.26, z/H = 0.57$)

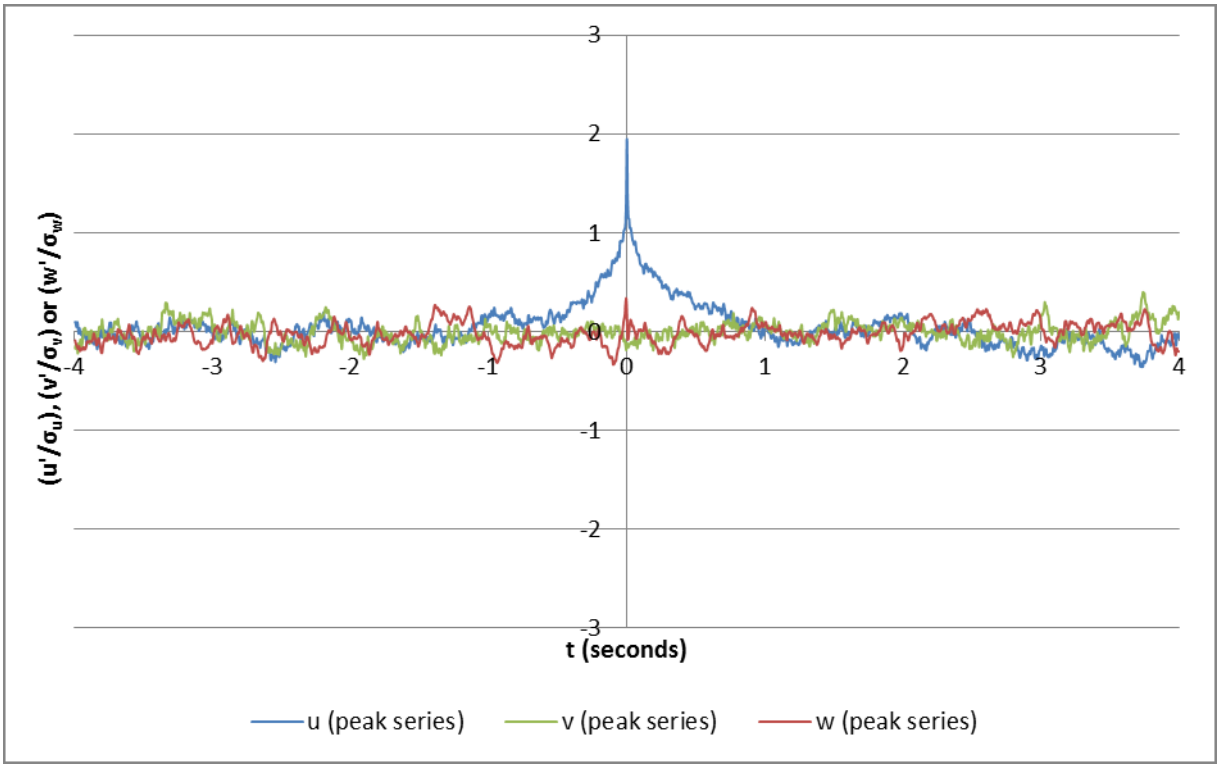

Figure 237: Peak Measurement Ensemble-Mean Time Series (BC2 F1 CS2, $y/B = 0.26, z/H = 0.57$)

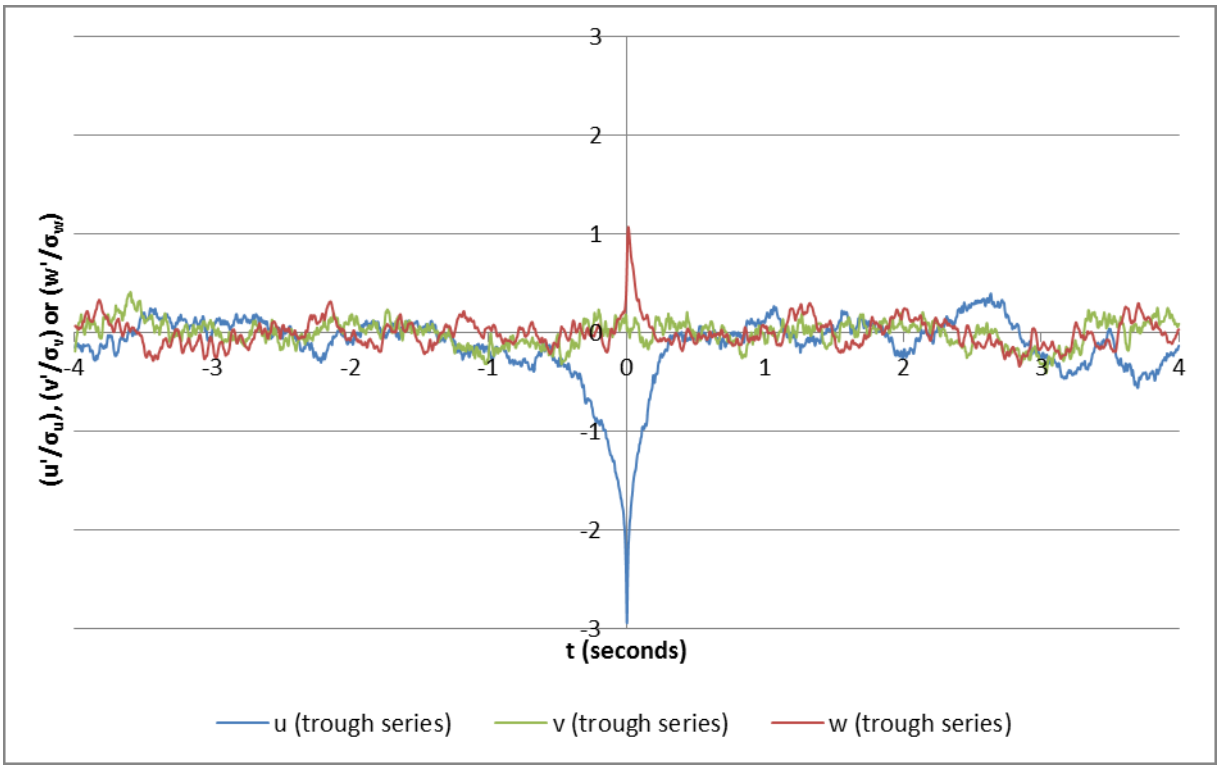

Figure 238: Trough Measurement Ensemble-Mean Time Series (BC2 F1 CS2, $y/B = 0.26, z/H = 0.57$)

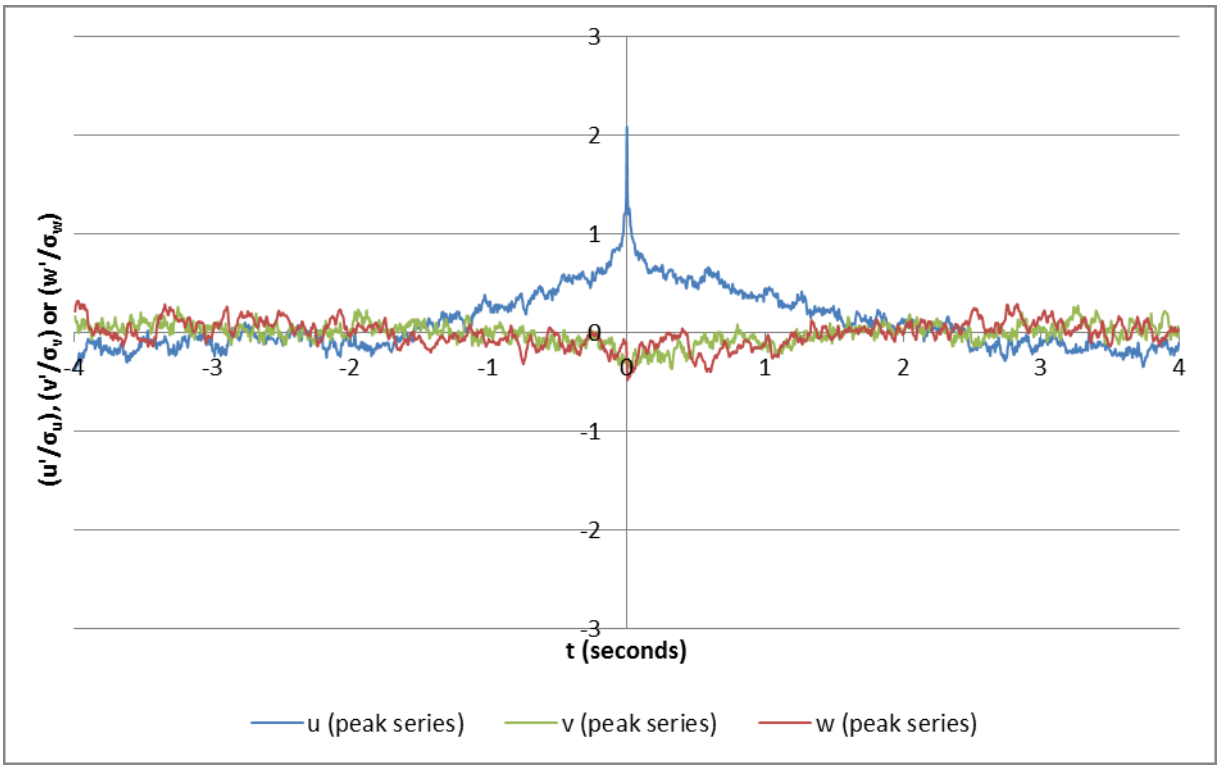

Figure 239: Peak Measurement Ensemble-Mean Time Series (BC2 F2 CS2, $y/B = 0.26, z/H = 0.57$)

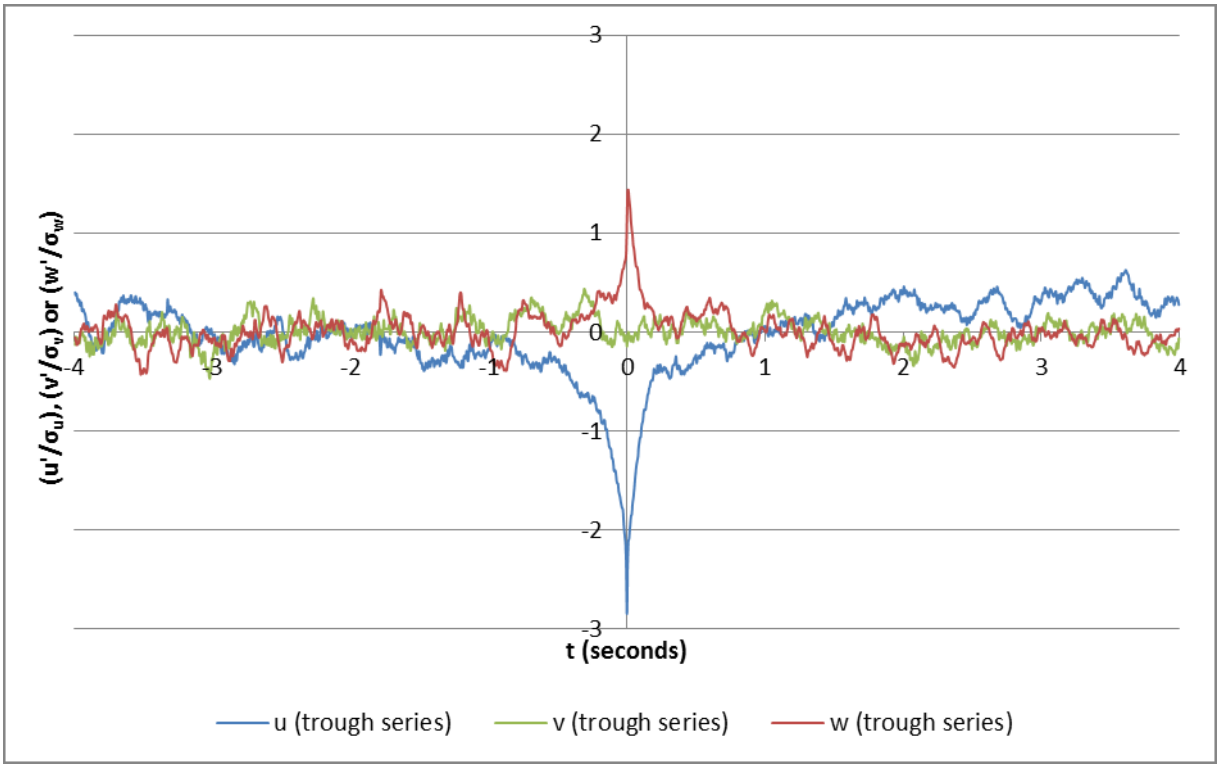

Figure 240: Trough Measurement Ensemble-Mean Time Series (BC2 F2 CS2, $y/B = 0.26, z/H = 0.57$)

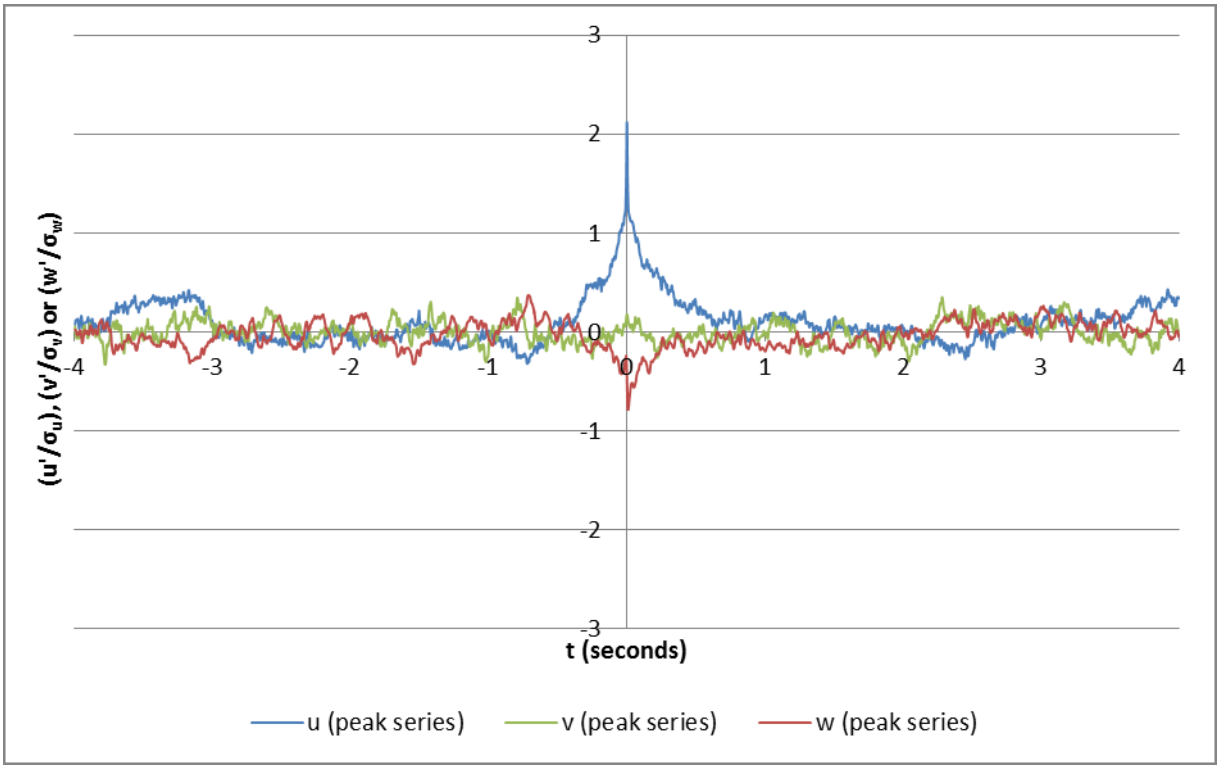

Figure 241: Peak Measurement Ensemble-Mean Time Series (BC2 F1 CS2, $y/B = 0.50, z/H = 0.57$)

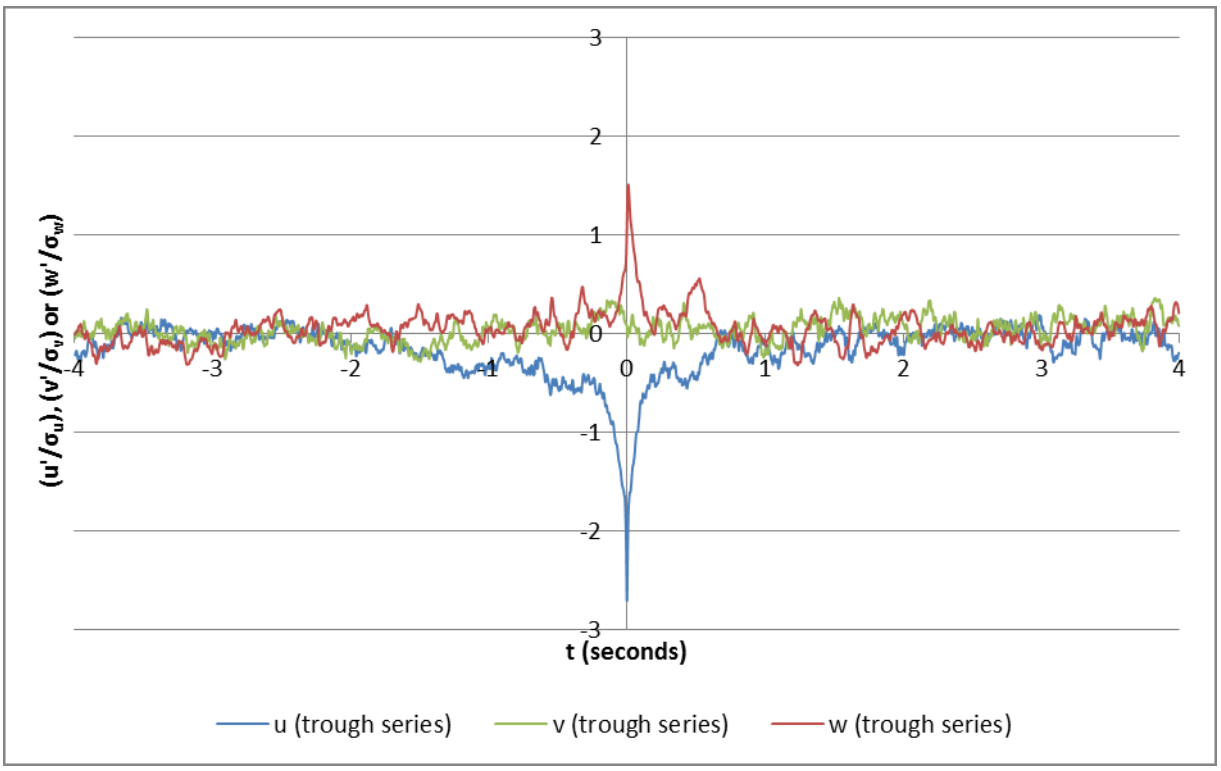

Figure 242: Trough Measurement Ensemble-Mean Time Series (BC2 F1 CS2, $y/B = 0.50, z/H = 0.57$)

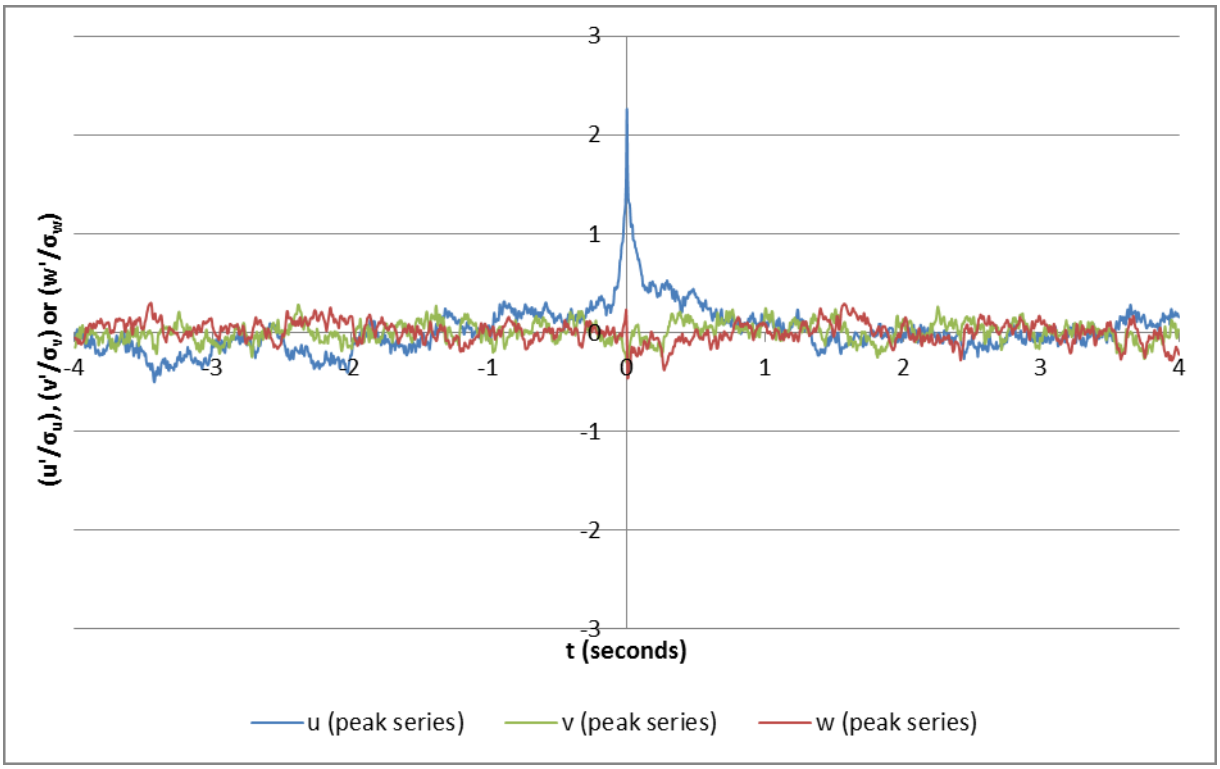

Figure 243: Peak Measurement Ensemble-Mean Time Series (BC2 F2 CS2, $y/B = 0.50, z/H = 0.57$)

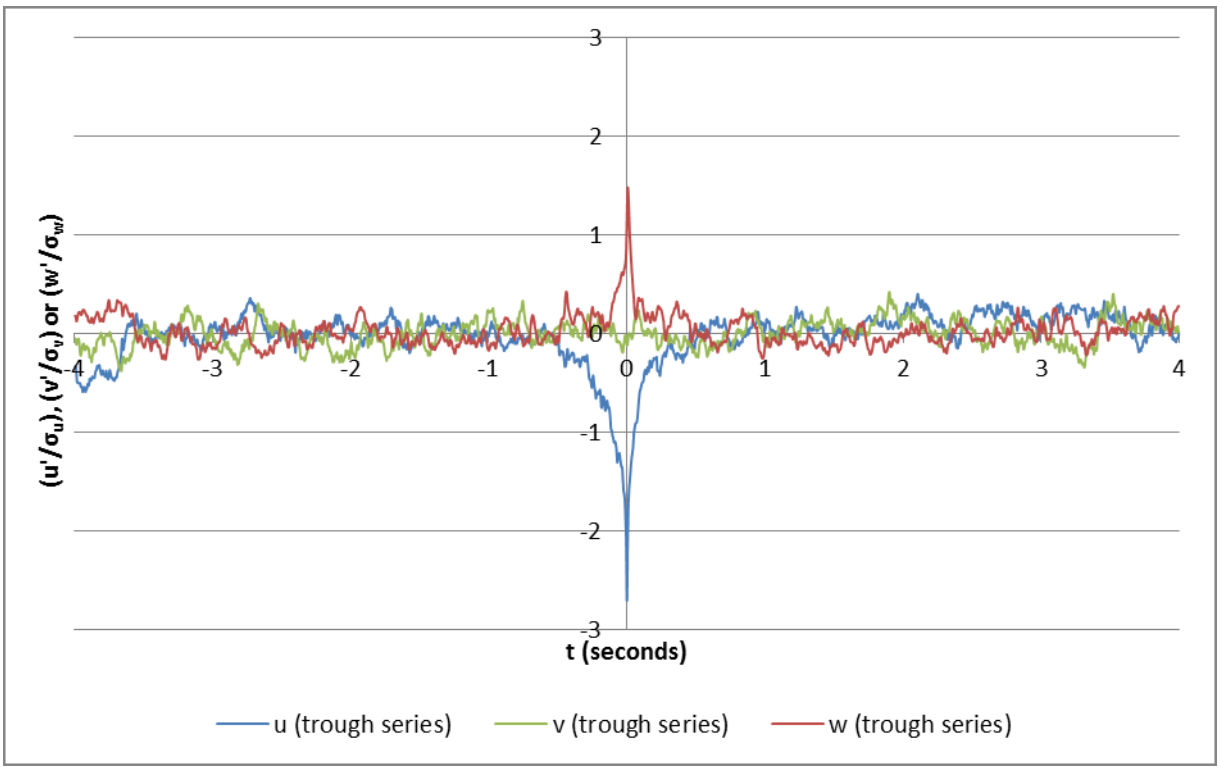

Figure 244: Trough Measurement Ensemble-Mean Time Series (BC2 F2 CS2, $y/B = 0.50, z/H = 0.57$)

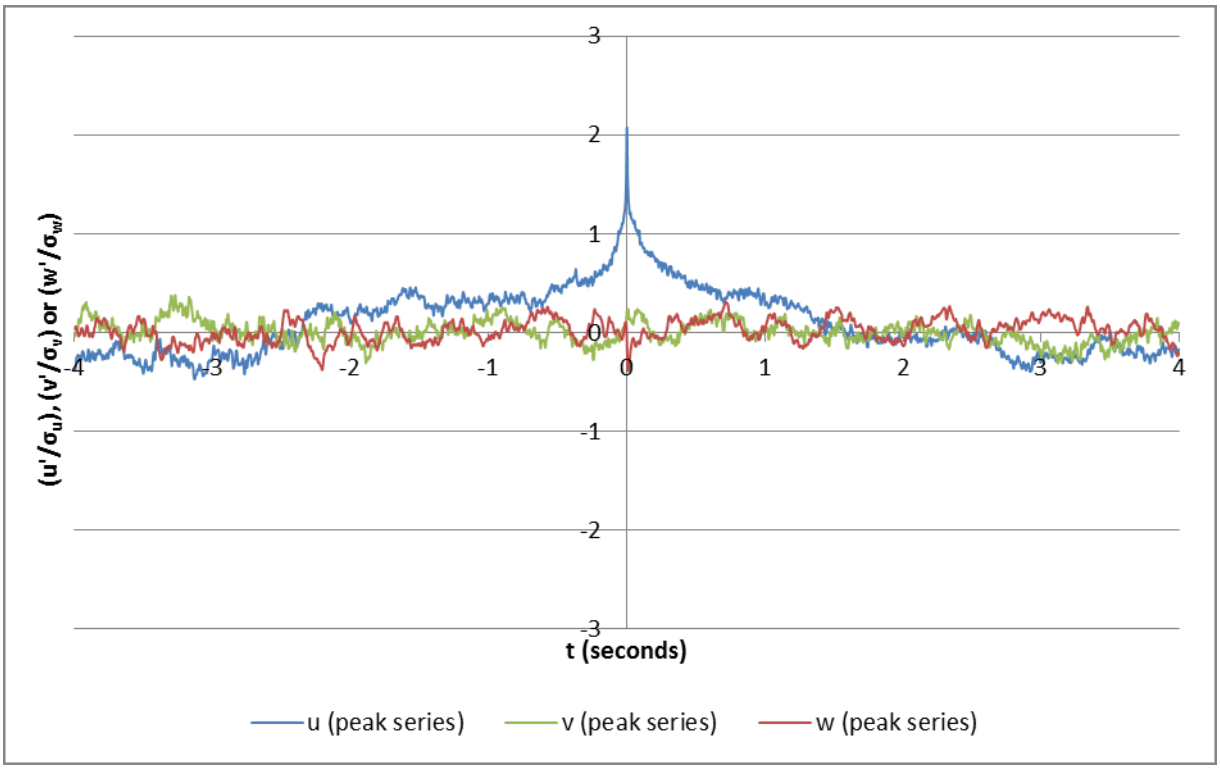

Figure 245: Peak Measurement Ensemble-Mean Time Series (BC2 F1 CS2, $y/B = 0.74, z/H = 0.57$)

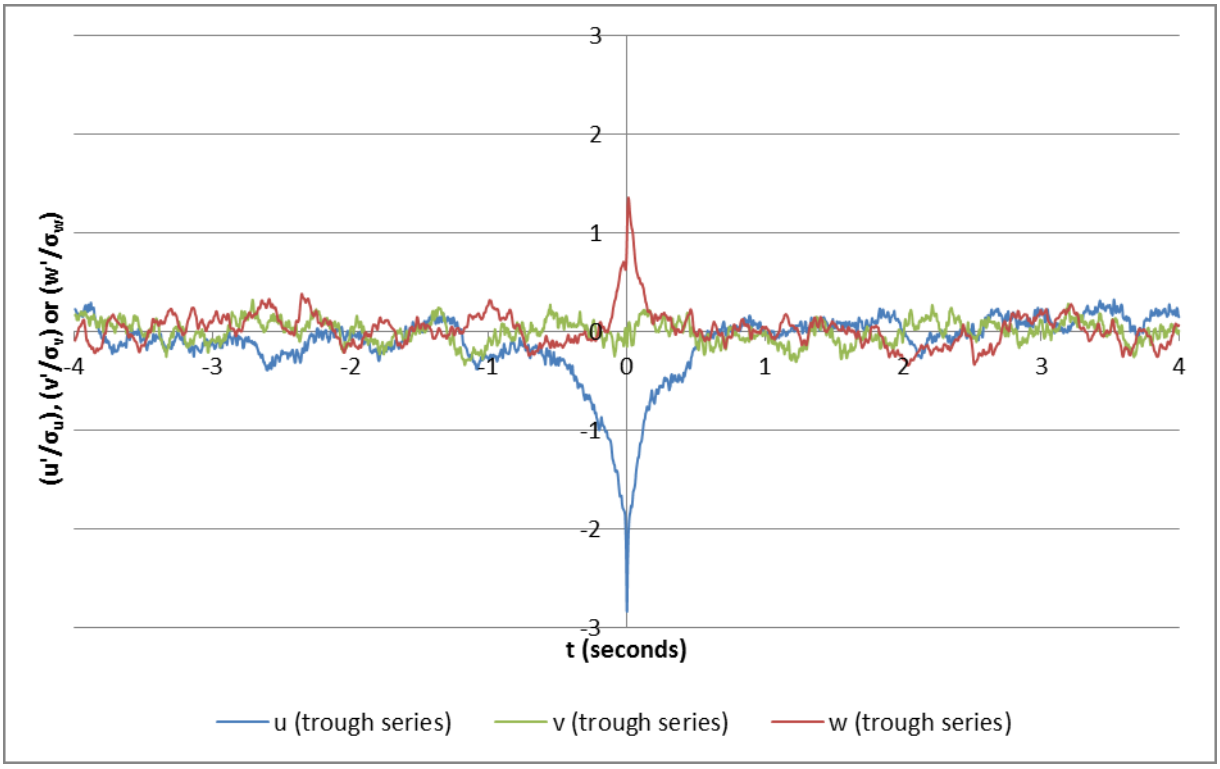

Figure 246: Trough Measurement Ensemble-Mean Time Series (BC2 F1 CS2, $y/B = 0.74, z/H = 0.57$)

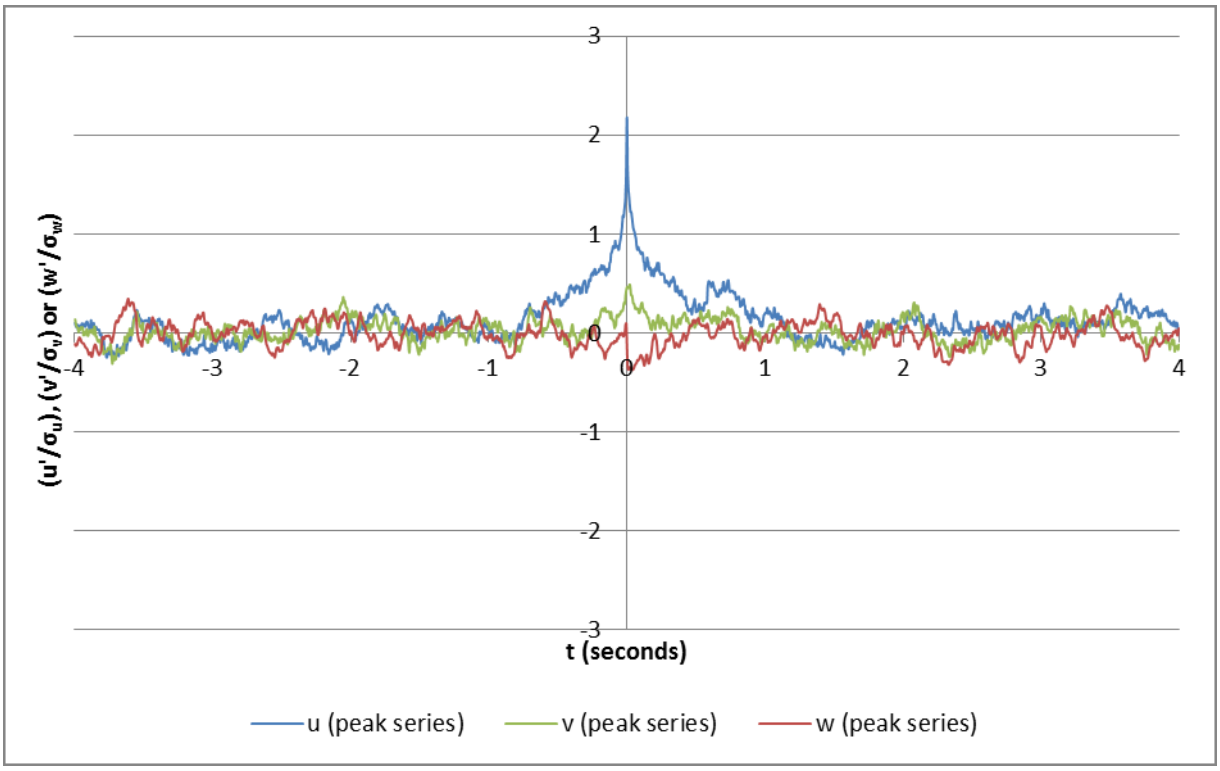

Figure 247: Peak Measurement Ensemble-Mean Time Series (BC2 F2 CS2, $y/B = 0.74, z/H = 0.57$)

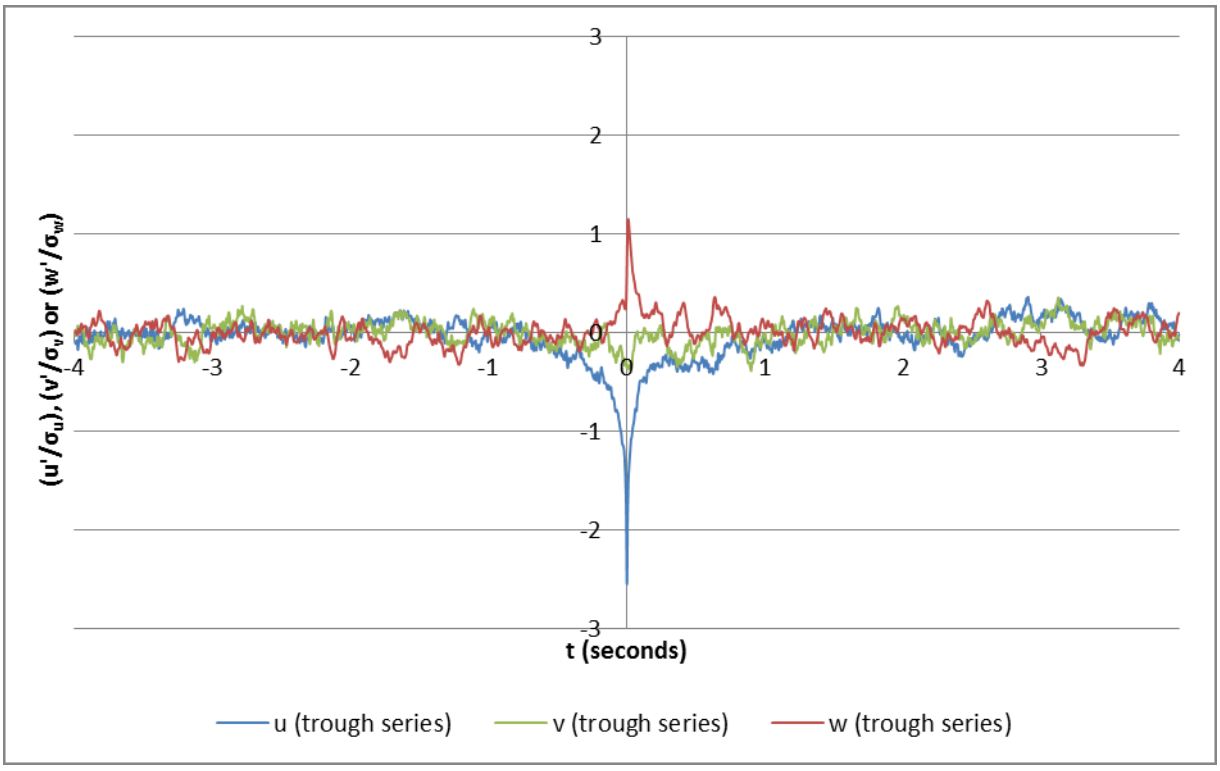

Figure 248: Trough Measurement Ensemble-Mean Time Series (BC2 F2 CS2, $y/B = 0.74, z/H = 0.57$)

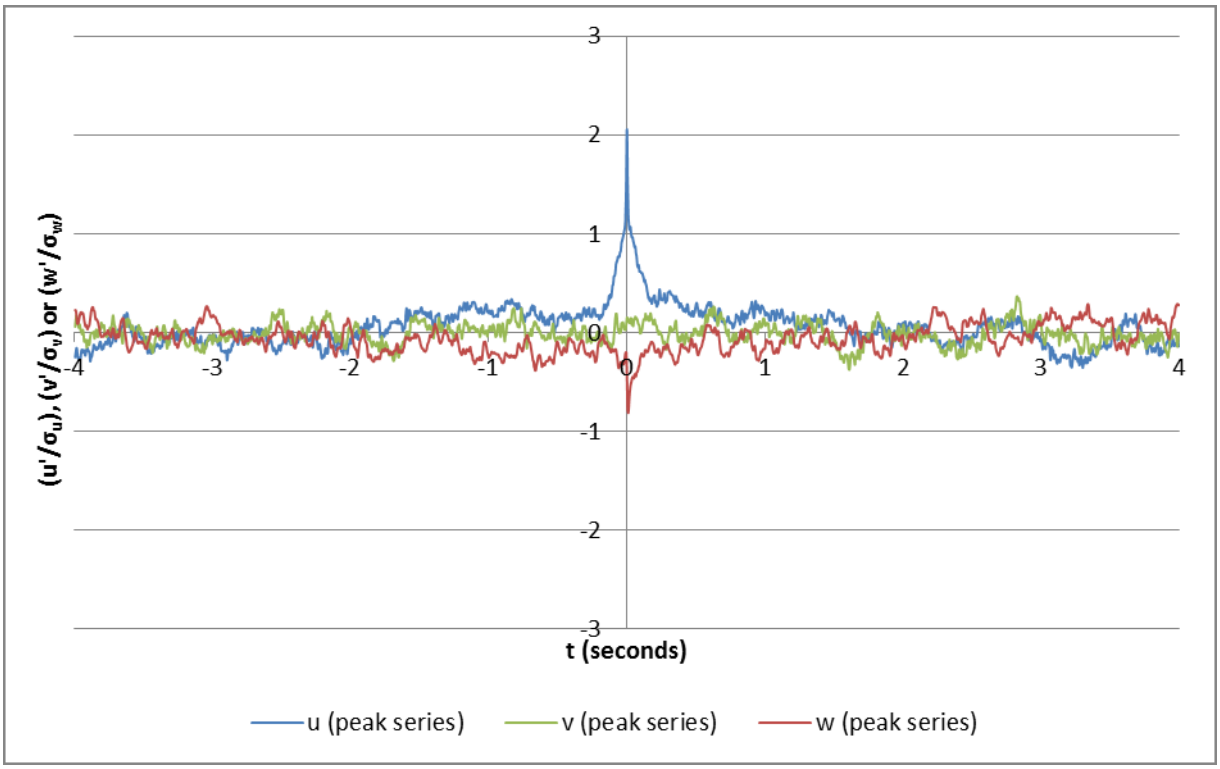

Figure 249: Peak Measurement Ensemble-Mean Time Series (BC2 F1 CS4, $y/B = 0.50, z/H = 0.57$)

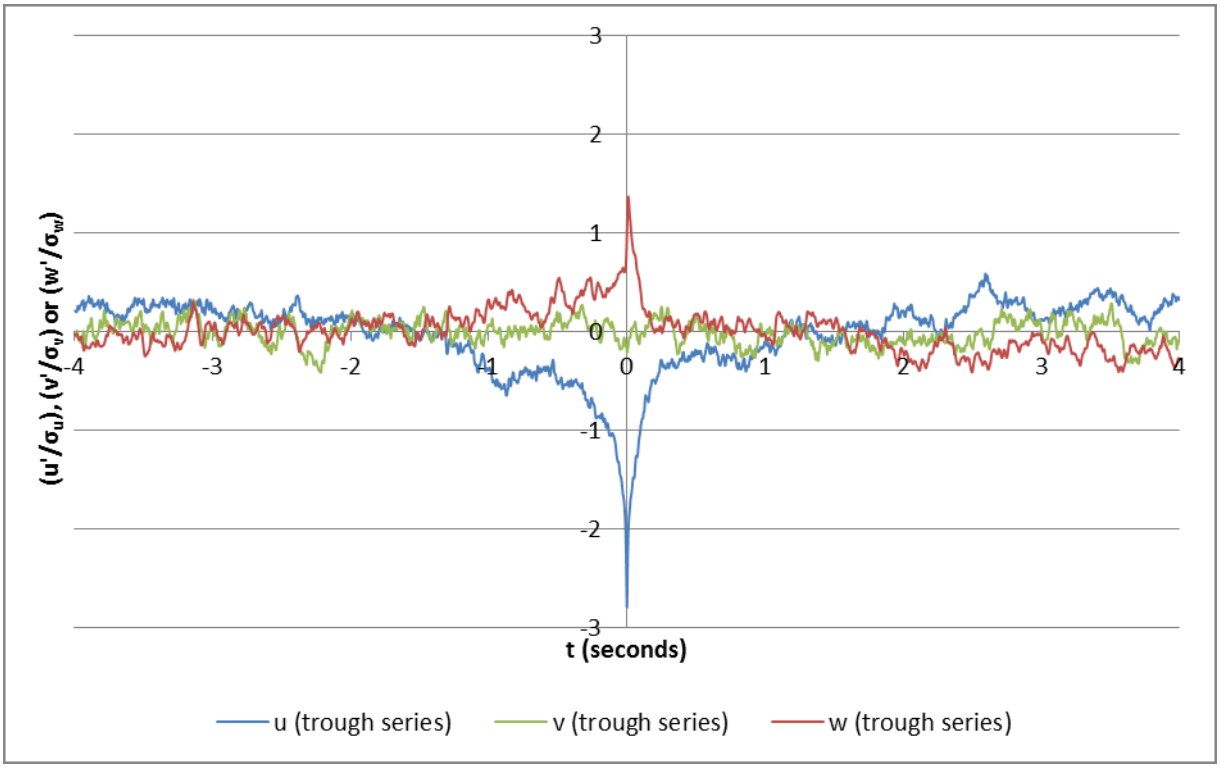

Figure 250: Trough Measurement Ensemble-Mean Time Series (BC2 F1 CS4, $y/B = 0.50, z/H = 0.57$)

APPENDIX B

This appendix contains abstracts of the author's published papers - two conference papers and one journal paper. These are:

(i) "Turbulent Flow Structures in a Heterogeneous Channel and their Effects on Conveyance Characteristics" – Presented at the First European IAHR Congress, Edinburgh, 4th May 2010

(ii) "Open-Channel Discharge Characteristics and Secondary Flow Development Over a Biotope-Scale Heterogeneous Channel Bed" – Presented at the 6th IASME / WSEAS International Conference on Water Resources, Hydraulics and Hydrology, 23rd February 2011

(iii) "An Experimental Study of Turbulence in a Heterogeneous Channel" (Proceedings of ICE – Water Management; In Press)

TURBULENT FLOW STRUCTURES IN A HETEROGENEOUS CHANNEL AND THEIR EFFECTS ON CONVEYANCE CHARACTERISTICS

M. Jesson, M. Sterling & J. Bridgeman
School of Civil Engineering, University of Birmingham, Birmingham, UK.
email: maj727@bham.ac.uk

ABSTRACT

Within natural rivers, sediment and vegetation can vary significantly from reach to reach and within a cross section. As a result, lateral bed heterogeneity is a feature of almost all in-bank river flow. Despite this common occurrence, there is a lack understanding of how such changes in roughness can alter the overall resistance of a particular reach of river and how this in turn affects its conveyance capacity.

This paper presents the preliminary results of a research programme aimed at characterising flow in a heterogeneous channel. Rather than focusing simply on adjustments to empirical flow parameters such as Manning's n and roughness coefficients, the research aims to identify turbulent structures and secondary flows within the channel, enabling a physical understanding of the effects of the heterogeneous bed to be evaluated. In order to achieve this, an idealised heterogeneous channel bed was constructed in a 22m experimental channel at the University of Birmingham. Detailed 3-D velocity and boundary shear stress measurements were recorded at more than 500 grid points over a cross-section of the channel at a fixed flow rate. From these measurements, the mean parameters and turbulent velocity fluctuations were determined. Quadrant-Hole analysis was used to highlight the propagation of turbulence from the channel bed.

Open-Channel Discharge Characteristics and Secondary Flow Development Over a Biotope-Scale Heterogeneous Channel Bed

MICHAEL JESSON, JOHN BRIDGEMAN &. MARK STERLING
School of Civil Engineering
University of Birmingham
Birmingham
UNITED KINGDOM
maj727@bham.ac.uk

Abstract: Understanding the effect of variations in bed roughness on overall channel resistance plays an important, though little researched, part in accurately modelling river flow. Changes in bed material, from sediment to gravel for example, mean that river bed roughness is generally heterogeneous, with both lateral and streamwise variation. The research described herein extends the authors' previous work, which experimentally investigated the effect of full-length, longitudinal strip roughness, by examining the flow in a channel with both lateral and streamwise step changes in bed roughness.

An idealised heterogeneous channel with a "checkerboard" bed roughness pattern was constructed in a 22m long, 0.6m wide experimental channel at the University of Birmingham. When scaled with respect to the channel width, the streamwise length of each section approximately corresponds to changes in bed roughness which may be observed in a natural river. The structure of the 3-D velocity field has been measured at a number of channel cross-sections and has enabled the development of the mean streamwise velocity distribution and secondary flow cells to be observed. With the current roughness distribution, the development of secondary flow cells near the rough-smooth boundary appears to occur over a relatively short distance. While detailed analysis of the results is in the preliminary stages, a noticeable difference in the stage-discharge curves of the full-length and checkerboard configurations is seen, particularly at lower discharges, where differences of up to 15% are observed.

Key-Words: Open-channel, heterogeneous, secondary flow, turbulence, Quadrant-Hole, stage-discharge

An Experimental Study of Turbulence in a Heterogeneous Channel

Michael Jesson, BSc, MSc; PhD Student
Dr Mark Sterling*, BEng, PhD, CEng, CEnv, FRMetS, MIAgrE, MICE; Reader in Fluid Dynamics
Dr John Bridgeman, BEng, MSc, PhD, CEng, CSci, MICE, FCIWEM; Reader in Environmental Engineering
School of Civil Engineering, University of Birmingham, Birmingham, UK.
**Corresponding Author: email: m.sterling@bham.ac.uk; 0121 414 5145*

Abstract

This paper examines the velocity field in an idealised heterogeneous open channel during normal flow conditions, corresponding to two different subcritical flow conditions (discharges of 0.040 m^3/s and 0.056m^3/s, with corresponding Froude numbers 0.51 and 0.57). The bed of the channel is formed of two full-length, longitudinal strips of equal width, a smooth section constructed from PVC and a rough section constructed from gravel (d_{72} = 10mm). The results indicate that the turbulence appears to propagate vertically from the rough bed and horizontally over the rough-smooth boundary. There is also evidence to suggest that the turbulent momentum transfer is maximised at the rough/smooth boundary. Secondary flow structures are seen to exist due to the rough-smooth boundary which provide another mechanism for momentum transfer. These transfer mechanisms are of importance in understanding the effect of a heterogeneous channel bed on open-channel flow.

APPENDIX C

This appendix contains details of the derivation of the analytical solution to the SKM for a constant depth region, the form used in this research.

The general SKM equation is:

$$\frac{\partial H(\rho UV)_d}{\partial y} = \rho g H S_0 + \frac{\partial H\bar{\tau}_{yx}}{\partial y} - \tau_b \left(1 + \frac{1}{s^2}\right)^{\frac{1}{2}} \tag{41}$$

In a constant depth region this simplifies to:

$$\frac{\partial H(\rho UV)_d}{\partial y} = \rho g H S_0 + \frac{\partial H\bar{\tau}_{yx}}{\partial y} - \tau_b \tag{89}$$

Substitution from (43), (44) and (45) gives:

$$\Gamma = \rho g H S_0 + \frac{\partial H \rho \lambda H U_* \frac{\partial U_d}{\partial y}}{\partial y} - \tau_b \tag{90}$$

and further subsitution from (9), and the definition of U_*, gives:

$$\Gamma = \rho g H S_0 + \frac{\partial \rho \lambda H^2 \left(\frac{U_d^2 f}{8}\right)^{1/2} \frac{\partial U_d}{\partial y}}{\partial y} - \frac{\rho U^2 f}{8} \tag{91}$$

which, noting that $U_d \frac{\partial U_d}{\partial y} = \frac{1}{2}\frac{\partial U_d^2}{\partial y}$, becomes:

$$\Gamma = \rho g H S_0 + \frac{\rho \lambda H^2}{2}\left(\frac{f}{8}\right)^{1/2} \frac{\partial^2 U_d^2}{\partial y^2} - \frac{\rho U_d^2 f}{8} \tag{92}$$

or equivalently:

$$\left(\frac{\rho \lambda H^2}{2}\left(\frac{f}{8}\right)^{1/2}\right)\frac{\partial^2 U_d^2}{\partial y^2} + 0\frac{\partial U_d^2}{\partial y} + \left(-\frac{\rho f}{8}\right)U_d^2 + (\rho g H S_0 - \Gamma) = 0 \tag{93}$$

which is of the form:

$$a\frac{\partial^2 U_d^2}{\partial y^2} + b\frac{\partial U_d^2}{\partial y} + cU_d^2 + d = 0 \tag{94}$$

The complimentary function is the solution to the homogeneous equation:

$$a\frac{\partial^2 U_d^2}{\partial y^2} + b\frac{\partial U_d^2}{\partial y} + cU_d^2 = 0 \tag{95}$$

which may be shown to be:

$$U_d^2 = A_{i1}e^{\gamma y} + A_{i2}e^{-\gamma y} \tag{96}$$

where A_{i1} and A_{i2} are the SKM solution constants introduced in (47) and γ is the solution to the quadratic equation:

$$am^2 + bm + c = 0 \tag{97}$$

which is the value stated in (49):

$$\gamma = \left(\frac{2}{\lambda}\right)^{\frac{1}{2}}\left(\frac{f}{8}\right)^{\frac{1}{4}}\frac{1}{H} \tag{49}$$

$$\beta = \frac{\Gamma}{\rho g S_0 H}$$

With d being a constant, the particular integral is likely to be a constant, $U^2 = k$.

Substituting this into (94) gives:

$$ck + d = 0 \Rightarrow k = -\frac{d}{c} = \frac{8gS_0H}{f}(1-\beta) \tag{98}$$

Thus the full solution, the sum of the complementary function and the particular integral, is (47):

$$U_d = \left[A_{i1}e^{\gamma y} + A_{i2}e^{-\gamma y} + \frac{8gS_0H}{f}(1-\beta)\right]^{\frac{1}{2}} \tag{99}$$